Error characterisation and reduction in trapped ion quantum computers

One Woman's Guide to the Ion-ing

CLAIRE L. EDMUNDS

Doctor of Philosophy

Supervisor: Prof. Michael J. Biercuk
Associate Supervisor: Dr. Cornelius Hempel

A thesis submitted in fulfilment of
the requirements for the degree of
Doctor of Philosophy

School of Physics
Faculty of Science
The University of Sydney
Australia

May 2021

"Science is magic that works."

- Kurt Vonnegut, *Cat's Cradle*

Abstract

For the field of quantum computing and technology to continue its growth and begin to solve truly useful problems, it must overcome the limitations imposed by errors affecting quantum devices. Leading modern devices can be classed as "noisy intermediate-scale quantum" or NISQ devices. These are devices that have not realised fault-tolerance nor utilise error correction, but nonetheless could solve genuinely useful, classically intractable problems. However, the scalability and reliability of current NISQ devices is limited by the impact of errors. This thesis uses the principles of quantum control to work towards improving quantum technology reliability. By characterising the errors affecting a quantum device and tailoring robust, dynamic control solutions, I am able to achieve superior performance in a trapped-ion quantum device compared to its baseline or primitive operation. I begin by characterising our experimental system, a trapped $^{171}\mathrm{Yb}^{+}$ ion. Following on, I demonstrate three quantum control techniques. First, I work to improve the measurement fidelity of a trapped-ion hyperfine qubit using electron shelving to a metastable level. Second, this work develops and demonstrates an error characterisation tool to diagnose the correlation properties of errors affecting a quantum device. Building from this, I demonstrate the use of dynamically corrected gates to both improve single-qubit gate fidelities and reduce error correlations temporally between gates and spatially between qubits. Finally, I discuss and implement a more robust and flexible two-qubit entangling Mølmer-Sørensen gate using phase modulation of the interaction laser. All of this work adds to the "toolkit" of quantum control and can be used to improve both the reliability of modern device performance – in particular by reducing susceptibility to noise – and assist with building up to larger numbers of qubits and gates by tailoring more robust, scalable entangling gates between qubits.

Acknowledgements

"You meet saints everywhere. They can be anywhere. They are people behaving decently in an indecent society."

- Kurt Vonnegut

This thesis is the culmination of the last five year's work and none of it has been done in isolation. I owe everything here to the guidance, friendship and mentoring that I have received throughout my PhD both professionally and personally. I would like to take the time to thank all of these people whose support has made this PhD possible. There are more contributions than I can name, and any omissions are entirely faults of my own. They say it takes a village to raise a child, and much the same could be said about completing a PhD.

This is my village.

To my family. First and foremost, now and forever, thank you to my parents Ian and Hayley. Nothing I have done would be possible without the incredible life you have given me. You are my role models, my confidants, and the two kindest, most generous and brilliant people that I have ever met. Alongside my parents, my incredible siblings Sr Susanna, Julie, John and Patrick continue to support and guide me. Whether it's conversations about physics, food or philosophy, I know I can count on all of you. To all my family, my wonderful grandparents, my cousins, aunts and uncles, nieces and nephew, thank you. I would not be the person I am without you. To Papa and Big Nan, thank you for your love. I wish I could have celebrated this with you.

To Alex, there is nothing I can write here that can express what you mean to me and how much your companionship has supported me. I look forward to our next steps. Thank you.

To my comrades. I have had the pleasure and privilege of working alongside some of the most talented physicists I have ever met. Thank you all for your help, your company, your conversation and your

friendship. It has meant the world to me. In particular, to Riddhi, Harrison, Virginia, Christian, Jen, Calida, Claire, Ashwin, Federico, Alex, Trung, Robert and Alex, thank you.

A truly special thank you has to be given to my lab partner and irreplaceable friend for the last six years. Alistair, I don't know if I could have done this without you. There's no one I'd rather have done it with – our conversations about physics, politics, philosophy and veganism helped get me through it. Pour yourself a cold one for me.

To my teachers. None of this – my PhD, my education, my passion – would be possible without my mentors and teachers who have both taught and inspired me. In particular, to Cornelius, Ting Rei and Mike. Your guidance has been invaluable; I have learnt so much from all of you; one such thing is my overuse of semicolons; I still think it's an excellent punctuation mark. To Cornelius, thank you – you have been the mentor every student dreams of. Knowledgeable, inspiring and patient, I owe this PhD to your constant support.

To my friends. All of our nights and coffees and conversations have helped me through this. A huge thank you to Declan, Evie, Jarrah, Katy, Laura, Maggie, Mike, Paddy, Pip, Rupert and Tom.

To my communities. This work would have not been possible in the most literal sense without the organisations and communities that have made it possible – physically, financially, and socially. The University of Sydney and the NMI gave me a home away from home in world-class labs. EQUS made me feel like I'm a part of something incredible and offered me amazing opportunities. Thank you. I also owe IARPA, the Australian Academy of Science, and Hugh and Anne Harley a great debt of gratitude for their financial support that made this possible.

To my caffeinaters. Over all these years, thank you for keeping me wired and inspired.

Thank you all for believing in me.

Statement of Contribution

This thesis is a combination of pre-published and peer-reviewed manuscripts, and new contributions. Here, I detail the relevant origins and contributions for each chapter individually.

The first and final chapters of this thesis, Chapter 1 and Chapter 9, represent new work that was written entirely by me for the purpose of this thesis. The experimental setup chapter, Chapter 2, is largely new material written by me for this thesis, but also samples from the experimental setup components of papers that I published throughout my PhD, which form later chapters in my thesis.

Chapter 3: Precision measurements in $^{171}\mathrm{Yb}^+$ for improved state detection

> **Publishing status**: This chapter constitutes two manuscripts currently being reviewed: "Scalable hyperfine qubit state detection via the $^2\mathrm{S}_{1/2} - {}^2\mathrm{D}_{5/2}$ transition in $^{171}\mathrm{Yb}^+$" [**1**], and "Precision Characterization of the $^2\mathrm{D}_{5/2}$ State and Quadratic Zeeman Coefficient in $^{171}\mathrm{Yb}^+$" [**2**].
>
> **Author list:** C. L. Edmunds, T. R. Tan, A. R. Milne, A. Singh, M. J. Biercuk, C. Hempel
>
> **Contributions:** The project was led by T. R. Tan, C. Hempel and me. C. Hempel conceived the original research direction for this project. A. Singh, C. Hempel and I developed the new experimental setup including building the 411 nm and 760 nm laser beam-paths and putting the high finesse locking cavities under vacuum. A. R. Milne and I wrote the new control software to control the experiments. T. R. Tan and I jointly performed the atomic physics experiments measuring the properties of $^{171}\mathrm{Yb}^+$. I performed the experiments characterising and improving the state detection results. I wrote the analysis code and performed the data analysis for the atomic physics and state detection results. The text in this chapter was written by me, with my coauthors C. Hempel, T. R. Tan and M. J. Biercuk. I created all of the figures within this chapter.

Chapter 4: Modelling quantum verification protocols in the presence of temporally correlated noise

Publishing status: This chapter is primarily based on the Supplementary Material of "Experimental quantum verification in the presence of temporally correlated noise" published in npj Quantum Information Volume 4, Article number: 7 (2018) [**3**], and the Appendix of "Dynamically corrected gates suppress spatio-temporal error correlations as measured by randomised benchmarking" published in Phys. Rev. Research 2, 013156 (2020) [**4**].

Author list: C. L. Edmunds, S. Mavadia, C. Hempel, R. Harris, H. Ball, T. M. Stace, M. J. Biercuk

Contributions: The work and text from the former project (Supplementary Material of "Experimental quantum verification in the presence of temporally correlated noise") was a collaboration, with contributions from S. Mavadia, H. Ball, T. M. Stace and me. In particular, I developed the theoretical modifications from H. Ball and T. M. Stace's original model to make it appropriate for use in experiments by considering the physical measurement protocol and error channel. The theoretical work from the second source (Appendix of "Dynamically corrected gates suppress spatio-temporal error correlations as measured by randomised benchmarking") was a collaboration between R. Harris, T. M. Stace and me, with R. Harris and me leading the development. The text from the second work was written primarily by me. The research direction for both projects was conceived by M. J. Biercuk.

Chapter 5: Experimental quantum verification in the presence of temporally correlated noise

Publishing status: This chapter is reproduced with minimal changes from the manuscript "Experimental quantum verification in the presence of temporally correlated noise" published in npj Quantum Information volume 4, Article number: 7 (2018) [**3**].

Author list: S. Mavadia*, C. L. Edmunds*, C. Hempel*, H. Ball, F. Roy, T. M. Stace, M. J. Biercuk

Contributions: S. Mavadia, C. Hempel and I contributed equally to this project. M. J. Biercuk conceived the original research direction for this project. S. Mavadia and I led the experimental setup, including the optical setup and microwave control. I wrote and implemented the control software to perform the experiments. S. Mavadia and I led the experimental data collection and data analysis. C. Hempel led experimental design, simulations, and analysis of GST. The theoretical analyses and calculations were performed by H. Ball, F. Roy, T. M. Stace and me.

M. J. Biercuk led the paper writing along with co-authors C. Hempel, S. Mavadia and me. S. Mavadia, C. Hempel and I jointly produced the figures.

Chapter 6: Dynamically corrected gates suppress spatio-temporal error correlations as measured by randomised benchmarking

Publishing status: This chapter is reproduced with minimal changes from "Dynamically corrected gates suppress spatio-temporal error correlations as measured by randomised benchmarking" published in Phys. Rev. Research 2, 013156 (2020) [**4**].

Author list: C. L. Edmunds, C. Hempel, R. J. Harris, V. Frey, T. M. Stace, and M. J. Biercuk

Contributions: This project was led by me alongside my coauthors C. Hempel, R. J. Harris, V. Frey, T. M. Stace, and M. J. Biercuk. M. J. Biercuk conceived the original research direction for this project. The experimental setup including optical setup, microwave control, and the control software used to perform experiments was led by me with C. Hempel and V. Frey. I performed the experimental data taking and analysis, with contributions from V. Frey for the block-correlated data in Fig. 6.5. The theoretical work was led by R. J. Harris, T. M. Stace and me. I created the paper figures, and led the paper writing along with my coauthors C. Hempel and M. J. Biercuk. The DCG robustness figure (Fig. 6.3) and the text in Section 6.3.1, as well as the RB error homogenisation figure (Fig. 6.7) were published as a part of a separate manuscript by Ball et al. [**5**] to which I contributed this data.

Chapter 7: Theoretical background about the Mølmer-Sørensen gate

Publishing status: This chapter is partially reproduced from the Supplementary Material of "Phase-modulated entangling gates robust to static and time-varying errors" published in Physical Review Applied **13**, 024022 (2020) [**6**].

Author list: C. L. Edmunds

Contributions: The text in this chapter, and in the original Supplementary Material, was written by me. In this chapter, I derive the axial and transverse motional mode frequencies and eigenvectors, which were essential to the work in the following experimental chapter. This work has not been previously published. This is an extension of a similar calculation that only considered the axial motion, published by D. F. V. James in 1998 [**7**]. The calculation of the observable evolution after applying the MS gate was originally derived by Kirchmair et al. [**8**] in 2009 to describe the entanglement of two ions via one shared mode of motion. In this chapter I extend the calculation to consider entangling any two ions within an N ion register, and with coupling to any number of the $3N$ motional modes. This calculation was partially published in an abridged form in the Supplementary Material of "Phase-modulated entangling gates robust to static and time-varying errors", only considering two ions. Finally, the analytic filter function for detuning noise is derived by me, and was published in the Supplementary Materials. Similar work for amplitude noise was derived by Green et al. [**9**] in 2015.

Chapter 8: Phase-modulated entangling gates robust to static and time-varying errors

Publishing status: This chapter is reproduced with minor changes from "Phase-modulated entangling gates robust to static and time-varying errors" published in Physical Review Applied **13**, 024022 (2020) [**6**].

Author list: A. R. Milne*, C. L. Edmunds*, C. Hempel*, F. Roy, S. Mavadia, and M. J. Biercuk

Contributions: I contributed equally to this work with two other lead authors A. R. Milne and C. Hempel. M. J. Biercuk conceived the original research direction for this project. A. R. Milne led the paper writing alongside co-authors C. Hempel and M. J. Biercuk, with assistance from me. A. R. Milne developed the control software used to perform these experiments. A. R. Milne and I jointly set up the experimental optics and electronics, performed the experiments in this work, and ran the data analysis. I was the sole contributor on the theoretical work in this paper, building on earlier theory by Green et al. [**9**] to create analytic phase-modulated gates, and work by Kirchmair et al. [**8**], Roos et al. [**10**] to calculate the expected observable evolution including the ion populations and the gate fidelity. This work was discussed in detail in the prior chapter (Chapter 7) and is applied to the experimental data here. In addition, I derived the filter function framework for detuning noise demonstrated here.

Authorship attribution

In addition to the statements above, in cases where I am not the corresponding author of a published item, permission to include the published material has been granted by the corresponding author.

Name: Claire Louise Edmunds

Signature:

Date: 27th February 2021

As supervisor for the candidature upon which this thesis is based, I can confirm that the authorship attribution statements above are correct.

Name: Professor Michael J. Biercuk

Signature:

Date: 28th February 2021

Statement of Originality

This is to certify that to the best of my knowledge, the content of this thesis is my own work. This thesis has not been submitted for any degree or other purposes.

I certify that the intellectual content of this thesis is the product of my own work and that all the assistance received in preparing this thesis and sources have been acknowledged.

Name: Claire Louise Edmunds

Signature:

Date: 27th February 2021

Contents

List of Figures

List of Tables

CHAPTER 1

Introduction

“The universe is a big place, perhaps the biggest.” [1]

- Kurt Vonnegut, *Venus on the Half Shell*

1.1 A brief introduction to quantum computing

During the last century, humanity developed a new technology potentially more revolutionary than any that came before it: the electronic computer. A device with such enhanced calculation power, memory resources and connectivity that it profoundly advanced the state of research and innovation, and created entirely new fields of study. New classes of problems that had previously never even been considered now became tractable; month-long calculations could be achieved in seconds; knowledge could be communicated across distances and in time frames that were previously unimaginable. The result was extraordinary advancements throughout science, technology and society, ranging from medicine to warfare. Today, there is barely a job existing that does not rely partially or wholly on the power of computers.

In parallel with the development of the computer, a new field of physics was being born. Quantum mechanics, largely emerging throughout the 20th century, shone a new light on the microscopic world of atoms, electrons and other fundamental particles, revealing counter-intuitive – even seemingly impossible – behaviour. As the technological wars over the hardware-development of the computer began to settle, with advancements in semiconductor-based microprocessors rendering their competition obsolete, people began to question whether the bizarre rules of quantum physics could be used to further enhance computer performance, or even enable new types of computation entirely [**11**–**13**].

---

[1] ...but let’s start small.

The state of "quantum computing" progressed significantly in the late 20th century both in software, with the developments of novel algorithms exploiting the properties of quantum physics [**14**, **15**], and hardware, with the first demonstrations of quantum logic gates in a trapped-ion based quantum device [**16**]. Alongside these advancements were innovations in the field of error correction, trying to ensure that an eventual quantum processor would be robust and reliable [**17**, **18**]. By 2021, quantum processors have been demonstrated with tens of qubits [**19**], even achieving "quantum advantage" [**20**, **21**], wherein a quantum computer solves a specific problem that would classically require an unfeasible computational time – possibly even longer than the lifetime of the computer [**22**]. Large scale quantum entanglement has been demonstrated, with the largest entangled states created using up to 16 superconducting qubits [**23**, **24**], 18 photonic qubits [**25**], and up to 24 trapped-ion qubits [**26**–**28**].

To build a quantum device, the system is required to be highly isolated, small and cold in order to minimise its interaction with the environment; any contact can degrade both the quality of the information stored and the performance of an algorithm run on the device. Several physical systems are being explored as quantum platforms, each with its own advantages and disadvantages. These include trapped ions [**29**], superconducting qubits via circuit quantum electrodynamics (cQED) [**30**], electron spins confined in semiconductor quantum dots [**31**], photon-based systems using linear optics [**32**], nitrogen-vacancy (NV) centres in diamonds [**33**], and even exotic topological quasi-particles termed "Majorana fermions" [**34**].

Despite significant progress, modern quantum devices are still limited by errors. While these devices are powerful, they are extraordinarily sensitive to noise in their environment or in the electromagnetic fields used to manipulate them. Just as noise can interfere with classical devices, it can similarly induce errors in quantum processors. Where these technologies diverge, however, is the way in which the resulting errors affect an algorithm. The probability of error in classical computers has a discrete outcome for every gate – either an error occurs or it does not. In a quantum computer, errors *accumulate*. They build up over the course of an algorithm, eventually reaching a point at which the results become unreliable. Analogous to classical computers, quantum error correction routines are being designed to provide robustness to these errors; however, current proposals require extremely large numbers of qubits and gates for their implementation [**35**, **36**].

The work in this thesis is concerned with understanding the types of noise that induce errors in quantum devices and minimising their effect before the application of quantum error correction. By characterising noise to understand *how* it impacts the device, one can tailor specific solutions to protect the device –

and any operations run on it – from the noise, using techniques sampled from the field of "quantum control".

In this work, I will demonstrate several examples of open loop, dynamic control solutions using trapped $^{171}\mathrm{Yb}^{+}$ ions. I begin by outlining a selection of background material on general quantum theory, introducing notation and formalisms that will be used throughout this work. In Chapter 2 I discuss both the general experimental implementation of a trapped-ion quantum device, and the specific details of the ion traps and control systems used in this work. Chapter 3 presents an in-depth discussion of selected atomic physics of $^{171}\mathrm{Yb}^{+}$, in particular characterising the $^2\mathrm{S}_{1/2} \leftrightarrow {}^2\mathrm{D}_{5/2}$ transition at 411 nm. In this chapter, I will demonstrate an electron-shelving method to decrease errors in the final qubit measurement, which is a critical component of the quantum processor required to interpret the results of a quantum algorithm accurately.

Chapters 4-8 contain demonstrations of control techniques for single and two-qubit gates in $^{171}\mathrm{Yb}^{+}$. In Chapter 4, I present an analytic framework to interpret the results of two common quantum error characterisation protocols, randomised benchmarking and gate-set tomography, by mapping quantum circuits to random walks. In Chapter 5 I show that this framework can be used to predict the results of randomised benchmarking and gate-set tomography under different types of noise (static vs. rapidly varying), and develop methods to detect static error processes. In Chapter 6 I extend this work to quantitatively measure the strength of noise with different correlation lengths affecting a quantum circuit. I experimentally validate this framework and provide the first demonstration that dynamically corrected gates, a form of quantum control, can reduce correlated errors affecting single-qubit gates. Chapters 7 and 8 demonstrate a two-qubit quantum control technique using phase-modulated lasers to reduce errors in two-qubit "Mølmer-Sørensen" entangling gates. The errors treated arise due to residual coupling between the qubits and the bosonic oscillator modes at the gate's conclusion, which can occur due to poor gate design or noise in the control laser frequency or amplitude. Chapter 7 presents the relevant background theory as well as new derivations about the evolution of the qubits under the application of the Mølmer-Sørensen gate, and Chapter 8 provides the experimental validation of this technique.

1.2 Background theory

I begin this thesis with an introduction to some of the basic concepts upon which quantum computing relies – how quantum information is encoded, manipulated, and measured.

1.2.1 The quantum bit

The fundamental unit of information in quantum computing is called the "qubit", or quantum bit. Just as a classical computer stores and manipulates information using classical bits, qubits are used to store and process quantum information. However unlike the bit, which can only take one of two discrete values, a qubit is able to exist in "superposition states", which are linear combinations of two extreme values. The space of all possible qubit states is a two-dimensional Hilbert space spanned by the two vectors

$$|0\rangle \equiv \begin{pmatrix} 1 \\ 0 \end{pmatrix} \qquad |1\rangle \equiv \begin{pmatrix} 0 \\ 1 \end{pmatrix}, \tag{1.1}$$

which are given the labels $|0\rangle$ and $|1\rangle$ analogous to a classical bit. The qubit state can be written using "Dirac" or "bra-ket" notation, using the "ket" to label a quantum state, $|\psi\rangle$, and a "bra" to label its complex conjugate, $\langle\psi|$. The inner product between a bra and ket is given by a "braket", $\langle\phi|\psi\rangle$. A general quantum state can be made using any complex, linear combination of the states $|0\rangle$ and $|1\rangle$ as long as the vector is normalised to one. That is,

$$|\psi\rangle = \begin{pmatrix} a_1 \\ a_2 \end{pmatrix}, \qquad \langle\psi|\psi\rangle = \begin{pmatrix} a_1^* & a_2^* \end{pmatrix} \begin{pmatrix} a_1 \\ a_2 \end{pmatrix} = |a_1|^2 + |a_2|^2 = 1. \tag{1.2}$$

The space of all possible qubit states can be visualised using the "Bloch sphere", a two-dimensional spherical surface with unit-length radius, as shown in Fig. 1.1. A qubit state is represented by the "Bloch vector": a unit-length vector, $\boldsymbol{r}$, that points to a position on the surface of the sphere with Cartesian coordinates (r_x, r_y, r_z) and spherical coordinates $(|r| = 1, \theta, \phi)$. The two basis states $|0\rangle$ and $|1\rangle$ are conventionally assigned to the positive and negative poles along the z-axis. A general state $|\psi\rangle$ can then be written as a superposition of $|0\rangle$ and $|1\rangle$ using either the longitudinal and azimuthal angles, θ and ϕ, or the Cartesian coordinates,

$$|\psi\rangle = \cos\left(\frac{\theta}{2}\right)|0\rangle + e^{i\phi}\sin\left(\frac{\theta}{2}\right)|1\rangle \tag{1.3}$$

$$= \frac{1}{\sqrt{2}}\left[\sqrt{1+r_z}\,|0\rangle + \frac{r_x + ir_y}{\sqrt{1+r_z}}\,|1\rangle\right], \tag{1.4}$$

with the limit $|\psi\rangle \to |1\rangle$ as $(r_x, r_y, r_z) \to (0, 0, -1)$.

The basis states $|0\rangle$ and $|1\rangle$ are actually eigenstates of the generator of rotations about the z-axis, called the Pauli-z spin matrix, $\hat{\sigma}_z$. There are three Pauli matrices in total corresponding to the infinitesimal generators of rotation about the three axes, x, y and z. The set containing the three Pauli matrices

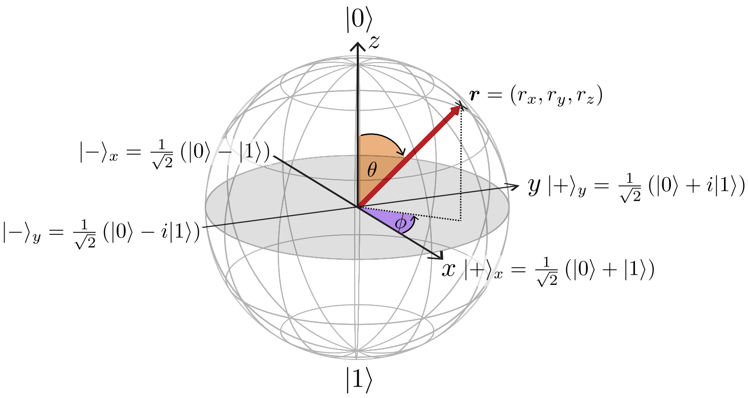

FIGURE 1.1. **Qubit representation using the Bloch sphere**. A pure quantum state can be represented as a point on the two-dimensional surface of the unit-radius Bloch sphere. The basis states $|0\rangle$ and $|1\rangle$ are shown as the antipodal pole positions along the z-axis. The positive and negative basis states in the x- and y-bases can be expressed as superpositions of the z-basis states.

in addition to the two-dimensional identity matrix spans the space of all two-dimensional Hermitian matrices. The Pauli matrices can be written as follows,

$$\hat{\mathbb{I}} = \begin{pmatrix} 1 & 0 \\ 0 & 1 \end{pmatrix}, \quad \hat{\sigma}_x = \begin{pmatrix} 0 & 1 \\ 1 & 0 \end{pmatrix}, \quad \hat{\sigma}_y = \begin{pmatrix} 0 & -i \\ i & 0 \end{pmatrix}, \quad \hat{\sigma}_z = \begin{pmatrix} 1 & 0 \\ 0 & -1 \end{pmatrix}. \tag{1.5}$$

Just as the poles along the z-axis of the Bloch sphere correspond to the two eigenstates of $\hat{\sigma}_z$, the poles along the x- and y-axes are the eigenstates of the $\hat{\sigma}_x$ and $\hat{\sigma}_y$ operators respectively. The $\pm\hat{\sigma}_x$ and $\pm\hat{\sigma}_y$ eigenstates can be written as in terms of the $\hat{\sigma}_z$ basis states, $\{|0\rangle, |1\rangle\}$,

$$|+\rangle_x \equiv \frac{1}{\sqrt{2}}\begin{pmatrix} 1 \\ 1 \end{pmatrix}, \quad |-\rangle_x \equiv \frac{1}{\sqrt{2}}\begin{pmatrix} 1 \\ -1 \end{pmatrix}, \quad |+\rangle_y \equiv \frac{1}{\sqrt{2}}\begin{pmatrix} 1 \\ i \end{pmatrix}, \quad |-\rangle_y \equiv \frac{1}{\sqrt{2}}\begin{pmatrix} 1 \\ -i \end{pmatrix}, \tag{1.6}$$

such that $\hat{\sigma}_x |+\rangle_x = +1\,|+\rangle_x$, and so on for the other states.

Mixed Quantum States

Until now, we have only considered "pure" quantum states. That is, states that contain all of the relevant information needed to describe them. Pure states are not even restricted to a single qubit – they can also refer to entangled multi-qubit systems, as long as all components of the system are known and measurable. If a quantum system has some coupling to either the environment or to an unmeasurable system generally, then it is referred to as a "mixed" quantum state. Due to the environmental coupling, we cannot describe or measure all of the information needed to characterise the system. Instead, a mixed state is expressed as a statistical ensemble of pure states, as we must average over all possibilities of the state of the environment.

Unlike a pure state, mixed states cannot be represented in Dirac notation. Instead, we use a formalism called a "density matrix" to represent them, containing the probabilities for the state to be measured in the basis states along the diagonal, and the complex "coherences" (or relative phases) between the basis states on the off-diagonals. A density matrix, commonly represented by the symbol ρ, is a Hermitian, positive-definite linear operator described by a linear combination of pure states with probabilities λ_k

$$\rho = \sum_k \lambda_k \left|\psi_k\right\rangle \left\langle\psi_k\right|, \qquad \lambda_k \in \mathbb{R}. \tag{1.7}$$

All quantum states, mixed or pure, must obey $\text{Tr}[\rho] = 1$ to conserve probability; it is equivalent to stating that the sum of a state's probability densities (modulus squared probability amplitudes) over a complete orthonormal basis must equal one. Pure states can also be expressed as density matrices and have the unique property $\text{Tr}[\rho^2] = 1$, while for mixed states $\text{Tr}[\rho^2] < 1$. Indeed, the parameter $\text{Tr}[\rho^2]$ is called the "purity" of the state, which can take an upper value of 1 (for a pure state) and a lower value of $1/d$ for a d-dimensional system. For a qubit, the minimum purity is 1/2, corresponding to a completely random system, containing no meaningful information. It is equivalent to a classical coin flip.

The mixed state can also be visualised using the Bloch sphere, however, the point now lies *within* the sphere's volume, described by a Bloch vector with length less than one. The maximally mixed state corresponds to a zero-length Bloch vector at the origin of the sphere. This state has equal probability to be measured in the positive and negative eigenstates along all three axes, and hence contains no useful information. The Cartesian coordinates of a mixed state can be used to express the density matrix in terms of the Pauli matrices as

$$\rho = \frac{1}{2}(\hat{\mathbb{I}} + r_x\hat{\sigma}_x + r_y\hat{\sigma}_y + r_z\hat{\sigma}_z). \tag{1.8}$$

The trace operation can then be used to decompose a density matrix into its different Pauli components using

$$r_\alpha = \text{Tr}[\rho\hat{\sigma}_\alpha] \tag{1.9}$$

for $\alpha \in \{x, y, z\}$.

1.2.2 Quantum operators and quantum channels

To modify a qubit state, we act upon it using a two-dimensional matrix called an "operator", $\hat{U}$. This operator must be unitary in order to conserve probability. A pure quantum state can be represented in Dirac notation, $|\psi\rangle$, and is acted upon by a unitary operator via right multiplication to the qubit state,

$$\hat{U}(|\psi\rangle) = \hat{U}\,|\psi\rangle\,. \tag{1.10}$$

Here, we use the notation $\hat{U}(|\psi\rangle)$ to describe the general concept of an operator "acting" on a state. Unitary operators for a single qubit are rotation operators, moving the Bloch vector around the surface of the sphere. They can also be used to translate density matrices, however, the action is now given by conjugation,

$$\hat{U}(\rho) = \hat{U}\rho\hat{U}^{\dagger}. \tag{1.11}$$

In this case, the unitary evolution is an example of a "quantum channel".

In general, a quantum channel can describe either a coherent process, such as the controlled manipulation of a qubit by a electromagnetic field, or an uncontrolled noise process, such as interference from a Markovian noise bath. A quantum channel is a linear, completely positive, trace-preserving map (CPTP) that maps density matrices to other density matrices. Unlike a unitary operator, which must preserve a quantum state's purity, quantum channels can describe processes that *reduce* purity through a phenomenon called "decoherence". Decoherence causes a quantum state to lose information. For some types of decoherence, such as depolarisation, it can cause an initially pure qubit state to be eventually degraded to the maximally mixed state.

To describe the action of a quantum channel $\hat{\Lambda}$ on a density matrix ρ, we decompose the action in terms of the constituent "Kraus operators", $\hat{A}_k$,

$$\hat{\Lambda}(\rho) = \sum_k \hat{A}_k \rho \hat{A}_k^{\dagger}. \tag{1.12}$$

The Kraus operators are a set of linear operators that obey the completeness relation,

$$\sum_k \hat{A}_k^{\dagger} \hat{A}_k = \hat{\mathbb{1}}. \tag{1.13}$$

The number of Kraus operators required to represent the action of $\hat{\Lambda}$ denotes the channel's "rank". A unitary operator is described using a "pure" channel with rank one. In this thesis, I will utilise the channel notation to describe error channels, often associated with either qubit decoherence or noise on the control field. Two basic examples of quantum channels are listed here.

(1) The bit flip channel: in analogy to a classical bit flip error, a quantum state can be flipped about the $\hat{\sigma}_x$-axis with probability p. The rank-two channel describing this process is

$$\hat{\Lambda}(\rho) = (1-p)\hat{\mathbb{I}}\rho\hat{\mathbb{I}} + p\hat{\sigma}_x\rho\hat{\sigma}_x, \tag{1.14}$$

created using two constituent Kraus operators,

$$\hat{A}_1 = \sqrt{1-p}\,\hat{\mathbb{I}} \quad \hat{A}_2 = \sqrt{p}\,\hat{\sigma}_x \tag{1.15}$$

$$\sum_k \hat{A}_k^\dagger \hat{A}_k = (1-p)\hat{\mathbb{I}} + p\hat{\mathbb{I}} = \hat{\mathbb{I}}. \tag{1.16}$$

(2) Depolarisation: qubit depolarisation is a form of decoherence describing the uniform contraction of the Bloch sphere, or equivalently the qubit state becoming more highly mixed. For a depolarisation probability p, this process is generated by three equal-weight Pauli channels in addition to the identity operator,

$$\hat{A}_1 = \sqrt{1-\frac{3p}{4}}\,\hat{\mathbb{I}}, \quad \hat{A}_2 = \sqrt{\frac{p}{4}}\,\hat{\sigma}_x, \quad \hat{A}_3 = \sqrt{\frac{p}{4}}\,\hat{\sigma}_y, \quad \hat{A}_4 = \sqrt{\frac{p}{4}}\,\hat{\sigma}_z \tag{1.17}$$

$$\sum_k \hat{A}_k^\dagger \hat{A}_k = \left(1-\frac{3p}{4}\right)\hat{\mathbb{I}} + \frac{p}{4}(3\hat{\mathbb{I}}) = \hat{\mathbb{I}}. \tag{1.18}$$

The four Kraus operators correspond to a rank-four quantum error channel,

$$\hat{\Lambda}(\rho) = \left(1-\frac{3p}{4}\right)\hat{\mathbb{I}}\rho\hat{\mathbb{I}} + \frac{p}{4}(\hat{\sigma}_x\rho\hat{\sigma}_x + \hat{\sigma}_y\rho\hat{\sigma}_y + \hat{\sigma}_z\rho\hat{\sigma}_z) \tag{1.19}$$

$$= (1-p)\,\rho + \frac{p}{2}\hat{\mathbb{I}} \tag{1.20}$$

where I have used Eqn. (1.8) to show that

$$\hat{\mathbb{I}} = \frac{1}{2}(\hat{\mathbb{I}}\rho\hat{\mathbb{I}} + \hat{\sigma}_x\rho\hat{\sigma}_x + \hat{\sigma}_y\rho\hat{\sigma}_y + \hat{\sigma}_z\rho\hat{\sigma}_z). \tag{1.21}$$

1.2.3 Definitions of fidelity

To quantify the accuracy of a quantum state compared to an ideal state, I introduce the concept of “fidelity”, $\mathcal{F}$. Fidelity measures the closeness of two quantum states or operators, which can be used as a quantitative measure of the success of an algorithm. The fidelity of an arbitrary quantum state represented by the density operator ρ when compared to an ideal density operator σ is given by

$$\mathcal{F}(\rho,\sigma) = \mathcal{F}(\sigma,\rho) = \mathrm{Tr}\left[\sqrt{\sqrt{\rho}\sigma\sqrt{\rho}}\right]^2. \tag{1.22}$$

If ρ is a pure state, then $\rho^2 = \rho = \sqrt{\rho} = |\psi\rangle\langle\psi|$, and the fidelity can be rewritten in several useful simplified forms.

$$\begin{aligned}\mathcal{F}(\rho,\sigma) &= \mathrm{Tr}\left[\sqrt{|\psi\rangle\langle\psi|\,\sigma\,|\psi\rangle\langle\psi|}\right]^2 \\ &= \langle\psi|\sigma|\psi\rangle\,\mathrm{Tr}\left[\sqrt{|\psi\rangle\langle\psi|}\right]^2 \\ &= \langle\psi|\sigma|\psi\rangle \\ &= \mathrm{Tr}\left[|\psi\rangle\langle\psi|\,\sigma\right] \\ &= \mathrm{Tr}\left[\rho\sigma\right] \end{aligned}\tag{1.23}$$

When both ρ and σ represent pure states, the expression can be further simplified. If we consider a (pure) state $\rho = |\psi\rangle\langle\psi|$, then the fidelity comparing to the ideal state $\sigma = |\phi\rangle\langle\phi|$ is given by the state overlap

$$\mathcal{F} = |\langle\phi|\psi\rangle|^2. \tag{1.24}$$

All of these expressions calculate fidelity by comparing two quantum states with one another, often taken to be the real and ideal outputs of an operation or algorithm. One can instead quantify the fidelity of the individual *operations*. In this case, the fidelity for an operator $\tilde{U}$ and an ideal operator $\hat{U}$ of dimension d is given by the Hilbert-Schmidt inner product

$$\mathcal{F}(\tilde{U},\hat{U}) = \left|\frac{1}{d}\mathrm{Tr}\left[\hat{U}^{\dagger}\tilde{U}\right]\right|^2. \tag{1.25}$$

In this work, we refer to the metric in Eqn. (1.25) as “trace fidelity”.

1.2.4 Further resources

The work in this thesis will draw from several fields of research, for which excellent comprehensive resources exist for a beginner reader. A cornerstone of the ion trapping literature is the paper “Experimental Issues in Coherent Quantum-State Manipulation of Trapped Atomic Ions” published in 1998 by D. J. Wineland et al. [**37**]. While this paper was published 23 years ago at the time of writing this thesis, it remains one of the most comprehensive and relevant resources for understanding the basic physics of ion trapping, the behaviour of trapped ions, and the manipulation of ions with a laser or microwave field. Specific details about a trapped ion system using the 171 isotope of Ytterbium can be found in work by S. Olmschenk, both the 1997 paper [**38**] and his thesis [**39**]. For an introduction to the field of quantum information, I highly recommend a two-part lecture series by J. Preskill [**40**–**42**]. Furthermore, J. Preskill's lecture notes for the course Physics 229 given at the California Institute of Technology provide a broad and in-depth technical analysis of quantum computing and information [**43**]. Although the original notes were published in 1998, several chapters have been updated between 2015-2020 to incorporate recent advancements and achievements. A broad review of quantum computing can be found in Nature by T. D. Ladd et al. in 2010 [**44**], discussing the basic principles of quantum computing as well as its implementation via different physical architectures. An excellent introduction to the concept of quantum error correction, including several illustrations of basic error correcting codes, can be found in the introductory paper by S. J. Devitt et al. [**45**]. To understand the current state of quantum devices during the "NISQ" (Noisy Intermediate-Scale Quantum) era, the 2018 paper by J. Preskill [**46**] is a good place to start. Finally, underpinning this entire thesis is the concept of quantum control. To understand quantum control and its applications, a five-part video series by the startup quantum company Q-CTRL, for which I worked part-time during my PhD, provides a good non-technical introduction [**47**–**51**]. A more technical overview about the development and theoretical foundation of error compensating pulses is given by J. T. Merrill and K. R. Brown [**52**]. Due to the existence of such comprehensive resources, I have omitted in-depth introductions and derivations for concepts from some of these fields. I have included derivations for several important topics throughout this work where I feel a strong background is particularly relevant for understanding the work being communicated in this thesis, such as ion trapping, microwave-based ion manipulation, and quantum control.

The basic quantum concepts presented here are a vital part of the foundation upon which this thesis is built. Moving ahead, I will continue to explore and utilise these ideas, going into greater depth about how quantum operators work, and the manner in which errors can arise and affect quantum algorithms. In the next chapter, I will introduce the experimental setup which was used to explore these fundamental quantum concepts and obtain the results in this thesis.

CHAPTER 2

Experimental Details

"Another flaw in the human character is that everybody wants to build and nobody wants to do maintenance."

- Kurt Vonnegut, *Hocus Pocus*

For the work contained in this thesis I use a system of trapped $^{171}\mathrm{Yb}^{+}$ ions, ranging from a single ion to a string of 10 confined ions. In this section, I introduce the basic hardware required to trap and manipulate ions, as well as discuss the intrinsic properties of the $^{171}\mathrm{Yb}^{+}$ itself. Finally, I present several basic examples of the manipulation $^{171}\mathrm{Yb}^{+}$ ions with a microwave field, showing Rabi flops and Ramsey spectroscopy.

2.1 Linear Paul traps

Creating an electromagnetic potential that can confine a charged particle in three dimensions is non-trivial. Indeed, Earnshaw's theorem states that it is not possible to create such a potential using only static electric fields. If two directions are confining, then the third *must* be anti-confining. This principle has its origins in Gauss's law for free space, which requires that electric fields be divergenceless. Mathematically, this means that an electric potential $U(\boldsymbol{r})$ must satisfy Laplace's equation,

$$-\nabla^2 U = 0 \tag{2.1}$$

where $\nabla^2 = \nabla \cdot \nabla$ is the Laplace operator and $\nabla = \left[\frac{\partial}{\partial x}, \frac{\partial}{\partial y}, \frac{\partial}{\partial z}\right]$ is the divergence (or "div") operator.

To contain a positively charged particle, the confining electromagnetic field must have a *stable* equilibrium point. Such a position requires a local minimum in the field, where all lines of force lines point inwards. This would ensure that any small deviation away from the equilibrium position is quickly corrected by a restoring force, returning the particle to its original position. If, in any direction, the force lines point away from the equilibrium position, then it is an *unstable* equilibrium point. In that case, any deviation from the equilibrium would be accelerated by the force in the anti-confining direction, causing the charged particle to be expelled from the trap. Eqn. (2.1) can be equivalently expressed by stating that no point in free space can be a complete source or sink for the force lines created by an electric field, implying that it is not possible to create a stable equilibrium point if we are limited to solely using static electric fields. Rather, only unstable "saddle points" can be created. This suggests that more complex solutions must be sought to engineer a confining potential in three dimensions.

Two potential solutions were suggested. Firstly, the quadrupole radio-frequency (RF) Paul trap was designed by Wolfgang Paul to create a "dynamic" electric potential using time-varying electric fields [**53**–**55**]. Alternatively, the magnetic-field-based Penning trap was developed to create a "static" confining potential using a combination of static electric and magnetic fields [**56**–**59**]. In this thesis, I will focus on the Paul trap; for details about building and operating a Penning trap I suggest H. B. Ball's thesis as a resource [**60**].

One disadvantage of the RF Paul trap is that while using a dynamic electric potential enables confinement, it also induces a driven "micromotion" in the charged particles at the frequency of the RF field, Ω_t. Any such micromotion can inhibit the efficacy of laser cooling. The quadrupole RF trap design has a central "RF-null" location, where the particle would experience minimal micromotion; however, this position can only be occupied by a single particle. The Coulomb repulsion between similarly charged particles forces any additional particles away from the RF-null region. To refine the Paul trap, the linear Paul trap was developed with an elongated RF-null area where multiple ions – even strings of many ions – could be confined along a line [**61**]. In this work I use the linear version of the RF Paul trap.

The linear trap is created using four electrodes to provide radial confinement and two endcaps to provide axial confinement, as illustrated in Fig. 2.1(a),(b). Ideally, the electrodes are created with hyperbolic cross-sections to minimise anharmonicities, however, in practice circular cross-sections are an acceptable substitute as they still produce an approximately harmonic potential along the trap axis and are generally easier to fabricate. The longitudinal direction parallel to the electrodes corresponds to the weakest trapping axis, and is assigned to the z-axis, often referred to as the "axial direction". The surface of the electrodes are separated from the trap axis by distance R. To create a three-dimensional confining potential, equal DC voltages, U_0, are applied to both of the trap endcaps to confine the particles axially along the z-axis. To confine the particle in the radial xy-plane, an RF voltage, $V_0 \cos(\Omega_t t)$, is applied to two diagonally opposite electrodes while the remaining two are grounded. Along the axial direction

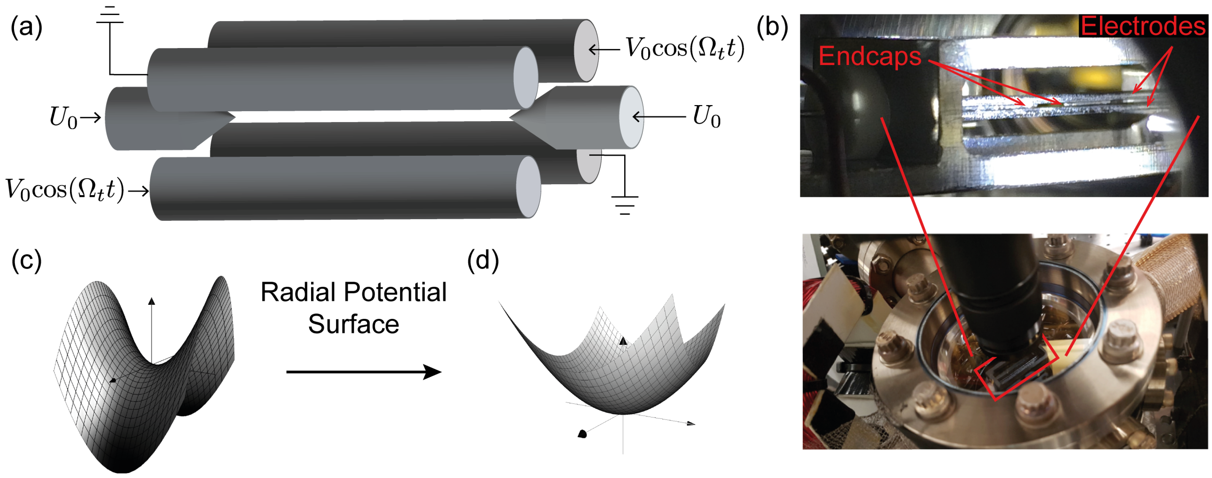

FIGURE 2.1. **The rod-style linear Paul trap.** (a) Schematic of the trap showing two DC endcaps at voltage U_0, two electrodes driven with an RF voltage, $V_0 \cos(\Omega_t t)$, and two electrodes held at ground. (b) One of the ion traps used in this work created with metal rod electrodes shown (top) enlarged for the trap details and (bottom) embedded within the vacuum chamber. Two thin endcaps can be seen protruding from either side in the top image. (c) The RF electrodes create a saddle potential in the radial xy-plane, which is inverted at a frequency Ω_t. The resulting equations of motion for a charged particle correspond to a harmonic trapping pseudo-potential, which is confining along both axes, as shown in (d).

we can calculate the potential due to the DC endcap voltages, U_0. At the trap centre, the potential can be approximated as [**37**, **61**]

$$\Phi_z(x, y, z) = \frac{\kappa U_0}{z_0^2}\left[z^2 - \frac{1}{2}(x^2 + y^2)\right] =: \frac{m}{2q}\omega_z^2\left[z^2 - \frac{1}{2}(x^2 + y^2)\right] \tag{2.2}$$

$$\omega_z := \sqrt{\frac{2q\kappa U_0}{z_0^2 m}} \tag{2.3}$$

for a particle with mass m and charge q. Here, κ is a geometric factor specific to the trap construction, z_0 is half the axial trapping region length, and ω_z is the angular frequency describing oscillations along the axial direction. The potential results in an axial equation of motion

$$\frac{d^2 z}{dt^2}(t) = -\frac{2q\kappa U_0}{z_0^2 m} z(t) = -\omega_z^2 z(t) \tag{2.4}$$

describing harmonic motion along the z-axis with angular frequency ω_z. This motion can be considered as macroscopic motion (or "macromotion") when compared to the RF-driven, high frequency micromotion. The macromotion oscillation frequencies along each of the trap axes, $\{\omega_x, \omega_y, \omega_z\}$, are often called the "trap" or "secular" frequencies.

The radial confinement of an RF Paul trap works by creating a saddle potential that is continuously inverted [**55**], as illustrated in Fig. 2.1(c). In one direction, the saddle potential is confining, enabling stable harmonic motion of the charged particles to continually refocus the particles to their original positions. In the other direction, it is anti-confining and hence "defocuses" the particles by increasing their amplitude until they escape the trap. By periodically inverting the saddle potential using an RF field, it alternates between focusing and defocusing the particle, creating a "pseudo-potential" that is effectively confining in all three dimensions (Fig. 2.1(d)).

Mathematically, this can by shown by deriving the equations of motion for a charged particle along the two radial axes. The radial time-varying potential near the trap axis is approximated as

$$\varphi_r(x,y,t) = \frac{V_0}{2}\left[1+\frac{x^2-y^2}{R^2}\right]\cos(\Omega_t t). \tag{2.5}$$

Combining the contributions from the static axial and time-varying radial potentials, Eqns. (2.2) and (2.5), we can write the Hamiltonian for a charged particles with mass m and charge q,

$$\mathcal{H} = \frac{|\boldsymbol{p}|^2}{2m} + q\left[\varphi_r(x,y,t) + \Phi_z(x,y,z)\right]. \tag{2.6}$$

Here, $\boldsymbol{p} = [p_x, p_y, p_z]$ is the momentum vector, with $|\boldsymbol{p}|^2 = \boldsymbol{p}\cdot\boldsymbol{p} = p_x^2 + p_y^2 + p_z^2$. Using the Hamilton equations of motion,

$$\frac{\partial \mathcal{H}}{\partial p_x} = \frac{dx}{dt} \qquad \text{and} \qquad \frac{\partial \mathcal{H}}{\partial x} = -\frac{dp_x}{dt}, \tag{2.7}$$

we can derive the equations of motion for a charged particle as follows.

$$\begin{aligned}\frac{d^2x}{dt^2}(t) &= \frac{\partial}{\partial t}\left(\frac{\partial \mathcal{H}}{\partial p_x}\right)\\ &= -\frac{1}{m}\left(\frac{\partial \mathcal{H}}{\partial x}\right)\\ &= -\frac{q}{m}\left[\frac{V_0}{R^2}\cos(\Omega_t t) - \frac{\kappa U_0}{z_0^2}\right]x(t)\end{aligned} \tag{2.8}$$

The derivation for the equation of motion along the y-axis follows similarly.

The equations of motion can be rewritten as in the form of the classical Mathieu equations,

$$\frac{d^2x}{d\zeta^2} + [a_x + 2q_x\cos(2t)]x(t) = 0 \tag{2.9}$$

$$\frac{d^2y}{d\zeta^2} + [a_y + 2q_y\cos(2t)]y(t) = 0 \tag{2.10}$$

by substituting

$$\zeta = \frac{\Omega_t t}{2} \tag{2.11}$$

$$a_x = a_y = -\frac{4q\kappa U_0}{z_0^2 m \Omega_t^2} \tag{2.12}$$

$$q_x = -q_y = \frac{2qV_0}{mR^2\Omega_t^2}. \tag{2.13}$$

The Mathieu equations can be solved using Floquet theory to derive expressions for $x(t)$ and $y(t)$ that contain two harmonic oscillation terms: (1) a smaller amplitude oscillation at frequency Ω_t, which describes the driven "micromotion" that is induced by the trap RF; and (2) a larger amplitude oscillation at frequency ω_r', the "secular" motion term. Assuming the charged particles are located closed to the RF null position of the trap potential, and $a_x \ll q_x \ll 1$ and $a_y \ll q_y \ll 1$, we can neglect the fast oscillating micromotion terms. In this case, the equations of motion correspond to a "pseudo-potential" of the form

$$\begin{aligned}\Phi_r(x,y) &= \left(\frac{qV_0^2}{4m\Omega_t^2 R^4} - \frac{\kappa U_0}{2z_0^2}\right)(x^2+y^2) \\ &=: \frac{m}{2q}{\omega_r'}^2(x^2+y^2) \qquad (2.14)\\ \omega_r' &:= \sqrt{\frac{q^2V_0^2}{2m^2\Omega_t^2R^4} - \frac{q\kappa U_0}{z_0^2 m}} \\ &=: \sqrt{\omega_r^2 - \frac{1}{2}\omega_z^2} \qquad (2.15)\\ \omega_r &:= \frac{qV_0}{\sqrt{2}m\Omega_t R^2} \qquad (2.16)\end{aligned}$$

where ω_r is the secular frequency in the *absence* of the static axial potential. The addition of the field produced by the endcaps weakens the radial potential, reducing the secular oscillation frequency from ω_r to ω_r'. Both secular frequencies along the x- and y-axes are equal and denoted ω_r in the case of an isotropic radial potential as considered here. I defer full derivations of the three-dimensional motion of charged particles in a linear Paul trap to Chapter 7. This includes the calculation of separate radial frequencies along the x- and y-axes due to the non-isotropic radial potentials required for laser cooling. More extensive derivations of the ion trap dynamics using Floquet theory and including faster rotating terms at Ω_t and $2\Omega_t$ can be found in Refs. [**37**,**39**,**62**].

2.2 The ^{171}Yb^{+} ion

To perform the experiments in this thesis, I utilise the 171 isotope of Ytterbium to realise a qubit. The ^{171}Yb^{+} ion has a rich history for use in metrology as a frequency standard [**63**] and has been utilised for quantum computing research by several groups including Refs. [**38**, **64**, **65**]. The ^{171}Yb^{+} ion has a spin-1/2 nucleus, resulting in a hyperfine splitting of its internal energy levels due to the interaction between the magnetic moments arising from the electron and nuclear spins. We choose to encode our qubit across the $^2\mathrm{S}_{1/2}$ hyperfine ground states, which are split by 12.64 GHz, denoting $|0\rangle := {}^2\mathrm{S}_{1/2}\,|F = 0, m_F = 0\rangle$ and $|1\rangle := {}^2\mathrm{S}_{1/2}\,|F = 1, m_F = 0\rangle$. Using a hyperfine qubit has several advantages. The upper states are extremely long-lived, far longer than any other relevant timescales in our experiments, and the qubit can be encoded in a pair of first-order magnetic-field insensitive states, called "clock states" due to their common use in metrology. Furthermore, as the qubit control field is on the order of several to tens of GHz, rather than THz as required for an optical transition, it enables the use of well established and highly controllable microwave systems ranging from standard telecommunication hardware [1] to novel technologies providing ultra-low phase noise, such as a cryogenically cooled sapphire oscillator (CSO) [**66**]. The benefits of reducing phase noise in control systems has been studied by Ball et al. [**67**], with forthcoming experimental results set to demonstrate the improvement in gate fidelity with low phase noise microwave systems.

Selected energy levels and laser transitions for ^{171}Yb^{+} are shown in Fig. 2.2. The $^2\mathrm{S}_{1/2}$ qubit levels are located in the bottom left. The qubit transition is first-order magnetic-field insensitive, with frequency

$$\omega_q/2\pi = 12642812118.466 + (310.8)B^2\ \mathrm{Hz} \tag{2.17}$$

where B is the magnetic field magnitude in Gauss. Doppler cooling, state preparation and state detection are all performed on the $^2\mathrm{S}_{1/2} \leftrightarrow {}^2\mathrm{P}_{1/2}$ transition using a diode laser near 369.5 nm[2], which is nominally tuned to excite the inner $^2\mathrm{S}_{1/2}\,|F = 1\rangle \leftrightarrow {}^2\mathrm{P}_{1/2}\,|F = 0\rangle$ transition. The laser is split into three separate beam paths for these three objectives. In each beam path, acousto-optic modulators (AOMs) are used for switching and precise frequency control, and electro-optic modulators (EOMs) induce sidebands around the centre laser frequency. For Doppler cooling, a second-order sideband induced by an EOM driven at 7.374 GHz [3] simultaneously excites the $^2\mathrm{S}_{1/2}\,|F = 0\rangle \leftrightarrow {}^2\mathrm{P}_{1/2}\,|F = 1\rangle$

---

[1] Keysight E8267D Vector Signal Generator (VSG)

[2] Moglabs ECD Littrow Configuration

[3] Newport EOM Model 4851, driven by a Vaunix Lab Brick LMS-103

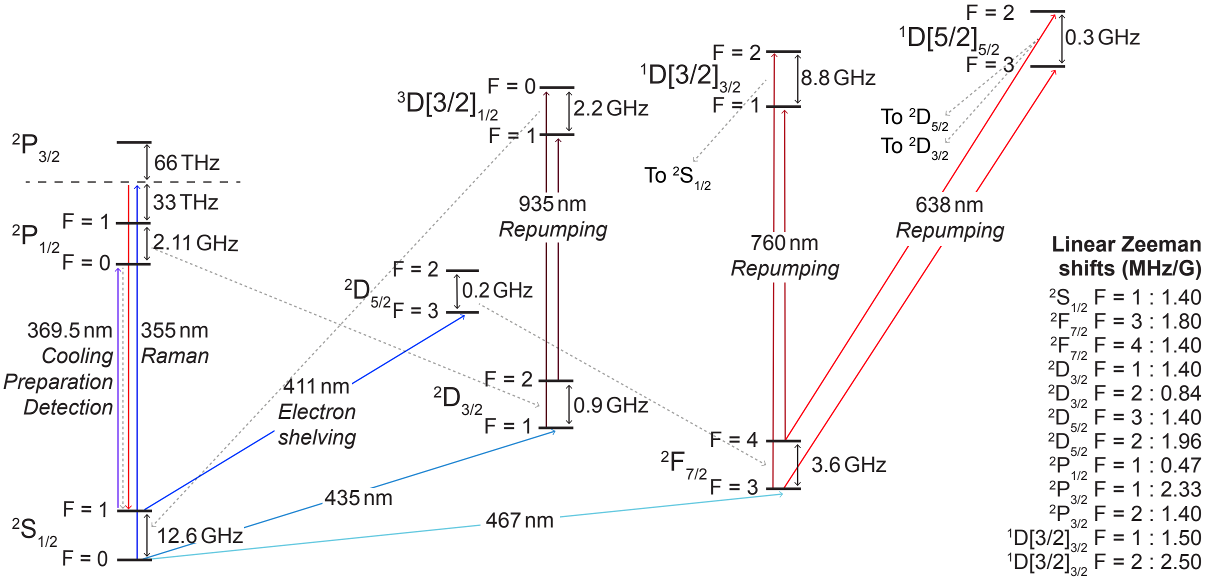

FIGURE 2.2. **Selected energy levels and laser transitions in ^{171}Yb^{+}** (not to scale). The qubit states are encoded in ^{2}S$_{1/2}$, shown in the bottom left corner. The lasers used in this thesis are highlighted, including the 370 nm laser used for Doppler cooling, state preparation and detection, the 935 nm, 638 nm and 760 nm laser used for repumping, and the 411 nm laser introduced in Chapter 3 for state detection via electron shelving. Additional states due to Zeeman splittings are omitted for visual clarity and dashed grey lines represent spontaneous decays. The linear Zeeman shifts for many of the energy levels depicted are tabulated on the right hand side in MHz/G.

transition, ensuring that all levels within the qubit manifold are addressed. A separate 2.105 GHz EOM [4] in the state preparation beam path is used to optically pump any population initially in $^2\mathrm{S}_{1/2}\,|F=1\rangle$ to $^2\mathrm{S}_{1/2}\,|F=0\rangle$ via $^2\mathrm{P}_{1/2}\,|F=1\rangle$ at the start of each experiment. Finally, standard state detection is performed by selectively exciting the $|1\rangle$ qubit state using the 370 nm light with no modulation. As such, the $|1\rangle$ state is referred to as the "bright" qubit state and $|0\rangle$ as the "dark" qubit state. Details about these fundamental techniques for ion trapping – Doppler cooling, optical pumping, and state detection via a cycling transition – can be found in Ref. [**37**].

Decays and occasional collisions necessitate the use of "repump" lasers to clear out any auxiliary states, returning the ion to the qubit manifold. A decay from ^{2}P$_{1/2}$ to ^{2}D$_{3/2}$ that occurs with 0.5 % probability removes the ion from the Doppler cooling cycle. We utilise a diode laser at 935 nm [5] to repump the ion via ^{3}D[3/2]$_{1/2}$, adding a 3.1 GHz EOM-induced sideband [6] to simultaneously address both hyperfine levels. Collisions can occasionally cause the ion to transition to the long-lived ^{2}F$_{7/2}$-state, with a lifetime

---

[4] QUBIG EOM EO-T2100M3 driven by a Mini-Circuits VCO ZX95-2252C-S+

[5] Moglabs ECDL Littrow Configuration

[6] EOSPACE fibre EOM PM-0K5-10-PFA-PFA-935 driven by a Vaunix Lab Brick LSG-602-13

in excess of 5 years [**68**]. Repumping from the $^2F_{7/2}$-state has traditionally been achieved via the $^1D[5/2]_{5/2}$ level with a 638 nm diode laser [7] that was scanned across a 5 GHz range to clear out both hyperfine levels. It was also noted that the high power 355 nm pulsed laser used for Raman transitions was also able to repump the ion from $^2F_{7/2}$, although we are currently unsure of the mechanism via which this occurs. Two new lasers at 411 nm and 760 nm are introduced in Chapter 3 for the purpose of electron shelving on the $^2S_{1/2} \leftrightarrow {}^2D_{5/2}$ transition to improve the detection fidelity. The 411 nm laser [8] is used for shelving and the 760 nm laser [9] is introduced to more efficiently clear out population in the $^2F_{7/2}$ levels via $^1D[3/2]_{3/2}$. A 5.26 GHz EOM is used for the 760 nm to address both $^2F_{7/2}$ hyperfine levels simultaneously [10].

Finally, in order to engineer two-qubit entangling gates, we employ a high power pulsed laser at 355 nm to create an optical frequency comb [11], with 2.5 W average power, $\sim$ 80 MHz repetition rate, and 5-10 ps pulse duration. The 355 nm wavelength is 66 THz red detuned from $^2P_{3/2}$ and 33 THz blue detuned from $^2P_{1/2}$. This division minimises the potential Stark shift induced by the laser, with the contributions from the two P manifolds destructively interfering and approximately cancelling [**69**]. The 355 nm laser interacts with the ion via a "two-photon Raman interaction", wherein one photon is absorbed by the ion and another is emitted through stimulated emission, essentially simultaneously. The result is an effective transition with a frequency equivalent to the difference frequency of the two photons. Further details about inducing a Raman transition in $^{171}Yb^+$ using a pulsed laser can be found in Ref. [**70**].

2.3 Trapping and optical setup

For the experiments in this thesis, I utilise two different linear Paul ion traps. One is a "rod trap", which is constructed with electrodes that are long cylindrical metal rods and is shown in Fig. 2.1(b). The rod trap is used for the quantum characterisation, validation and verification (QCVV) experiments in Chapter 5. The remaining work in this thesis uses a "blade-style trap" [**71**], which operates in a similar manner to the rod trap, but replaces cylindrical metal rods with rigid blades with circularly-arced edges. The blade trap has the advantage of mechanical stability and greater optical access due to the larger solid angle, improving fluorescence collection efficiency. For details about the blade trap

---

[7] Moglabs CEL

[8] Moglabs LDL001 Littow Configuration with a Moglabs Fast Servo Controller (FSC)

[9] Moglabs CEL002

[10] EOSPACE fibre EOM PM-0S5-05-PFA-PFA-760-UL driven by a Vaunix Lab Brick LSG-602

[11] SpectraPhysics Vanguard 355-2500

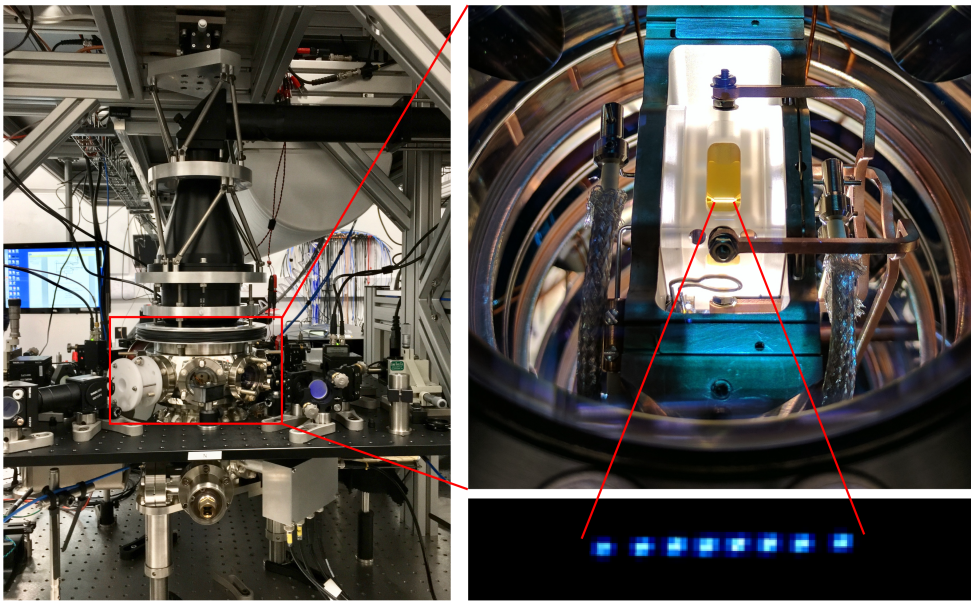

FIGURE 2.3. **Setup of the blade-style trap.** (Left) The vacuum chamber containing the blade trap is shown inside the red box. The white ring on the left holds the permanent magnet setting the quantisation field. (Right) Photo of the gold-plated blade trap in its holder, as well as a example string of eight $^{171}\mathrm{Yb}^{+}$ ions (bottom right) fluorescing due to excitation from the Doppler cooling laser.

construction, see A. R. Milne's forthcoming thesis [**72**]. An image of the blade trap and its surrounding setup is shown in Fig. 2.3. Both traps performances' with a single qubit have been characterised using a protocol called randomised benchmarking (RB), which can be used to extract an average gate error (see Section 4.1.3 for details on the protocol). Using the cylindrical rod trap, we measure an average gate error of $p_{\mathrm{RB}} = 5.99 \times 10^{-5}$ and a state preparation and measurement error (SPAM) $\kappa = 3.64 \times 10^{-3}$. On the blade-style trap, we record an average error $p_{\mathrm{RB}} = (1.89 \pm 0.12) \times 10^{-5}$ and a SPAM error of $\kappa = (3.3 \pm 0.1) \times 10^{-3}$. These values are sufficiently low to ensure that any engineered errors used in this thesis dominate the intrinsic background errors, in particular for the experiments presented in Chapter 5 and Chapter 6. As most of the work in this thesis was developed using the blade-style trap, I proceed with a description of the setup used for the blade trap experiment. Much of this information, however, will also be relevant to the rod trap setup.

The ion is confined in a blade-style linear Paul trap with RF frequency $\Omega_t/2\pi = 19$ MHz and secular trap frequencies $\{\omega_x, \omega_y, \omega_z\}/2\pi = \{1.6, 1.5, 0.5\}$ MHz (Fig. 2.3). The trap is contained in a octagonal vacuum chamber, which is pumped with a Non-Evaporable Getter (NEG) pump and an ion pump to

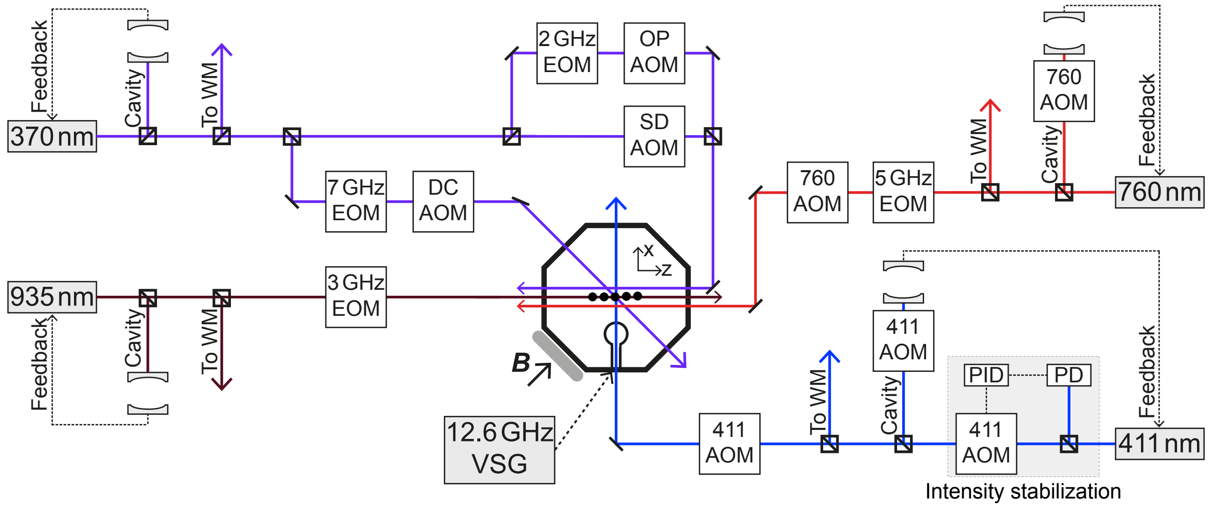

FIGURE 2.4. Simplified overview of the laser and trap geometry for this work. Beam paths for the four relevant lasers are shown, 370, 935, 411 and 760 nm, including any pertinent EOMs or AOMs, the Fabry-Perot optical cavities used for frequency locking, and the pick-offs for the wavemeter (WM). The 370 nm laser is split into three beam paths for Doppler cooling (DC), optical pumping (OP), and state detection (SD). The 411 nm laser is intensity stabilised using a photodiode (PD) and PID controller. In the centre, a schematic of the octagonal vacuum chamber containing the trap is shown with five ions along the trap axis. The bottom loop in the chamber is a 12.64 GHz microwave antenna powered by a vector signal generator (VSG). The grey bar at the lower left indicates a permanent magnet setting the quantisation magnetic field.

below 1e-11 Torr pressure for good isolation from other atoms and molecules. The magnetic quantisation field is produced by a permanent magnet, creating a 4.409(6) G magnitude field at the ion position, which is measured using the $^2S_{1/2}$ linear Zeeman shift, 1.398(1) MHz/G [**73**].

A simplified optical setup for the experiment is shown in Fig. 2.4. More detailed schematics can be found in Ref. [**72**]. Here, the schematic illustrates a simplified beam path for the 370 nm, 935 nm, 411 nm and 760 nm diode lasers, including the cavities used to lock the frequency, pick-offs for the wavelength meter (WM), and any modulation from electro- or acousto-optic modulators (EOMs/AOMs). In addition, an intensity stabilisation PID [12] regulates the 411 nm laser power to improve the cavity lock stability and achieve a more stable laser power at the trap. In the centre of the diagram, the laser-trap geometry is illustrated. Five ions are shown along the horizontal trap axis, which is oriented at 45° to the quantisation axis $\boldsymbol{B}$, set by a permanent magnet at the lower left window. The 935 nm, 760 nm, and optical pumping and state detection 370 nm lasers are aligned along the trap axis to equally illuminate all ions. The Doppler cooling 370 nm laser is oriented 45° to the trap axis in order to overlap with all three secular

---

[12] Stanford Research Systems (SRS) SIM960 Analog PID Controller

Wavelength (nm)	FSR (GHz)	Finesse	AR (%)	Part number
370	1.5	200-400	<0.2	SLS-NPLcav-4
935	1.5	200-400	<0.2	SLS-NPLcav-4
760	1.5	1,000-2,000	<0.1	SLS-100mm-nontunable
411	1.5	20,000-40,000	<0.15	6010-4 with vacuum housing VH6010-4

TABLE 2.1. Properties of the Fabry-Perot laser reference cavities, including free spectral range (FSR), finesse at the centre wavelength listed in the first column, and the anti-reflection measurement for the mirror backside at the centre wavelength.

motion directions for cooling. The 411 nm laser is perpendicular to the trap axis to ensure that it only interacts with the radial motional modes. As the secular frequencies are higher for the radial modes, they will have a lower mean phonon number associated with the Doppler cooling temperature limit, which will enable better transfer fidelity using the 411 nm laser.

In the physical experiment, all lasers are delivered to the trap via optical fibres [13]. The fibres used to couple the light from the diode lasers are commercially available. For the high power Raman laser, however, fibre coupling is achieved with specially modified UV photonic crystal fibres [**74**] that are hydrogen loaded and UV cured, as well as nitrogen purged on the inputs, to prevent damage such as solarisation. All previous attempts to couple the Raman laser into standard commercial fibres, even those equipped with endcaps to reduce damage from high power inputs, resulted in rapid fibre degradation.

All of the diode lasers introduced above (370 nm, 935 nm, 638 nm, 760 nm and 411 nm) are controlled using Moglabs laser diode controllers [14]. Frequency monitoring is performed with wavelength meters [15] that are calibrated using a HeNe reference at 633 nm [16]. Other than the 638 nm laser, each diode laser is frequency locked to an individual Fabry-Perot cylindrical cavity with 50 mm diameter and 100 mm length [17]. The 370 nm and 935 nm reference cavities are all frequency tunable and built into a single spacer block. The 411 nm and 760 nm cavities are both standalone and non-tunable (fixed frequency). All of the cavities are vacuum pumped to <3e-7 Torr and temperature controlled. Specific properties of the cavities are listed in Tab. 2.1.

---

[13] e.g. from Thorlabs and Schäfter + Kirchhoff GmbH

[14] MOGbox DLC-202 (for 935, 638 and 760 nm) and DLC-102HC (for 370 and 411 nm)

[15] HighFinesse WSU-10 and WS7

[16] SIOS SL 03 frequency-stabilised laser and controller

[17] Stable Laser Systems, Boulder CO, USA

Frequency tuning and light switching is performed with acousto-optic modulators (AOMs) for each of the laser setups. The AOMs for the 370 nm laser are driven at 200 MHz [18] and are operated in single pass configuration. The AOMs used in the 411 nm and 760 nm setups are both operated in double pass configurations [**75**]. The advantage of a double pass setup is that there is no frequency-dependent beam steering effect; any diffraction angle change during the first pass is countered in the second. A second advantage of using double pass AOMs for the 411 nm and 760 nm laser setups is that the AOM bandwidth is effectively doubled across the two passes. As the 411 nm and 760 nm Fabry-Perot cavities cannot be tuned, it is critical to have wide frequency tuning range in our AOM arrangement to scan the laser frequency to match the ion's transition frequencies.

The two 411nm AOMs are both made from a Tellurium Dioxide substrate, with centre frequency 200 MHz and ±25 MHz 3 dB bandwidth [19]. The two 760nm AOMs are also made with a Tellurium Dioxide substrate. One has a 110 MHz centre frequency and ±12.5 MHz bandwidth [20], and the other has a 300 MHz centre frequency and ±100 MHz bandwidth [21]. All four of these AOMs can be operated using any light polarisation, which makes it possible to use the double pass scheme presented by Donley et al. [**75**] using a quarter wave plate. See their work for full details.

At the end of each experiment, the final qubit state is measured using state-selective fluorescence excited by the 370 nm state detection laser. The fluorescence emitted during the Doppler cooling and state detection periods is collected with a custom designed objective with NA = 0.56 (see A.R. Milne's thesis for more details [**72**]), and imaged either onto an avalanche photodiode (APD) [22] or a electron multiplying CCD camera (EMCCD) [23] with $\sim 20\times$ magnification. Photons collected during the Doppler cooling period are used in post-processing to eliminate points where the qubit state was not prepared properly, possibly having heated or driven into a dark state due to a collision. Photons collected during state detection are used to determine the projected final qubit state. Further details about traditional methods of state detection can be found in Chapter 3 where I quantitatively compare the performance of different analysis routines and demonstrate a novel detection method based on electron shelving with the 411 nm laser.

---

[18] IntraAction ASM-2002B8

[19] Brimrose TEF-200-50-411nm

[20] Brimrose TEMF-110-25-760

[21] Brimrose TEF-300-200-760

[22] Laser Components COUNT-10B

[23] Andor iXon Ultra 897

All of the RF frequency synthesisers in our lab, both digital and analogue, are referenced to a common 10 MHz frequency reference source. The 10 MHz signal is produced by a Rubidium frequency standard [24] that is "cleaned up" by a 10 MHz stress-compensated (SC) phase-locked crystal oscillator [25] for high frequency stabilisation. A distribution amplifier is then used to send the 10 MHz reference signal to all relevant devices around the laboratory [26].

2.4 Manipulation of ^{171}Yb^{+} with a microwave field

A critical element of a trapped-ion quantum processor is the coherent control field used to manipulate the qubit state. Recall from Section 1.2.1 that the qubit state can be visualised as a vector on the Bloch sphere where the two poles represent the qubit states $|0\rangle$ and $|1\rangle$ in the $\hat{\sigma}_z$-basis. The control field then rotates the qubit vector around the surface of the Bloch sphere. For a hyperfine qubit such as $^{171}\mathrm{Yb}^{+}$, the control can be realised using a microwave field [**63**, **76**]. In this section, I derive the Hamiltonian describing the interaction between a microwave field and an atomic qubit, detail the implementation of a microwave-based control system in our lab, and demonstrate several fundamental experiments using a microwave field.

2.4.1 The qubit-microwave interaction Hamiltonian

I begin by describing the interaction between a microwave field and an atom with spin-1/2 nucleus, as originally investigated by I. I. Rabi [**77**]. Consider the time-varying magnetic component of a microwave field $\boldsymbol{B}(t) = B\cos(\omega t+\phi)\boldsymbol{x}$ with angular frequency ω, phase ϕ and amplitude B. Then, when applied to an atom with qubit frequency ω_q and magnetic moment $\mu\hat{\sigma}_x$, we can describe the total system dynamics with a two part Hamiltonian,

$$\hat{H}_0 = -\frac{\omega_q}{2}\hat{\sigma}_z + \mu B\cos{(\omega t+\phi)}\hat{\sigma}_x. \tag{2.18}$$

The first component describes the atom's internal energy and the second component characterises the interaction between the magnetic moment and the applied magnetic field.

To simplify the microwave-atom Hamiltonian, one can transform to a frame based on the Hamiltonian $\hat{H}_R = -\frac{\omega_q}{2}\hat{\sigma}_z$ and corresponding unitary $\hat{U}_R(t) = e^{i\omega_q t\hat{\sigma}_z/2}$, i.e., move into a rotating frame at the qubit

---

[24] Stanford Research Systems (SRS) FS725

[25] Wenzel Associates, Inc. 501-09815 Revision G

[26] SpectraDynamics (SDI) HPDA-15RMi-B

frequency. The resulting interaction Hamiltonian is expressed as

$$\begin{aligned}
\hat{H}_I &= \hat{U}_R^\dagger \hat{H}_0 \hat{U}_R - \hat{H}_R \\
&= \mu B \cos(\omega t + \phi) e^{-i\omega_q t \hat{\sigma}_z/2} \hat{\sigma}_x e^{i\omega_q t \hat{\sigma}_z/2} \\
&= \mu B \cos(\omega t + \phi) \left[\cos\left(\frac{\omega_q t}{2}\right)\hat{\mathbb{I}} - i \sin\left(\frac{\omega_q t}{2}\right)\hat{\sigma}_z\right] \hat{\sigma}_x \left[\cos\left(\frac{\omega_q t}{2}\right)\hat{\mathbb{I}} + i \sin\left(\frac{\omega_q t}{2}\right)\hat{\sigma}_z\right] \\
&= \mu B \cos(\omega t + \phi)[\cos(\omega_q t)\hat{\sigma}_x + \sin(\omega_q t)\hat{\sigma}_y]. \qquad (2.19)
\end{aligned}$$

By assuming the microwave field frequency is close to resonant with the qubit, and then eliminating all fast rotating terms at $\pm(\omega_q + \omega) \approx \pm 2\omega$ with the rotating wave approximation, this expression can be rewritten in terms of the angular detuning between the qubit and microwave frequencies, $\Delta = \omega_q - \omega$, as

$$\begin{aligned}
\hat{H}_I &\approx \mu B \left(\frac{e^{i([\omega_q - \omega]t - \phi)} + e^{-i([\omega_q - \omega]t - \phi)}}{4} \hat{\sigma}_x + \frac{e^{i([\omega_q - \omega]t - \phi)} - e^{-i([\omega_q - \omega]t - \phi)}}{4i} \hat{\sigma}_y \right) \\
&= \frac{\mu B}{2} \left(\cos(\Delta t - \phi)\hat{\sigma}_x + \sin(\Delta t - \phi)\hat{\sigma}_y\right). \qquad (2.20)
\end{aligned}$$

The interaction Hamiltonian Eqn. (2.20) can be transformed again using a Hamiltonian rotating at the detuning frequency, $\hat{H}_R' = \frac{\Delta}{2}\hat{\sigma}_z$ with corresponding unitary $\hat{U}_R'(t) = e^{-i\Delta t \hat{\sigma}_z/2}$.

$$\begin{aligned}
\hat{H}_I' &= \hat{U}_R'^\dagger \hat{H}_I \hat{U}_R' - \hat{H}_R' \\
&= -\frac{\Delta}{2}\hat{\sigma}_z + \frac{\mu B}{2} e^{i\Delta t \hat{\sigma}_z/2} \left(\cos(\Delta t - \phi)\hat{\sigma}_x + \sin(\Delta t - \phi)\hat{\sigma}_y\right) e^{-i\Delta t \hat{\sigma}_z/2} \\
&= -\frac{\Delta}{2}\hat{\sigma}_z + \frac{\mu B}{2} \left(\cos(\phi)\hat{\sigma}_x - \sin(\phi)\hat{\sigma}_y\right) \qquad (2.21)
\end{aligned}$$

Equation (2.21) describes the qubit rotation driven by a microwave field. Changing the phase of the field, ϕ, changes the equatorial axis of rotation on the Bloch sphere, e.g. setting $\phi = 0$ corresponds to a rotation about the $\hat{\sigma}_x$-axis. The angular "Rabi frequency" is defined to be

$$\Omega = \mu B, \qquad (2.22)$$

corresponding to the inverse of the time taken to complete a 2π revolution about the Bloch sphere. The rotation angle can then be calculated using $\theta_t = \Omega t$.

By examining Eqn. (2.21), one can observe that if the microwave field and qubit are not exactly resonant, it will introduce a $\hat{\sigma}_z$-rotation term, with strength proportional to the detuning Δ. This term has the effect of *tilting* the rotation axis away from the equatorial plane, creating rotations with a faster frequency and smaller amplitude. In this case, the faster rotation frequency is termed the "generalised Rabi frequency", and is described by

$$\tilde{\Omega} = \sqrt{\Omega^2 + \Delta^2}. \tag{2.23}$$

A microwave rotation about the $\hat{\sigma}_x$-axis (with $\phi = 0$) translates the qubit state between $|0\rangle$ and $|1\rangle$, where the final qubit state probability oscillates as

$$\begin{aligned} P(|1\rangle) &= \left(\frac{\Omega}{\tilde{\Omega}}\right)^2 \sin^2\left(\frac{\tilde{\Omega}t}{2}\right) \\ &= \frac{1}{1+\frac{\Delta^2}{\Omega^2}} \sin^2\left(\Omega\sqrt{1+\frac{\Delta^2}{\Omega^2}}\,\frac{t}{2}\right). \end{aligned} \tag{2.24}$$

This is an example of "Rabi cycling" or "flopping". In Fig. 2.5(a) I show an example of a single qubit undergoing Rabi flopping. A resonant 12.64 GHz microwave field is applied for a set window of time and the evolved state is measured to show oscillations between $|0\rangle$ and $|1\rangle$. Here, the Rabi frequency is measured to be $\Omega = 4.2$ kHz.

Equation (2.24) shows that the effective error introduced by detuning the microwave (or qubit) frequency is normalised by the Rabi frequency, $\delta = \Delta/\Omega$. In Fig. 2.5(b), detuned Rabi flops are calculated and plotted for four normalised detuning errors, $\delta = \{0, 0.5, 1, 2\}$. Larger detuning errors result in higher frequency, lower amplitude oscillations due to the increasing $\hat{\sigma}_z$ component in the rotation axis. As the detuning error increases, the $\hat{\sigma}_z$ component begins to dominate the interaction and the rotation axis eventually coincides with the z-axis of the Bloch sphere. If that occurs, then the highly detuned microwave field can only rotate a qubit initially prepared in $|0\rangle$ or $|1\rangle$ about its own axis.

A note on the definition of the "Rabi frequency"

There are differing conventions for defining the Rabi frequency in the trapped ion and quantum information literature. Some references define the Rabi frequency as the inverse of the time taken for the qubit to complete a 2π revolution, i.e. the time taken to rotate from $|0\rangle$ to $|1\rangle$ and to $|0\rangle$ again. This 2π revolution returns the initial state with an additional -1 phase factor, $|\psi\rangle \rightarrow -|\psi\rangle$. Other sources define the Rabi frequency as the inverse of the time taken to complete a 4π revolution, in order to return the qubit state to the initial state *with no additional phase*, $|\psi\rangle \rightarrow |\psi\rangle$.

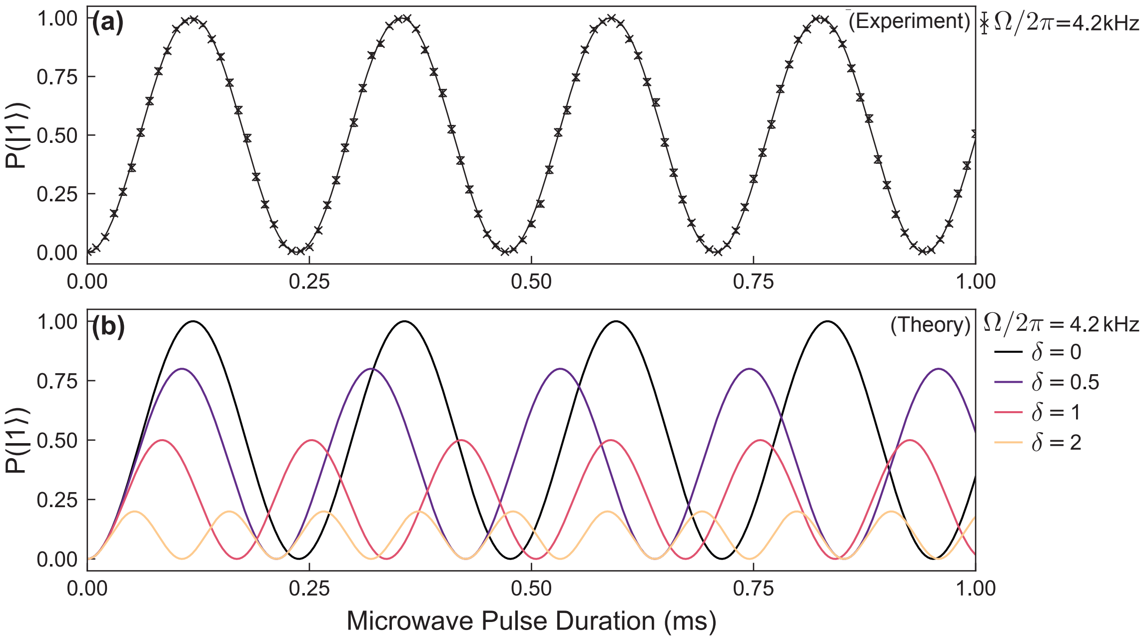

FIGURE 2.5. **Rabi flopping with a single qubit and a microwave control field**. (a) Experimentally measured single-qubit Rabi flops are illustrated, where a continuous microwave field rotates the state between $|0\rangle$ and $|1\rangle$ before it is measured. Markers show data points averaged over $r = 1000$ repetitions, and the solid line is a fit to Eqn. (2.24). The Rabi frequency is determined to be $\Omega/2\pi$ = 4.2 kHz. (b) Theoretically calculated single-qubit Rabi flops are shown with $\Omega/2\pi$ = 4.2 kHz and an increasing normalised detuning error, $\delta = \Delta/\Omega = \{0, 0.5, 1, 2\}$.

Whilst these two definitions appear inconsistent, they are both founded on physical principles. The variation arises due to the difference in quantifying the oscillation frequency of the qubit state *probability* compared to the qubit state *amplitude*, which vary by a factor of two. In this work, we use the first definition, which is the time taken to complete a 2π revolution of the qubit state about the Bloch sphere.

2.4.2 Microwave gate implementation

Single-qubit and global single-qubit rotations are driven with a 12.64 GHz microwave field that is produced by a vector signal generator (VSG) [27] and emitted from an in-vacuum loop antenna (Fig. 2.4). Standard experiments requiring a constant phase microwave field, either continuously driven or gated, can be performed using the unmodulated carrier frequency of the VSG. The carrier frequency was used to perform the Rabi flops in Fig. 2.5. More complex quantum circuits with rotations about different axes are achieved using I/Q modulation.

---

[27] Keysight E8267D

In several projects within this thesis, we use predefined "gates" rather than continuously driven or gated microwaves. Each gate has a set phase ϕ and duration t determining the axis of rotation and rotation angle respectively. I define the "rotation operator", which describes a rotation on the Bloch sphere by target angle $\theta_t = \Omega t$ about axis $\boldsymbol{n} = [\cos(\phi), -\sin(\phi), 0]$ as

$$\begin{aligned}\hat{U}(\hat{\boldsymbol{\sigma}} \cdot \boldsymbol{n}, \theta_t) &:= e^{-i\theta_t \hat{\boldsymbol{\sigma}} \cdot \boldsymbol{n}/2} \\ &= \cos\left(\frac{\theta_t}{2}\right)\hat{\mathbb{I}} - i\sin\left(\frac{\theta_t}{2}\right)\hat{\boldsymbol{\sigma}} \cdot \boldsymbol{n} \qquad (2.25)\end{aligned}$$

where $\hat{\boldsymbol{\sigma}} = [\hat{\sigma}_x, \hat{\sigma}_y, \hat{\sigma}_z]$ is the vector of Pauli spin operators.

To adjust the phase of the microwave field created by the VSG, and hence set the rotation axis, we utilise I/Q modulation. This involves two digital-to-analogue converters (DACs) that are combined 90° out of phase to create an in-phase (I) and quadrature (Q) component. If the carrier frequency is resonant with the qubit frequency, the I and Q components will drive qubit rotations about the x- and y-axes of the Bloch sphere respectively. By combining the two components with different amplitudes, rotations about *any* axis lying in the equatorial xy-plane of the Bloch sphere can be driven, with $\phi = \arctan(Q/I)$.

The target angle can be achieved by tuning the length or amplitude of the gate. In practise, for I/Q-modulated gates, the gates are predefined with a set number of digital samples of a fixed amplitude. The gate length is then tuned by adjusting the sampling rate of the I/Q DACs, which changes the gate duration. Rotations around the z-axis are carried out as frame-updates, i.e. pre-calculated, instantaneous changes of the subsequent gate I/Q values to account for the phase shift. A subtlety of this procedure is that we are changing the phase of the microwave system, whereas standard implementation of a $\hat{\sigma}_z$-gate changes the phase of the *qubit*. As such, the phase shift must occur in the *opposite* direction. Identity operations are realised as idle periods, wherein no signals are applied for a time equivalent to that of a π-rotation. We additionally utilise an in-built modulation routine in the VSG called "RF blanking" for fast switching to suppress transients in microwave power at pulse edges.

2.4.3 Microwave spectroscopy

The microwave interaction in Eqn. (2.21) does not exclusively describe interactions using the qubit clock transition, $^2\mathrm{S}_{1/2}\,|F=0, m_F=0\rangle \leftrightarrow {}^2\mathrm{S}_{1/2}\,|F=1, m_F=0\rangle$. By changing the drive frequency, additional "stretch state" transitions can be driven to the $m_F = \pm 1$ Zeeman levels of the upper $|F=1\rangle$

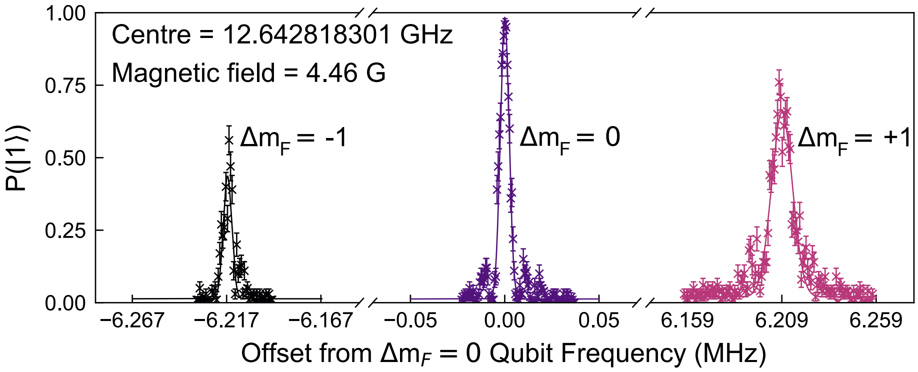

FIGURE 2.6. Microwave spectra taken by driving the $^2\mathrm{S}_{1/2}\,|F=0\rangle \rightarrow {}^2\mathrm{S}_{1/2}\,|F=1\rangle$ transition for $\Delta m_F = -1, 0, +1$. The three scans used microwave interrogation durations of {0.3, 0.115, 0.5} ms respectively, where the coupling strength for each transition depends on the microwave polarisation and magnetic field orientation. The relative widths of the peaks are partially set by the interrogation time. The magnetic field strength B can be calculated using the first-order magnetic-field insensitive clock state transition frequency, $12642812118.466 + (310.8)^2 B$ Hz.

manifold. The $m_F = \pm 1$ states are displaced from the zero-field energy by a linear Zeeman shift, with coefficient 1.398(1) MHz/G for $^2\mathrm{S}_{1/2}\,|F=1\rangle$. As the stretch states are first-order magnetic-field sensitive, they are significantly more susceptible to fluctuations in the magnetic field than the qubit clock states, resulting in a shorter coherence time. We can measure the frequencies of the qubit and stretch transitions using Rabi spectroscopy. This is achieved by preparing the ion in the state $|0\rangle$, applying a microwave interrogation pulse to the ion, and measuring the probability that the ion has transitioned to $^2\mathrm{S}_{1/2}\,|F=1\rangle$, $P(|1\rangle)$. The frequency of the microwave pulse is changed and the process is repeated to measure the full spectrum.

In Fig. 2.6, the microwave frequency was scanned across the three transitions, $\Delta m_F = -1, 0, +1$, and the peaks were fitted with Gaussian functions to extract the centre frequency. The qubit frequency was measured to be 12.642818301(84) GHz. The offset from the zero-field frequency corresponds to the quadratic Zeeman shift, 6.18(8) kHz. Using the quadratic Zeeman coefficient for the $^2\mathrm{S}_{1/2}$ ground state, 310.8 Hz/G [**78**], the magnetic field strength was measured to be 4.46(3) G, equating to a linear Zeeman shift of 6.24(4) MHz.

The frequencies of the lower stretch state transition, $\Delta m_F = -1$, and the higher transition, $\Delta m_F = +1$, were measured to be $-6.2165(2)$ MHz and $+6.2091(3)$ MHz respectively relative to the qubit transition. Due to the quadratic displacement of the $m_F = 0$ levels, the linear Zeeman shift is offset from these measurement values by half the quadratic Zeeman shift. The linear shift was calculated to be $-6.2134(2)$ MHz and $+6.2121(3)$ MHz respectively, which are consistent with the value calculated using the magnetic field measurement, but are slightly outside the uncertainty ranges of each other.

2.4.4 Ramsey spectroscopy

To create high fidelity microwave-based gates in a trapped-ion quantum processor, we require a method of accurately calibrating the microwave field frequency to be resonant with the qubit transition. Any detuning between these two frequencies will result in an error. The calibration can be achieved by measuring the qubit frequency with "Rabi spectroscopy", as illustrated in Fig. 2.6, wherein the frequency of a microwave interrogation pulse is scanned and the probability of transitioning from $|0\rangle$ to $|1\rangle$ is measured. However, the measurement precision is relatively poor, as observed in the qubit frequency measurement, 12.642818301(84) GHz. Indeed, if the detuning after calibration was equivalent to the maximum uncertainty, 84 Hz, then the dimensionless error for a 5 kHz Rabi frequency would be $\delta = \Delta/\Omega = 1.7\%$.

To improve the frequency resolution, a new spectroscopic technique was proposed by N. Ramsey, commonly referred to as a "Ramsey measurement" [**79**,**80**]. The protocol involves two $\pi/2$-rotations enclosing an idle period (Fig. 2.7), and can enable frequency calibrations with nearly 500× superior measurement precision than that achieved using Rabi spectroscopy, with typical uncertainties of several hundred millihertz [28] in our experiments.

A standard Ramsey interrogation with an idle period of length τ_R has the following form,

$$\begin{aligned} \hat{U}_{\text{Ramsey}} &= \hat{U}_1\hat{U}_2\hat{U}_1 \\ &= e^{-i\pi\hat{\sigma}_x/4}e^{-i\Delta\tau_R\hat{\sigma}_z/2}e^{-i\pi\hat{\sigma}_x/4} \end{aligned} \tag{2.26}$$

for an angular detuning Δ between the qubit and control field. Here, we begin by assuming that the $\pi/2$-rotations are error-free, both from off-resonance and over-rotation errors. Whilst the first assumption is unrealistic, as if there is any non-zero detuning it will cause an off-resonance error in the driven gates, the relative error contribution to the total sequence of operations is small. In general, the length of a $\pi/2$-rotation, $\tau_{\pi/2}$, is significantly shorter than the Ramsey idle period, resulting in a considerably smaller error associated with the $\pi/2$-rotations. For example, in our experiments $\tau_{\pi/2} \approx 0.05$ ms and typical Ramsey times τ_R range from 20-200 ms.

---

[28] For an idle period of 50 ms, we achieve uncertainties of approximately ±200 mHz [**2**]

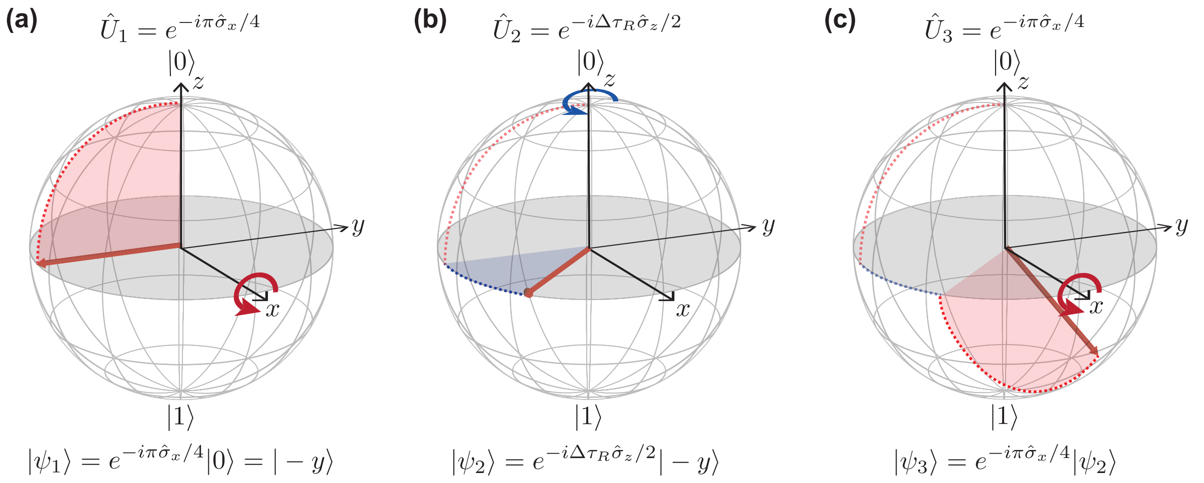

FIGURE 2.7. **Bloch spheres showing the evolution of the qubit Bloch vector during a single-ion Ramsey experiment.** The unitary operator for each step in the Ramsey protocol is shown above the diagram and the resulting qubit state after the evolution is shown below. The qubit is initially prepared in the $|0\rangle$ state at the north pole of the Bloch sphere. (a) A microwave $\pi/2$-rotation about the x-axis brings the qubit vector to the $|{-y}\rangle$ state on the equator (red). (b) During an idle period of duration τ_R, the qubit dephases relative to the microwave field, causing it to rotate about the z-axis of the Bloch sphere with frequency Δ (blue). (c) Finally, a second $\pi/2$-rotation about the x-axis ideally transfers to the qubit to $|1\rangle$ if no dephasing has occurred. If the detuning Δ is non-zero, then the qubit will be rotated to a final state away from $|1\rangle$, unless the accumulated phase $\Delta\tau_R$ is commensurate with a 2π rotation.

The Ramsey protocol is illustrated on a Bloch sphere in Fig. 2.7. The qubit is initially prepared in $|0\rangle$ and the first $\pi/2$-rotation about the x-axis brings the qubit vector state to the state $|{-y}\rangle$ on the equator (red, panel (a)). A subsequent idle period allows phase to accumulate between the control field and the qubit transition at a rate equivalent to the detuning Δ, displacing the qubit vector azimuthally (blue, panel (b)). If the qubit and microwave field are resonant, then the second $\pi/2$-rotation about the x-axis continues the first rotation, bringing the qubit to $|1\rangle$. However, any accumulated phase during the idle period due to a detuning causes the final rotation to return the qubit vector to a displaced position on the Bloch sphere (red, panel (c)).

As an example, if the idle period accumulates a phase of $\pi/2$ about the z-axis, then the qubit state is displaced from $|{-y}\rangle$ to $|{+x}\rangle$ during the idle period. Then, the second $\pi/2$-rotation rotates the qubit vector about its own axis, returning a final projective measurement onto the z-axis of $P(|1\rangle) = 1/2$. Alternatively, if the accumulated phase is π, then the qubit rotates from $|{-y}\rangle$ to $|{+y}\rangle$ during the idle period, and the final $\pi/2$-rotation returns the qubit to the initial $|0\rangle$ state, which is a 100% error from the expected final state, $|1\rangle$.

By scanning the length of the Ramsey idle period, τ_R, oscillations between the two qubit states can be observed at a frequency commensurate with the detuning. Figure 2.8 shows a single ion evolving via a Ramsey interaction. The detuning can be extracted from the oscillation frequency using

$$P(|1\rangle) = \cos\left(\frac{\Delta\tau_R}{2}\right)^2 = \frac{1}{2}\left(1 + \cos\left(\Delta\tau_R\right)\right), \tag{2.27}$$

which corresponds to $\Delta/2\pi = 7.9$ Hz for the data in Fig. 2.8. In addition to the coherent oscillations, we observe an exponentially narrowing envelope in the recorded data, eventually decaying to $P(|1\rangle) = 1/2$. The decay occurs because the Ramsey interrogation is not just affected by systematic, static detuning errors, which could be straightforwardly corrected with a spin echo, but also higher frequency dephasing errors in either the control field or qubit frequency. As with most quantum experiments, the Ramsey protocol and subsequent projective measurement must be repeated many times to gain statistics about the true qubit vector $\hat{\sigma}_z$ projection. If the detuning is not constant throughout these repetitions then we will average over the reconstructed state vectors, reducing the contrast of the oscillations. The dephasing error introduces an exponential decay that modifies Eqn. (2.27) to

$$P(|1\rangle) = \frac{1}{2}\left(1 + \cos\left(\Delta\tau_R\right)e^{-\tau_R/\tau}\right), \tag{2.28}$$

where τ is the exponential decay time and gives a measure of the observed dephasing time. For the experiment in Fig. 2.8 measured on the blade-style trap with a single ion and a microwave field created by the VSG 12.64 GHz carrier frequency, we measure $\tau = 1.337$ s.

I now consider the effect of an amplitude error on the $\pi/2$-rotations, using $\frac{\pi}{2} \to \frac{\pi}{2}(1+\epsilon)$, with the dimensionless error ϵ. In this case, the equations describing the Ramsey interaction, Eqns. (2.26) and (2.28), are modified to

$$\hat{U}_{\text{Ramsey}} = e^{-i\pi/4(1+\epsilon)\hat{\sigma}_x} e^{-i\Delta/2\tau_R\hat{\sigma}_z} e^{-i\pi/4(1+\epsilon)\hat{\sigma}_x}, \tag{2.29}$$

$$P(|1\rangle) = \frac{1}{2}\left(1 + \cos\left(\Delta\tau_R\right)e^{-\tau_R/\tau}\right)\cos\left(\frac{\epsilon\pi}{2}\right)^2. \tag{2.30}$$

Eqn. (2.30) shows that an over- or under-rotation error in the $\pi/2$-gates will reduce the overall amplitude of the oscillations, but still allow the detuning to be accurately measured from the oscillatory period as long as ϵ is small enough to achieve sufficient signal-to-noise in the measurement. Figure 2.9 shows theoretical calculations of Ramsey oscillations with the same parameters as the experimental data in Fig. 2.8, $\Delta/2\pi = 7.9$ Hz and $\tau = 1.337$ s. An over-rotation error has been introduced to affect the $\pi/2$-rotations, causing the oscillation amplitude and mean to decrease as ϵ goes from 0 (black) to 0.5

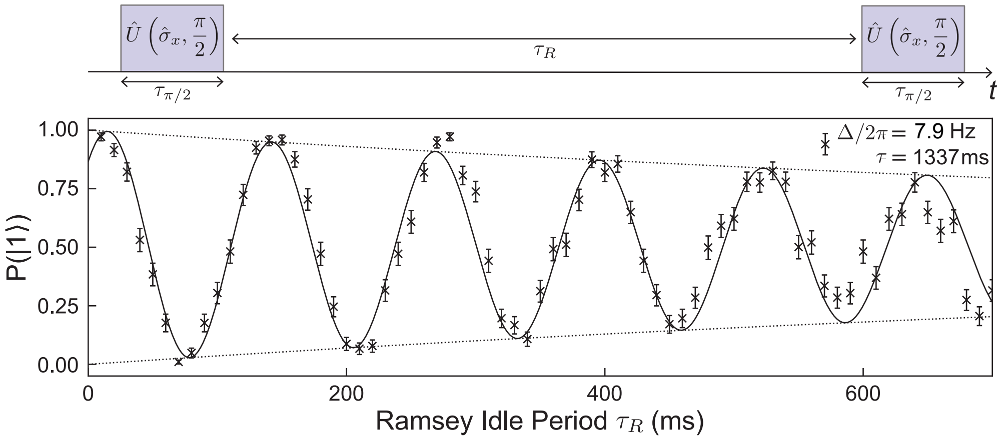

FIGURE 2.8. **Data showing a single-ion Ramsey experiment.** (Top) Schematic showing the Ramsey experiment procedure. Two microwave $\pi/2$-pulses are separated by a variable wait time, during which the microwave field and qubit frequency can become out of phase, either due to coherent/systematic errors or higher frequency incoherent dephasing. (Bottom) Data from a single-ion Ramsey experiment for which the microwave field was deliberately detuned by $\Delta/2\pi = 7.9$ Hz to achieve an oscillating pattern as the wait time, τ_R, was scanned. An exponentially decaying sine wave is fitted to find a decay constant $\tau = 1.337$ s, with the decay envelope indicated by dotted lines.

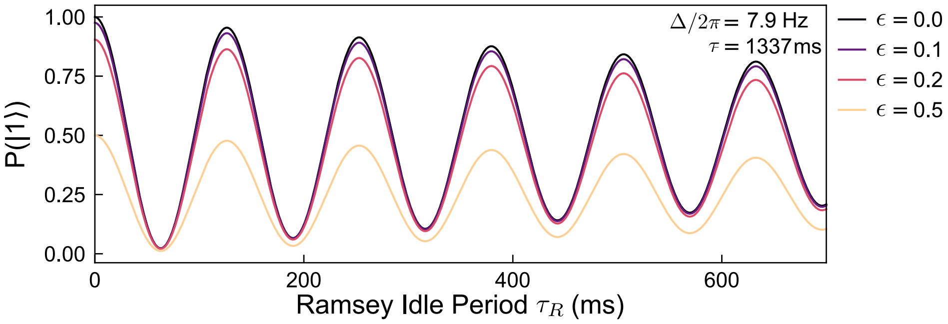

FIGURE 2.9. **Theoretical calculations of a single-ion Ramsey experiment.** The detuning and decay constant are set to be $\Delta/2\pi = 7.9$ Hz and $\tau = 1.337$ s. A relative amplitude error in the $\pi/2$-rotations is varied through values $\epsilon = \{0, 0.1, 0.2, 0.5\}$, showing a reduction in the oscillation amplitude and mean, but a consistent oscillation frequency.

(yellow). For all values of ϵ in Fig. 2.9, the oscillation frequency is unchanged and the detuning can be extracted.

The phase Ramsey experiment

One disadvantage of calibrating the control frequency via an oscillatory Ramsey time scan measurement is the required run-time. To measure small frequency errors, one must use sufficiently long interrogation times τ_R. Achieving sub-Hz resolution requires interrogation times of many hundreds of milliseconds, and each measurement must be repeated sufficiently in order to average over the projective measurement results. The full procedure can result in run-times of many minutes to resolve the oscillatory pattern, which is incompatible with the regular control field re-calibrations eventually required for a quantum processor to run long, complex algorithms. A second disadvantage of the time-scan method is that the results are symmetric about $\Delta = 0$. Consequently, one cannot distinguish between positive and negative detuning errors. Instead, this must be determined experimentally by shifting the control field frequency, repeating the calibration and observing if the measured detuning increases or decreases.

An alternative method, still founded in Ramsey interferometry, requires only two measurements for a fixed interrogation time. This method is termed the "phase Ramsey" or "clock" experiment [**81**, **82**] (Fig. 2.10). Here, the phase of the second $\pi/2$-rotation axis is changed by $\pi/2$ relative to the first, such that the second rotation occurs about the y-axis rather than the x-axis. As such, in the case of no detuning error, the second rotation should cause the Bloch vector to rotate about its own axis, resulting in a final projection onto the z-axis of $P(|1\rangle) = 1/2$. The second data point follows similarly but with the second rotation about the $-y$-axis. Both sequences of gates are illustrated schematically in Fig. 2.10(a). The two points, when averaged over sufficient projective measurements, should both result in the measurement $P(|1\rangle) = 1/2$ when there is no detuning error. If there is a positive detuning, then the first measurement will record $P(|1\rangle) > 1/2$ and the second measurement should be symmetrically *below* 1/2. If the detuning is negative, then the first and second results are swapped, clearly allowing us to determine not just the magnitude of the detuning but also its sign. As with the time-scan measurement, the phase Ramsey is largely insensitive to errors in the amplitude of the $\pi/2$-rotations; any error will simply result in the two measurement points being symmetric about a point away from 1/2.

The measurements are described by the following sequences of operations,

$$\hat{U}_A = e^{-i\pi(1+\epsilon)\hat{\sigma}_y/4} e^{-i\Delta\tau_R\hat{\sigma}_z/2} e^{-i\pi(1+\epsilon)\hat{\sigma}_x} \tag{2.31}$$

$$\hat{U}_B = e^{i\pi(1+\epsilon)\hat{\sigma}_y/4} e^{-i\Delta\tau_R\hat{\sigma}_z/2} e^{-i\pi(1+\epsilon)\hat{\sigma}_x/4} \tag{2.32}$$

where I have neglected decoherence effects and assumed there is a negligible off-resonance error during the $\pi/2$-rotations. I have allowed for over-rotation errors in the $\pi/2$-rotations quantified by the dimensionless error ϵ. Applying the circuits $\hat{U}_A$ and $\hat{U}_B$ to a qubit prepared in $|0\rangle$ and averaging over many projective measurements results in the respective values P_A and P_B,

$$P_A = \frac{1}{2}\cos\left(\frac{\epsilon\pi}{2}\right)^2 (1+\sin(\Delta\tau_R)) \tag{2.33}$$

$$P_B = \frac{1}{2}\cos\left(\frac{\epsilon\pi}{2}\right)^2 (1-\sin(\Delta\tau_R)) . \tag{2.34}$$

The detuning can be extracted from Eqn. (2.34) using,

$$\begin{aligned} \sin(\Delta\tau_R) &= \frac{2}{1+\frac{P_B}{P_A}} - 1 \\ &= \frac{P_A - P_B}{P_A + P_B} \qquad (2.35) \\ \Delta &= \frac{1}{\tau_R}\arcsin\left(\frac{P_A - P_B}{P_A + P_B}\right). \qquad (2.36) \end{aligned}$$

This expression for detuning is only valid in the regime $\tau_R \leq \pi/(2|\Delta|)$, due to the periodicity of the sine function.

While I do not consider a full treatment of the $\pi/2$-gate off-resonance error that results from a non-zero detuning here, the effect can be estimated by modifying the final expression to

$$\Delta = \frac{1}{\tau_R + 4\tau_{\pi/2}/\pi}\arcsin\left(\frac{P_A - P_B}{P_A + P_B}\right). \tag{2.37}$$

where $(\tau_R + 4\tau_{\pi/2}/\pi)$ is the *effective* Ramsey interrogation time including the two $\pi/2$-rotations. The extra factor of $2/\pi$ multiplying the length of the two $\pi/2$-rotations, $2\tau_{\pi/2}$, arises because the dephasing error is occurring during a *driven* gate. This results in a more complex multi-axis error for which the accumulated $\hat{\sigma}_z$-phase is approximately $\Delta \times 4\tau_{\pi/2}/\pi$. For full details, see Appendix B.1 of J. Benhelm's thesis [**83**].

Figure 2.10 presents theoretical calculations about the results after a phase Ramsey measurement with no added amplitude error, $\epsilon = 0$. Panel (a) illustrates the two experiment circuits and their differing final $\pi/2$-rotations. For any phase Ramsey measurement, both circuits are run with the same interrogation time τ_R. We calculate the expected results after applying the circuits to a qubit prepared in $|0\rangle$, P_A and P_B, which are plotted for different values of τ_R in panel (b) and three detunings, $\Delta/2\pi = \{2.5, 5, -10\}$ Hz. For a non-zero detuning, the values of P_A (solid lines) and P_B (dashed lines) are symmetric about 1/2 and oscillate at frequency Δ. If the sign of the detuning is negated, then the curves P_A, P_B are swapped, as shown for the negative detuning $\Delta/2\pi = -10$ Hz (pink). This

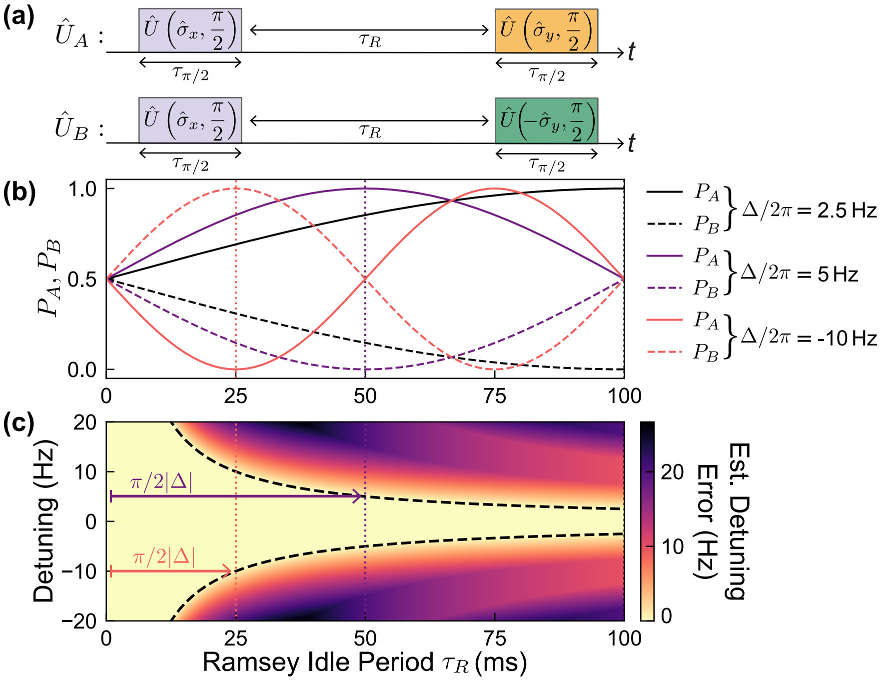

FIGURE 2.10. **Theoretical calculations demonstrating the phase Ramsey experiment for frequency calibration.** (a) Experimental schematic for the two measurements involved in a phase Ramsey experiment: the circuit $\hat{U}_A$ with a final rotation about the y-axis, and the circuit $\hat{U}_B$ with a final rotation about the $-y$-axis. (b) Calculated final measurement values $P(|1\rangle)$ are shown for the two circuits, P_A (solid lines) and P_B (dashed lines). Three different detunings are plotted, $\Delta/2\pi = \{2.5, 5, -10\}$ Hz, with varying idle periods, τ_R. (c) The error in the extracted estimate of $\Delta/2\pi$ is plotted for a range of detunings and interrogation times. For each value of detuning, the estimate is only valid for $\tau_R < \pi/2|\Delta|$, indicated by the black dashed lines. The limits for the data in panel (b) with $\Delta/2\pi = 5$ (purple) and $\Delta/2\pi = -10$ Hz (pink) are indicated by the dotted lines.

behaviour allows us to successfully measure both the magnitude and sign of the detuning Δ. If there is no detuning error, then the results of P_A, P_B would remain fixed at 1/2.

The phase Ramsey measurements are only valid for idle periods within the first quarter of the oscillation, indicated by dotted lines with colours corresponding to the main curves. Indeed, in Fig. 2.10(c) I calculate the estimated detunings using Eqn. (2.37) and plot the error between these values and the true detunings. The estimated detuning is only valid for $\tau_R \leq \pi/(2|\Delta|)$, as indicated by the black dashed curves. This phenomenon suggests that the length of the idle period must be chosen judiciously. It is generally advantageous to choose a longer idle time to increase the signal-to-noise of the measurement by separating the values P_A and P_B. However, if τ_R is too long then the calculated detuning will be incorrect. The approach we use in our experiments is to repeat the phase Ramsey calibration three times with increasing resolution, generally using $\tau_R = \{8, 25, 50\}$ ms. This allows us to catch larger deviations in the detuning with the first calibration (up to $\sim \pm 30$ Hz), and then improve the estimation precision with the higher resolution calibrations, typically achieving a precision of ± 200 mHz for $\tau_R = 50$ ms.

2.5 Field inhomogeneity

As a trapped-ion quantum device is scaled up to larger numbers of qubits, the error rates should ideally remain constant across the string of qubits. As will be discussed in Chapter 6, homogeneous error rates between qubits is a common requirement of quantum error correction protocols, and is necessary if one wants to exploit the intrinsic errors to implement a decoherence-free subspace. This requirement, however, is rarely true. There are many reasons why qubits have differing error rates. In the case of fabricated semiconductor or superconducting qubits, it can be due to manufacturing faults or defects. By contrast, realising a qubit in the atomic physics of a trapped ion should result in identical, indistinguishable qubits. However, in practice, while the ions may be identical, this is not necessarily true of the environments into which they are embedded.

One example of this can be observed in our blade-style trap. Along the length of the trap axis, the magnetic field used to set the qubit quantisation axis is not constant. This is likely due to the location of the ion pump relative to the trap and its insufficiently shielded magnet having a large influence on the magnetic field in the trap. We can measure the magnitude of the gradient using Ramsey experiments, as introduced previously for microwave frequency calibrations.

We confine a string of five $^{171}\mathrm{Yb}^{+}$ qubits in the blade-style trap. Multi-qubit measurements are performed using the EMCCD camera rather than the APD to resolve individual ions' fluorescence. To measure the qubit frequencies, we perform a Ramsey experiment using two $\pi/2$-rotations about the x-axis and a variable wait period τ_R, with the results shown in Fig. 2.11. By measuring the period of each qubit's oscillation, we find a 4.8 Hz variation in the qubit frequencies between the first and fifth ions. The inter-ion spacing can be calculated using the axial trap frequencies when multiple ions are confined [7]. With this technique, we obtain the EMCCD camera resolution that can then be used to determine the length of a trapped ion string. We find that the five ion string is 22 μm long, corresponding to a 218 mHz/μm frequency gradient along the string.

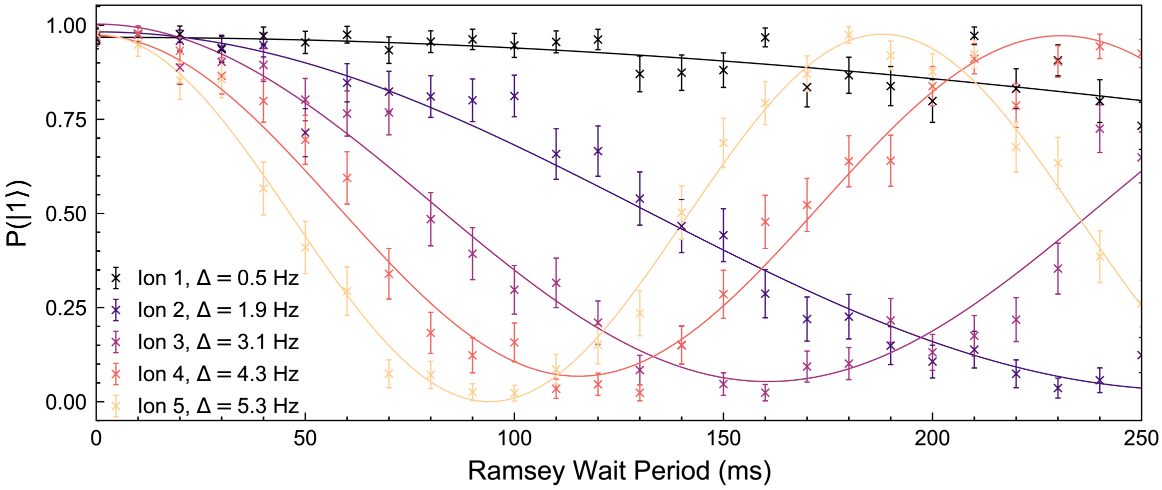

FIGURE 2.11. **Ramsey interferometry with five qubits in an inhomogeneous magnetic field.** A global microwave field of a fixed frequency, 12.642818036 GHz, was used to measure the qubit frequencies with a Ramsey measurement. The final qubit states were measured using ion fluorescence observed on an EMCCD camera. The detunings between the global microwave field frequency and the individual qubit transition frequencies were extracted from the oscillation period for each ion, finding a 4.8 Hz variation between the first (black) and fifth (yellow) qubit.

In addition to a magnetic field gradient, we also observe a gradient in the applied microwave field strength across the trapped ion string. The microwaves are emitted from an in-vacuum loop antenna (Fig. 2.4), which has a resonance at approximately 12.64 GHz. Due to internal reflections off the trap and the trap holder, the average microwave field intensity varies along the trap axis, and hence between the qubit locations. As with the magnetic field gradient, the microwave strength inhomogeneity can be measured using a simple experiment. We chose to measure the magnetic field gradient with a Ramsey measurement, as it is highly sensitive to qubit frequency errors and largely insensitive to amplitude errors. Now, we use a Rabi interrogation measurement to record the variation in microwave field amplitude, as this technique is more sensitive to amplitude errors. The Rabi flop oscillation period is dependent on the microwave field amplitude, $\Omega = \mu B$ (Eqn. (2.24)), and consequently any variation of the microwave field intensity between qubit locations will be translated to differences in the measured Rabi frequency.

We applied a continuous microwave field to a string of five trapped ions and measured their evolution (Fig. 2.12). Over a period of 0 - 30 ms of microwave interrogation, it can be observed that the initially in-phase Rabi flops gradually become out of sync due to differences in the individual qubits' Rabi frequencies. From Fig. 2.12, the Rabi frequency was measured using Eqn. (2.24), recording a 1.4 Hz/µm

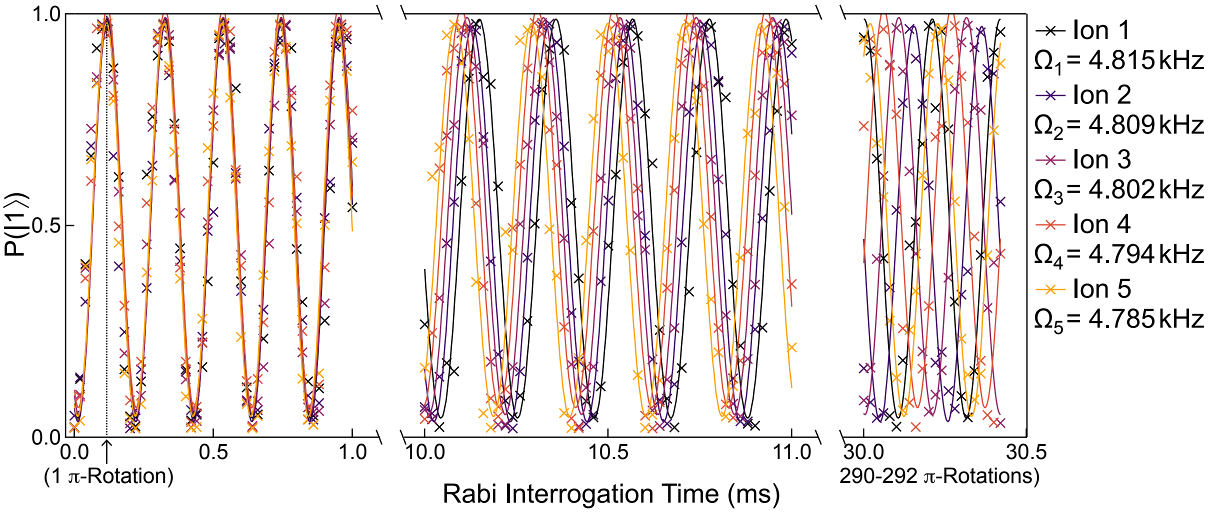

FIGURE 2.12. **Rabi oscillations with five qubits in an inhomogeneous microwave field**. Five trapped-ion qubits were excited with continuously applied microwaves to drive oscillations between $|0\rangle$ and $|1\rangle$ for Rabi interrogation times ranging from 0 - 30 ms. The Rabi frequencies for each ion are proportional to the microwave field strength, which is not homogeneous across the ion string, resulting in a 1.4 Hz/μm gradient in the measured Rabi frequencies.

gradient in the Rabi frequency. While small, this error will quickly accumulate when either circuit length or qubit numbers are increased. Over a string of only seven qubits, this becomes a 1% variation in Rabi frequency between the first and final qubit, for an average Rabi frequency of 5 kHz.

These inhomogeneities present an immediate concern for using a global control field to drive global multi-qubit rotations – it becomes impossible to calibrate the frequency and amplitude of the field for all qubits simultaneously. In Section 6.4, I will show the effect of these inhomogeneities on the variation of randomised benchmarking error rates across a trapped ion string. There, I will also introduce a quantum control technique called a “dynamically corrected gate” (DCG) that can be used to homogenise error rates and enable global microwave gates despite field inhomogeneities.

In the next chapter, I continue a detailed exploration of the physical quantum system that we are employing for our experiments. I perform a precision characterisation of some of the relevant atomic physics transitions in $^{171}\text{Yb}^{+}$ and introduce the reader to the first example of an error suppressing control technique, using electron shelving to reduce measurement errors in a hyperfine trapped-ion qubit.

CHAPTER 3

Precision measurements in ^{171}Yb^{+} for improved state detection

---

“What’s the point of being alive," she said, "if you’re not going to communicate?”

- Kurt Vonnegut, *Bluebeard*

*This chapter includes a variety of precision measurements in ^{171}Yb^{+} to characterise the $^2S_{1/2} - {}^2D_{5/2}$ transition, and introduces a new method of state detection using electron shelving to the metastable $^2D_{5/2}$ state. This work constitutes two manuscripts currently being reviewed: “Scalable hyperfine qubit state detection via the $^2S_{1/2} - {}^2D_{5/2}$ transition in ^{171}Yb^{+}” [**1**], and “Precision Characterization of the $^2D_{5/2}$ State and Quadratic Zeeman Coefficient in ^{171}Yb^{+}” [**2**].*

Trapped ions have seen a resurgence as a leading platform for the development of quantum information systems. In recent years, a primary area of research has been the quality of single- and two-qubit gates, where fidelities of better than 99.99% [**84–86**] and 99.9% [**85**, **87**] have been reported, respectively. Enabled by quantum control techniques, such as amplitude, frequency and phase-modulation [**6**, **88**, **89**], high-fidelity two-qubit gates are now possible at high speeds [**90**, **91**] and also across larger qubit registers [**92**, **93**]. Progress in this domain has allowed for the implementation of longer and more complex quantum circuits, e.g. Refs. [**94–96**]. Yet, as the number of qubits in a joint register – and thereby the potential size of a correlated state – grows, an increasingly important area for improvement becomes state-detection fidelity. Detection errors are generally statistically independent and scale at least linearly with the number of qubits. They therefore quickly become a significant factor limiting the overall performance of a multi-qubit register, e.g. in the context of active quantum error correction conditioned on stabiliser measurements [**96–99**].

Various qubit encodings are available in trapped ions which bring with them different advantages and drawbacks – including in the area of demonstrated measurement fidelity. One can either choose two ground states of the fine- or hyperfine structure for the encoding, or split the logical states across a ground- and a metastable state to form an optical qubit [**100**]. Hyperfine qubits such as ^{9}Be^{+} [**85**], ^{43}Ca^{+} [**101**, **102**] or ^{171}Yb^{+} [**38**] as considered here, are an attractive choice in that they do not suffer from energy relaxation (T_1 decay) like optical qubits, and also offer so-called "clock states" that are first-order insensitive to perturbations from magnetic fields (providing long T_2 coherence). In hyperfine qubits, the qubit states are separated by microwave frequencies on the order of several to tens of GHz enabling the use of low-noise microwave sources for high-fidelity qubit control [**4**, **67**, **84**].

Measurement on either category of trapped-ion qubit is generally performed using state-dependent laser-induced fluorescence [**103**], whereby one logical state, the "bright state", scatters photons and the other does not, hence being referred to as the "dark state". Optical qubits enable efficient discrimination between the bright and dark states and have shown high detection fidelities, leveraging the large energy-level separation of the qubit manifold [**104**, **105**]. By contrast, when using hyperfine qubits the relatively small energy gap between the qubit states results in unwanted off-resonant scattering during detection. This scattering limits the useful duration of the detection period and thereby the number of photons that can be collected in it, negatively impacting the ability to distinguish qubit states from associated photon-detection-probability distributions. To overcome this obstacle, one may pursue the use of new complex imaging and detection hardware [**106–110**] or software-based data processing of time-resolved information [**104**, **107**, **111–114**]. As qubit numbers are increased, however, the overhead for detection hardware and software can become limiting, motivating an exploration of complementary "physics-based" schemes to improve measurement fidelity in hyperfine qubits.

In this work, we borrow a detection technique widely employed in optical qubits to perform electron shelving on a hyperfine ^{171}Yb^{+} qubit to increase detection fidelity without modification of detection hardware or software. By shelving the population of one of the qubit states to a metastable state separated by an optical transition, we can detect population remaining in the qubit manifold without being limited by off-resonant scattering and the resulting leakage to the other logical state. We implement this method using a quadrupole transition at 411 nm from the ^{2}S$_{1/2}$ qubit manifold to the ^{2}D$_{5/2}$ state, and separately to the extremely long-lived metastable ^{2}F$_{7/2}$ level (Fig. 3.1). We also employ a repump laser at 760 nm to efficiently restore all population to the qubit manifold after the detection period via the rapidly decaying ^{1}D$[3/2]_{3/2}$ state. In our work, we further combine the shelving routine with efficient software post-processing techniques using photons collected on an avalanche photodiode (APD) and an electron multiplying charged coupled device (EMCCD) camera, using a time-resolved, non-adaptive maximum likelihood protocol on the APD [**113**] and a machine-learning-based image classifier on the

EMCCD. We characterise and compare the various routines, demonstrating measurement-fidelity improvements up to $300\times$ leveraging the $^2\mathrm{F}_{7/2}$ level, and describe how this may be efficiently integrated into quantum information experiments.

3.1 Trapped ion qubit state detection

Various approaches are being pursued to improve qubit state detection with ions, which can be broadly classed as hardware-, software-, or physics-based. The first category uses specialised detectors, such as superconducting nanowire single photon detectors (SNSPDs) either stand-alone [**108**] or embedded in a surface-electrode RF trap [**109**], multi-channel photomultiplier tubes (PMTs) [**106**, **107**], or fast intensified cameras [**110**]. Several software-based methods have been demonstrated to improve the final state estimation. Combining a record of the incident timing of photons during detection with prior knowledge such as the expected fluorescence rate and decay times τ_B and τ_D from the bright and dark states, one can infer the final state from a maximum likelihood calculation [**104**]. Furthermore, if real-time data processing is available, the same detection fidelity can be achieved in shorter detection times using an adaptive version of this technique. Wölk et al. [**113**] analyse the time-resolved detection methods for the case of $^{171}\mathrm{Yb}^+$, which had been experimentally demonstrated for optical qubits by Myerson et al. [**104**], and hyperfine qubits by Hume et al. [**111**] and Hemmerling et al. [**112**]. Other software-based approaches include recent work by Ding et al. [**114**] investigating the use of machine-learning methods for state estimation, implemented in hardware on an FPGA with a single $^{171}\mathrm{Yb}^+$ qubit; they achieve similar results to Seif et al. [**107**], who apply machine learning methods to the time-resolved readout from a PMT array in post-processing.

Detection of optical qubits falls under the physics-based approaches, achieving a very high signal-to-noise ratio through what is generally referred to as "electron shelving" after Hans Dehmelt [**115**, **116**]. In such settings, measurement fidelities of $\geq 99.99\%$ have been reported for an optical qubit encoded in $^{40}\mathrm{Ca}^+$ using time-resolved measurements of fluorescence [**104**], and separately, without time resolution, on an EMCCD camera [**105**]. The detection fidelity of an optical qubit is fundamentally limited by the lifetime of the metastable state (a T_1 decay process). Although the associated decay rate during detection is often low under typical detection times, the decay probabilities are independent for each ion and can thereby quickly become the limiting factor to the overall *state* detection fidelity in larger qubit registers. To address this problem, a newer generation of fast cameras is being developed, which allow time-resolved measurements to be carried out while also providing spatial resolution for identification of the

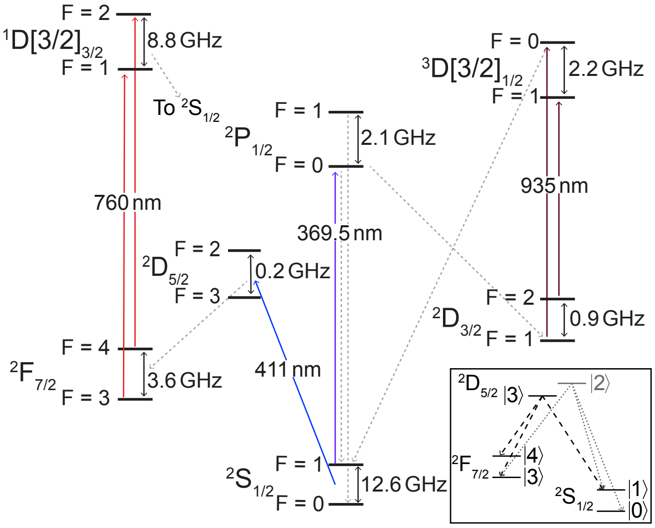

FIGURE 3.1. Selected energy levels and laser frequencies for ^{171}Yb^{+}. The qubit levels are encoded in the ^{2}S$_{1/2}$ hyperfine manifold, shown at the bottom centre. Additional energy levels due to Zeeman splittings have been omitted for visual clarity and the dashed grey lines show relevant spontaneous decays. (Inset) Decay channels from ^{2}D$_{5/2}$, with a simplified hyperfine notation.

unique quantum state in a multi-qubit register. First demonstrations have recently been reported for an electron-shelved read-out in ^{138}Ba^{+} [**110**], reaching $\sim$ 99.99% fidelity for a single qubit and at least 99.7% in a four-qubit register.

In ^{171}Yb^{+} the measurement-fidelity limiting factor is leakage between the hyperfine qubit levels during detection. The two logical states encoded in the ^{2}S$_{1/2}$ levels can be distinguished by state-selective fluorescence induced by a 370 nm laser resonant with the $^2\mathrm{S}_{1/2}\,|F=1\rangle \leftrightarrow {}^2\mathrm{P}_{1/2}\,|F=0\rangle$ transition, which, aside from a small branching ratio to ^{2}D$_{3/2}$, forms a closed cycling transition (Fig. 3.1). However, the small hyperfine splitting of 2.11 GHz between adjacent ^{2}P$_{1/2}$ levels results in a comparatively large off-resonant scattering probability causing leakage primarily from the bright state $^2\mathrm{S}_{1/2}\,|F=1\rangle$ to the dark state $^2\mathrm{S}_{1/2}\,|F=0\rangle$. The inverse occurs as well, but with a lower probability due to the effective 14.75 GHz detuning. The dynamics of this asymmetric leakage during state detection in hyperfine qubits have been analysed theoretically by Acton et al. [**121**] and, more specifically for the case of ^{171}Yb^{+}, by Wölk et al. [**113**]. A further challenge in ^{171}Yb^{+} is its low fluorescence yield compared to other isotopes without nuclear spin, such as ^{174}Yb^{+}. Fluorescence increases with the strength of an applied magnetic field [**64**], but so does the magnetic field sensitivity of the clock transition encoding the qubit, negatively impacting the available phase coherence time (T_2).

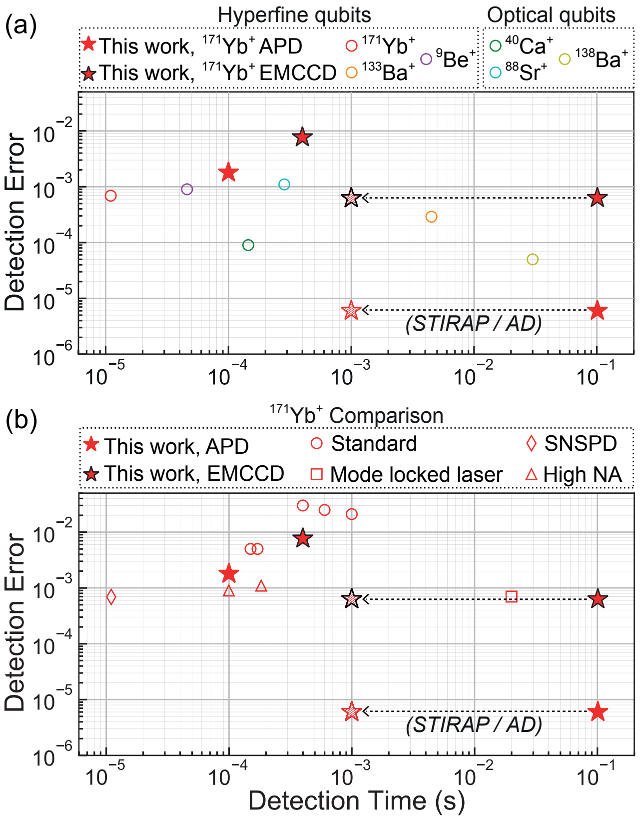

FIGURE 3.2. Comparison of single-qubit detection errors and times for trapped-ion qubits. (a) Overview of representative results for different hyperfine qubits, with ^{171}Yb^{+} [**108**], ^{133}Ba^{+} [**117**] and ^{9}Be^{+} [**109**], and optical qubits, with ^{40}Ca^{+} [**104**], ^{88}Sr^{+} [**118**] and ^{138}Ba^{+} [**110**]. Star markers represent the work presented here in ^{171}Yb^{+} using the APD (red outline) and the EMCCD (black outline). The shaded star markers at 1 ms detection are achieved by detecting in the long-lived $^{2}F_{7/2}$ manifold in ^{171}Yb^{+}. Currently, this procedure requires $\sim$ 100 ms (filled star markers) for shelving, but additional laser hardware should reduce this time by two orders of magnitude using STIRAP or an active depopulation technique (AD) (see Sec. 3.4.2). (b) Results for ^{171}Yb^{+}, with circle markers representing standard detection techniques that can be straightforwardly implemented without advanced detector technology [**38**,**64**,**107**,**113**,**114**]. The work presented here, shown as star markers, similarly requires no additional detector hardware. The remaining markers require special hardware such as a mode-locked laser [**119**] (square marker), superconducting nanowire single photon detectors (SNSPDs) [**108**] (diamond marker), or a high NA objective [**120**] (triangle markers).

The efficiency of a detection protocol can be quantified in two dimensions, through the measured detection error and the required detection time – both of which should be ideally minimised for practical use in quantum computing. In Fig. 3.2(a) we show an overview of results reported in the trapped-ion field for both hyperfine and optical qubits together with the results (red stars) described in this manuscript using the APD (red outline) and the EMCCD (black outline). Figure 3.2(b) compares detection errors for the specific case of ^{171}Yb^{+}. Open-circle markers represent measurements achieved without special hardware for photon collection. The open-triangle markers show ^{171}Yb^{+} detection fidelities achieved using a high NA objective [**120**] and the open-square marker is a measurement in ^{171}Yb^{+} using a mode-locked laser to achieve near background free detection in the dark periods between ultra-short pulses [**119**]. The open-diamond marker uses an SNSPD for photon collection [**108**]. The work we report here exceeds the results achieved with "standard" detection hardware in ^{171}Yb^{+}, and if combined with high-speed optical pumping via STIRAP provides a route for field-leading performance in detection error at practically relevant measurement times.

3.2 Experimental setup

As discussed in Chapter 2, the qubit is realised in the hyperfine ^{2}S$_{1/2}$ energy levels of ^{171}Yb^{+}, split by 12.64 GHz, using the "clock states" $|0\rangle \equiv |F = 0, m_F = 0\rangle$ and $|1\rangle \equiv |F = 1, m_F = 0\rangle$ for first-order magnetic-field insensitivity. The magnetic quantisation field is produced by a permanent magnet, creating a 440.9(6) µT magnitude field at the ions' position, which was measured using the ^{2}S$_{1/2}$ linear Zeeman shift of 13.98(1) kHz/µT [**73**]. Single-qubit operations are driven with a microwave field produced by a vector signal generator (VSG) that is delivered through an in-vacuum loop antenna. Photons emitted during laser cooling and state detection are collected by a custom-made objective with an effective NA = 0.56 and imaged onto either an APD or an EMCCD.

A simplified energy-level diagram showing the states and transitions in ^{171}Yb^{+} relevant to this work is shown in Fig. 3.1. The hyperfine ^{2}S$_{1/2}$ qubit states are shown in the bottom centre of the diagram, separated by 12.64 GHz. Doppler cooling (DC), optical pumping (OP), and state detection (SD) utilise the ^{2}S$_{1/2}$ $\leftrightarrow$ ^{2}P$_{1/2}$ transition; this requires a diode laser near 369.5 nm, nominally tuned to the inner $|F = 1\rangle \leftrightarrow |F = 0\rangle$ transition, that is split into three different beamlines. A second-order sideband from a 7.374 GHz electro-optic modulator (EOM) simultaneously excites the outer $|F = 0\rangle \leftrightarrow |F = 1\rangle$ transition during Doppler cooling ensuring all manifold states are addressed. At the start of each experiment, following Doppler cooling, the ion is prepared in the qubit state $|0\rangle$ by adding a 2.105 GHz sideband via a separate EOM to the 370 nm laser; this optically pumps any population in $|1\rangle$ to $|0\rangle$ via ^{2}P$_{1/2}\,|F = 1\rangle$ [**38**]. To directly measure the final qubit state, the 370 nm laser light is applied to the ion without any additional modulation to selectively excite $|1\rangle$, the "bright" qubit state. Occasional decays from ^{2}P$_{1/2}$ to ^{2}D$_{3/2}$ (0.5%) remove the ion from the cooling cycle and necessitate a "clear-out" laser at

935 nm that is operated continuously to return the ion to the qubit manifold [**122**]. An EOM running at 3.067 GHz adds sidebands to the 935 nm laser to ensure both hyperfine levels of the ^{2}D$_{3/2}$ are repumped.

In this work, we introduce two additional lasers for the purpose of state detection: a 411 nm laser for electron shelving from ^{2}S$_{1/2}$ to ^{2}D$_{5/2}$ [**2, 119, 123–125**], and a 760 nm laser [**126–128**] for repumping from the long-lived ^{2}F$_{7/2}$ state ($\tau \approx 5.4$ years [**68**]) via ^{1}D$[3/2]_{3/2}$. The 760 nm laser replaces a 638 nm laser [**129**] commonly used for this purpose and gives the benefit of substantially faster repumping. An EOM driven at 5.260 GHz adds sidebands to the 760 nm laser to excite both ^{2}F$_{7/2}$ hyperfine states. We stabilise both laser frequencies through Pound-Drever-Hall locks to cylindrical Fabry-Pérot cavities with a free spectral range of 1.5 GHz; the 411 nm (760 nm) cavity has a finesse of approximately 32,000 (1,000$-$2,000) and a drift rate of $\sim$ 320 mHz/s ($\sim$ 3.2 Hz/s). The ultra-low expansion spacer of the 411 nm cavity is temperature stabilised close to the minimum of its coefficient of thermal expansion (CTE) located at 38.2°C. Absolute frequency measurements use a HeNe-calibrated wavemeter[1] with a 500 kHz precision, 10 MHz absolute accuracy at 760 nm and 177 MHz absolute accuracy at 411 nm (due to operating $>$ 200 nm from the 633 nm calibration wavelength). All laser beams are controlled by acousto-optic modulators (AOMs) driven by direct digital synthesis sources referenced to a rubidium frequency standard.

3.3 Characterisation of the ^{171}Yb$^+$ ^{2}S$_{1/2} \leftrightarrow {}^2D_{5/2}$ transition

In order to implement electron-shelved detection to ^{2}D$_{5/2}$ or ^{2}F$_{7/2}$, we must first characterise the ^{2}S$_{1/2} \leftrightarrow {}^2D_{5/2}$ transition driven by the 411 nm laser, as well as the clear-out transition using the 760 nm laser. Table 3.1 contains a summary of the relevant parameters that have been measured in this work required for high fidelity, electron-shelved state detection. From here we use simplified notation for the hyperfine levels by omitting the F and m_F labels in the Dirac notation for hyperfine states, $|F, m_F\rangle$.

3.3.1 Characterisation of the 411 nm shelving transition

We begin by performing spectroscopy on the ^{2}S$_{1/2} \leftrightarrow {}^2D_{5/2}$ optical transition near 411 nm, resolving individual hyperfine and Zeeman levels as shown in Figure 3.3. The 411 nm laser is locked to a high finesse cavity with fixed length and 1.5 GHz free spectral range. By scanning the RF frequency driving an AOM, we achieve finer frequency control than allowed by the discrete cavity lock points.

---

[1] HighFinesse WSU-10

Parameter	This work (exp.)
411 nm frequency for ^{2}S$_{1/2}\,\|0,0\rangle \leftrightarrow {}^2D_{5/2}\,\|2,0\rangle$ (THz)	729.487752(177)
411 nm frequency for ^{2}S$_{1/2}\,\|1,0\rangle \leftrightarrow {}^2D_{5/2}\,\|3,0\rangle$ (THz)	729.474917(177)
Hyperfine constant of ^{2}D$_{5/2}$ (MHz)	-63.368(1)
Linear Zeeman coefficient of ^{2}D$_{5/2}\,\|3\rangle$ (kHz/μT)	13.96(2)
Linear Zeeman coefficient of ^{2}D$_{5/2}\,\|2\rangle$ (kHz/μT)	19.61(3)
Quadratic Zeeman coefficient for ^{2}D$_{5/2}\,\|3,0\rangle$ (Hz/μT^2)	-0.350(1)
Lifetime of ^{2}D$_{5/2}\,\|3\rangle$ (ms)	7.1(4)
Decay from ^{2}D$_{5/2}\,\|3\rangle$ to ^{2}S$_{1/2}\,\|1\rangle$	17.6(4)%
Decay from ^{2}D$_{5/2}\,\|3\rangle$ to ^{2}F$_{7/2}$	82.4(4)%
Lifetime of ^{2}D$_{5/2}\,\|2\rangle$ (ms)	7.4(4)
Decay from ^{2}D$_{5/2}\,\|2\rangle$ to ^{2}S$_{1/2}\,\|0\rangle$	11.1(3)%
Decay from ^{2}D$_{5/2}\,\|2\rangle$ to ^{2}S$_{1/2}\,\|1\rangle$	7.4(3)%
Decay from ^{2}D$_{5/2}\,\|2\rangle$ to ^{2}F$_{7/2}$	81.6(4)%
760 nm repumper centre frequency (THz) after preparing ^{2}D$_{5/2}\,\|3,0\rangle$	394.430203(16)
760 nm repumper centre frequency (THz) after preparing ^{2}D$_{5/2}\,\|2,0\rangle$	394.424943(20)

TABLE 3.1. Relevant parameters for electron-shelved state detection via the ^{2}S$_{1/2} \leftrightarrow {}^2D_{5/2}$ transition in ^{171}Yb^{+}.

Although absolute frequency measurements are limited by the accuracy of the wavemeter (177 MHz at 411 nm), differential measurements on the same cavity mode do not require the wavemeter and achieve significantly higher accuracy.

The procedure to measure the ^{2}S$_{1/2} \leftrightarrow {}^2D_{5/2}$ spectra is illustrated schematically in Fig. 3.3(a); the recorded spectra are shown in the lower panels for (b) ^{2}S$_{1/2}\,|1,0\rangle \leftrightarrow {}^2D_{5/2}\,|3,m_F\rangle$, (c) ^{2}S$_{1/2}\,|1,0\rangle \leftrightarrow {}^2D_{5/2}\,|2,m_F\rangle$, and (d) ^{2}S$_{1/2}\,|0,0\rangle \leftrightarrow {}^2D_{5/2}\,|2,m_F\rangle$. The ion is initially Doppler cooled (DC) and prepared in ^{2}S$_{1/2}\,|0,0\rangle$ via optical pumping (OP), followed by a microwave π pulse (μw) to transfer the ion to ^{2}S$_{1/2}\,|1,0\rangle$ for the measurements in panels (b) and (c). To shelve the population to ^{2}D$_{5/2}$, we apply 50-100 μs of 411 nm light and scan the AOM frequency. The shelving success is measured using 250 μs of high power, resonant Doppler cooling light (DC$^{(*)}$), which has EOM-induced sidebands to excite both qubit states, to distinguish between a "dark" ion that has been successfully shelved and a "bright" ion remaining in the ^{2}S$_{1/2}$ qubit manifold. Between each point, 20 ms of 760 nm light

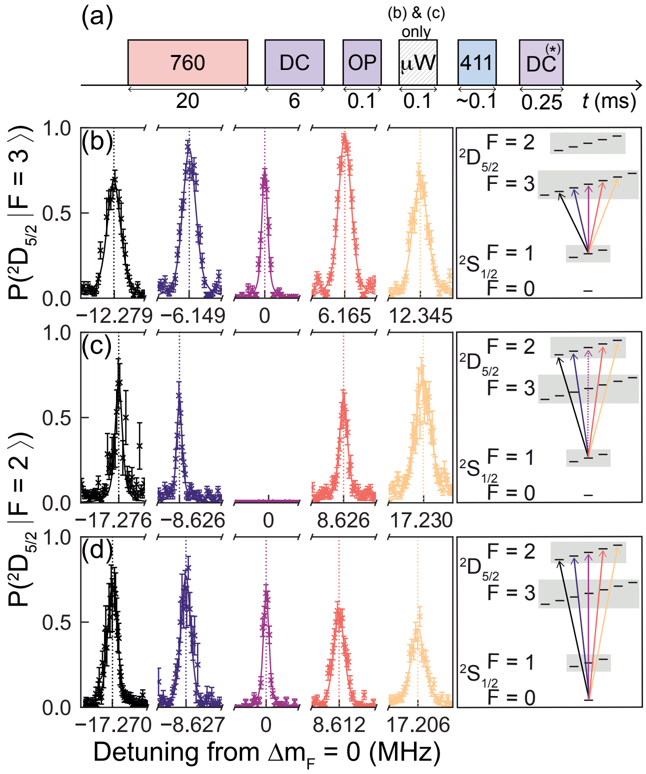

FIGURE 3.3. Spectra of the $^2\mathrm{S}_{1/2} \leftrightarrow {}^2\mathrm{D}_{5/2}$ transition. (a) Schematic of the measurement protocol for measuring the 411 nm spectra, showing when the 760 nm, 411 nm, and Doppler cooling (DC) and optical pumping (OP) 370 nm light is applied. The final detection is performed using Doppler cooling light at high-power and tuned near resonance (DC$^{(*)}$). A microwave π pulse (μw) is applied to prepare $^2\mathrm{S}_{1/2}\,|1,0\rangle$ for (b) and (c) only. (b)-(d) The $^2\mathrm{S}_{1/2} \leftrightarrow {}^2\mathrm{D}_{5/2}$ spectra are measured for $\Delta m_F = 0, \pm1, \pm2$ (left). Energy level diagrams are shown with corresponding colours for the different Zeeman transitions (right). We measure (b) $^2\mathrm{S}_{1/2}\,|1\rangle \leftrightarrow {}^2\mathrm{D}_{5/2}\,|3\rangle$, (c) $^2\mathrm{S}_{1/2}\,|1\rangle \leftrightarrow {}^2\mathrm{D}_{5/2}\,|2\rangle$, and (d) $^2\mathrm{S}_{1/2}\,|0\rangle \leftrightarrow {}^2\mathrm{D}_{5/2}\,|2\rangle$. In (c), we observe that the $\Delta m_F = 0$ transition cannot be driven, as expected due to atomic selection rules. Any repetition with insufficient Doppler cooling photons is rejected in post-processing. Error bars are calculated from quantum projection noise and each data-set is fitted to a Voigt profile.

clears out any population that has decayed to the $^2\mathrm{F}_{7/2}$ manifold after shelving. Post-processing on the initial Doppler cooling photons ensures that the ion has successfully returned to the qubit manifold by eliminating any point with insufficient cooling counts.

For each spectrum, the five accessible Zeeman transitions are detected, $\Delta m_F = 0, \pm1, \pm2$, with the exception of $^2\mathrm{S}_{1/2}\,|1,0\rangle \leftrightarrow {}^2\mathrm{D}_{5/2}\,|2,0\rangle$, which is forbidden by selection rules, as is the remaining hyperfine transition $^2\mathrm{S}_{1/2}\,|0\rangle \leftrightarrow {}^2\mathrm{D}_{5/2}\,|3\rangle$. The relative coupling strengths of the five Δm_F transitions can be tuned by changing the polarisation of the incoming 411 nm light. The centre frequency for each transition is measured by fitting the peaks to a Voigt profile to account for residual Doppler broadening;

relative frequencies measured on the same cavity mode are only limited by the accuracy of the fitting routine (0.1-2 kHz). The absolute measurement of $^2\mathrm{S}_{1/2}\,|0,0\rangle \leftrightarrow {}^2\mathrm{D}_{5/2}\,|2,0\rangle$, 729.487752(177) THz, is consistent with previous measurements [**123**, **130**].

3.3.2 Measurement of the $^2\mathrm{D}_{5/2}$ lifetime and branching ratios

To measure the lifetime and branching ratios for $^2\mathrm{D}_{5/2}$, we prepare the two hyperfine states $^2\mathrm{D}_{5/2}\,|2\rangle$ and $^2\mathrm{D}_{5/2}\,|3\rangle$ and allow the state to decay. The measurement protocol is illustrated schematically in Fig. 3.4(a). To maximise shelving fidelity to $^2\mathrm{D}_{5/2}$, multiple 411 nm π pulses to different Zeeman levels are used. We use five successive π pulses, $\Delta m_F = 0, \pm 1, \pm 2$, to shelve to $|F = 2\rangle$ and three pulses, $\Delta m_F = 0, \pm 2$, to shelve to $|F = 3\rangle$ (see Section 3.4.1 for further details). Directly after shelving, 100 μs of high-power resonant Doppler cooling light identifies any point that was not shelved – in post-processing any point with sufficiently high photons recorded in this period likely remains in the $^2\mathrm{S}_{1/2}$ manifold and is consequently eliminated. From $^2\mathrm{D}_{5/2}$ the ion is allowed to decay for a variable wait period scanned between 0-30 ms, after which we detect the final state. To determine the final ion state, an initial 250 μs pulse of state-selective state detection light (SD) is used to distinguish between the two qubit states $|0\rangle$ and $|1\rangle$. Following this, we apply 500 μs of high-power resonant Doppler cooling light to distinguish between an ion in the qubit states $^2\mathrm{S}_{1/2}$ (bright), and the shelved states $^2\mathrm{D}_{5/2}$ and $^2\mathrm{F}_{7/2}$ (dark).

The three measured populations, P($|0\rangle$), P($|1\rangle$) and P($|\mathrm{shelf}\rangle$), are plotted in Fig. 3.4(b, c) after the ion decays from the prepared state (b) $^2\mathrm{D}_{5/2}\,|2\rangle$ and (c) $^2\mathrm{D}_{5/2}\,|3\rangle$. In these experiments we are not able

	Decay to $^2\mathrm{S}_{1/2}$	Decay to $^2\mathrm{F}_{7/2}$	Lifetime (ms)
This work (exp.) $^{171}\mathrm{Yb}^{+}\,|F = 3\rangle$	17.6(4)%	82.4(4)%	7.1(4)
This work (exp.) $^{171}\mathrm{Yb}^{+}\,|F = 2\rangle$	18.4(4)%	81.6(4)%	7.4(4)
Taylor et al. [**131**] (1997 exp.) $^{172}\mathrm{Yb}^{+}$	17(4)%	83(3)%	7.2(3)
Yu et al. [**132**] (2000 exp.) $^{174}\mathrm{Yb}^{+}$	-	-	7.0(4)
Fawcett et al. [**133**] (1991 calc.) Yb II	19.7%	80.3%	5.74

TABLE 3.2. Branching ratios and lifetime for the $^2\mathrm{D}_{5/2}$ state calculated by fitting an exponential decay to the populations in Fig. 3.4. Both hyperfine states $^2\mathrm{D}_{5/2}\,|3\rangle$ and $^2\mathrm{D}_{5/2}\,|2\rangle$ are prepared and analysed independently. Uncertainties are one standard deviation errors resulting from the fits. The results are compared to previous measurements and theoretical calculations.

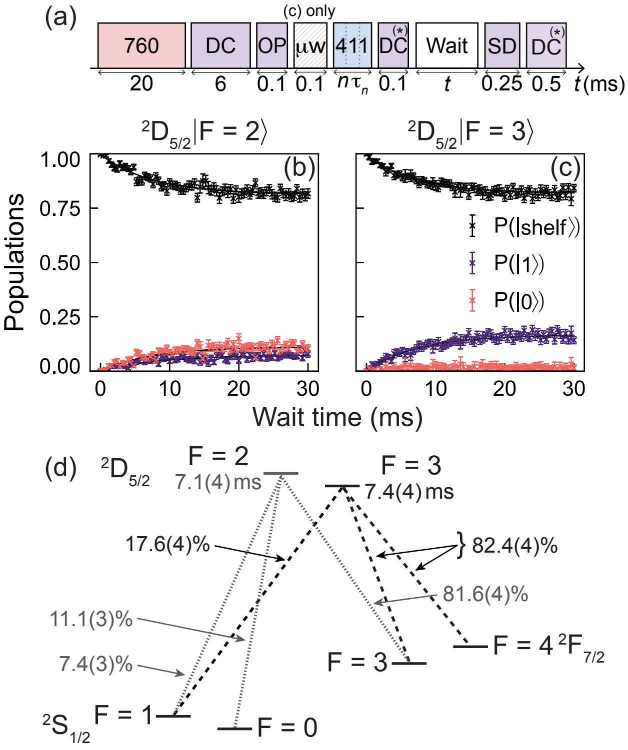

FIGURE 3.4. Measurement of the ^{2}D$_{5/2}$ lifetime and branching ratios to ^{2}S$_{1/2}$ and ^{2}F$_{7/2}$. (a) Measurement protocol for measuring branching ratios and lifetimes, showing when the 760 nm, 411 nm, and Doppler cooling (DC), optical pumping (OP), state detection (SD) and high-power resonant Doppler cooling (DC$^{(*)}$) 370 nm light is applied. The ion is first prepared in ^{2}S$_{1/2}$ $|1,0\rangle$ for panel (c) using a microwave π pulse (μw). Multiple 411 nm π pulses of length τ_n are used to shelve to ^{2}D$_{5/2}$, with (b) $n = 5$ pulses to ^{2}D$_{5/2}$ $|2, m_F\rangle$, and (c) $n = 3$ pulses to ^{2}D$_{5/2}$ $|3, m_F\rangle$. (b, c) The populations P($|0\rangle$), P($|1\rangle$) and P($|$shelf$\rangle$) are plotted after shelving to (b) ^{2}D$_{5/2}$ $|2\rangle$ or (c) ^{2}D$_{5/2}$ $|3\rangle$ and waiting for the ion to decay during an idle period of variable length. The term P($|$shelf$\rangle$) combines any population in ^{2}D$_{5/2}$ and ^{2}F$_{7/2}$. Error bars are calculated from quantum projection noise, and any repetition with insufficient initial Doppler cooling photons is rejected in post-processing. (d) Measured decays with corresponding branching ratios extracted from exponential decay fits in (b, c) are shown for ^{2}D$_{5/2}$ $|2\rangle$ (grey, dotted) and ^{2}D$_{5/2}$ $|3\rangle$ (black, dashed).

to distinguish between the states ^{2}D$_{5/2}$ and ^{2}F$_{7/2}$; the combined populations are labelled P($|$shelf$\rangle$). However, given the vastly different lifetimes of ^{2}D$_{5/2}$ and ^{2}F$_{7/2}$ [**133**], we can be confident that in the long-time limit the population P($|$shelf$\rangle$) →P(^{2}F$_{7/2}$). Indeed, given the extracted lifetime of ^{2}D$_{5/2}$, after 100 ms only 6e-5% of the population remains in ^{2}D$_{5/2}$.

To measure the branching ratios and lifetimes, an exponential decay is fitted to P($|$shelf$\rangle$). The branching ratios are obtained from the expected asymptotic limit of the fitted curve, with any remaining population in P($|\text{shelf}\rangle$) assumed to have decayed to $^2\text{F}_{7/2}$. The lifetime of $^2\text{D}_{5/2}$ is measured to be 7.1(4) ms (7.4(4) ms) when the ion is prepared in $^2\text{D}_{5/2}\,|3\rangle$ ($^2\text{D}_{5/2}\,|2\rangle$). Examining the qubit state populations, we confirm that the hyperfine level $^2\text{D}_{5/2}\,|3\rangle$ has no observable decay to $|0\rangle$, as expected for an electric quadrupole E2 transition. The asymptotic limits for the $|F = 0\rangle$ and $|F = 1\rangle$ populations after preparing $^2\text{D}_{5/2}\,|2\rangle$ are 11.1(3)% and 7.4(3)%, which agree well with expected Clebsch-Gordon coefficients. The branching ratios and lifetimes for both hyperfine levels are shown in Figure 3.4(d) and Table 3.1. These measurements are in agreement with previous experimental results [**131**, **132**].

3.3.3 Measurement of the second-order Zeeman coefficient of $^2\text{D}_{5/2}$

To deduce the second-order Zeeman coefficient of the $^2\text{D}_{5/2}\,|3,0\rangle$ state, we measure the 411 nm optical transition with respect to the ground state microwave transition at different magnetic field strengths. The B-field is varied between $\sim$ 4.4 G to $\sim$ 10 G by adjusting the placement of a permanent magnet and current passing through a coil. For each B-field setting the frequencies of the $^2\text{S}_{1/2}\,|0,0\rangle \leftrightarrow {}^2\text{S}_{1/2}\,|1,0\rangle$ hyperfine transition and the $^2\text{S}_{1/2}\,|1,0\rangle \leftrightarrow {}^2\text{D}_{5/2}\,|3,0\rangle$ 411 nm transition are recorded. The measurements are interleaved, with Ramsey interrogation times of 50 ms and 0.1 ms for the microwave and 411 nm transitions respectively. At each point, the measured hyperfine frequency is *added* to the optical 411 nm frequency to obtain the $^2\text{S}_{1/2}\,|0,0\rangle \leftrightarrow {}^2\text{D}_{5/2}\,|3,0\rangle$ frequency, eliminating the quadratic $^2\text{S}_{1/2}$ shift. The ratio of the relative shift of these two transition frequencies is plotted in Fig. 3.5.

Applying a linear fit to the data produces a ratio -11.27(4), where the uncertainty is the standard error of the fit. If we take the commonly reported value of 0.03108 Hz/μT^2 as the quadratic Zeeman coefficient of $^2\text{S}_{1/2}$, we find the quadratic Zeeman coefficient of $^2\text{D}_{5/2}\,|3,0\rangle$ to be -0.350(1) Hz/μT^2. This value is nearly two orders of magnitude more precise than the best published result (Table 3.3) [**123**].

	Quadratic Zeeman coefficient (Hz/μT^2)
This work (exp.) $^2\text{D}_{5/2}\,|3,0\rangle$	-0.350(1)
Roberts et al. [**123**] (1999 exp.) $^2\text{D}_{5/2}\,|2,0\rangle$	+0.38(8)

TABLE 3.3. Quadratic Zeeman coefficients measured for $^2\text{D}_{5/2}$. The coefficient has opposite signs for the two hyperfine levels $|F = 3\rangle$, $|F = 2\rangle$.

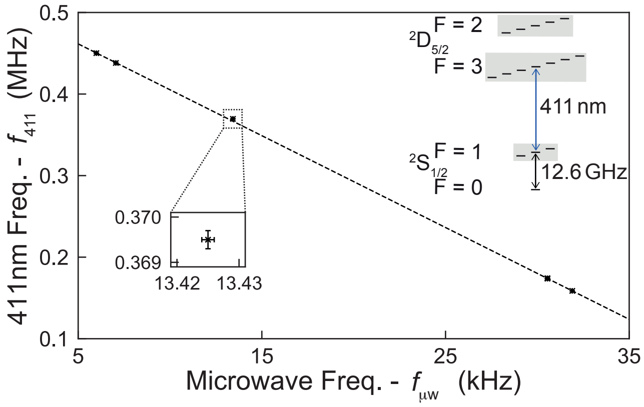

FIGURE 3.5. Frequency of the ^{2}S$_{1/2}$ $|0,0\rangle \leftrightarrow$ ^{2}D$_{5/2}$ $|3,0\rangle$ 411 nm transition vs. the ^{2}S$_{1/2}$ $|0,0\rangle \leftrightarrow$ ^{2}S$_{1/2}$ $|1,0\rangle$ microwave transition at different magnetic field strengths. The relevant transitions are illustrated in the upper right energy level diagram. The optical frequency has been compensated for cavity drift, which was measured to be 320(60) mHz per second. Typical statistical uncertainties of the frequency measurements are approximately 200 Hz and 0.2 Hz for the optical and microwave frequencies, respectively, with the error bar size highlighted in the lower inset. The frequency offsets are $f_{\mu W} = 12.642812118466$ GHz and $f_{411} = 729.487559$ THz. Applying a linear fit to the data we find a ratio of -11.27(4).

3.3.4 Measurement of the ^{2}D$_{5/2}$ hyperfine splitting

The hyperfine splitting of ^{2}D$_{5/2}$ can be measured using the difference between the transition frequencies of ^{2}S$_{1/2}$ $|1,0\rangle \leftrightarrow$ ^{2}D$_{5/2}$ $|2,0\rangle$ and ^{2}S$_{1/2}$ $|1,0\rangle \leftrightarrow$ ^{2}D$_{5/2}$ $|3,0\rangle$. Electric quadrupole selection rules forbid the ^{2}S$_{1/2}$ $|1,0\rangle \leftrightarrow$ ^{2}D$_{5/2}$ $|2,0\rangle$ transition. We instead record the frequency of four transitions: ^{2}S$_{1/2}$ $|1,0\rangle \leftrightarrow$ ^{2}D$_{5/2}$ $|2,\pm1\rangle$ and ^{2}S$_{1/2}$ $|1,0\rangle \leftrightarrow$ ^{2}D$_{5/2}$ $|3,\pm1\rangle$ to infer the frequency of the centre transition. All four excitations are achievable on the same cavity mode allowing us to take a differential measurement using the RF AOM frequencies that are not limited by the accuracy of the wavemeter. The measurements were taken on the same day over a period of four hours; we compensate for drift in the cavity frequency over this period.

The energy levels are shown schematically in Fig. 3.6, illustrating the effect of the hyperfine and Zeeman interactions. From this, we see that calculating the average frequency of the $\Delta m_F = +1$ and $\Delta m_F = -1$ transitions for both $\Delta F = 1, 2$, and then taking the difference of the two average values, Δf, gives [**134**]

$$\Delta f = -\Delta_{D,5/2} - \frac{8}{9} Q_{D,3}. \tag{3.1}$$

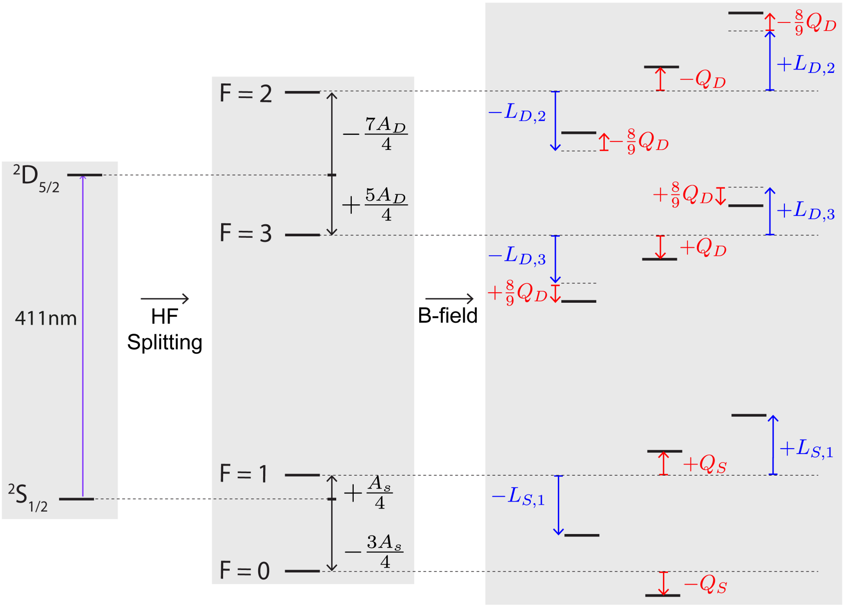

FIGURE 3.6. Illustration of the level splitting of ^{2}S$_{1/2}$ and ^{2}D$_{5/2}$ due to the hyperfine interaction and Zeeman effect. The two levels are separated by a frequency near 411 nm. The one half nuclear spin of ^{171}Yb$^+$ causes the states to split into hyperfine doublets with hyperfine interaction constants A_S and A_D for ^{2}S$_{1/2}$ and ^{2}D$_{5/2}$ respectively. An applied magnetic field causes the levels to further split due to the Zeeman interaction. Only three Zeeman levels are shown $m_F = 0, \pm 1$. The linear Zeeman shift for ^{2}S$_{1/2}\,|1\rangle$ is given by $L_{S,1}$. Similarly, $L_{D,F}$ represents the linear shift for ^{2}D$_{5/2}\,|F\rangle$. The second-order term of the interaction gives rise to a quadratic Zeeman term, Q_S and Q_D. The quadratic term on the $m_F = \pm 1$ states is $\frac{8}{9}\times$ that of the $m_F = 0$ state [**134**].

Here, $\Delta_{D,5/2}$ is the hyperfine splitting of ^{2}D$_{5/2}$ at zero magnetic field and $Q_{D,3}$ is the quadratic Zeeman shift on the clock state ^{2}D$_{5/2}\,|3,0\rangle$, which differs from the quadratic Zeeman shift on the ± 1 stretch states by a factor of 8/9. The second-order Zeeman coefficient for ^{2}D$_{5/2}\,|3,0\rangle$ was measured to be -0.350(1) Hz/μT^2, which equates to $Q_{D,3} = -68.2(2)$ kHz for a magnetic field strength of 441.27(2) μT. Using Eqn. (3.1), we then find $\Delta_{D,5/2} = -190.104(3)$ MHz, corresponding to a hyperfine interaction constant $A_{D,5/2} = -63.368(1)$. The uncertainty is limited by the standard error of the estimated 411 nm peak centre in the Voigt fits, and the uncertainties of the second-order Zeeman coefficient and cavity drift rate. This value is compared to previous measurements and calculations in Table 3.4; it agrees with the previous experimental measurement and achieves a 700× improvement in the precision.

Reference	$A_{D,5/2}$
This work (exp.)	-63.368(1)
Roberts et al. [**123**] (1999 exp.)	-63.6(7)
Itano [**135**] (2006 calc.)	-12.58
Sahoo et al. [**136**] (2011 calc.)	-48(15)
Porsev et al. [**137**] (2012 calc.)	-96
Nandy et al. [**138**] (2014 calc.)	-69(6)

TABLE 3.4. Comparison of measurements and calculations of the hyperfine splitting constant of ^{2}D$_{5/2}$. The measurement in this work compared the frequencies of the ^{2}S$_{1/2}\,|1,0\rangle \leftrightarrow {}^2D_{5/2}\,|2,\pm1\rangle$ and ^{2}S$_{1/2}\,|1,0\rangle \leftrightarrow {}^2D_{5/2}\,|3,\pm1\rangle$ transitions, measured on the same day and locked to the same cavity mode.

3.3.5 Characterisation of the 760 nm clear-out transition

After each experiment involving the ^{2}D$_{5/2}$ state, any population that has decayed to ^{2}F$_{7/2}$ must be returned to the qubit manifold. There are several possible transitions over a range of wavelengths that can be driven to achieve this goal: 638 nm [**122**], 760 nm [**126**], 828 nm [**129**], or 864 nm [**131**]. Here, we employ a 760 nm laser as it has been observed to have the most rapid clear-out time. This phenomenology owes to its excited energy level ^{1}D[3/2]$_{3/2}$ exhibiting a short upper-state lifetime (29 ns [**139**]), and a decay path primarily to the ^{2}S$_{1/2}$ ground states rather than other D-levels [**129**]. To address both ^{2}F$_{7/2}$ hyperfine levels, a 5.260 GHz EOM is added to the 760 nm laser.

In Fig. 3.7, we present the measured spectra for the 760 nm ^{2}F$_{7/2} \leftrightarrow {}^1$D[3/2]$_{3/2}$ transition, with the measurement protocol illustrated schematically in panel (a). We first prepare the ion in one of the ^{2}D$_{5/2}$ levels using the 411 nm shelving laser. A subsequent 10 ms wait period allows the ion to decay to either ^{2}S$_{1/2}$ or ^{2}F$_{7/2}$. Following the wait period, a 100 µs period of high power, on resonance Doppler cooling induces fluorescence in cases where the ion has not decayed to ^{2}F$_{7/2}$, and we discard these experiments in post-processing. The 760 nm laser is then applied to clear out the ^{2}F$_{7/2}$ state at a frequency adjusted through AOMs. To detect the final state, high power, on resonance Doppler cooling light is used to determine whether the ion has returned to the ^{2}S$_{1/2}$ manifold or remains in ^{2}F$_{7/2}$ after repumping. The probability of excitation from ^{2}F$_{7/2}$ is plotted in Fig. 3.7(b),(c) for states prepared in different m_F levels of (b) ^{2}D$_{5/2}\,|2\rangle$ and (c) ^{2}D$_{5/2}\,|3\rangle$. The energy level diagrams in Fig. 3.7(d),(e) show the potentially occupied ^{2}F$_{7/2}$ states populated through the electric dipole decay from (d) ^{2}D$_{5/2}\,|2,0\rangle$ or (e)

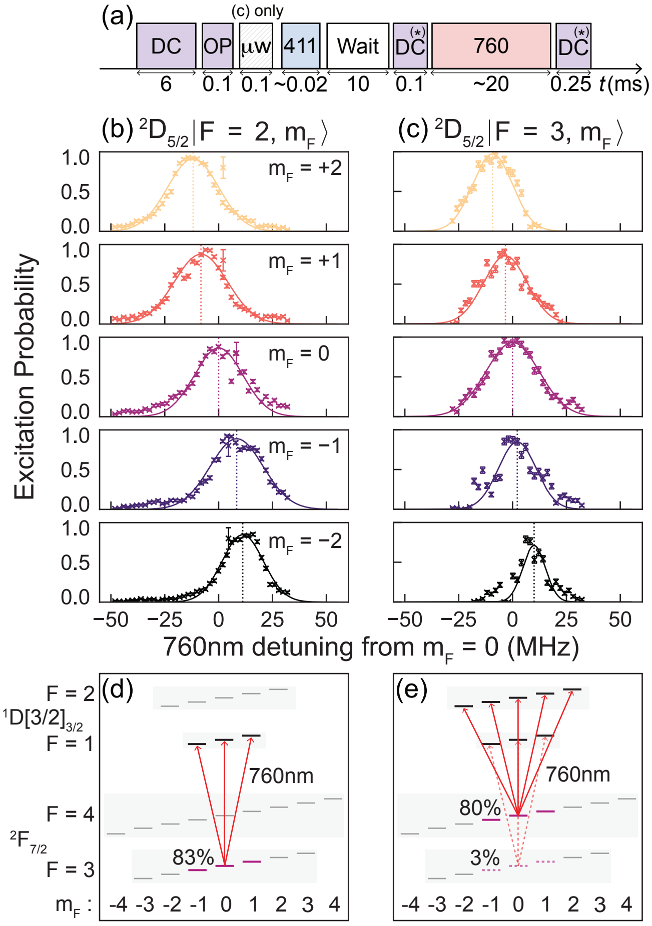

FIGURE 3.7. Measurement of the 760 nm ^{2}F$_{7/2}$ repump transition. (a) Schematic for the measurement protocol using the 760 nm, 411 nm, as well as Doppler cooling (DC) and optical pumping (OP) light at 370 nm. High power, on resonance Doppler cooling light is utilised for detection (DC$^{(*)}$). A microwave π pulse (µw) is used in (c) to prepare ^{2}S$_{1/2}\,|1,0\rangle$. (b, c) Transitions observed at 760 nm after shelving the ion to ^{2}D$_{5/2}\,|2,m_F\rangle$ or ^{2}D$_{5/2}\,|3,m_F\rangle$. For both transitions, the five Zeeman states $m_F = 0, \pm1, \pm2$ are individually prepared by a 411 nm pulse and the recovery probability for a given 760 nm laser frequency is shown with error bars are derived from quantum projection noise. The centre frequency of each excitation pathway from ^{2}F$_{7/2}$ is extracted from a Gaussian fit. (d, e) Energy diagrams illustrating the possible ^{2}F$_{7/2}$ states to which the ion can decay from ^{2}D$_{5/2}\,|F, m_F = 0\rangle$ as well as the allowed 760 nm excitations from ^{2}F$_{7/2}\,|F, m_F = 0\rangle$.

^{2}D$_{5/2}\,|3,0\rangle$ with the corresponding decay probabilities from the ^{2}D$_{5/2}$ levels [**2, 123**], and the possible repump pathways from ^{2}F$_{7/2}\,|F, m_F = 0\rangle$.

Each peak in the spectrum is a combination of clearing out multiple prepared states in ^{2}F$_{7/2}$ with the 760 nm laser. We can only deterministically prepare a specific m_F state in the ^{2}D$_{5/2}$ manifold using the 411 nm laser. From there, the ion decays probabilistically to ^{2}F$_{7/2}$ with $\Delta m_F = 0, \pm1$ (electric dipole

	Centre clear-out frequency (THz) after preparing	
	$^2\mathrm{D}_{5/2}\,\|3,0\rangle$	$^2\mathrm{D}_{5/2}\,\|2,0\rangle$
This work (exp.)	394.430203(16)	394.424943(20)
Mulholland et al. [**128**] (2019 exp.)	394.430026(519)	394.424837(519)

TABLE 3.5. The centre frequency of the 760 nm transition after preparing $^2\mathrm{D}_{5/2}\,|3,0\rangle$ and $|2,0\rangle$ compared to previous measurements [**128**]. The absolute frequency uncertainties are calculated from the standard deviation of the Gaussian fit combined with the specified 3σ accuracy of the WSU-10 wavemeter, which is 10 MHz at 760 nm.

(E1) coupling) or $^2\mathrm{S}_{1/2}$ with $\Delta m_F = 0, \pm1, \pm2$ (electric quadrupole (E2) coupling). While we can ensure that the ion has not decayed back to the $^2\mathrm{S}_{1/2}$ using a short Doppler cooling pulse, we are unable to determine which m_F level it has decayed to within the $^2\mathrm{F}_{7/2}$ manifold. In addition, $^2\mathrm{D}_{5/2}\,|3\rangle$ can decay to both $^2\mathrm{F}_{7/2}$ hyperfine levels with 80% (3%) probability to $^2\mathrm{F}_{7/2}\,|4\rangle$ ($^2\mathrm{F}_{7/2}\,|3\rangle$) [**123**]. Finally, when the ion is excited from $^2\mathrm{F}_{7/2}$ with the 760 nm clear-out laser, it can be excited with five possible Zeeman transitions, $\Delta m_F = 0, \pm1, \pm2$, as $^2\mathrm{F}_{7/2} \leftrightarrow {}^1\mathrm{D}[3/2]_{3/2}$ is an E2 coupling. Consequently, given a prepared m_F level in $^2\mathrm{D}_{5/2}$, the 760 nm shown in the measurements comprise between 6 and 22 possible unresolved individual transitions of varying probabilities. The centre frequencies of the transitions, obtained from Gaussian fits, are reported in Tab. 3.5 with a $\sim 25\times$ improvement in precision relative to previous results [**128**].

3.4 ^{171}Yb^{+} state detection using electron shelving

The standard detection protocol used to discriminate between the qubit states $|0\rangle$ and $|1\rangle$ in $^{171}\mathrm{Yb}^{+}$ relies on detecting state-selective laser-induced fluorescence at 370 nm. Ideally, the collected photons result in two well-separated Poisson distributions corresponding to the different states. However, leakage between the qubit levels due to off-resonant excitation during detection create one-sided tails on the photon distributions that overlap and thereby lead to detection errors.

In the following, we augment the standard detection method by prepending the measurement with pulses at 411 nm in order to transfer population from one qubit state to a metastable level. State detection is then performed using 370 nm light that drives all transitions between the $^2\mathrm{S}_{1/2}$ and $^2\mathrm{P}_{1/2}$ manifolds, effectively eliminating off-resonant excitations. Here, the achievable detection fidelity is limited by the shelving transfer accuracy and the finite lifetime of the metastable state. As indicated in Tab. 3.1, the

^{2}D$_{5/2}$ state lifetime is ~ 7 ms, after which it decays to ^{2}F$_{7/2}$ ($\sim 82\%$) or ^{2}S$_{1/2}$ ($\sim 18\%$). This presents two possibilities for an electron-shelving based detection protocol: (1) transfer the population of one qubit state to ^{2}D$_{5/2}$ and detect for duration $t \ll 7$ ms before any significant decay occurs; or (2) optically pump the $|1\rangle$ state to ^{2}F$_{7/2}$ via ^{2}D$_{5/2}$. In this section, we describe the detection protocols using both shelving methods, discuss different software-based techniques to improve state discrimination under these protocols, and finally compare the achieved state detection fidelities.

3.4.1 Electron-shelved detection in ^{2}D$_{5/2}$

The first protocol requires us to achieve an effective transfer of population from either hyperfine level in the qubit manifold to the metastable ^{2}D$_{5/2}$ state. We begin by measuring the effectiveness of applying a π pulse on two transitions: ^{2}S$_{1/2}\,|1\rangle \rightarrow {}^2D_{5/2}\,|3\rangle$ and ^{2}S$_{1/2}\,|0\rangle \rightarrow {}^2D_{5/2}\,|2\rangle$ (Fig. 3.8(a)). The linewidth of the 411 nm laser as well as the non-zero temperature of the motional modes limit the shelving efficiency associated with a single π pulse. Thus, in order to maximise population transfer, we implement a series of π pulses tuned to address multiple ^{2}D$_{5/2}$ Zeeman levels. When shelving via ^{2}S$_{1/2}\,|0\rangle \rightarrow {}^2D_{5/2}\,|2\rangle$, five Zeeman transitions can be driven successively, $\Delta m_F = 0, \pm 1, \pm 2$. By contrast, the ^{2}S$_{1/2}\,|1\rangle \rightarrow {}^2D_{5/2}\,|3\rangle$ transition only allows three successive pulses on $\Delta m_F = 0, \pm 2$ to be used, as the first-order Zeeman shift is approximately equal for the upper and lower states (~ 14 kHz/µT). If the $\Delta m_F = \pm 1$ transitions are excited, then any population initially transferred to ^{2}D$_{5/2}\,|3, 0\rangle$ will be *de-shelved* by the subsequent pulses.

The residual population in the qubit manifold after shelving is plotted in Fig. 3.8(b). As the number of shelving pulses is increased, the shelving fidelity improves from 93.9(2)% to 98.4(1)% for ^{2}S$_{1/2}\,|1\rangle \rightarrow {}^2D_{5/2}\,|3\rangle$ (black), and from 97.9(2)% to 99.3(1)% for ^{2}S$_{1/2}\,|0\rangle \rightarrow {}^2D_{5/2}\,|2\rangle$ (pink). The clock transition between the $m_F = 0$ states is driven first as its first-order magnetic-field insensitivity allows for the highest state transfer probability. In general, we observe no significant difference when changing the order of the subsequent pulses tuned to other Zeeman levels.

When using this protocol in large multi-qubit registers, it is critical to ensure that the population transfer efficiency remains high for all ions throughout the experiment. Its effectiveness will be limited by laser frequency drifts and variations in coupling strength due to laser intensity or polarisation gradients across the ion string. As both of these effects are often slowly varying or even static "systematic" errors, mitigation through advanced pulse sequences [**5**, **140**–**142**] can be considered in addition to regular calibration. Another commonly used routine for accurate population transfer is Rapid Adiabatic Passage

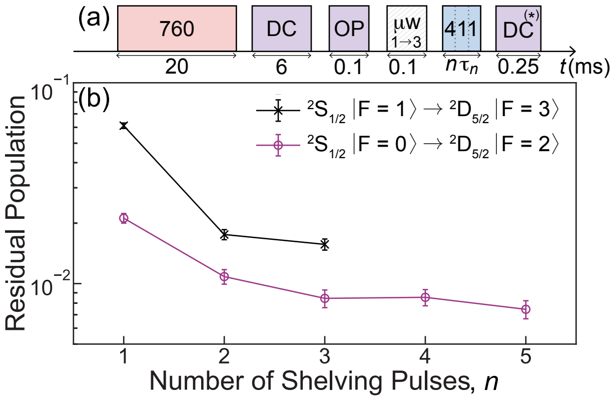

FIGURE 3.8. Shelving efficiency of multiple π pulses to different Zeeman levels. (a) Schematic showing the experimental sequence including n 411 nm shelving π pulses of length τ_n, a microwave pulse (μw) used to initialise the ion in $^2\mathrm{S}_{1/2}\,|1,0\rangle$ before the $^2\mathrm{S}_{1/2}\,|1\rangle \rightarrow {}^2\mathrm{D}_{5/2}\,|3\rangle$ transition, and 370 nm light used for Doppler cooling (DC), optical pumping (OP) and detection (DC$^{(*)}$). (b) The residual population in the qubit manifold $^2\mathrm{S}_{1/2}$ after shelving via (black) $^2\mathrm{S}_{1/2}\,|1\rangle \rightarrow {}^2\mathrm{D}_{5/2}\,|3\rangle$ using three successive shelving pulses, $\Delta m_F = 0, \pm 2$, and (pink) $^2\mathrm{S}_{1/2}\,|0\rangle \rightarrow {}^2\mathrm{D}_{5/2}\,|2\rangle$ using five successive shelving pulses, $\Delta m_F = 0, \pm 1, \pm 2$. The maximum shelving fidelity is 99.3(1)% after five shelving pulses to $^2\mathrm{D}_{5/2}\,|2\rangle$. Error bars are calculated from quantum projection noise.

(RAP) [**130**, **143**–**145**]. This technique involves linearly sweeping the frequency of the shelving laser, while simultaneously shaping the amplitude of pulse to follow a Gaussian profile. The procedure is more robust to systematic errors in the pulse frequency or length than a simple π pulse, at the cost of enhanced sensitivity to high-frequency and dephasing errors [**4**, **146**, **147**].

In Fig. 3.9 we examine the theoretical maximum transfer fidelity using RAP for different inverse laser coherence times, Γ, and Rabi frequencies, Ω. The probability of transfer using a Landau-Zener model [**148**] for RAP is given by

$$P_{LZ} = 1 - e^{-\pi^2\Omega^2/\alpha}, \tag{3.2}$$

where α is the frequency sweep rate used for the RAP pulse. To incorporate the effect of a finite laser linewidth, the theory is modified to include a Markovian noise bath in a two-level dephasing model [**145**, **149**]. The transfer probability now depends on the inverse of the laser coherence, Γ, becoming

$$P = \frac{1}{2}\left(1 - e^{-2\pi^2\Gamma\Omega/\alpha}\right) + e^{-2\pi^2\Gamma\Omega/\alpha} P_{LZ}, \tag{3.3}$$

which results in a sharp dropoff in transfer fidelity at lower sweep rates.

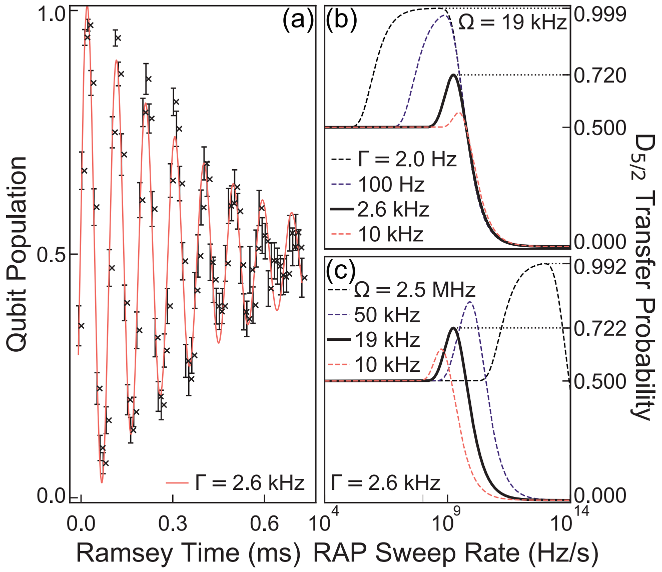

FIGURE 3.9. Transfer fidelity using Rapid Adiabatic Passage (RAP) on the $^2S_{1/2} \leftrightarrow {}^2D_{5/2}$ transition. (a) Ramsey interferometry using the 411 nm laser on the $^2S_{1/2}\,|0,0\rangle \leftrightarrow {}^2D_{5/2}\,|2,0\rangle$ transition, giving an inverse laser coherence $\Gamma = 2.6$ kHz. (b, c) Maximum population transfer using RAP for (b) fixed Rabi frequency $\Omega = 19$ kHz and varying Γ, or (c) fixed $\Gamma = 2.6$ kHz and varying Ω. In both figures, the solid black line is the result of our current experimental parameters and the black dashed line shows the maximum achievable transfer.

In our experiment we record a Rabi frequency of 19 kHz on the $^2S_{1/2}\,|0,0\rangle \rightarrow {}^2D_{5/2}\,|2,0\rangle$ clock transition and a 0.392 ms phase coherence time. This number is inferred from Ramsey interferometry shown in Fig. 3.9(a) and corresponds to an inverse coherence time of $\Gamma = 2.6$ kHz, which we attribute to laser linewidth. In Fig. 3.9(b),(c) we plot the calculated transfer fidelity against the sweep rate, as given by Eqn. (3.3). Given our parameters, $\Gamma = 2.6$ kHz, $\Omega = 19$ kHz, we could achieve a maximum transfer fidelity of 0.72 (solid black lines), which is significantly worse than the fidelity of a single π pulse ($\sim$98%). To achieve $> 99\%$ transfer fidelity, we would either need to improve our laser coherence to 2 Hz or increase our Rabi frequency to 2.5 MHz (dashed black lines); both of these are unfeasible in our current system. However, more reasonable parameter regimes achieving the same target can be found with two-dimensional parameter analysis, e.g. reducing the inverse coherence time to $\sim$130 Hz and increasing the Rabi frequency to 100 kHz. This would be achievable using higher laser lock-bandwidth and a different laser source, respectively. We further plan to investigate numerically optimised robust control waveforms [**5**] to improve state transfer efficiency.

3.4.2 Electron-shelved detection in ^{2}F$_{7/2}$

Another attractive option for electron-shelved detection in ^{171}Yb^{+} uses the ^{2}F$_{7/2}$ state with a lifetime in excess of 5 years [**68**], enabling longer detection periods, while still eliminating off-resonant scattering. Given that ^{2}S$_{1/2}$ $\rightarrow$ ^{2}F$_{7/2}$ is an electric octupole transition, direct shelving to this state requires ultra-stable laser systems generally only available in specialised frequency metrology laboratories [**126, 130, 150**]. To investigate this level for state detection without such a laser, we optically pump the $|1\rangle$ qubit state to the ^{2}F$_{7/2}$ manifold via ^{2}D$_{5/2}$ $|3\rangle$ using 411 nm light. As before with the electron-shelved detection in ^{2}D$_{5/2}$, once the population has been transferred to ^{2}F$_{7/2}$, we use high power Doppler cooling light tuned to be resonant with the entire ^{2}S$_{1/2}$ and ^{2}P$_{1/2}$ manifolds to measure laser induced fluorescence from the population remaining in the qubit manifold.

The incoherent shelving process used by us requires $\sim$ 100 ms to ensure >99.9% population transfer to ^{2}F$_{7/2}$, which makes it impractical for use in quantum computing. One way to achieve fast shelving to the F-state is via a STIRAP-like scheme [**151**] to a state that rapidly decays to the ^{2}F$_{7/2}$ manifold. To implement such a scheme, one could use a laser at 410 nm connecting the ^{2}D$_{3/2}$ metastable state to the $^1[5/2]_{5/2}$ level [**129, 152**] and combine it with light at 435 nm connecting the ^{2}S$_{1/2}$ manifold to the ^{2}D$_{3/2}$ state. As this scheme relies on the rapid decay of the $^1[5/2]_{5/2}$ state, it could be executed repeatedly akin to optical pumping, ensuring a high transfer efficiency to the long lived ^{2}F$_{7/2}$ state. Alternatively, a pulsed two-stage scheme could be used, where multiple shelving pulses (similar to Fig. 3.8) are combined with active depopulation (AD in Fig. 3.2) of the ^{2}D$_{5/2}$ state via resonant light at 3.4 μm [**123**].

3.4.3 State-detection protocol comparison

In this section, we now compare the detection fidelity for three different detection protocols: (1) ^{2}S$_{1/2}$ standard detection with light resonant only with the $|1\rangle$ state in the qubit manifold, (2) ^{2}D$_{5/2}$-shelved detection with the Doppler cooling laser tuned on resonance at high power after shelving the $|0\rangle$ qubit state to ^{2}D$_{5/2}$ $|2\rangle$ via five successive π pulses to different Zeeman states, and (3) ^{2}F$_{7/2}$-shelved detection with the resonant Doppler cooling laser after incoherently shelving the $|1\rangle$ qubit state via ^{2}D$_{5/2}$.

In all cases measurements are conducted using either an APD recording global fluorescence or an EMCCD camera providing the spatially resolved information required for experiments with multi-qubit registers. Except for protocol (3), we compare the performance of a simple threshold-based detection with a time-resolved maximum likelihood analysis for the APD data. For all three protocols, we compare thresholding and a classifier-based software routine for analysis of EMCCD data.

The detection error is calculated by interleaving preparation of a dark and bright qubit state and averaging the respective errors. We define the dark state error, ϵ_d, as the fraction of points prepared in the dark state that are recorded as bright, and the bright state error ϵ_b accordingly. The overall detection error is then quantified as $\epsilon = (\epsilon_d + \epsilon_b)/2$. In order to derive a threshold value and train the image classifier, five percent of measured data are dedicated to calibration/training, with the analysis being conducted on the remaining 95% of the data.

APD-based detection

To find the lowest detection error achievable with the APD, we vary the length of the detection period for the three different protocols as shown in Fig. 3.10(a). In the simplest protocol (1) of state-dependent fluorescence detection in the qubit manifold, the photon count histograms of the bright (dark) state are described by a Poissonian distribution modified with a tail towards the dark (bright) state counts [**121**]. This leads to a significant overlap between the histograms visible in Fig. 3.10(b) and correspondingly a large detection error. When one of the qubit states is shelved by five successive π pulses to $^2\mathrm{D}_{5/2}\,|2\rangle$ as in protocol (2), the application of detection light resonant with the entire $^2\mathrm{S}_{1/2}$ manifold eliminates the off-resonant scattering and hence the decay tail of the bright state completely, which is shown in Fig. 3.10(c). A residual but suppressed tail from the dark-state distribution remains due to decays from $^2\mathrm{D}_{5/2}$ back to the qubit manifold, with an 18% branching ratio. Lastly, incoherent shelving to the long-lived $^2\mathrm{F}_{7/2}$ state in protocol (3) maximally suppresses the decay tails on both distributions as illustrated in Fig. 3.10(d). To reduce the prohibitively long shelving times to $^2\mathrm{F}_{7/2}$ under optical pumping via $^2\mathrm{D}_{5/2}$ in these measurements, the ion is shelved only once every 1000 points before the dark state error is measured. The ion is then returned to the qubit manifold with the 760 nm laser in order to measure the bright state error for another 1000 points. These interleaved blocks are repeated 1000 times yielding a total of 10^6 datapoints for each case. The total detection period is extended up to 1 ms for $^2\mathrm{F}_{7/2}$-shelved detection as illustrated in the inset of Fig. 3.10(a).

To further improve on the detection error in the two protocols that show state decays, we also implement a maximum likelihood estimation based on time-resolved data [**113**], referred to hereafter as "subbinning". Here, additional information about the decay dynamics during a measurement period is obtained by dividing the 250 µs overall detection period into five smaller "subbins" of length 50 µs. This approach

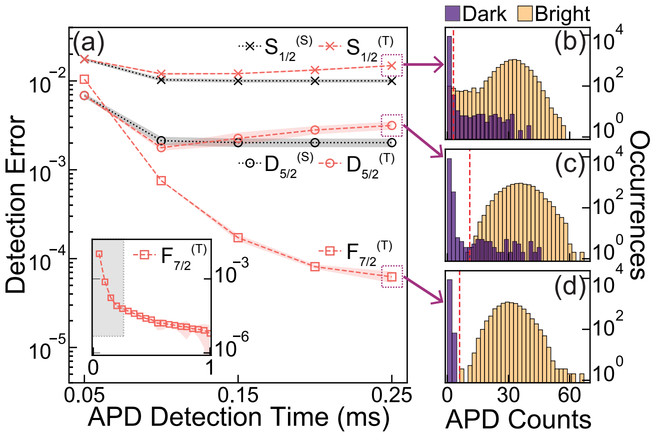

FIGURE 3.10. APD detection for three different detection protocols and two analysis methods. (a) Detection error as a function of detection time for $^2S_{1/2}$ standard detection with thresholding (red crosses), $S_{1/2}{}^{(T)}$, and with subbinning (black crosses), $S_{1/2}{}^{(S)}$; $^2D_{5/2}$-shelved detection with thresholding (red circles), $D_{5/2}{}^{(T)}$, and with subbinning (black circles), $D_{5/2}{}^{(S)}$; and $^2F_{7/2}$-shelved detection with thresholding only (red squares), $F_{7/2}{}^{(T)}$. For both the bright and dark state measurements 20,000 points are taken when using $^2S_{1/2}$ and $^2D_{5/2}$ detection, while for $^2F_{7/2}$ we measure 1,000,000 points to resolve errors at the 1×10^{-6} level. (Inset) Extended $^2F_{7/2}$-shelved results for detection periods up to 1 ms. The grey region indicates the size of the main panel. (b)-(d) Bright and dark state distributions with 250 µs detection time for the three methods $^2S_{1/2}$, $^2D_{5/2}$, $^2F_{7/2}$ respectively. The red dashed line represents the optimal threshold between the photon distributions determined from five percent of the data. Error bands in (a) show the standard deviation resulting from 20 different optimisation runs to find the optimal threshold by subsampling the data.

improves the ability to identify decay dynamics and allows for better discrimination of dark counts originating from electronic noise or cosmic particles. For the analysis, we further require an independent measurement of average count rates and the off-resonant scattering rates for the bright and dark states. Given our standard parameters for standard $^2S_{1/2}$ detection, we measure decay times from the bright and dark states of $\tau_B \approx 2$ ms and $\tau_D \approx 30$ ms, respectively. For $^2D_{5/2}$-shelved detection, τ_D is given by the ~ 7 ms upper state lifetime of the shelved state, while τ_B has an effectively infinite value. Given that there is no measurable decay during detection after shelving to $^2F_{7/2}$, we do not perform time-resolved analysis under that protocol. For details on the subbinning routine, see App. B.

EMCCD-based detection

To obtain spatially resolved measurements as required for multi-qubit experiments, we employ an EMCCD detector. Camera-based detection requires the identification of regions of interest (ROIs) for pixel-based analyses. We locate these through Gaussian fits to the 2D ion location(s) of calibration images

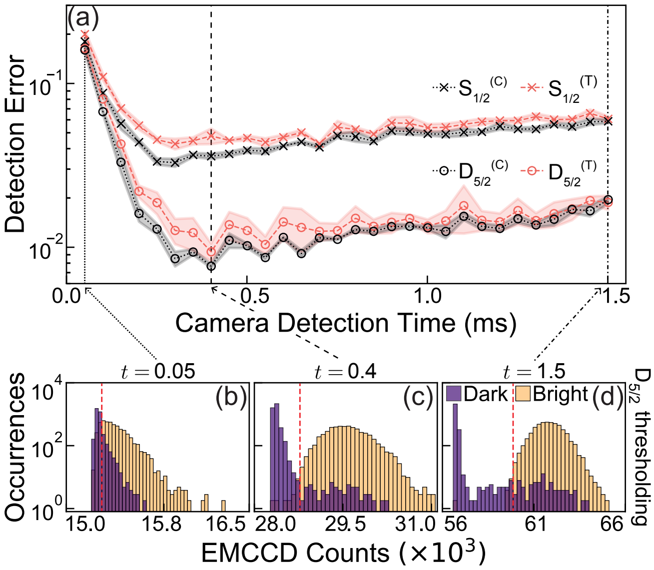

FIGURE 3.11. EMCCD based detection for two different detection protocols and analysis methods. (a) Detection error using $^2S_{1/2}$ standard detection with thresholding (red crosses), $S_{1/2}{}^{(T)}$, and the image classifier (black crosses), $S_{1/2}{}^{(C)}$; and electron-shelved detection after quintuple shelving to $^2D_{5/2}\,|2\rangle$ with thresholding (red circles), $D_{5/2}{}^{(T)}$, and the classifier, $D_{5/2}{}^{(C)}$. The lines show the means after sampling five different sets of training data, and shaded bands are $\pm 1\sigma$. 5000 measurements are taken at each point for both the bright and dark prepared states. Five percent of the total data set is employed for training and used for identification of hot pixels, thresholds, and classifier training. (b)-(d) Camera histograms for $^2D_{5/2}$-shelved detection at three detection times, illustrating how an optimum time is found for thresholding. For each histogram, the dashed red line marks the optimal threshold between "dark" and "bright".

of (a) bright ion(s). Further processing then happens only on ROI data extracted from the full camera images, which decreases processing time and can readily be parallelised.

As an ROI consists of multiple pixels, the thresholding method integrates their values over a certain number of "hot" pixels (corresponding to a subset of the brightest pixels) to obtain a measure of total counts in a given ROI. Alternatively, a set of calibration images obtained using ions prepared in the dark and bright states can be used to train a Random Forest classifier [**153**] for each ROI in order to identify a dark and bright ion. If trained on reliable data, this method is expected to be superior to the simple thresholding model, as it will consider not just the net fluorescence in the region of interest but also *correlations* between the counts on different pixels.

We compare the two spatial analysis methods across the three different detection protocols: standard $^2S_{1/2}$, $^2D_{5/2}$-shelved and $^2F_{7/2}$-shelved. In Fig. 3.11(a), we evaluate the measured detection error as a function of detection time for the first two protocols. The $^2S_{1/2}$ standard detection (cross markers) is compared to the $^2D_{5/2}$-shelved detection (open circles) and each dataset is analysed using the thresholding method (red) and the image classifier (black). These data clearly show that the shelved detection is superior to standard and that the image classifier can yield appreciable improvements under short to intermediate detection times. This is likely related to a larger number of mislabeled training images due to state decays, potentially offering room for further improvement.

The change in detection error at different detection times can be understood by examining the bright and dark histograms for $^2D_{5/2}$-shelved detection (Fig. 3.11(b)-(d)). At short detection times, the distributions have a large overlap, with electrical noise in the camera dominating the signal (Fig. 3.11(b), 0.05 ms detection period). At long detection periods (Fig. 3.11(d), 1.5 ms), the bright distribution mean has increased sufficiently to separate it from the dark distribution, but state decays become dominant due to the 7 ms lifetime of $^2D_{5/2}$ producing a decay tail from the dark distribution. At the optimum detection period, these two error contributions are balanced (Fig. 3.11(c), 0.4 ms detection period).

The detection error after using incoherent shelving to $^2F_{7/2}$ is measured on the EMCCD for only one detection time, 1 ms. This is due to the prohibitively long experimental run-times and the lack of timing resolution on the EMCCD, which we had exploited on the APD to get multiple detection time measurements. This data point is taken in the same style as for the APD, with blocks of 1000 interleaved dark and bright measurements, between which the ion is prepared in the appropriate bright $^2S_{1/2}$ or dark $^2F_{7/2}$ state. Both the classifier and the threshold are used to analyse this data, with a minimum error found using the classifier at $6.3(3) \times 10^{-4}$.

3.4.4 Summary of results

We summarise our findings of the lowest measured errors for all detection protocols and analysis methods in Table 3.6. Overall, we achieve a 5.6× improvement in fidelity using electron-shelved detection in $^2D_{5/2}$ compared to standard $^2S_{1/2}$ detection, measuring an error of $1.8(2) \times 10^{-3}$ with a 100 μs detection time on the APD. When using the EMCCD, we record a minimum error of $7.7(2) \times 10^{-3}$ using $^2D_{5/2}$-shelved detection, 4.3× lower than the best observed error using standard detection. For $^2F_{7/2}$-shelved detection with a 1 ms detection time, the detection error is reduced by another factor of 300× to $6(7) \times 10^{-6}$ on the APD, and a factor of $12\times$ to $6.3(3) \times 10^{-4}$ on the EMCCD.

Analysis	EMCCD thresholding		EMCCD classifier	
Detection	Error	Time (ms)	Error	Time (ms)
$^2S_{1/2}$ standard	$4.3(3) \times 10^{-2}$	0.3	$3.3(2) \times 10^{-2}$	0.3
$^2D_{5/2}$-shelved	$9(1) \times 10^{-3}$	0.4	$7.7(2) \times 10^{-3}$	0.4
$^2F_{7/2}$-shelved	$2(1) \times 10^{-3}$	1	$6.3(3) \times 10^{-4}$	1

Analysis	APD thresholding		APD subbinning	
Detection	Error	Time (ms)	Error	Time (ms)
$^2S_{1/2}$ standard	$1.20(6) \times 10^{-2}$	0.1	$1.00(5) \times 10^{-2}$	0.15
$^2D_{5/2}$-shelved	$1.8(2) \times 10^{-3}$	0.1	$2.0(2) \times 10^{-3}$	$\geq$0.15
$^2F_{7/2}$-shelved	$6(7) \times 10^{-6}$	1	-	-

TABLE 3.6. State detection errors and optimum detection times on the EMCCD and APD using three detection protocols: (1) standard detection in $^2S_{1/2}$, (2) electron-shelved detection in $^2D_{5/2}$, and (3) incoherently shelved detection in $^2F_{7/2}$. These are compared for different analysis methods: basic thresholding, camera image classification, and time-resolved subbinning.

3.5 Conclusion

In this work, we demonstrate that it is possible to combine the benefits of a long-lived, first-order magnetic-field insensitive hyperfine qubit with the high-fidelity detection typically observed in an optical qubit. By first shelving the population in one qubit state of ^{171}Yb^{+} to a metastable level, we are able to use high-power, near-resonant Doppler cooling light to perform efficient state discrimination without suffering off-resonant leakage. To enable scaling to larger qubit registers, we also characterise the detection error after shelving to $^2D_{5/2}$ when using a spatially-resolving EMCCD. For both the APD and EMCCD detectors we compare the performance of software routines for processing photon detection data. This involves either analysing time-resolved information about the incoming photons collected on the APD, or exploiting spatial correlations between EMCCD pixels using a classifier routine. We also validate that the state detection error in our system can be further reduced by shelving to the long-lived $^2F_{7/2}$ manifold. New laser systems used in one of two schemes we outline could be used to overcome the prohibitively long optical pumping time to $^2F_{7/2}$, making this a viable avenue for ultra-high-fidelity detection.

Ultimately our results foreshadow the possibility of combining novel data-processing software routines with physics-based techniques in the future to further reduce measurement errors without requiring extensive hardware modifications. When combined with an efficient repump laser at 760 nm to reset the qubit state, we believe the electron-shelving based detection routine presented here will improve the practicality and scalability of current $^{171}\mathrm{Yb}^{+}$ quantum devices.

CHAPTER 4

Modelling quantum verification protocols in the presence of temporally correlated noise

---

"I want to stay as close to the edge as I can without going over. Out on the edge you see all kinds of things you can't see from the center."

- Kurt Vonnegut, *Player Piano*

*The work in this chapter models the behaviour of common quantum characterisation, validation and verification protocols to predict their response to noise with different correlation lengths. It forms the theoretical foundation upon which the following two experimental chapters are based. The work is largely based on the Supplementary Material of "Experimental quantum verification in the presence of temporally correlated noise" published in npj Quantum Information Volume 4, Article number: 7 (2018) [**3**], and the Appendix of "Dynamically corrected gates suppress spatio-temporal error correlations as measured by randomised benchmarking" published in Phys. Rev. Research 2, 013156 (2020) [**4**].*

Quantum characterisation, validation and verification (QCVV) techniques are widely used in the quantum information community in order to evaluate the performance of experimental hardware. A variety of techniques have emerged including randomised benchmarking (RB) [**154, 155**], purity benchmarking [**156**], process tomography [**157–160**], adaptive methods [**161**], and gate set tomography (GST) [**162, 163**]. Each protocol has relative strengths and weaknesses; for instance, RB has low experimental overhead but only provides average information about gate performance, while process tomography provides more information at the cost of unfavourable scaling in measurement overhead [**164**]. Despite their differences, these protocols share the common theme that they were originally developed and mathematically formalised assuming that error processes are statistically independent and do not exhibit strong correlations in time [**154, 155, 163**]. In the following chapters, I will present work examining the behaviour of common QCVV protocols in the presence of correlated noise processes. We will show how the protocol outputs are affected by correlations, and outline simple modifications to extract information about the underlying error correlations.

In this chapter, I begin by describing the two techniques under examination – randomised benchmarking and gate set tomography. I will outline a theoretical model originally presented by Ball et al. [**165**] that can be used to predict the results of randomised benchmarking in the presence of correlated errors. Following this, I will detail the modifications that had to be made in order for this theory to be applicable to realistic experimental conditions.

4.1 Introduction to quantum characterisation, validation and verification techniques

I begin by introducing two QCVV techniques, randomised benchmarking and gate set tomography, with a particular focus on the former. In this section I will outline the mathematical formalism on which randomised benchmarking is based, and explain the physical implementation and analysis of both routines.

4.1.1 Theoretical background of randomised benchmarking (RB)

Randomised benchmarking or RB is one of the most commonly used QCVV protocols, largely due to its low overhead and relatively rapid run-times. In addition, it has a low sensitivity to state preparation and measurement errors (SPAM). The aim of randomised benchmarking is to quantify the gate fidelity for a given qubit and control system in its laboratory conditions. It was first proposed by Emerson et al. [**154**], wherein they theoretically demonstrated that the average gate error could be estimated using a simple "motion-reversal" sequence – a unitary $\hat{U}$ followed by its inverse $\hat{U}^{\dagger}$. Unlike more complex QCVV protocols such as gate set tomography (GST), it cannot extract information about individual gate errors, instead returning an *average* error per gate (EPG).

The error affecting the net sequence can be represented as a completely positive, trace-preserving (CPTP) error channel $\hat{\Lambda}$. Consider a unitary operator $\hat{U}$ that acts on an initial qubit density operator ρ via conjugation. Then, the effect of an error channel on the gate is to modify the ideal evolution as follows,

$$\hat{\Lambda}(\hat{U}(\rho)) = \hat{\Lambda}(\hat{U}\rho\hat{U}^\dagger) = \sum_k \hat{A}_k \hat{U}\rho\hat{U}^\dagger \hat{A}_k^\dagger, \tag{4.1}$$

where the error channel has been decomposed into its constituent Kraus operators $\hat{A}_k$. Here, I have used the notation $\hat{\Lambda}(\cdot)$ and $\hat{U}(\cdot)$ to represent the generalised "action" of an operator.

The original proposal obtained the average gate error by generating random unitary operators with respect to the Haar measure. This measure is left-translation-invariant and creates a uniform distribution over the unitary matrices. For a d-dimensional Hilbert space, I represent the group of unitary operators in $\mathbb{C}^d$ as $\mathcal{U}(d)$. The individual gate fidelities F_g are averaged over all operators in this group, $\hat{U} \in \mathcal{U}(d)$, to obtain an estimate of the mean fidelity $\mathbb{E}_{\hat{U}}(F_g)$. Using the Haar measure dU, the average gate fidelity for gates affected by the error channel $\hat{\Lambda}$ is given by [**154**]

$$\begin{aligned}\mathbb{E}_{\hat{U}}(F_g) &= \int_{\mathcal{U}(d)} dU \mathrm{Tr}\left[\sqrt{\sqrt{\hat{U}\rho\hat{U}^\dagger}\,\hat{\Lambda}(\hat{U}\rho\hat{U}^\dagger)\sqrt{\hat{U}\rho\hat{U}^\dagger}}\right]^2 \\ &= \int_{\mathcal{U}(d)} dU \mathrm{Tr}\left[\hat{U}\rho\hat{U}^\dagger\hat{\Lambda}(\hat{U}\rho\hat{U}^\dagger)\right].\end{aligned} \tag{4.2}$$

Here, the fidelity metric has been simplified using Eqn. (1.23) by assuming that ρ, and hence $\hat{U}\rho\hat{U}^\dagger$, are pure states. Note that I have *not* assumed that the error-affected state, $\hat{\Lambda}(\hat{U}\rho\hat{U}^\dagger)$, is pure. It can be shown that Eqn. (4.2) reduces to

$$\mathbb{E}_{\hat{U}}(F_g) = \frac{\sum_k \left|\mathrm{Tr}[\hat{A}_k]\right|^2 + d}{d^2 + d}. \tag{4.3}$$

Hence, the average fidelity can be written as a polynomial of degree two in the matrix elements of the error channel $\hat{\Lambda}$ and their complex conjugates, i.e. degree (2, 2).

Measuring the average gate fidelity using Haar-random unitaries is experimentally inefficient due to the number of gates required to produce the operators. Later work showed that one could simplify the experimental implementation, and still achieve the same effective result, by using a subset of the unitary group called the "Clifford group", a type of unitary 2-design [**166**]. Operators from the Clifford group are appealing as they can be straightforwardly implemented in quantum devices [**167**,**168**]. In general, a unitary t-design is a subset of the unitary operators with K elements, $\{\hat{U}_k\} \in \mathcal{U}(d)$, that can simulate the results of sampling from the Haar-random unitaries for the purpose of estimating a polynomial of degree at most t in both the matrix elements of $\hat{U}_k$ and their complex conjugates. That is, for a polynomial of degree (t,t), $P_{(t,t)}(\hat{U})$, one finds [**166**]

$$\frac{1}{K}\sum_{k=1}^{K} P_{(t,t)}(\hat{U}_k) = \int_{\mathcal{U}(D)} dU P_{(t,t)}(\hat{U}) \tag{4.4}$$

where dU is the Haar measure. Equation (4.3) shows that $\mathbb{E}_{\hat{U}}(F_g)$ is a polynomial of degree (2, 2). As the Clifford group is a unitary 2-design, it is an appropriate substitute for Haar-random unitaries to estimate the average gate fidelity and hence for the implementation of randomised benchmarking.

4.1.2 Clifford group representation for a single qubit

The Clifford group can be generated using only the Hadamard, CNOT and phase gates, or simply the Hadamard and phase gates for a single qubit [**167, 168**]. Furthermore, the inverse gate for a sequence comprising purely Clifford operations (required for motion-reversal) can be efficiently calculated on a classical computer. If we define the "Pauli group" using the Pauli and identity operators as

$$\mathbb{P} = \{\pm\hat{\mathbb{I}}, \pm\hat{\sigma}_x, \pm\hat{\sigma}_y, \pm\hat{\sigma}_z\}, \tag{4.5}$$

then a unitary operation $\hat{C}_j$ is an element of the Clifford group if and only if

$$\hat{C}_j \mathbb{P} \hat{C}_j^\dagger = \mathbb{P}. \tag{4.6}$$

That is, the Clifford group is the normaliser of the Pauli group, such that for every Pauli operation $P \in \mathbb{P}$ and every Clifford gate $\hat{C}_j$, there exists $P' \in \mathbb{P}$ such that $\hat{C}_j P \hat{C}_j^\dagger = P'$. For a single qubit, if we consider a Cartesian basis associated with the Pauli operators that we denote "Pauli space", then the set of all Clifford gates can be thought of as rotations of the Bloch sphere that permute the orientation of $\pm\hat{\sigma}_x, \pm\hat{\sigma}_y, \pm\hat{\sigma}_z$ in this space. To obtain a clearer physical picture of this phenomenon, consider associating $\hat{\sigma}_x$ to any of the six Cartesian axes $\{\pm\hat{\boldsymbol{x}}, \pm\hat{\boldsymbol{y}}, \pm\hat{\boldsymbol{z}}\}$. With this axis fixed, we may rotate the axes about $\hat{\sigma}_x$ into four possible orientations while preserving xyz right-handedness. This is the action of the Clifford group: the group of rotational symmetries of the cube.

We construct our representation as follows. Let $\hat{R}_i(\theta)$ represent one of nine elementary unitaries generating a *clockwise* rotation (looking down the axis of rotation toward the origin) through angle $\theta \in \{\pi, \pm\pi/2\}$ about axis $i \in \{x, y, z\}$. Up to a global phase, the three π rotations correspond to

$$\hat{R}_i(\pi) = e^{-i\hat{\sigma}_i\pi/2} \equiv \hat{\sigma}_i, \qquad i \in \{x, y, z\}. \tag{4.7}$$

#	Gate Name	Action on $(\hat\sigma_x, \hat\sigma_y, \hat\sigma_z)$	Minimal Mapping	Notes	Gate Time (τ_π)
$\hat C_1$	$\hat{\mathbb{I}}$	$(\hat\sigma_x, \hat\sigma_y, \hat\sigma_z)$	$\hat R_i^- \hat R_i^+,\ i \in \{1,2,3\}$	Identity	1
$\hat C_2$	$\hat\sigma_x$	$(\hat\sigma_x, -\hat\sigma_y, -\hat\sigma_z)$	$\hat\sigma_x$	π rotation	1
$\hat C_3$	$\hat\sigma_y$	$(-\hat\sigma_x, \hat\sigma_y, -\hat\sigma_z)$	$\hat\sigma_y$		1
$\hat C_4$	$\hat\sigma_z$	$(-\hat\sigma_x, -\hat\sigma_y, \hat\sigma_z)$	$\hat\sigma_z$		0
$\hat C_5$	$\hat R_x^+$	$(\hat\sigma_x, -\hat\sigma_z, \hat\sigma_y)$	$\hat R_x^+$	$+\pi/2$ rotations	$1/2$
$\hat C_6$	$\hat R_y^+$	$(\hat\sigma_z, \hat\sigma_y, -\hat\sigma_x)$	$\hat R_y^+$		$1/2$
$\hat C_7$	$\hat R_z^+$	$(-\hat\sigma_y, \hat\sigma_x, \hat\sigma_z)$	$\hat R_z^+$		0
$\hat C_8$	$\hat R_x^-$	$(\hat\sigma_x, \hat\sigma_z, -\hat\sigma_y)$	$\hat R_x^-$	$-\pi/2$ rotations	$1/2$
$\hat C_9$	$\hat R_y^-$	$(-\hat\sigma_z, \hat\sigma_y, \hat\sigma_x)$	$\hat R_y^-$		$1/2$
$\hat C_{10}$	$\hat R_z^-$	$(\hat\sigma_y, -\hat\sigma_x, \hat\sigma_z)$	$\hat R_z^-$		0
$\hat C_{11}$		$(-\hat\sigma_x, -\hat\sigma_z, -\hat\sigma_y)$	$\hat R_x^+ \hat\sigma_z$		$1/2$
$\hat C_{12}$		$(-\hat\sigma_x, \hat\sigma_z, \hat\sigma_y)$	$\hat R_x^- \hat\sigma_z$		$1/2$
$\hat C_{13}$		$(-\hat\sigma_y, -\hat\sigma_x, -\hat\sigma_z)$	$\hat\sigma_x \hat R_z^+$		1
$\hat C_{14}$		$(\hat\sigma_y, \hat\sigma_x, -\hat\sigma_z)$	$\hat\sigma_x \hat R_z^-$		1
$\hat C_{15}$		$(-\hat\sigma_y, -\hat\sigma_z, \hat\sigma_x)$	$\hat R_x^+ \hat R_z^+$		$1/2$
$\hat C_{16}$		$(-\hat\sigma_y, \hat\sigma_z, -\hat\sigma_x)$	$\hat R_x^- \hat R_z^+$		$1/2$
$\hat C_{17}$		$(-\hat\sigma_z, -\hat\sigma_x, \hat\sigma_y)$	$\hat R_z^- \hat R_x^+$		$1/2$
$\hat C_{18}$		$(-\hat\sigma_z, -\hat\sigma_y, -\hat\sigma_x)$	$\hat R_y^- \hat\sigma_z$		$1/2$
$\hat C_{19}$		$(-\hat\sigma_z, \hat\sigma_x, -\hat\sigma_y)$	$\hat R_y^- \hat R_z^+$		$1/2$
$\hat C_{20}$		$(\hat\sigma_z, -\hat\sigma_x, -\hat\sigma_y)$	$\hat R_y^+ \hat R_z^-$		$1/2$
$\hat C_{21}$	$\hat H$	$(\hat\sigma_z, -\hat\sigma_y, \hat\sigma_x)$	$\hat R_y^+ \hat\sigma_z$	Hadamard	$1/2$
$\hat C_{22}$		$(\hat\sigma_y, -\hat\sigma_z, -\hat\sigma_x)$	$\hat R_x^+ \hat R_z^-$		$1/2$
$\hat C_{23}$		$(\hat\sigma_z, \hat\sigma_x, \hat\sigma_y)$	$\hat R_y^+ \hat R_z^+$		$1/2$
$\hat C_{24}$		$(\hat\sigma_y, \hat\sigma_z, \hat\sigma_x)$	$\hat R_x^- \hat R_z^-$		$1/2$

TABLE 4.1. Representation of the Clifford group for a single qubit from products of elementary rotations. Relevant transformations of the coordinate system $\hat\sigma_x, \hat\sigma_y, \hat\sigma_z$ under the action of each Clifford shown in column 3. Minimal product of elementary operations needed to generate each Clifford shown in column 4, in the order of physical gate-application from right to left (as would be multiplied with a qubit state). Column 5 indicates where these geometric rotations map to logical operations of interest for quantum information. Column 6 indicates the physical time of the gate implementation relative to a driven π rotation incorporating instantaneous, and consequently dephasing-free, $\hat\sigma_z$ operations.

For the remaining six $\pi/2$ rotations we introduce the shorthand

$$\hat R_i^{\pm} := \hat R_i\left(\pm\frac{\pi}{2}\right) = e^{\mp i\hat\sigma_i\pi/4}, \qquad i \in \{x, y, z\}. \tag{4.8}$$

For example, the operators $\hat{R}_i^{\pm}$ permute the Pauli operators/axes as

$$\hat{R}_x^{+}: \quad (\hat{\sigma}_x, \hat{\sigma}_y, \hat{\sigma}_z) \rightarrow (\hat{\sigma}_x, -\hat{\sigma}_z, \hat{\sigma}_y) \tag{4.9}$$

$$\hat{R}_y^{+}: \quad (\hat{\sigma}_x, \hat{\sigma}_y, \hat{\sigma}_z) \rightarrow (\hat{\sigma}_z, \hat{\sigma}_y, -\hat{\sigma}_x) \tag{4.10}$$

$$\hat{R}_z^{+}: \quad (\hat{\sigma}_x, \hat{\sigma}_y, \hat{\sigma}_z) \rightarrow (-\hat{\sigma}_y, \hat{\sigma}_x, \hat{\sigma}_z). \tag{4.11}$$

Products of these nine elementary operations generate a representation of the 24 elements of the single-qubit Clifford group as tabulated in Table 4.1. The final column relates to the physical implementation of the gates in our experiment, showing the relative length compared to a driven π rotation.

4.1.3 Implementing single-qubit randomised benchmarking

To implement single-qubit randomised benchmarking, sequences are constructed by concatenating unitary operations selected at random from the Clifford group. A distinct randomisation containing J gates is represented by the index vector $\boldsymbol{\eta} = [\eta_1, \eta_2, \ldots, \eta_J]$ containing references to the 24 Clifford gates, such that $\eta_j \in \{1, \ldots, 24\}$ and $\hat{C}_{\eta_j}$ is a Clifford operation. For a sequence of J gates, the first $J-1$ gates are sampled at random. The final operation is pre-calculated to invert the preceding rotations,

$$\hat{C}_{\eta_J} = \left(\prod_{j=1}^{J-1} \hat{C}_{\eta_j} \right)^{-1}, \tag{4.12}$$

such that the total sequence implements a net identity $\prod_{j=1}^{J} \hat{C}_{\eta_j} = \hat{\mathbb{I}}$, resulting in 24^{J-1} distinct sequence possibilities. **Note, for the products of operators, each successive term is right multiplied to the previous operator, as the operations act with right multiplication to the qubit.** Hence, the big Pi product notation in Eqn. (4.12) multiplies terms from the opposite side compared to its standard usage. The pre-calculated sequences are applied to a qubit prepared in $|0\rangle$ and the final qubit state after the evolution is measured. Any deviation from the ideal final state, $\hat{\mathbb{I}}\,|0\rangle = |0\rangle$, is an error. By constructing sequences with increasing numbers of gates and measuring how the resulting error scales, we can obtain a measure of the average gate error.

The procedure for randomised benchmarking is outlined below.

1. For a particular choice of sequence length J, randomly select $J-1$ gates from the Clifford group and store the indices in the vector $\boldsymbol{\eta}$.

2. Calculate the final Clifford gate to be the inverse operator of the preceding $(J-1)$-length sequence, such that $C_{\eta_J}\cdots C_{\eta_1}=\hat{\mathbb{I}}$.
3. Using the minimal physical mappings for each Clifford gate shown in Table 4.1, apply the total J-length sequence to a qubit prepared in the state $|0\rangle$.
4. Measure the final qubit state using a projective measurement onto the z-axis, $P(|1\rangle)$.
5. Repeat steps (3)-(4) for r repetitions to obtain a estimate of the final state projection onto the z-axis. In the presence of noise or decoherence, the sequence will not necessarily implement a net identity operation, and consequently the qubit population will not precisely return to $|0\rangle$. Any deviation will be averaged over different instances of the noise across the repetitions, producing the sequence "survival probability", $\mathcal{P}:=1-\langle P(|1\rangle)\rangle_r$.
6. Repeat steps (1)-(5) using k different randomly composed Clifford sequences of length J to obtain a mean survival probability averaged over sequences for the particular sequence length J, denoted $\overline{\mathcal{P}}(J)$.
7. Repeat steps (1)-(6) for different choices of sequence length J to obtain an exponentially decaying mean qubit survival probability with sequence length. The exponential decay constant gives an estimate of the average error per gate (EPG), p_{RB}, by fitting the expression,

$$\overline{\mathcal{P}}(J)=0.5+(0.5-\kappa)e^{-p_{\mathrm{RB}}J} \tag{4.13}$$

   where κ is the state preparation and measurement (SPAM) error. As the number of gates is increased, the exponential survival probability decay in Eqn. (4.13) tends towards 0.5, as would be expected for a completely decohered or mixed qubit state.

The sequences generated in the protocol above can also be shuffled, such that sequences with different numbers of gates (different J) are interleaved with one another. This reduces the effect of systematic drifts that may occur over the course of the experiment, which would otherwise bias sequences implemented later in the protocol.

A key aim of this work is to understand the behaviour of QCVV protocols in the presence of noise with particular characteristics, such as correlation length. Consequently, in many instances we engineer the noise to be a known quantity to test the system response. To implement noise engineering, another step is added to the randomised benchmarking protocol after step (5), i.e. before moving to a different sequence. At this point, the same sequence is repeated for n different realisations of the engineered noise process, obtaining a noise-averaged estimate of the survival probability, $\langle\mathcal{P}\rangle_n$.

4.1.4 Implementing single-qubit gate set tomography

While randomised benchmarking is efficiently implemented and analysed, it only returns an average gate error. To quantify gate-specific errors, a more complex QCVV protocol must be utilised. In this work, we employ gate set tomography (GST) for this purpose to examine its response to correlated error processes. Here, I outline how GST is implemented; for more comprehensive details see Refs. [**163**,**169**].

In experimental GST, as defined by the pyGSTi python-based package [**169**], operations are selected deterministically according to a tabulated routine to create specifically crafted sequences that are designed to maximise overall sensitivity to all detectable error types. These sequences are constructed by concatenating so-called "germs", short sequences implementing predefined unitary rotations, which, in our case, are constructed from a subset of Clifford gates. The germs are generated from a specific gate set, several of which are suggested in the pyGSTi tutorials. The recommended "standard" GST gate set is $\{G_I, G_x, G_y\}$, corresponding to a $\pi/2$-length idle period, a $\pi/2$ rotation about the x-axis, and a $\pi/2$ rotation about the y-axis respectively. This gate set produces the following 11 germs,

$$\begin{aligned} G \in \big\{&(G_x),\, (G_y),\, (G_I),\, (G_xG_y),\, (G_xG_yG_I),\, (G_xG_IG_y),\, (G_xG_IG_I),\\ &(G_yG_IG_I),\, (G_xG_xG_IG_y),\, (G_xG_yG_yG_I),\, (G_xG_xG_yG_xG_yG_y)\big\} \end{aligned} \tag{4.14}$$

which we use in our experiments, identical to those used by Blume-Kohout et al. [**163**]. In our numerical analyses, we extend the standard gate set from $\{G_I, G_x, G_y\} \rightarrow \{G_I, G_x, G_y, -G_x, -G_y\}$, while also expanding the generated germ set from 11 to 39 elements to maintain amplificational completeness. Each of these germs is concatenated with itself up to a maximum length that successively increases as $L = \{1, 2, 4, 8, 16, 32, \ldots\}$. More concretely, this implies that the germ is repeated as many times as possible until the number of constituent gates would exceed L, or alternatively, if $|G|$ is the number of constituent gates in the germ G, then it is repeated $l = \left\lfloor \frac{L}{|G|} \right\rfloor$ times, using the mathematical "floor" notation. For example, the germ $(G_yG_IG_I)$ has three constituent gates and cannot be implemented at all for $L = 1, 2$. It is repeated once for $L = 4$, twice for $L = 8$, and so on.

Each concatenated germ sequence is appended with an initial and final unitary termed the "fiducial" operations F_α and F_β respectively, which set the reference frame for state-preparation and measurement. The six fiducial operations are taken from the set

$$F_\alpha, F_\beta \in \{\emptyset,\, \hat{G}_x,\, \hat{G}_y,\, \hat{G}_x\hat{G}_x,\, \hat{G}_x\hat{G}_x\hat{G}_x,\, \hat{G}_y\hat{G}_y\hat{G}_y\}, \tag{4.15}$$

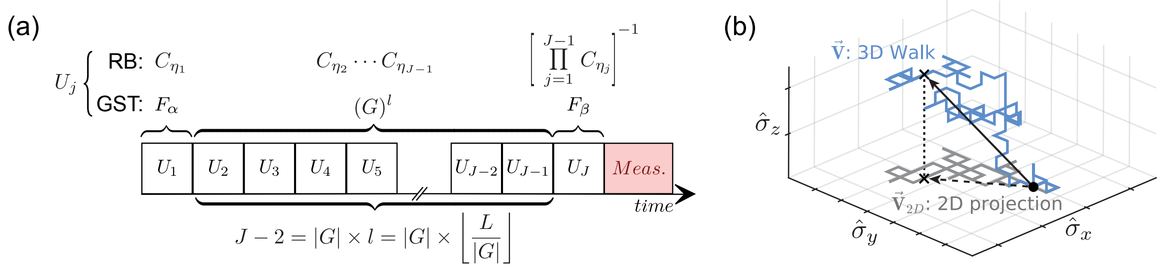

FIGURE 4.1. QCVV sequence construction and mapping to accumulated error. (a) Overview of unitary sequence construction for RB and GST using Clifford gates, $\hat{C}_{\eta_j}$ or fiducial operations, $F_{\alpha,\beta}$ and repeated germs $(G)^l$ respectively. (b) Sequence-dependent "random walk" calculated for an arbitrary QCVV sequence (here according to the RB prescription) with $J = 100$ in Pauli space. Black dot indicates origin and black cross indicates sequence terminus. Blue line represents the 3D walk, which can be used to calculate the trace infidelity, while grey represents the 2D projection, which is measurable using a standard projective measurement. The black solid and dashed arrows indicates the net walk vectors for $\boldsymbol{V}$ and $\boldsymbol{V}_{2D}$ respectively, given unit-length step size.

where $\emptyset$ stands for no gate operation, and G_x and G_y stand for $\pi/2$ rotations around the x and y-axes of the Bloch sphere. They are chosen to form an informationally complete set of input states and measurement bases akin to quantum process tomography. Each germ sequence is measured in all 36 combinations of the fiducials F_α and F_β.

The construction of both an RB sequence and a GST sequence is shown in Fig. 4.1(a). The j^{th} unitary in the general sequence is denoted by $\hat{U}_j$, where $j \in \{1, \ldots, J\}$. For RB, the first $J-1$ gates are randomly selected Clifford gates indexed by the sequence vector $\boldsymbol{\eta}$, $\hat{C}_{\eta_j}$, and the final gate is the inverse of the preceding operations. For GST, the first and last gates are one of the six fiducials, $F_{\alpha,\beta}$, and the central gates comprise one of the 11 germ sequences specified in Eqn. (4.14) repeated l times to a produce a total of $|G| \times l = |G| \times \left\lfloor \frac{L}{|G|} \right\rfloor = (J-2)$ constituent Clifford gates.

4.2 Mapping Clifford sequences to random walks in Pauli space

The key analytic tool for our study is a formalism mapping an applied noise model to an output error for a given Clifford sequence. This section sets out the theory used to model the randomised benchmarking data presented in the following chapters. The theory is adapted from the model originally presented Ref. [**165**], and involves a number of modifications incorporating the previously underappreciated role of the experimental readout process and the experimental implementation itself (i.e. the structure of the error model). We begin by reviewing the original model presented by Ball et al. in Ref. [**165**].

In single-qubit RB, random sequences of Clifford operators are implemented. Multiple such randomisations are performed, and from the ensemble statistics of the resulting fidelity measurements experimentalists may extract the average EPG arising from the system's interaction with the noise environment. For an RB sequence of length J, including the final inverting Clifford operation, we write the net operation as the operator product

$$\hat{\mathcal{S}}_{\boldsymbol{\eta}} := \prod_{j=1}^{J} \hat{C}_{\eta_j} = \hat{\mathbb{I}} \tag{4.16}$$

where each new term uses right multiplication to the preceding term and $\boldsymbol{\eta}$ contains the Clifford gate references for the particular sequence.

When the system interacts with the underlying noise environment, the target Clifford operations $\hat{C}_{\eta_j}$ are implemented imperfectly as $\widetilde{C}_{\eta_j,\delta_j}$, resulting in the *noise-affected* product

$$\widetilde{\mathcal{S}}_{\boldsymbol{\eta},\boldsymbol{\delta}} := \prod_{j=1}^{J} \widetilde{C}_{\eta_j,\delta_j} \neq \hat{\mathbb{I}} \tag{4.17}$$

where $\boldsymbol{\delta}$ is a J-length vector denoting the random noise realisation, with each element representing the strength of the noise during the gate, e.g. δ_j is the noise affecting the j^{th} gate. The net operator product is therefore no longer necessarily equal to the identity gate, reducing the operational fidelity compared to implementing the ideal sequence $\hat{\mathcal{S}}_{\boldsymbol{\eta}}$.

The noise-averaged fidelity for a particular sequence $\boldsymbol{\eta}$ is therefore written as $\langle \mathcal{F}(\boldsymbol{\eta},\boldsymbol{\delta})\rangle_n$ where $\langle\cdot\rangle_n$ denotes the expectation value of the fidelity $\mathcal{F}(\boldsymbol{\eta},\boldsymbol{\delta})$ averaged over n realisations of the noise random variable, $\boldsymbol{\delta}$. The original analytic model employed the "trace fidelity" metric, as outlined in Section 1.2.3, defined as

$$\mathcal{F}_{\text{trace}}\left(\boldsymbol{\eta},\boldsymbol{\delta}\right) := \left|\frac{1}{2}\text{Tr}\left(\hat{\mathcal{S}}_{\boldsymbol{\eta}}^{\dagger}\widetilde{\mathcal{S}}_{\boldsymbol{\eta},\boldsymbol{\delta}}\right)\right|^2 = \frac{1}{4}\left|\text{Tr}\left(\widetilde{\mathcal{S}}_{\boldsymbol{\eta},\boldsymbol{\delta}}\right)\right|^2 \tag{4.18}$$

to quantify the fidelity of implementing the RB sequence $\boldsymbol{\eta}$ in the presence of the noise realisation $\boldsymbol{\delta}$. This operator-based trace fidelity metric captures the overlap between ideal, $\hat{\mathcal{S}}_{\boldsymbol{\eta}} = \hat{\mathbb{I}}$, and noise-affected sequences, $\widetilde{\mathcal{S}}_{\boldsymbol{\eta},\boldsymbol{\delta}}$, via the Hilbert-Schmidt inner product. The expression for the noise-averaged fidelity therefore takes the form

$$\langle \mathcal{F}_{\text{trace}}(\boldsymbol{\eta},\boldsymbol{\delta})\rangle_n = \frac{1}{4}\left\langle\left|\text{Tr}\left(\widetilde{\mathcal{S}}_{\boldsymbol{\eta},\boldsymbol{\delta}}\right)\right|^2\right\rangle_n . \tag{4.19}$$

To model the error, we initially consider a $\hat{\sigma}_z$ phase error of strength δ_j following each Clifford gate, as studied in Ref. [**165**]. The effect of the "interleaved dephasing" error can be expressed in terms of an imperfect Clifford gate

$$\widetilde{C}_{\eta_j,\delta_j} = e^{i\delta_j\hat{\sigma}_z}\hat{C}_{\eta_j}. \tag{4.20}$$

In this case the total noisy sequence $\widetilde{\mathcal{S}}_{\boldsymbol{\eta},\boldsymbol{\delta}}$ can be expression using a Taylor expansion in δ_j, yielding

$$\widetilde{\mathcal{S}}_{\boldsymbol{\eta},\boldsymbol{\delta}} = \prod_{j=1}^{J}\left(\hat{\mathbb{I}} + i\delta_j\hat{\sigma}_z - \frac{\delta_j^2}{2}\hat{\sigma}_z^2 + \dots\right)\hat{C}_{\eta_j}. \tag{4.21}$$

If we assume the average EPG is small, then the expansion can be truncated after second order. For noise variables sampled from a zero-mean normal distribution with root-mean-square (rms) σ, $\delta_j \sim \mathcal{N}(0,\sigma^2)$, the assumption of small EPGs translates to the condition that $J\sigma^2 \ll 1$. In this case we approximate the total noisy sequence as

$$\widetilde{\mathcal{S}}_{\boldsymbol{\eta},\boldsymbol{\delta}} \approx \prod_{j=1}^{J}\left(\hat{\mathbb{I}} + i\delta_j\hat{\sigma}_z - \frac{\delta_j^2}{2}\hat{\sigma}_z^2\right)\hat{C}_{\eta_j} \tag{4.22}$$

$$\approx \xi^{(0)} + \xi_1^{(1)} + \xi_{1,1}^{(2)} + \xi_2^{(2)}. \tag{4.23}$$

Here, the product cross-terms have been grouped into terms labelled $\xi_b^{(a)}$, which contain terms of order a in δ, with the subscript b referring to the order in δ of the individual error terms that have been combined. For example, a subscript $b = 1,1$ has two distinct noise terms $\delta_j, \delta_{k\neq j}$ contributed from different error operator steps that have been combined, whereas $b = 2$ refers to a second-order term from a single step, δ_j^2. Explicitly, using the shorthand $\hat{C}_{k,j} := \hat{C}_{\eta_k}\cdots\hat{C}_{\eta_j}$,

$$\xi^{(0)} = \hat{C}_{\eta_J}\cdots\hat{C}_{\eta_1} =: \hat{C}_{J,1} = \hat{\mathbb{I}}, \tag{4.24}$$

$$\begin{aligned}\xi_1^{(1)} &= \sum_{j=1}^{J}(i\delta_j)\hat{C}_{J,j+1}\hat{\sigma}_z\hat{C}_{j,1}\\ &= \sum_{j=1}^{J}(i\delta_j)\hat{C}_{j,1}^{\dagger}\hat{\sigma}_z\hat{C}_{j,1},\end{aligned} \tag{4.25}$$

$$\begin{aligned}\xi_{1,1}^{(2)} &= \sum_{j<k}(i\delta_j)(i\delta_k)\hat{C}_{J,k+1}\hat{\sigma}_z\hat{C}_{k,j+1}\hat{\sigma}_z\hat{C}_{j,1}\\ &= -\sum_{j<k}\delta_j\delta_k\hat{C}_{J,k+1}\hat{\sigma}_z\left(\hat{C}_{J,k+1}^{\dagger}\hat{C}_{J,k+1}\right)\hat{C}_{k,j+1}\hat{\sigma}_z\hat{C}_{j,1}\\ &= -\sum_{j<k}\delta_j\delta_k\hat{C}_{k,1}^{\dagger}\hat{\sigma}_z\hat{C}_{k,1}\hat{C}_{j,1}^{\dagger}\hat{\sigma}_z\hat{C}_{j,1},\end{aligned} \tag{4.26}$$

$$\begin{aligned}\xi_2^{(2)} &= -\frac{1}{2}\sum_{j=1}^{J}\delta_j^2\hat{C}_{J,j+1}\hat{\sigma}_z^2\hat{C}_{j,1}\\ &= -\frac{1}{2}\sum_{j=1}^{J}\delta_j^2\hat{\mathbb{I}},\end{aligned}\tag{4.27}$$

using $\hat{C}_{J,k+1}\hat{C}_{k,j+1} = \hat{C}_{J,j+1}$ and $\hat{\sigma}_z^2 = \hat{\mathbb{I}}$. Additionally, we have used the fact that the net sequence in the absence of error is the identity gate, hence the sub-sequence $\hat{C}_{J,j+1}$ must be the inverse of the complementary sub-sequence $\hat{C}_{j,1}$, such that $\hat{C}_{J,j+1} = \hat{C}_{j,1}^{\dagger}$.

Using group theoretic properties of the Clifford group, which state that the conjugation of a Pauli operator with a Clifford operator maps to another Pauli operator, we may express

$$\xi^{(0)} = \hat{\mathbb{I}},\tag{4.28}$$

$$\xi_1^{(1)} = \sum_{j=1}^{J}(i\delta_j)\hat{\mathbf{P}}_j,\tag{4.29}$$

$$\xi_{1,1}^{(2)} = -\sum_{j<k}\delta_j\delta_k\hat{\mathbf{P}}_k\hat{\mathbf{P}}_j,\tag{4.30}$$

$$\xi_2^{(2)} = -\frac{1}{2}\sum_{j=1}^{J}\delta_j^2\hat{\mathbb{I}},\tag{4.31}$$

in terms of random signed Pauli operators defined as $\hat{\mathbf{P}}_j := \hat{C}_{j,1}^{\dagger}\hat{\sigma}_z\hat{C}_{j,1} \in \pm\{\hat{\sigma}_x, \hat{\sigma}_y, \hat{\sigma}_z\}$. Using the vector of Pauli operators $\hat{\boldsymbol{\sigma}} = [\hat{\sigma}_x, \hat{\sigma}_y, \hat{\sigma}_z]$, $\hat{\mathbf{P}}_j$ can be written generally as

$$\hat{\mathbf{P}}_j = x_j\hat{\sigma}_x + y_j\hat{\sigma}_y + z_j\hat{\sigma}_z =: \boldsymbol{r}_j \cdot \hat{\boldsymbol{\sigma}}.\tag{4.32}$$

The coefficients $x_j, y_j, z_j \in \{0, \pm 1\}$ are subject to the constraint $|x_j|^2 + |y_j|^2 + |z_j|^2 = 1$, such that there is only one non-zero coefficient, and we define

$$\boldsymbol{r}_j := [x_j,\, y_j,\, z_j], \quad \|\boldsymbol{r}_j\| = 1.\tag{4.33}$$

That is, $\boldsymbol{r}_j \in \pm\{\boldsymbol{x}, \boldsymbol{y}, \boldsymbol{z}\}$ are unit vectors pointing at random along the principal Cartesian axes, mapping the “direction” of the operators $\hat{\mathbf{P}}_j$ in the operator space spanned by the Pauli operators.

Returning to the expression for the noise-affected sequence, and noting that for the trace fidelity metric Eqn. (4.19) we need keep only terms with non-vanishing trace, using Tr$[\hat{\sigma}_{xyz}] = 0$ and Tr$[\hat{\mathbb{I}}] = 2$ we can write the following expressions.

$$\widetilde{\mathcal{S}}_{\boldsymbol{\eta},\boldsymbol{\delta}} \approx \left(1 - \frac{1}{2}\sum_{j=1}^{J} \delta_j^2\right)\hat{\mathbb{I}} + \sum_{j=1}^{J}(i\delta_j)\hat{\mathbf{P}}_j - \sum_{j<k} \delta_j\delta_k \hat{\mathbf{P}}_j\hat{\mathbf{P}}_k \tag{4.34}$$

$$\frac{1}{2}\mathrm{Tr}[\widetilde{\mathcal{S}}_{\boldsymbol{\eta},\boldsymbol{\delta}}] \approx 1 - \frac{1}{2}\sum_{j=1}^{J}\delta_j^2 - \frac{1}{2}\sum_{j<k}\delta_j\delta_k \mathrm{Tr}[\hat{\mathbf{P}}_j\hat{\mathbf{P}}_k] \tag{4.35}$$

Moving to the vector notation defined in Eqn. (4.32), we can rewrite the final term, again utilising the fact that the Pauli operators are trace zero,

$$\begin{aligned}\frac{1}{2}\mathrm{Tr}[\hat{\mathbf{P}}_j\hat{\mathbf{P}}_k] &= \frac{1}{2}\mathrm{Tr}[(\boldsymbol{r}_j \cdot \hat{\boldsymbol{\sigma}})(\boldsymbol{r}_k \cdot \hat{\boldsymbol{\sigma}})] \\ &= \frac{1}{2}\mathrm{Tr}\left[(\boldsymbol{r}_j \cdot \boldsymbol{r}_k)\hat{\mathbb{I}} + i(\boldsymbol{r}_j \times \boldsymbol{r}_k)\cdot\hat{\boldsymbol{\sigma}}\right] \\ &= \boldsymbol{r}_j \cdot \boldsymbol{r}_k,\end{aligned} \tag{4.36}$$

where all other terms in the second last line are trace zero. Then, we can write

$$\begin{aligned}\frac{1}{2}\mathrm{Tr}[\widetilde{\mathcal{S}}_{\boldsymbol{\eta},\boldsymbol{\delta}}] &\approx 1 - \frac{1}{2}\sum_{j=1}^{J}\delta_j^2 - \sum_{j<k}\delta_j\delta_k\boldsymbol{r}_j\cdot\boldsymbol{r}_k \\ &= 1 - \frac{1}{2}\sum_{j=1}^{J}\delta_j^2 - \frac{1}{2}\sum_{j,k=1}^{J}\delta_j\delta_k\boldsymbol{r}_j\cdot\boldsymbol{r}_k + \frac{1}{2}\sum_{j=1}^{J}\delta_j^2\|\boldsymbol{r}_j\|^2 \\ &= 1 - \frac{1}{2}\sum_{j,k=1}^{J}\delta_j\delta_k\boldsymbol{r}_j\cdot\boldsymbol{r}_k\end{aligned} \tag{4.37}$$

by changing the restricted sum to be non-restrictive due to the commutativity of the dot product in the second last line, and substituting $\|\boldsymbol{r}_j\| = 1$ in the final line.

From this result, we see that the use of an interleaved $\hat{\sigma}_z$ phase error model, where dephasing error operators are inserted between Clifford gates, yields the central result

$$\langle\mathcal{F}_{\text{trace}}(\boldsymbol{\eta},\boldsymbol{\delta})\rangle_n = \frac{1}{4}\left|\mathrm{Tr}\left(\widetilde{\mathcal{S}}_{\boldsymbol{\eta},\boldsymbol{\delta}}\right)\right|^2 = 1 - \langle\|\boldsymbol{R}\|^2\rangle_n + \mathcal{O}(\delta^4), \tag{4.38}$$

$$\boldsymbol{R} := \sum_{j=1}^{J}\delta_j\boldsymbol{r}_j, \tag{4.39}$$

where we eliminate all terms with $\mathcal{O}(\delta^3)$ because $\langle\delta_j\rangle_n = 0$ and $\langle\delta_j^3\rangle_n = 0$ for $\delta \sim \mathcal{N}(0,\sigma^2)$. Furthermore, any combination of $\langle\delta_j\delta_k\delta_l\rangle_n = 0$ as the terms can be separated if they are independent, e.g. $\langle\delta_j\delta_k\delta_l\rangle = \langle\delta_j\rangle_n\langle\delta_k\rangle_n\langle\delta_l\rangle_n = 0$ if $j \neq k \neq l$.

From this analysis we obtain the following geometric interpretation. Error accumulation over a J-gate Clifford sequence maps to a random walk, $\boldsymbol{R}$, in a three-dimensional vector space. The step directions $\boldsymbol{r}_j$ represent the action of the error unitaries $\hat{\mathbf{P}}_j$ in the operator space spanned by the Pauli operators ("Pauli space"), and the step lengths, δ_j, capture the phase error applied after the j^{th} gate. The overall form of the walk is a statistical measure of how the sequence itself interacts with the noise process to produce a net, measurable accumulation of error. Sequences that are highly susceptible to error accumulation produce walks that migrate far from the origin, while sequences exhibiting error suppression produce walks that meander back towards the origin. The net walk length is captured in the mean-squared distance from the origin $\langle ||\boldsymbol{R}||^2 \rangle_n$, averaged over noise realisations.

At this stage we can link the correlation properties of the noise to the form of the walk for a specific sequence. Considering only the underlying properties of the sequence, we set the step lengths δ_j to one in order to create a deterministic sequence-dependent walk defined by $\boldsymbol{V} \equiv \sum_{j=1}^{J} \boldsymbol{r}_j$. The presence or absence of temporal noise correlations is now captured through a rescaling of the individual steps in the deterministic walk for a specific sequence. In the case of slowly varying or static noise that is constant throughout the sequence realisation ($\delta_j \equiv \delta$ for all j) the net error can be separated into two independent parts, $||\boldsymbol{R}||^2 = \delta^2 ||\boldsymbol{V}||^2$. However, in the case of rapidly varying noise these two terms are no longer separable and the net error must be calculated as the convolution of the noise value at each time-step and each individual step in the random walk, $||\boldsymbol{R}||^2 = || \sum_{j=1}^{J} \delta_j \boldsymbol{r}_j ||^2$.

We can calculate the noise-averaged fidelity distributions over the randomly constructed Clifford sequences, $\boldsymbol{\eta}$. Firstly, the probability density function (PDF) for the unscaled walk length squared corresponds to the distance square of an unbiased three-dimensional walk, and takes the form of the gamma distribution [**165**]

$$||\boldsymbol{V}||^2 \sim \Gamma\left(a = \frac{3}{2}, b = \frac{2}{3}J\right) \tag{4.40}$$

with shape parameter $a = \frac{3}{2}$ and scale parameter $b = \frac{2}{3}J$. Then, for slowly varying or static noise sampled from a zero-mean normal distribution, we assume all noise random variables $\delta_j \equiv \delta \sim \mathcal{N}(0, \sigma^2)$ are identical over a given noise realisation $\widetilde{\mathcal{S}}_{\eta,\delta}$. The noise then scales the unscaled random walk distribution by σ^2,

$$1 - \langle \mathcal{F}_{\text{trace}}(\boldsymbol{\eta}, \boldsymbol{\delta}) \rangle_n \sim \Gamma\left(a = \frac{3}{2}, b = \frac{2}{3}J\sigma^2\right). \tag{4.41}$$

Finally, for rapidly varying noise that changes for each gate, the PDF is modified to be

$$1 - \langle \mathcal{F}_{\text{trace}}(\boldsymbol{\eta}, \boldsymbol{\delta}) \rangle_n \sim \Gamma\left(a = \frac{3n}{2}, b = \frac{2}{3n} J\sigma^2\right) \tag{4.42}$$

where n is the number of noise realisations sampled from the zero-mean normal distribution with rms σ, $\delta_j \sim \mathcal{N}(0, \sigma^2)$.

4.3 Linking random walk theory to experiment

I now describe the modifications to the above model from Ref. [**165**] that are necessary for good agreement with experimental data. As above, we start with the choice of fidelity metric before moving onto the structure of the error model.

4.3.1 Fidelity modifications for projective measurements

Appropriately linking the picture of error accumulation to standard laboratory measurements requires consideration of the measurement routine itself. In typical measurements, at the end of the sequence the qubit Bloch vector is projected onto the quantisation axis, z, with basis states $|0\rangle$ and $|1\rangle$. We consequently substitute the noise-averaged fidelity $\langle \mathcal{F}(\boldsymbol{\eta}, \boldsymbol{\delta}) \rangle_n$ for the "noise-averaged survival probability",

$$\langle \mathcal{P}\left(\boldsymbol{\eta}, \boldsymbol{\delta}\right) \rangle_n := \langle | \langle 0 | \widetilde{\mathcal{S}}_{\boldsymbol{\eta}, \boldsymbol{\delta}} | 0 \rangle |^2 \rangle_n \tag{4.43}$$

ascertained using projective measurements. A measurement of this type is insensitive to rotations around the projective z-axis of the Bloch sphere. Consequently, the metric is sufficiently different from the *trace* fidelity used in the original model to prevent good agreement between first principles PDF calculations and experimental projective measurements.

Here, I seek to reconcile this difference by re-evaluating the formalism for projective measurements. As with the trace fidelity, the Taylor expansion of the error operator can be used to predict the sequence fidelity. Recall the expression for the noise-affected sequence from Eqn. (4.34),

$$\widetilde{\mathcal{S}}_{\boldsymbol{\eta}, \boldsymbol{\delta}} \approx \left(1 - \frac{1}{2}\sum_{j=1}^{J} \delta_j^2\right)\hat{\mathbb{I}} + \sum_{j=1}^{J}(i\delta_j)\hat{\mathbf{P}}_j - \sum_{j<k} \delta_j \delta_k \hat{\mathbf{P}}_j \hat{\mathbf{P}}_k, \tag{4.44}$$

which I now use to calculate

$$\langle 0| \widetilde{\mathcal{S}}_{\boldsymbol{\eta},\boldsymbol{\delta}} |0\rangle \approx \left(1 - \frac{1}{2}\sum_{j=1}^{J}\delta_j^2\right) + \sum_{j=1}^{J}(i\delta_j)\langle 0| \hat{\mathbf{P}}_j |0\rangle - \sum_{j<k}\delta_j\delta_k \langle 0| \hat{\mathbf{P}}_j\hat{\mathbf{P}}_k |0\rangle \tag{4.45}$$

based on the expected projective measurements outcomes. I proceed by using the relations $\langle 0| \hat{\sigma}_z |0\rangle = 1$ and $\langle 0| \hat{\sigma}_x |0\rangle = \langle 0| \hat{\sigma}_y |0\rangle = 0$. Consequently, the single Pauli-step term, $\hat{\mathbf{P}}_j = \boldsymbol{r}_j \cdot \hat{\boldsymbol{\sigma}}$, can be replaced purely with its z-component,

$$\sum_{j=1}^{J} i\delta_j \langle 0| \hat{\mathbf{P}}_j |0\rangle = \sum_{j=1}^{J} i\delta_j z_j =: iR_z, \tag{4.46}$$

where R_z is the component of the three-dimensional Pauli-space random walk in the $\hat{\sigma}_z$ direction, i.e. $\boldsymbol{R} = [R_x, R_y, R_z]$.

To simplify the final term, $\langle 0| \hat{\mathbf{P}}_j\hat{\mathbf{P}}_k |0\rangle$, one can use the relation

$$\hat{\sigma}_\alpha\hat{\sigma}_\beta = \delta_{\alpha,\beta}\hat{\mathbb{I}} + i\epsilon_{\alpha\beta\gamma}\sigma_\gamma \tag{4.47}$$

where $\delta_{\alpha,\beta}$ is the Kronecker delta (distinct from the noise term δ_j and identified by two subscripts rather than one) and $\epsilon_{\alpha\beta\gamma}$ is the Levi-Civita product for $\alpha, \beta, \gamma \in \{x, y, z\}$. Applying this relation, and only taking the resulting terms proportional to $\hat{\sigma}_z$ and $\hat{\mathbb{I}}$ because $\langle 0| \hat{\sigma}_x |0\rangle = \langle 0| \hat{\sigma}_y |0\rangle = 0$, one can write

$$\begin{aligned}\sum_{j<k}\delta_j\delta_k \langle 0| \hat{\mathbf{P}}_j\hat{\mathbf{P}}_k |0\rangle &= \sum_{j<k}\delta_j\delta_k(\boldsymbol{r}_j\cdot\boldsymbol{r}_k + i(x_jy_k - x_ky_j)) \\ &= \frac{1}{2}\sum_{j,k=1}^{J}\delta_j\delta_k\boldsymbol{r}_j\cdot\boldsymbol{r}_k - \frac{1}{2}\sum_{j=1}^{J}\delta_j^2\|\boldsymbol{r}_j\|^2 + i\sum_{j<k}\delta_j\delta_k(x_jy_k - x_ky_j) \\ &= \frac{1}{2}\|\boldsymbol{R}\|^2 - \frac{1}{2}\sum_{j=1}^{J}\delta_j^2 + i\sum_{j<k}\delta_j\delta_k(x_jy_k - x_ky_j)\end{aligned} \tag{4.48}$$

by recasting part of the restricted sum into a non-restricted sum and using $\|\boldsymbol{r}_j\| = 1$.

Combining Eqns. (4.46) and (4.48) into the noise-averaged survival probability, Eqn. (4.43), one finds

$$\begin{aligned}\langle\mathcal{P}(\boldsymbol{\eta},\boldsymbol{\delta})\rangle_n &= \left\langle\left|1 - \frac{1}{2}\sum_{j=1}^{J}\delta_j^2 + iR_z - \frac{1}{2}\|\boldsymbol{R}\|^2 + \frac{1}{2}\sum_{j=1}^{J}\delta_j^2 - i\sum_{j<k}\delta_j\delta_k(x_jy_k - x_ky_j)\right|^2\right\rangle_n \\ &= 1 - \langle\|\boldsymbol{R}\|^2\rangle_n + \langle|R_z|^2\rangle_n + \mathcal{O}(\delta^4) \\ &= \langle\mathcal{F}_{\text{trace}}(\boldsymbol{\eta},\boldsymbol{\delta})\rangle_n + \langle|R_z|^2\rangle + \mathcal{O}(\delta^4)\end{aligned} \tag{4.49}$$

where I eliminate all terms with $\mathcal{O}(\delta^3)$ due to the noise averaging for $\delta \sim \mathcal{N}(0, \sigma^2)$. Here, the random walk components along each direction are defined as

$$R_x = \sum_{j=1}^{J} \delta_j x_j, \qquad R_y = \sum_{j=1}^{J} \delta_j y_j, \qquad R_z = \sum_{j=1}^{J} \delta_j z_j \tag{4.50}$$

and $\boldsymbol{R} = [R_x,\, R_y,\, R_z]$. From Eqn. (4.49), it is apparent that the walk steps in the $\hat{\sigma}_z$ direction (measurement basis) do not contribute to the survival probability infidelity. By projecting the final state $\widetilde{\mathcal{S}}_{\boldsymbol{\eta},\boldsymbol{\delta}} \left|0\right\rangle$ onto the measurement basis in $\hat{\sigma}_z$, we become "blind" to error accumulation along this degree of freedom in Pauli space. By contrast, the trace fidelity involves no such projection, and measures errors associated with all operator outcomes in SU(2). Equation (4.49) shows that the survival probability maps to a J-step random walk in $\mathbb{R}^3$ *projected onto a two-dimensional subspace* (i.e. the xy-plane), which is illustrated in Fig. 4.1(b). This is formally equivalent to a random walk strictly in $\mathbb{R}^2$ of $\frac{2}{3}J$ steps.

Once averaged over the random noise variable $\boldsymbol{\delta}$, the distribution of $\left\langle \mathcal{P}(\boldsymbol{\eta}, \boldsymbol{\delta}) \right\rangle_n$ over different Clifford sequences still follows a gamma distribution with updated shape and scale parameters. The PDF for the unscaled walk length squared in two dimensions, $||\boldsymbol{V}_{2\text{D}}||^2$, matches that of the distance square of a two-dimensional random walk with $\frac{2}{3}J$ steps, which takes the form of a gamma distribution with shape $a = 1$ and scale $b = \frac{2}{3}J$,

$$||\boldsymbol{V}_{2\text{D}}||^2 \sim \Gamma\left(a = 1, b = \frac{2}{3}J\right). \tag{4.51}$$

The noise-averaged survival probabilities for a slowly varying or static noise process that is constant throughout a sequence realisation remain gamma distributed,

$$1 - \langle \mathcal{P}(\boldsymbol{\eta}, \boldsymbol{\delta}) \rangle_n \sim \Gamma\left(a = 1, b = \frac{2}{3}J\sigma^2\right) \tag{4.52}$$

where $\delta_j \equiv \delta \sim \mathcal{N}(0, \sigma^2)$ and σ^2 has entered as a scaling parameter as was done in obtaining Eqn. (4.41). While an explicit gamma distribution form for the rapidly varying errors has not yet been proven, in the limit of large n and J it approximately follows the distribution

$$1 - \langle \mathcal{P}(\boldsymbol{\eta}, \boldsymbol{\delta}) \rangle_n \sim \Gamma\left(a = n, b = \frac{2}{3n}J\sigma^2\right). \tag{4.53}$$

4.3.2 Random walk modifications for different error channels

Until now, I have used the terms "noise" and "errors" relatively interchangeably, assuming that any noise process affecting a gate will be translated into an identical magnitude error. This was possible using the "interleaved dephasing" error model, which introduces an error of equal magnitude to the hypothetical dephasing "noise" between gates. For realistic noise models, however, this translation is not so straightforward. In experiments, noise often acts *concurrently* with a gate's operation, resulting in multi-axis and gate-dependent errors for the different Clifford operations. Due to the introduced gate-dependence, an exactly constant noise process will not be directly translated to a constant error process with identical error operators for every gate, and hence the translation for each gate needs to be considered explicitly. In this section, I examine the translation of physical noise to experimental errors, studying how the bandwidth and implementation of the noise affects the resulting errors. In particular, I calculate the relationship between the rms magnitude of the physical noise process, ρ, and that of the resulting error operators, σ.

The method to transform noise strength to error strength for noisy, primitive Clifford gates is initially presented here for a general noise process that is static over the duration of a single gate. Each of the single-qubit Clifford gates are made up of rotations on the Bloch sphere with the rotation axis and angle specified by the Clifford gate index, $\eta_j \in \{1, \ldots, 24\}$. If the j^{th} gate in a sequence is affected by laboratory noise with value $\delta_j \sim \mathcal{N}(0, \rho^2)$, then the resulting noise-affected gate can be decomposed into an error operator and the ideal gate, $\widetilde{C}_{\eta_j,\delta_j} = \hat{\Lambda}_{\eta_j,\delta_j}\hat{C}_{\eta_j}$. In general, for a unitary semi-classical noise process, the error operator can be written in terms of the error vector $\boldsymbol{\epsilon}$ using the Magnus expansion,

$$\hat{\Lambda} = e^{i\sum_{\alpha=1}^{\infty}[\boldsymbol{\epsilon}]_\alpha \cdot \hat{\boldsymbol{\sigma}}} \tag{4.54}$$

where $\hat{\boldsymbol{\sigma}}$ is the vector of Pauli matrices and α is the Mangus expansion order. I explicitly separate the error vector into two components, allowing the error operator to be written as a function of the applied noise,

$$\begin{aligned}\hat{\Lambda}_{\eta_j,\delta_j} &= e^{i\sum_{\alpha=1}^{\infty}\delta_j^\alpha[\boldsymbol{\nu}_{\eta_j}]_\alpha \cdot \hat{\boldsymbol{\sigma}}} \\ &\approx \hat{\mathbb{I}} + i\delta_j[\boldsymbol{\nu}_{\eta_j}]_1 \cdot \hat{\boldsymbol{\sigma}}\end{aligned} \tag{4.55}$$

truncating the expansion at second order by requiring $\delta_j \ll 1$. For the Magnus expansion of order α, I have replaced $[\boldsymbol{\epsilon}_j]_\alpha = \delta_j^\alpha[\boldsymbol{\nu}_{\eta_j}]_\alpha$ to explicitly show the dependence on the physical noise strength δ_j, which will change between different realisations of the noise, and the particular gate's susceptibility to the error channel, described by the term $\boldsymbol{\nu}_{\eta_j}$. There will be 24 gate-specific error vector terms, $\boldsymbol{\nu}_{\eta_j}$, corresponding to the 24 Clifford operations, which can be calculated explicitly for a given noise process. We now consider how these terms modify our ideal randomised benchmarking sequence.

Starting with the standard randomised benchmarking procedure, we compile a sequence of randomly composed single-qubit Clifford operations, $\prod_{j=1}^{J}\hat{C}_{\eta_j} = \hat{\mathbb{I}}$. Then, the complete noise-affected sequence is given by

$$\widetilde{\mathcal{S}}_{\boldsymbol{\eta},\boldsymbol{\delta}} = \prod_{j=1}^{J}\hat{\Lambda}_{\eta_j,\delta_j}\hat{C}_{\eta_j}. \tag{4.56}$$

As before, we approximate the noise-affected sequence by translating the first-order term of each error operator to a step in Pauli-error space, with the total random walk in three dimensions given by

$$\boldsymbol{R}_{\text{3D}} = \sum_{j=1}^{J}\delta_j\boldsymbol{r}_{\text{3D},j}, \tag{4.57}$$

$$\begin{aligned}\boldsymbol{r}_{\text{3D},j}\cdot\hat{\boldsymbol{\sigma}} &:= \hat{C}_{\eta_J}\dots\hat{C}_{\eta_{j+1}}\left([\boldsymbol{\nu}_{\eta_j}]_1\cdot\hat{\boldsymbol{\sigma}}\right)\hat{C}_{\eta_j}\dots\hat{C}_{\eta_1}\\ &= \hat{C}_{j,1}^{\dagger}\left([\boldsymbol{\nu}_{\eta_j}]_1\cdot\hat{\boldsymbol{\sigma}}\right)\hat{C}_{j,1},\end{aligned} \tag{4.58}$$

where I now explicitly add a “3D” subscript to describe the steps in the full three-dimensional Pauli space. Recall that previously for the interleaved dephasing model, the error operator was always $\hat{\sigma}_z$, and the step was simply given by Eqn. (4.32),

$$\boldsymbol{r}_{\text{3D},j}\cdot\hat{\boldsymbol{\sigma}} = \hat{C}_{j,1}^{\dagger}\hat{\sigma}_z\hat{C}_{j,1}. \tag{4.59}$$

The crucial difference between these two derivations is that, due to the introduction of $\boldsymbol{\nu}_{\eta_j}$, *we no longer assume* $\|\boldsymbol{r}_{\text{3D},j}\| = 1$.

To obtain the sequence survival probability that would be measured via a single-axis projective measurement, the relevant steps are obtained from the projection of $\boldsymbol{r}_{\text{3D},j}$ in the two-dimensional $\hat{\sigma}_x\hat{\sigma}_y$-plane of Pauli-error space, $\boldsymbol{r}_{\text{2D},j}$. This allows us to write the noise-averaged survival probability for a qubit initially prepared in $|0\rangle$ as

$$\langle\mathcal{P}(\boldsymbol{\eta},\boldsymbol{\delta})\rangle_n = \langle|\langle 0|\,\widetilde{\mathcal{S}}_{\boldsymbol{\eta},\boldsymbol{\delta}}\,|0\rangle|^2\rangle_n = 1 - \langle\|\boldsymbol{R}_{\text{2D}}\|^2\rangle_n + \mathcal{O}\left(\rho^4\right), \tag{4.60}$$

where $\boldsymbol{R}_{\text{2D}}$ is the two-dimensional random walk and the noise is sampled from the zero-mean normal distribution $\delta \sim \mathcal{N}(0,\rho^2)$. Continuing forward, we will exclusively utilise the two-dimensional walk relevant to the projective measurements and, to simplify notation, consequently substitute $\boldsymbol{r}_{\text{2D},j} \equiv \boldsymbol{r}_j$ and $\boldsymbol{R}_{\text{2D}} \equiv \boldsymbol{R}$.

From the expression for noise-averaged survival probability, the distribution moments over sequences can be calculated for arbitrary step lengths. This is achieved by taking the expectation and variance of $\boldsymbol{R} = \sum_{j=1}^{J} \delta_j \boldsymbol{r}_j$, when the noise process is either correlated or uncorrelated. For a correlated noise process, constant across all gates, I represent the rms strength of the noise by ρ_C and calculate the statistical moments for the noise-averaged survival probability, denoted $\langle \mathcal{P}_C(\boldsymbol{\eta}, \boldsymbol{\delta}) \rangle_n$.

$$\mathbb{E}\left[\langle \mathcal{P}_C(\boldsymbol{\eta}, \boldsymbol{\delta}) \rangle_n\right] = 1 - J\mathbb{E}\left[\|\boldsymbol{r}_j\|^2\right] \rho_C^2, \tag{4.61}$$

$$\mathbb{V}\left[\langle \mathcal{P}_C(\boldsymbol{\eta}, \boldsymbol{\delta}) \rangle_n\right] = \frac{J(n+2)}{n} \left(\mathbb{E}\left[\|\boldsymbol{r}_j\|^4\right] + (J-2)\mathbb{E}\left[\|\boldsymbol{r}_j\|^2\right]^2\right) \rho_C^4 \tag{4.62}$$

For an uncorrelated noise process with the noise strength changing every gate time or more frequently, the rms strength is represented by ρ_U and the noise-averaged survival probability $\langle \mathcal{P}_U(\boldsymbol{\eta}, \boldsymbol{\delta}) \rangle_n$. Then the statistical moments are

$$\mathbb{E}\left[\langle \mathcal{P}_U(\boldsymbol{\eta}, \boldsymbol{\delta}) \rangle_n\right] = 1 - J\mathbb{E}\left[\|\boldsymbol{r}_j\|^2\right] \rho_U^2, \tag{4.63}$$

$$\mathbb{V}\left[\langle \mathcal{P}_U(\boldsymbol{\eta}, \boldsymbol{\delta}) \rangle_n\right] = \frac{J}{n} \left((2+n)\mathbb{E}\left[\|\boldsymbol{r}_j\|^4\right] + (J-1-n)\mathbb{E}\left[\|\boldsymbol{r}_j\|^2\right]^2\right) \rho_U^4. \tag{4.64}$$

These expressions are based on the expected values of $\|\boldsymbol{r}_j\|^2$ and $\|\boldsymbol{r}_j\|^4$ averaged across all gates. Their form entirely arises because we have relaxed the assumption that $\|\boldsymbol{r}_{3\mathrm{D},j}\| = 1$, allowing gate-dependent and multi-axis errors. In fact, if we analyse the case of unit-length steps in three dimensions corresponding to two-dimensional steps with $\|\boldsymbol{r}_j\|^2 = \|\boldsymbol{r}_j\|^4 = 2/3$, these expressions reduce to

$$\mathbb{E}\left[\langle \mathcal{P}_C(\boldsymbol{\eta}, \boldsymbol{\delta}) \rangle_n\right] = 1 - \frac{2}{3} J \rho_C^2, \tag{4.65}$$

$$\mathbb{V}\left[\langle \mathcal{P}_C(\boldsymbol{\eta}, \boldsymbol{\delta}) \rangle_n\right] = \frac{4}{9} \frac{J(n+2)}{n} \left(J - \frac{1}{2}\right) \rho_C^4 \approx \frac{4}{9} J^2 \rho_C^4 \tag{4.66}$$

$$\mathbb{E}\left[\langle \mathcal{P}_U(\boldsymbol{\eta}, \boldsymbol{\delta}) \rangle_n\right] = 1 - \frac{2}{3} J \rho_U^2, \tag{4.67}$$

$$\mathbb{V}\left[\langle \mathcal{P}_U(\boldsymbol{\eta}, \boldsymbol{\delta}) \rangle_n\right] = \frac{4}{9} \frac{J}{n} \left(J + 2 + \frac{n}{2}\right) \rho_U^4 \approx \frac{4}{9n} J^2 \rho_U^4, \tag{4.68}$$

where the approximations are made in the limit of large J and n. Hence, we recover the moments calculated from the original interleaved dephasing error model (Eqns. (4.52) and (4.53)).

In Table 4.2, I show the expectation values of $\|\boldsymbol{r}_j\|^2$ and $\|\boldsymbol{r}_j\|^4$ for a range of physical noise processes that can be used to calculate the expected statistical moments. In addition, I show a covariance value called $\mathrm{Cov}\left(\|\boldsymbol{r}_{U,j}\|^2, \|\boldsymbol{r}_{C,j}\|^2\right)$ that will be required when a correlated and uncorrelated noise component for the same error channel are *simultaneously* present, e.g. rapidly varying frequency errors added to a

Engineered Noise Process	$\mathbb{E}\left[\|\boldsymbol{r}_j\|^2\right]$	$\mathbb{E}\left[\|\boldsymbol{r}_j\|^4\right]$	$\mathrm{Cov}\left(\|\boldsymbol{r}_{U,j}\|^2, \|\boldsymbol{r}_{C,j}\|^2\right)$
Interleaved Dephasing	2/3	2/3	2/9
	$\frac{2}{3}\left(\frac{1}{2}+\frac{\pi^2}{96}\right)$	$\frac{2}{3}\left(\frac{7}{24}+\frac{\pi^4}{384}\right)$	$\frac{2}{3}\left(\frac{7}{24}+\frac{\pi^4}{384}\right)-\frac{4}{9}\left(\frac{1}{2}+\frac{\pi^2}{96}\right)^2$
Concurrent Detuning 1 value every primitive $\pi/2$ gate time	$\frac{2}{3}\left(\frac{1}{2}+\frac{\pi^2}{192}\right)$	$\frac{2}{3}\left(\frac{1}{4}+\frac{\pi^4}{1536}\right)$	$\frac{17}{108}+\frac{\pi^4}{1152}-\frac{4}{9}\left(\frac{1}{2}+\frac{\pi^2}{192}\right)\left(\frac{1}{2}+\frac{\pi^2}{96}\right)$
Over- and Under-rotation 1 value per primitive (π or $\pi/2$) gate	$\pi^2/18$	$5\pi^4/576$	$29\pi^4/5184$
Over- and Under-rotation 1 value every primitive $\pi/2$ gate time	$\pi^2/36$	$5\pi^4/2304$	$29\pi^4/10368$

TABLE 4.2. The expected step lengths in the Pauli $\hat{\sigma}_x\hat{\sigma}_y$-plane based on the average Clifford gate error for different engineered noise. These quantities are used to predict the statistical moments of the sequence survival-probability distributions in Eqns. (4.61)-(4.64). The covariance values are taken between the expected step value for a correlated noise process ($\|\boldsymbol{r}_{C,j}\|$) and an uncorrelated noise process ($\|\boldsymbol{r}_{U,j}\|^2$) from the same error model. They will be required to predict the behaviour of RB when correlated and uncorrelated noise processes are *simultaneously* present. For both the concurrent detuning and over-rotation errors, two bandwidths are considered for the uncorrelated error. The *correlated* error process step will be the same for both cases.

slow drift. In that case, if the uncorrelated noise process changes *within* an individual gate duration, then the expected single step lengths may have to be derived independently for the correlated noise ($\|\boldsymbol{r}_{C,j}\|$) and the uncorrelated noise ($\|\boldsymbol{r}_{U,j}\|$). This will be discussed in greater detail in Chapter 6. I finish this chapter by showing an explicit example of how to derive the terms $\|\boldsymbol{r}_j\|^2$ and $\|\boldsymbol{r}_j\|^4$ for a particular error model – the concurrent detuning error.

4.3.3 Expected random walk steps for concurrently applied detuning noise

The main error model studied in our work involves the application of a laboratory detuning between the control field and qubit transition during a non-zero-duration operation. Deliberately induced off-resonance errors are implemented via a fixed detuning Δ from the qubit's transition frequency. Only the physically implemented gates (proportional to $\hat{\sigma}_I \equiv \hat{\mathbb{I}}$, $\hat{\sigma}_x$ and $\hat{\sigma}_y$) will be affected by the off-resonance error; frame changes from $\hat{\sigma}_z$ rotations remain error free. The noise-affected gates can be rewritten as rotation operators modified by an additional concurrent $\hat{\sigma}_z$ rotation with strength normalised by the Rabi frequency Ω, $\delta = \Delta/\Omega$,

$$\hat{R}_i(\theta, \delta) = \exp\left\{-i\left(\frac{\theta}{2}\hat{\sigma}_i + \frac{|\theta|}{2}\delta\hat{\sigma}_z\right)\right\}, \quad i \in \{I, x, y\}. \tag{4.69}$$

The first term in the exponent corresponds to the unperturbed unitary where the rotation angle is chosen from $\theta \in \{-\pi/2, \pi/2, \pi\}$ and $\hat{\sigma}_I \equiv \hat{\mathbb{I}}$. The second term relates to the $\hat{\sigma}_z$ off-resonance error, for which the absolute value of θ ensures that the sign of the detuning term is preserved under positive and negative gate rotations.

Concurrently applied detuning noise leads to gate-dependent errors. For example, π rotations accumulate twice the phase in the presence of a non-zero detuning as $\pi/2$ rotations. Here, I provide the specific matrix form of the unitary operations employed in experiments and simulations where the error model involves a concurrently applied $\hat{\sigma}_z$ Hamiltonian term. The basic unperturbed operations about each axis are defined to be

$$\hat{C}_I(\theta) = e^{-i\frac{\theta}{2}\hat{\sigma}_I}, \tag{4.70a}$$

$$\hat{C}_x(\theta) = e^{-i\frac{\theta}{2}\hat{\sigma}_x}, \tag{4.70b}$$

$$\hat{C}_y(\theta) = e^{-i\frac{\theta}{2}\hat{\sigma}_y}, \tag{4.70c}$$

$$\hat{C}_z(\theta) = e^{-i\frac{\theta}{2}\hat{\sigma}_z}. \tag{4.70d}$$

In the presence of engineered off-resonance errors, the effective error magnitude $\delta = \Delta/\Omega$ modifies the unitary evolution of our gates by introducing a concurrent $\hat{\sigma}_z$ rotation

$$\widetilde{C}_I(\theta, \delta) = e^{-i\left(\frac{\theta}{2}\hat{\sigma}_I + \frac{|\theta|}{2}\delta\hat{\sigma}_z\right)}, \tag{4.71a}$$

$$\widetilde{C}_x(\theta, \delta) = e^{-i\left(\frac{\theta}{2}\hat{\sigma}_x + \frac{|\theta|}{2}\delta\hat{\sigma}_z\right)}, \tag{4.71b}$$

$$\widetilde{C}_y(\theta, \delta) = e^{-i\left(\frac{\theta}{2}\hat{\sigma}_y + \frac{|\theta|}{2}\delta\hat{\sigma}_z\right)}, \tag{4.71c}$$

$$\widetilde{C}_z(\theta, \delta) = e^{-i\frac{\theta}{2}\hat{\sigma}_z}. \tag{4.71d}$$

The modified unitaries can be written in matrix form as,

$$\widetilde{C}_I(\theta, \delta) = \begin{pmatrix} e^{-\frac{i(\theta\Omega + \Delta|\theta|)}{2\Omega}} & 0 \\ 0 & e^{\frac{i(\Delta|\theta| - \theta\Omega)}{2\Omega}} \end{pmatrix}, \tag{4.72a}$$

$$\widetilde{C}_x(\theta, \delta) = \begin{pmatrix} \cos\left(\frac{\tilde{\theta}}{2}\right) - \frac{i\Delta \sin\left(\frac{|\tilde{\theta}|}{2}\right)}{\sqrt{\Delta^2+\Omega^2}} & -\frac{i\Omega \sin\left(\frac{\tilde{\theta}}{2}\right)}{\sqrt{\Delta^2+\Omega^2}} \\ -\frac{i\Omega \sin\left(\frac{\tilde{\theta}}{2}\right)}{\sqrt{\Delta^2+\Omega^2}} & \cos\left(\frac{\tilde{\theta}}{2}\right) + \frac{i\Delta \sin\left(\frac{|\tilde{\theta}|}{2}\right)}{\sqrt{\Delta^2+\Omega^2}} \end{pmatrix}, \tag{4.72b}$$

$$\widetilde{C}_y(\theta, \delta) = \begin{pmatrix} \cosh\left(\frac{i|\tilde{\theta}|}{2}\right) - \frac{\Delta \sinh\left(\frac{i|\tilde{\theta}|}{2}\right)}{\sqrt{\Delta^2+\Omega^2}} & \frac{i\theta \sinh\left(\frac{i|\tilde{\theta}|}{2}\right)}{|\tilde{\theta}|} \\ -\frac{i\theta \sinh\left(\frac{i|\tilde{\theta}|}{2}\right)}{|\tilde{\theta}|} & \cosh\left(\frac{i|\tilde{\theta}|}{2}\right) + \frac{\Delta \sinh\left(\frac{i|\tilde{\theta}|}{2}\right)}{\sqrt{\Delta^2+\Omega^2}} \end{pmatrix}, \tag{4.72c}$$

$$\widetilde{C}_z(\theta, \delta) = \begin{pmatrix} e^{-\frac{i\theta}{2}} & 0 \\ 0 & e^{\frac{i\theta}{2}} \end{pmatrix}, \tag{4.72d}$$

where I define the modified rotation angle as $\tilde{\theta} = \frac{\theta\sqrt{\Delta^2+\Omega^2}}{\Omega}$, which reduces to θ when $\Delta = 0$. Note that $\widetilde{C}_z = \hat{C}_z$ because rotations around the z-axis are carried out instantaneously by absorbing them into the pre-calculated changes of the phase of the microwave output of the VSG.

The error operators affecting the Clifford operations can be calculated from the noise-affected gates using $\hat{\Lambda} = \widetilde{C}\hat{C}^\dagger$ and Taylor expanding in terms of δ to find,

$$\hat{\Lambda}^{(\hat{\mathbb{I}})}(\pi, \delta) = \hat{\mathbb{I}} - i\tfrac{\pi\delta}{2}\hat{\sigma}_z + \mathcal{O}\left(\delta^2\right) \tag{4.73a}$$

$$\hat{\Lambda}^{(\hat{\sigma}_x)}(\pi, \delta) = \hat{\mathbb{I}} + i\delta\hat{\sigma}_y + \mathcal{O}\left(\delta^2\right) \tag{4.73b}$$

$$\hat{\Lambda}^{(\hat{\sigma}_x)}(\pm\tfrac{\pi}{2}, \delta) = \hat{\mathbb{I}} \pm \tfrac{i\delta}{2}\hat{\sigma}_y - \tfrac{i\delta}{2}\hat{\sigma}_z + \mathcal{O}\left(\delta^2\right) \tag{4.73c}$$

$$\hat{\Lambda}^{(\hat{\sigma}_y)}(\pi, \delta) = \hat{\mathbb{I}} - i\delta\hat{\sigma}_x + \mathcal{O}\left(\delta^2\right) \tag{4.73d}$$

$$\hat{\Lambda}^{(\hat{\sigma}_y)}(\pm\tfrac{\pi}{2}, \delta) = \hat{\mathbb{I}} \mp \tfrac{i\delta}{2}\hat{\sigma}_x - \tfrac{i\delta}{2}\hat{\sigma}_z + \mathcal{O}\left(\delta^2\right) \tag{4.73e}$$

$$\hat{\Lambda}^{(\hat{\sigma}_z)}(\theta, \delta) = \hat{\mathbb{I}}, \tag{4.73f}$$

more generally expressed for the j^{th} operation in the sequence as

$$\hat{\Lambda}_{\eta_j}(\delta_j) = \hat{\mathbb{I}} + \delta_j[\boldsymbol{\nu}_{\eta_j}]_1 \cdot \hat{\boldsymbol{\sigma}} + \mathcal{O}\left(\delta_j^2\right). \tag{4.74}$$

Only eight error operators are required to treat all 24 Clifford operations due to the error-free nature of $\hat{\sigma}_z$-rotations, which are generally implemented via instantaneous phase-changes on the control field. Following the definition of the Clifford operations given in Table 4.1, there is only one non-$\hat{\sigma}_z$-rotation per Clifford, which exactly corresponds to one of the eight error maps described in Eqn. (4.73). If $\hat{\sigma}_z$

operations were also affected by the noise, the procedure would follow similarly but all 24 error maps would need to be calculated.

To find the expected random walk steps for this unitary error channel, recall from Eqn. (4.58) that the direction of the Pauli-error steps is determined by conjugating the first-order error vector component $[\boldsymbol{\nu}_{\eta_j}]_1 \cdot \hat{\boldsymbol{\sigma}}$ with the preceding operations in the randomly composed sequence. As such, a given step will remain deterministic in its size, yet be performed along an arbitrary direction in Pauli-error space, determined by the randomly selected, preceding gates. Studying the error maps for concurrent detuning noise, we can write the gate-dependent steps as

$$\hat{\Lambda}^{(\hat{\mathbb{I}})}(\pi) \rightarrow \tfrac{\pi}{2}\hat{m}_1 \tag{4.75}$$

$$\hat{\Lambda}^{(\hat{\sigma}_x)}(\pi) \rightarrow 1\hat{m}_1 \tag{4.76}$$

$$\hat{\Lambda}^{(\hat{\sigma}_x)}(\pm\tfrac{\pi}{2}) \rightarrow \tfrac{1}{2}\hat{m}_1 + \tfrac{1}{2}\hat{m}_2 \tag{4.77}$$

$$\hat{\Lambda}^{(\hat{\sigma}_y)}(\pi) \rightarrow 1\hat{m}_1 \tag{4.78}$$

$$\hat{\Lambda}^{(\hat{\sigma}_y)}(\pm\tfrac{\pi}{2}) \rightarrow \tfrac{1}{2}\hat{m}_1 + \tfrac{1}{2}\hat{m}_2 \tag{4.79}$$

$$\hat{\Lambda}^{(\hat{\sigma}_z)}(\theta) \rightarrow 0 \tag{4.80}$$

with $\hat{m}_1, \hat{m}_2 \in \pm\{\hat{\sigma}_x, \hat{\sigma}_y, \hat{\sigma}_z\}$. This implies that π-rotations about the x and y-axes of the Bloch sphere produce a unit-length step in Pauli-error space that will be randomly oriented along one of the six principal axes. Similarly, $\frac{\pi}{2}$-rotations produce a $\frac{1}{\sqrt{2}}$-length step oriented at 45° between two principal axes, $\hat{\mathbb{I}}$ gates produce a $\frac{\pi}{2}$-length step along a principal axis, and rotations about the z-axis contribute no step due to their error-free nature.

The probability of producing a particular non-zero $\|\boldsymbol{r}_j\|$ is shown in Table 4.3, based on the prevalence of different gates in the 24 Clifford gates and the likeliness of their projection into the $\hat{\sigma}_x\hat{\sigma}_y$-plane. Note that these steps are completely independent of the strength of the particular noise realisation, δ_j. The noise will eventually rescale each step length, but here we only consider the unscaled walk.

The particular error channel we are modelling is constant over at *least* an individual gate duration, as per the noisy gate definitions in Eqn. (4.71). If we consider "correlated" noise as constant over an entire sequence realisation and "uncorrelated" noise as constant over an individual gate duration and changing between every gate, then for this particular bandwidth it is not necessary to distinguish between $\mathbb{E}\left[\|\boldsymbol{r}_{C,j}\|^2\right]$ and $\mathbb{E}\left[\|\boldsymbol{r}_{U,j}\|^2\right]$. Both the correlated and uncorrelated error processes are static over the duration of an individual gate, and hence will result in the same expected average random walk

$\|\boldsymbol{r}_j\|$	1	$\frac{1}{\sqrt{2}}$	$\frac{1}{2}$	$\frac{\pi}{2}$
$\mathrm{Pr}_{\hat{\sigma}_x\hat{\sigma}_y}$	$\frac{4}{24} \times \frac{2}{3}$	$\frac{16}{24} \times \frac{4}{12}$	$\frac{16}{24} \times \frac{8}{12}$	$\frac{1}{24} \times \frac{2}{3}$

TABLE 4.3. Likelihood of producing particular length random walk steps in the $\hat{\sigma}_x\hat{\sigma}_y$-plane of Pauli-error space when engineered detuning noise is applied, based on the number of Clifford gates corresponding to the error map, and the chance of a randomly oriented step in the $\hat{\sigma}_x\hat{\sigma}_y$-plane.

steps. It is only when increasing the bandwidth of the uncorrelated noise that they need be distinguished. Using Table 4.3 one finds

$$\mathbb{E}\left[\|\boldsymbol{r}_j\|^2\right] = \frac{2}{3}\left(\frac{1}{2} + \frac{\pi^2}{96}\right) \tag{4.81}$$

$$\mathbb{E}\left[\|\boldsymbol{r}_j\|^4\right] = \frac{2}{3}\left(\frac{7}{24} + \frac{\pi^4}{384}\right) \tag{4.82}$$

$$\mathbb{E}\left[\|\boldsymbol{r}_{U,j}\|^2\|\boldsymbol{r}_{C,j}\|^2\right] = \mathbb{E}\left[\|\boldsymbol{r}_j\|^4\right]. \tag{4.83}$$

Using Eqns. (4.61) and (4.63) for the expectation of the noise-averaged survival probability, I find

$$\mathbb{E}\left[\langle\mathcal{P}(\boldsymbol{\eta},\boldsymbol{\delta})\rangle_n\right] \approx J\sigma^2 \tfrac{2}{3}\left(\tfrac{1}{2} + \tfrac{\pi^2}{96}\right) \tag{4.84}$$

for both correlated and uncorrelated noise. This illustrates the equivalence of the distribution mean, which is related to the parameter that standard randomised benchmarking analysis returns, for noise of the same strength despite vastly different correlation lengths.

The difference between the correlated and uncorrelated processes becomes evident when looking at the variance over survival probabilities with increased noise averaging, calculated using Eqns. (4.62) and (4.64). For uncorrelated errors,

$$\begin{aligned}\mathbb{V}\left[\mathcal{P}_U\right] \approx \tfrac{J^2\sigma^4}{n}&\left[\tfrac{4}{9}\left(\tfrac{1}{2} + \tfrac{\pi^2}{96}\right)^2 + \tfrac{1}{J}\left\{3\left(\tfrac{7}{36} + \tfrac{\pi^4}{576}\right) - \tfrac{8}{9}\left(\tfrac{1}{2} + \tfrac{\pi^2}{96}\right)^2\right\}\right.\\ &\left.+ \tfrac{(n-1)}{J}\left\{\tfrac{7}{36} + \tfrac{\pi^4}{576} - \tfrac{4}{9}\left(\tfrac{1}{2} + \tfrac{\pi^2}{96}\right)^2\right\}\right],\end{aligned} \tag{4.85}$$

which, in the limit $n \to \infty$, saturates at a value proportional to $\frac{1}{J}$ relative to the starting variance. For correlated errors,

$$\begin{aligned}\mathbb{V}\left[\mathcal{P}_C\right] \approx \tfrac{J^2\sigma^4}{n}&\left[\tfrac{12}{9}\left(\tfrac{1}{2} + \tfrac{\pi^2}{96}\right)^2 + \tfrac{1}{J}\left\{3\left(\tfrac{7}{36} + \tfrac{\pi^4}{576}\right) - \tfrac{8}{3}\left(\tfrac{1}{2} + \tfrac{\pi^2}{96}\right)^2\right\}\right.\\ &\left.+ (n-1)\left\{\tfrac{4}{9}\left(\tfrac{1}{2} + \tfrac{\pi^2}{96}\right)^2 + \tfrac{1}{J}\left(\tfrac{7}{36} + \tfrac{\pi^4}{576} - \tfrac{8}{9}\left(\tfrac{1}{2} + \tfrac{\pi^2}{96}\right)^2\right)\right\}\right],\end{aligned} \tag{4.86}$$

again tending towards a constant. However, the saturation occurs within a significantly smaller number of noise averages than for uncorrelated noise and saturates at a much larger variance, which is proportional to $1 + \frac{1}{J}$ relative to the starting variance.

Using the revised model, the noise-averaged survival-probability distributions under correlated noise remain Gamma distributed with an updated scale parameter. While this is yet to be shown explicitly for the uncorrelated case, the behaviour is approximated in the limit of large n and J, with $n < J^2$, by the gamma distributions

$$\mathcal{P}_C \sim \Gamma(a = 1, b = \tfrac{2}{3} J\sigma^2(\tfrac{1}{2} + \tfrac{\pi^2}{96})), \tag{4.87}$$

$$\mathcal{P}_U \sim \Gamma(a = n, b = \tfrac{2}{3n} J\sigma^2(\tfrac{1}{2} + \tfrac{\pi^2}{96})). \tag{4.88}$$

To adjust for higher bandwidth uncorrelated noise that take multiple values of δ in a single error map, such as changing every primitive $\pi/2$ times, I make use of the relation

$$\begin{aligned} \delta_1 \pm \delta_2 &\sim \mathcal{N}(0, 2\rho^2) \\ &\equiv \sqrt{2}\,\mathcal{N}(0, \rho^2) \end{aligned} \tag{4.89}$$

such that the multiple values of δ could be expressed as

$$\delta_1 \pm \delta_2 \equiv \sqrt{2}\,\delta, \quad \text{with} \quad \delta \sim \mathcal{N}(0, \rho^2) \tag{4.90}$$

from which point the previous method can be followed. The equivalence in Eqn. (4.90) occurs because δ_1, δ_2 are independent samples from a Gaussian distribution, meaning their combination is also Gaussian distributed. This relation was used to produce the expectation values of $\|\boldsymbol{r}_j\|$ in Table 4.2 for noise that changed every primitive $\pi/2$ time – corresponding to two noise values within a π-length gate.

*****

The theoretical model in this chapter translates unitary circuits of Clifford operators to random walks in “Pauli space”. This framework can be used to predict the susceptibility of individual circuits to correlated noise processes, as will be demonstrated through the next two chapters. I continue in the next chapter by validating the theoretical model and using it to augment the analysis of randomised benchmarking and gate set tomography.

CHAPTER 5

Experimental quantum verification in the presence of temporally correlated noise

---

“One might be led to suspect that there were all sorts of things going on in the Universe which he or she did not thoroughly understand.”

- Kurt Vonnegut, *Bluebeard*

*The following chapter studies the effect of correlated errors on the outputs of QCVV protocols, validating the theoretical model presented in the previous chapter. This work is reproduced with minimal changes from “Experimental quantum verification in the presence of temporally correlated noise” published in npj Quantum Information volume 4, Article number: 7 (2018) [**3**].*

Growth in the capabilities of quantum information hardware mandates access to techniques for performance verification that function under realistic laboratory conditions. Even in highly controlled laboratory environments there are a range of noise sources that, when applied to a qubit concurrent with logical gate operations, produce effective error models that diverge significantly from the assumptions underlying most quantum characterisation, verification and validation (QCVV) protocols. In particular, the assumptions that errors are statistically independent between gates and qubits, and gate independent. For example, slow variations in ambient magnetic fields or drifts in amplifier gain can produce temporally correlated noise processes, often characterised through a power spectral density possessing large weight at low frequencies [**170–172**]. So far such processes have been largely ignored in experimental QCVV, with predominantly phenomenological attempts used to explain deviations from ideal outputs [**173**]. Understanding that such an approach is untenable when attempting to rigorously compare QCVV results to metrics relevant to quantum error correction has recently led to an expansion of theoretical activity in this space [**156**, **165**, **174–177**].

In this work our objectives are to experimentally characterise and explain the impact of temporally correlated noise processes on the outputs of QCVV protocols, and to identify potential modifications enabling users to improve the utility of the information returned. Our analysis highlights the role of sequence structure in enhancing or suppressing the sensitivity of QCVV protocols to noise with different correlation lengths. We examine two commonly used QCVV protocols: randomised benchmarking (RB) and gate set tomography (GST). The construction of these protocols follows a similar pattern, a series of unitary quantum operations is applied to one or more qubits sequentially in time, followed by a projective measurement. Experimental measurements are acquired and combined, then experimental parameters are changed according to some prescription (e.g. changing the sequence length) and further data are collected. The variation in QCVV protocols predominantly comes from the different constituent operations that are applied and the analysis techniques by which measurement results are post-processed to extract information. The full prescriptions for both RB and GST are outlined in Section 4.1.

We perform QCVV experiments using a single trapped $^{171}\mathrm{Yb}^+$ ion as a long-lived, high-stability qubit. Engineered frequency noise in the control system ($\propto \hat{\sigma}_z$) enables quantitative analysis of the impact of different temporal noise correlations on QCVV results under known conditions. Noise is engineered in two distinct noise-correlation regimes. Firstly, the noise is implemented as a constant miscalibration over the entire sequence, which is the extreme case for slowly varying noise and produces highly temporally correlated errors. Secondly, the noise is engineered to be rapidly varying, yielding an approximately white power spectrum that leads to errors that are largely uncorrelated between gates. Measurements reveal that QCVV outputs diverge significantly when subject to these different types of noise, highlighting potential circumstances where the information extracted from a given protocol may no longer accurately represent the true error processes experienced by individual gates. Our experiments are compared against analytic calculations that link the impact of the underlying sequence structure with the presence of noise correlations using the framework presented in Chapter 4.

Experiments on RB validate predictions that measured fidelities over sequences are described by a gamma distribution varying between approximately Gaussian, and a broad, highly skewed distribution for rapidly and slowly varying noise respectively. Similarly we find a strong gate set dependence of default experimental GST procedures in the presence of correlated errors, leading to significant deviations between estimated and calculated diamond distances in the presence of correlated $\hat{\sigma}_z$ errors. Numerical simulations demonstrate that expansion of the gate set to include negative rotations can suppress these discrepancies and increase reported diamond distances by orders of magnitude for the same error processes. Similar effects do not occur for correlated $\hat{\sigma}_x$ or $\hat{\sigma}_y$ errors or depolarising noise processes, highlighting the critical interplay of selected gate set and the gauge optimisation process on the meaning of the reported diamond norm in correlated noise environments.

5.1 Experimental platform and engineered noise

We perform experiments using the $^{171}\text{Yb}^+$ experimental setup described in Chapter 2. In particular, we utilise a 12.64 GHz microwave field produced by a vector signal generator (VSG) to control the qubit and implement Clifford operations. Regularly spaced phase Ramsey calibrations track the qubit transition frequency to better than 1 Hz accuracy (see Section 2.4.4 for details on the calibration procedure). In our laboratory, this qubit and the associated control system have been demonstrated to possess a coherence time of $T_2 \sim 1$ s, measurement fidelity of $\sim 99.7\%$ limited by photon collection efficiency, and error rates from intrinsic system noise of $p_{\text{RB}} \approx 6 \times 10^{-5}$ using “baseline” RB experiments.

Experiments involve state preparation in the $|0\rangle$ state via optical pumping, application of a unitary sequence appropriate for the QCVV protocol while subject to engineered noise, and projective measurement of the qubit along the quantisation axis. The sequence of operations applied and the measurement procedure are determined by the protocol in use. To implement the full set of Clifford gates listed in Table 4.1, we generate I/Q-modulated gates in the VSG, as described in Chapter 2.4.1. In particular, all $\hat{\sigma}_z$ rotations are implemented as instantaneous pre-calculated frame rotations, and are hence error free (up to the relative phases of the digital-to-analogue converters (DACs) used for I and Q modulation), and identity gates are performed using π-rotation-length idle periods. All RB and GST sequences are uploaded to the VSG prior to the experiments and selected when required. When the number of implemented sequences is large, as is the case with GST, the latter step is the bottleneck as sequence selection can take up to tens of seconds, depending on the constituent number of gates J. This slowdown is due to the use of the in-built protocol “RF blanking”, which allows for superior suppression of both microwave leakage and amplitude instabilities at the edges of pulses, but adds significant overhead associated with switching between sequences.

We engineer $\hat{\sigma}_z$ noise applied concurrently with Clifford operations through the application of a detuning, Δ, of the qubit driving field from resonance using an externally modulated vector signal generator. This creates an effective error $\delta = \Delta/\Omega$, with Rabi frequency Ω fixed at $\Omega = 22.5\,\text{kHz}$. As the detuning

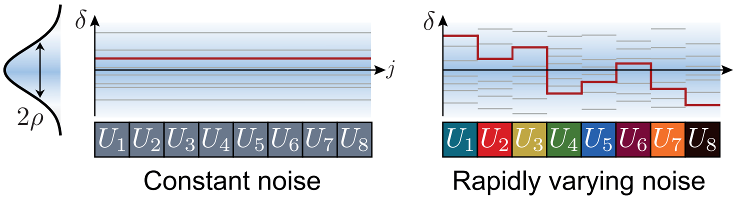

FIGURE 5.1. Schematic representation of constant and rapidly varying noise with relevant time scales defined by the sequence where $\delta = \Delta/\Omega$ represents the normalised instantaneous noise values drawn from a normal distribution with ρ^2 variance. Grey lines show examples of possible noise realisations, and the red solid line is one such realisation. For RB, the noise is sampled from this distribution and varies shot-to-shot between noise realisations, while in GST a single value is selected for the entire set of experiments.

is applied concurrently with driven qubit rotations about x and y-axes, rotation errors arise along multiple directions on the Bloch sphere, rather than being purely $\hat{\sigma}_z$ in character. An additional violation of typical assumptions employed in RB is that the errors are not gate-independent [**177**]. As different gates have varying durations (e.g. a $\pi/2$ rotation has half the duration of a π rotation), the same engineered noise will induce different strength errors for different gates.

We consider two limiting noise cases – rapidly varying noise that changes with every gate, and slowly varying noise that is constant for an entire sequence duration, as illustrated in Fig. 5.1. For both cases, we engineer n different noise "realisations" in order to average over an appropriate ensemble. We set both distributions of noise values to be $\delta = \Delta/\Omega \sim \mathcal{N}(0, \rho^2)$, where ρ^2 is the variance of the distribution, such that the root-mean-square (rms) value is approximately equivalent in both cases once averaged over all noise realisations. For each of the $n = 200$ noise realisations, the distribution is sampled either once (slowly varying) or J times (rapidly varying) for a sequence comprising J gates.

In RB experiments slowly varying noise is implemented by shifting the VSG drive frequency by a fixed amount based on a list of $n = 200$ samples from a zero-mean Gaussian distribution with rms value $\rho = 1\,\text{kHz}/22.5\,\text{kHz} = 0.044$ (Fig. 5.2(a)). The same list of noise realisations is repeated for each RB sequence in a set of given length J, yielding sets of noise-averaged survival probabilities, $\langle \mathcal{P} \rangle_n$. Rapidly varying noise in RB is implemented via the VSG's external frequency modulation, whereby the frequency offset is encoded as a series of calibrated offset voltages on an arbitrary waveform generator [1] and supplied time-synchronous to each gate within a sequence. Again, $n = 200$ different realisations, each consisting of J samples, are applied to each RB sequence to extract a noise-averaged fidelity

---

[1] Keysight 33622A

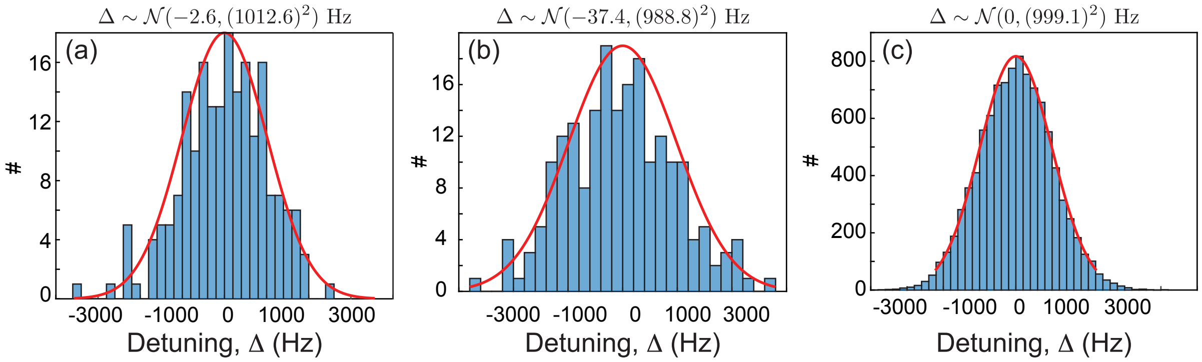

FIGURE 5.2. Real examples of engineered noise distributions used for randomised benchmarking with $\Delta/\Omega \sim \mathcal{N}(0, \rho^2)$ and $\rho = 1$ kHz/22.5 kHz. The distribution of detuning values are plotted for (a) 200 detuning values used for $n = 200$ individual realisations of a correlated noise process; (b) 100 values from a *single* realisation of rapidly varying noise, where the noise value changes with every gate for a sequence of $J = 100$ gates; and (c) all noise values from $n = 200$ noise realisations of rapidly varying noise applied to a $J = 100$ gate sequence (20,000 samples total). For all distributions, the actual sample mean and variance are displayed above the plot.

with rms $\rho = 1$ kHz/22.5 kHz $= 0.044$ (Fig. 5.2(b),(c)). Figure 5.2 shows examples of the real noise distributions employed in the experiment.

In the experimental implementation of GST, we implement constant noise of the same strength over all the sequences. In addition to a baseline experiment with no engineered noise, only a small set of noise detunings are implemented due to the large overhead imposed by sequence selection prior to execution. The values of detunings used for GST are shown in Table 5.1. The engineered error data for each of the 2737 sequences was acquired interleaved with the baseline $\Delta = 0$ case, such that the data sets are comparable and slow experimental drifts affect them equally. Due to overhead associated with switching between sequences, we recorded $r = 220$ repetitions for each sequence in direct succession.

Detuning Δ	$\delta = \Delta/\Omega$
75 Hz	0.33
500 Hz	2.2
1 kHz	4.4
1.4 kHz	6.2

TABLE 5.1. Engineered detuning values for GST with fractional errors normalised by Rabi frequency $\Omega = 22.5$ kHz.

The toolkit's authors advise to instead interleave sequences and repetitions to spread slow drifts across the data set in order to reduce model violations in the fitting routines [**178**].

5.2 Survival probability distributions for randomised benchmarking

In the limit of rapidly varying noise, all sequences of randomly ordered Clifford gates with length J are equivalent under noise averaging, and all sequence survival probabilities tend towards the mean. Recent theoretical studies have demonstrated that measurements on RB sequences in the presence of temporal noise correlations, can produce a divergence between average and worst-case reported trace fidelities [**165**, **175**]. Thus we find that measurement outcomes for different RB sequences are characterised by distributions with distinctly different shapes depending on the temporal correlations in the noise. The standard practice of combining all measurements to extract an average error per gate (EPG), p_{RB}, from the decay of the mean over all J-gate sequences as a function of J, results in a global ensemble average and does not take advantage of this information. That is, as the noise we implement exhibits temporal correlations, the value of p_{RB} one extracts may not be meaningful as a measure of average Clifford gate error. Our analysis takes advantage of the additional information which is always present in a RB experiment in order to evaluate the impact of noise correlations and deduce useful information about the underlying error process.

In our experimental study we measure the noise-averaged survival probabilities for a set of sequences $\{\boldsymbol{\eta}_i\}_J$, indexed by i and of length J, for different lengths $25 \leq J \leq 200$. We implement the same set of J-length RB sequences under application of either slowly or rapidly varying detuning noise. For an arbitrary individual sequence $\boldsymbol{\eta}_i$ and a single noise realisation, we perform r nominally identical repetitions of the experiment. We combine the information from the outcomes of these individual repetitions to produce a maximum-likelihood estimate of survival probability, $\mathcal{P}_i$. The use of multiple repetitions under identical conditions reduces quantum projection noise in the qubit measurement and assists in isolating specific quantitative contributions to the distribution of survival probabilities, though this is not possible without noise engineering. In general, we average measured outcomes over a fixed number of noise realisations, n, to yield the noise-averaged survival probability $\langle \mathcal{P}_i \rangle_n$ for a fixed sequence $\boldsymbol{\eta}_i$

Figure 5.3(a) shows the noise-averaged survival probabilities for each sequence with $k = 50$ sequence points per gate length. An exponential decay is fit to the noise-averaged mean values at each sequence

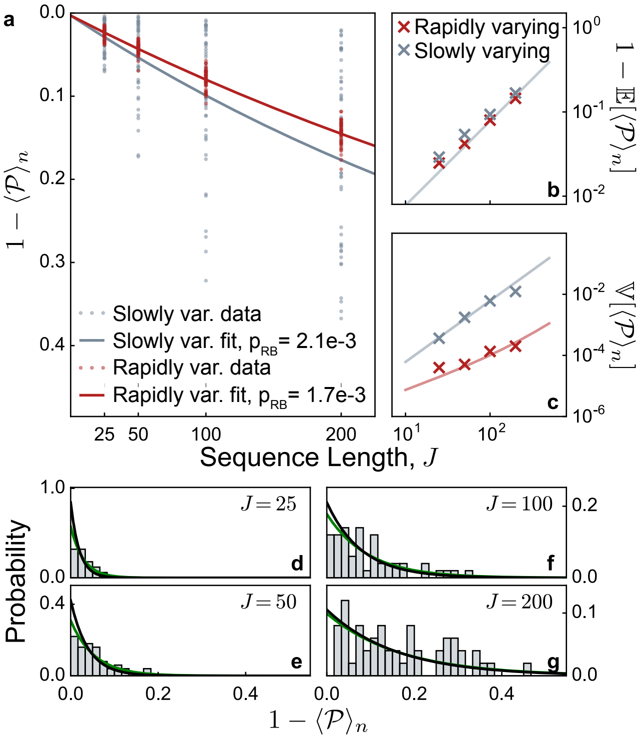

FIGURE 5.3. RB distributions over sequences in the presence of different noise correlations. **a** Standard RB protocol showing noise-averaged survival probability as a function of J for the same set of sequences implemented under slowly varying (grey) or rapidly varying (red) noise with $\rho = 0.044$. Each experiment is repeated $r = 25$ to $r = 30$ times under fixed conditions, and each survival probability is averaged over $n = 200$ noise realisations. Lines represent exponential fits to the mean survival probability used to extract the error-rate p_{RB}. **b-c** Scaling of the noise-averaged survival probability distribution expectation value and variance with sequence length J. Solid lines are theoretical predictions given the sequence length and noise strength ρ, with the theoretical expectation values coinciding for slowly and rapidly varying noise of the same strength. **d-g** Histograms for data in panel **a** in the presence of slowly varying noise. Black line: gamma distribution using input parameters calculated from first principles (see text). Green line: fitted gamma distribution with shape parameter fixed, $a = 1$. χ^2 values for calculated (fitted) gamma distributions are $\{0.354(0.091), 0.212(0.078), 0.241(0.204), 0.348(0.348)\}$.

length $\langle\overline{\mathcal{P}}(J)\rangle_n$ to calculate the average EPG p_{RB} using

$$1 - \langle\overline{\mathcal{P}}(J)\rangle_n = 0.5 - (0.5 - \kappa)e^{-p_{\mathrm{RB}}J} \tag{5.1}$$

where κ is the state preparation and measurement error (SPAM), found to be $\kappa = 3 \times 10^{-3}$ for both the rapidly and slowly varying noise. The fit is weighted by the variance over sequences for each J.

In the case of rapidly varying noise (red data points and fit) we observe the distribution of sequence outcomes is symmetrically spread around the sequence-averaged mean survival probability and the entire distribution shifts away from zero error with increasing J. The presence of slowly varying noise, by contrast, produces a broad distribution of measured $\langle\mathcal{P}\rangle_n$ over each set $\{\boldsymbol{\eta}_i\}_J$, demonstrating a positively skewed set of outcomes and the persistence of a long tail at higher error rates (lower survival probabilities). In this case, as J increases the distribution broadens and increases its mean, but remains skewed. Under both noise correlation cases, the measured $\langle\overline{\mathcal{P}}(J)\rangle_n$ remain approximately the same. The differences in the distribution of measured survival probabilities over sequences under these two noise models reproduces the central predictions of Ref. [**165**] and the previous chapter.

We compare the characteristics of the noise-averaged survival probability distributions against analytic predictions for both slowly and rapidly varying noise, beginning with the expectation and variance, $1-\mathbb{E}[\langle\mathcal{P}\rangle_n]$ and $\mathbb{V}[\langle\mathcal{P}\rangle_n]$ respectively (Fig. 5.3(b-c)). We find good agreement by taking only the applied noise strength as an input into a first-principles theoretical model modified for projective measurements (2D walk) and noise applied concurrently with gate implementation. More specifically, using Sections 4.3.2 and 4.3.3 from the previous chapter, the expectation and variance can be calculated from Eqns. (4.61)- (4.64), using the expected random walk steps in Table 4.2 for "Concurrent Detuning, 1 value per primitive (π or $\pi/2$) gate".

Theoretical predictions suggest that the distribution of outcomes under both noise models – as well as intermediate models described by coloured power spectra – should be well described by a gamma distribution [**165**]. The general gamma distribution probability density function is given by

$$\Gamma(a,b): \quad f(x)=\frac{x^{a-1}}{\Gamma(a)b^a}\exp\left[-\frac{x}{b}\right], \tag{5.2}$$

where a and b are the shape and scale parameters and $\Gamma(x)$ is the gamma function. The form of the gamma distribution will vary significantly between the limiting noise cases treated here, tending towards a symmetric Gaussian for rapidly varying noise and a broader positively skewed distribution in the presence of slowly varying noise, as determined by the values of a and b.

Figures 5.3(d-g) show histograms of RB sequence survival probabilities in the presence of the extreme case of slowly varying noise, quasi-DC miscalibration. We overlay gamma distributions calculated from first principles using no free parameters (black lines) using Eqn. (4.87)

$$\mathcal{I}=1-\mathcal{P}\sim\langle\Gamma\rangle_n\left(a=1,b=\frac{2J\rho^2}{3}\left(\frac{1}{2}+\frac{\pi^2}{96}\right)\right), \tag{5.3}$$

and alternatively by fitting a gamma distribution with $a = 1$ fixed while allowing b to vary as a fit parameter (green lines). The theoretical prediction captures both the measured skew towards high survival probabilities and the approximate “length” of the tail at low survival probabilities. We believe that residual disagreement between data and first-principles calculations arises due to both limited sequence sampling and contributions from higher-order analytic error terms when the approximation $J\rho^2 \ll 1$ is no longer valid. Importantly, data and theory show that the *mode* of the distribution for slowly varying noise is close to unity survival probability ($\langle \mathcal{P} \rangle_n = 1$) for all values of J and therefore corresponds to a lower error than the mean.

5.3 Modification of randomised benchmarking for identification of model violation

The fact that the distribution of sequence survival probabilities under slowly varying noise does not converge to the mean indicates sequence dependence in the resulting error accumulation. The emergence of this phenomenology is elucidated through an examination of the random walks for different sequences, beginning by considering the unscaled walk in two dimensions $\boldsymbol{V}_{\mathrm{2D}}$, calculated with unit-length steps. Certain sequences translate to walks with large displacements, $\|\boldsymbol{V}_{2D}\|^2$, hence amplifying the accumulation of error, while others tend back towards the origin and show reduced accumulated error (Fig. 5.4(a,b)). We classify sequences as “long-walk” if they possess a 2D projection beyond the diffusive mean-squared limit for an unbiased random walk, $\|\boldsymbol{V}_{2D}\|^2 > \frac{2}{3}J$.

To illustrate the link between the sequence walk in Pauli space and the noise-averaged survival probability, we plot the experimentally measured $1 - \langle \mathcal{P} \rangle_n$ for sequences of fixed length $J = 200$ against the calculated 2D walk length squared, $\|\boldsymbol{V}_{2D}\|^2$ in Fig. 5.4(c). Here, the random walk was calculated using the “interleaved dephasing” model presented in Section 4.2 modified to two dimensions for projective measurements[2]. Data are presented for both rapidly varying (red open markers) and slowly varying (grey solid markers) noise, where the same set of sequences is used for both noise models. Measurements for rapidly varying noise are fit with a line possessing a slope approximately consistent with zero, while for the same sequences under slowly varying noise, the measurements show a positive dependence on $\|\boldsymbol{V}_{2D}\|^2$ as expected. We believe the significant scatter in the plot is partially due to a concurrently acting

---

[2] At the time of writing this manuscript, the full theoretical model in the previous chapter had not been entirely developed. We relied on the interleaving dephasing model as a proxy for concurrent detuning noise in this particular demonstration.

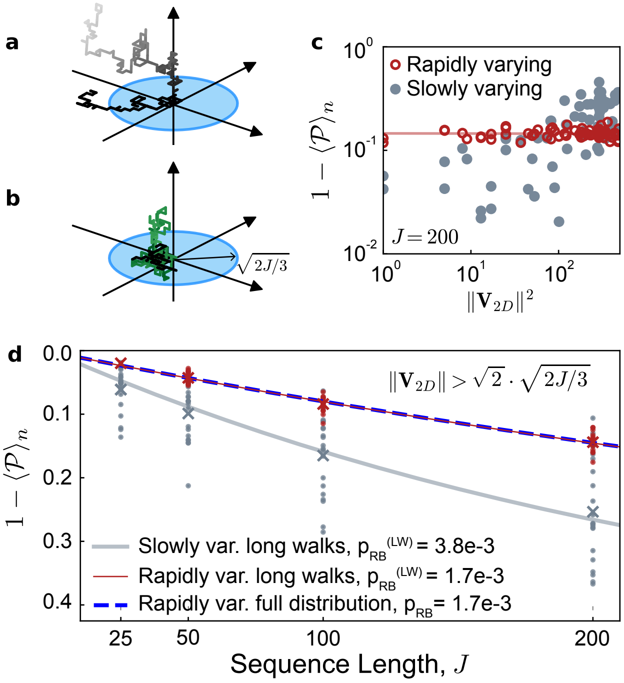

FIGURE 5.4. RB using long-walk sequences. **a-b**) Schematic representations of (a) "long" and (b) "short" unscaled walks $\boldsymbol{V}$ in 3D (coloured lines) and 2D (black lines). The short vs. long definition is set relative to a limit deduced from diffusive behaviour, as indicated by the blue circle, equal to $\sqrt{J}$ for 3D and $\sqrt{2J/3}$ for 2D walks. **c**) Noise-averaged survival probabilities for the same sequences as a function of walk length in the 2D plane $\|\boldsymbol{V}_{2D}\|^2$, when subject to slowly varying (grey) and rapidly varying (red) noise with linear fit overlaid. The slope of this fit is $(0.8 \pm 1) \times 10^{-5}$, consistent with zero. **d**) RB using pre-calculated long-walk sequences. Solid red line corresponds to RB performed using 20 long-walk sequences and rapidly varying noise. Extracted $p_{\text{RB}}^{(LW)}$ matches that extracted under the same conditions using an unbiased sampling of all sequences (dashed blue line). Grey line corresponds to RB using the same long-walk sequences and slowly varying noise. For the exponential fits, the SPAM is fixed to $\kappa = 3 \times 10^{-3}$.

noise source and higher-order contributions to error, neither of which are incorporated in the first principles calculation of the walk length. Nonetheless, the effect of sequence structure on measured survival probability is clearly visible for the case of slowly varying noise.

In aggregate, this phenomenology gives rise to the skewed gamma distribution under slowly varying noise described above, and the convergence of all individual sequence noise-averaged survival probabilities to the ensemble average when the noise is rapidly varying. However, pre-selection of RB sequences possessing large unscaled walk lengths also provides a mechanism to both identify the presence of temporally correlated errors and extract an RB outcome that more closely approximates worst-case errors.

In Fig. 5.4(d) we plot $1 - \langle \mathcal{P} \rangle_n$ against the sequence length for a subset of sequences pre-selected to possess long walks, whose error rates we denote $p_{(\mathrm{RB})}^{LW}$. For this demonstration, the long walk pre-selection condition is $\|\boldsymbol{V}_{2D}\|^2 > 2 \times \frac{2}{3} J$.

When these long-walk sequences are subjected to rapidly varying noise, the distribution of survival probabilities over sequences remains approximately Gaussian about the mean, and the expectation value over this subset closely approximates the expectation value over an unbiased random sampling of the 24^J possible J-gate sequences, $\langle \overline{\mathcal{P}}_{LW}^{\mathrm{rapid}}(J) \rangle_n \approx \langle \overline{\mathcal{P}}^{\mathrm{rapid}}(J) \rangle_n$. This can be seen in Fig. 5.4(d), comparing the red solid line for the long walk sub-selection and the blue dashed line for the full distribution results. However, in the presence of slowly varying noise we observe a larger mean in $\langle \overline{\mathcal{P}}_{LW}^{\mathrm{slow}}(J) \rangle_n$ (grey solid line) than that achieved with unbiased sampling. The difference between the sequence-averaged survival probabilities in these noise cases arises solely because of the intrinsic properties of the sequences in use.

Extracting an RB gate-error-rate, $p_{\mathrm{RB}}^{(LW)}$ from $\langle \overline{\mathcal{P}}_{LW}(J) \rangle_n$ in the presence of slowly varying noise, we typically find an increase $p_{\mathrm{RB}}^{(LW)} \sim 2$ - $5 \times p_{\mathrm{RB}}$ relative to standard sequence sampling, depending on the number of long-walk sequences employed, and the threshold value of $\|\boldsymbol{V}_{2D}\|^2$ used to define a "long walk". This approach effectively constitutes the construction of an RB protocol that increases the reported error rate by enhancing sensitivity to a particular noise type, which in our case is $\propto \hat{\sigma}_z$. Alternative sequences may also be calculated to enhance sensitivity to $\hat{\sigma}_x$ or $\hat{\sigma}_y$ noise compared to randomly selected RB sequences. These error enhancing sequences give a clear, qualitative signature of the violation of the assumption that the error process is uncorrelated in time, although we do not claim that such a signature is in general uniquely associated with the presence of temporal noise correlations. Furthermore, because calculation of $\|\boldsymbol{V}_{2D}\|^2$ and sequence pre-selection is performed numerically in advance, this approach alleviates the requirement to average extensively in experiment over sequences in order to reveal the skewed fidelity distribution.

5.4 Experimental GST in the presence of correlated noise

We now apply the sequence-dependent random walk framework to the default experimental GST gate set in order to understand the interplay of sequence structure and temporal noise correlations in the experimental GST estimation procedures. We begin by collating all standard experimental GST sequences up to $L = 256$ gates in length using gates $G_I \equiv \hat{\mathbb{I}}$, a $\pi/2$-length idle period identity, G_x, a $\pi/2$ rotation about $\hat{\sigma}_x$, and G_y, a $\pi/2$ rotation about $\hat{\sigma}_y$. We define sequences to include fiducial operations and germs (see Ref [**163**]), and calculate the corresponding walk lengths [3]. Here we assume unit step size under application of either a constant $\hat{\sigma}_z$ or $\hat{\sigma}_x$ unitary error process (Fig. 5.5(a,b)) such that $\|\boldsymbol{R}\|^2 = \delta^2 \|\boldsymbol{V}\|^2$, and plot $\|\boldsymbol{V}_{2D}\|^2$ as a proxy for projected sequence error vs. J. We overlay the results on the calculated probability distribution of unit-step walks for RB sequences, presented as a colour scale for comparison. Points appear clumped due to the experimental GST prescription using different fiducials (leading to different sequence lengths) surrounding a reported germ, as highlighted in Fig. 5.5(b).

Examining these data indicates that GST sequences used in the default package broadly sample the range of expected fidelities in the presence of strongly correlated $\hat{\sigma}_x$ errors, more effectively so than RB. However, their structure appears to systematically suppress measured errors in the presence of correlated $\hat{\sigma}_z$ errors. This mimics the positive skew of RB sequence survival probabilities in the presence of slowly varying noise, as observed in the colour scale. In the presence of correlated $\hat{\sigma}_z$ errors, only GST sequences consisting of repeated G_I germs, formally equivalent to Ramsey experiments [**179**], show sensitivity to this kind of error. We now explore the impact of these observations in further detail by both numerical investigations and experiments involving engineered unitary $\hat{\sigma}_z$ errors.

Given measurement outcomes (experimental or simulated) for the prescribed sequences, the open-source analysis package pyGSTi [**169**] extracts a large set of results characterising the gate set performance. One important metric calculated by the protocol for each gate is the diamond distance, $\|G_{\text{ideal}} - G_{\text{err}}\|_\diamond$, which is meant to provide a worst-case bound on the distance to the ideal gate operation. Experimental GST has found wide adoption in part because of its ability to calculate this metric, which is postulated to be important for formal analyses of fault-tolerance in the context of quantum error correction.

In our first test, we numerically probe the sensitivity of the experimental GST analysis procedure to correlated error using the aforementioned pyGSTi toolkit. We introduce constant $\hat{\sigma}_x$, $\hat{\sigma}_y$, or $\hat{\sigma}_z$ errors via concurrent unitary rotations added to the formerly ideal operations. Therefore the exact mathematical representation of each gate ($G_{I,x,y}$) is known from analytical transformations and we have two paths to evaluate gate performance (Fig. 5.5(c)). First, we directly calculate the diamond distance ($\|G_{\text{ideal}} - G_{\text{err}}\|_\diamond$) using the known matrix representation of G_{err} and maintaining the initial frame of reference. Second, we estimate it by employing pyGSTi to simulate data using G_{err} and determine the diamond distance ($\|G_{\text{ideal}} - G_{\text{err}}^{(\text{est})}\|_\diamond$) of the estimate $G_{\text{err}}^{(\text{est})}$ obtained by the toolkit's fitting routines.

---

[3] The walk was again calculated using an interleaved error model for either $\hat{\sigma}_z$ or $\hat{\sigma}_x$ errors

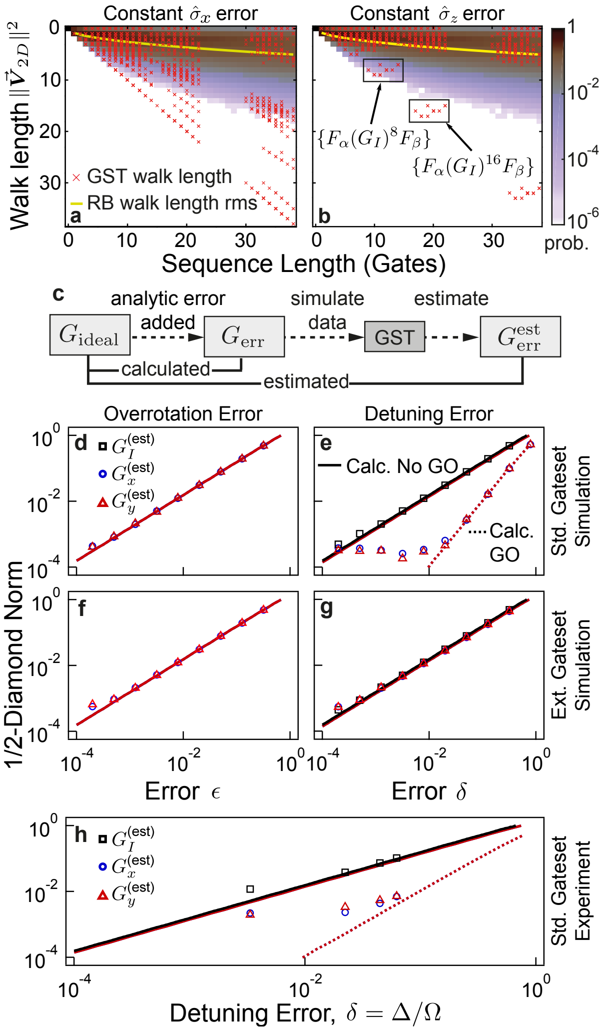

FIGURE 5.5. Demonstration of GST sensitivity to correlated error models. **a, b)** Sensitivity of GST sequences to $\hat{\sigma}_x$, $\hat{\sigma}_z$ interleaved errors using the length squared of the sequence-dependent walk vector $\|\boldsymbol{V}_{2D}\|^2$. GST sequence walks are shown as red crosses on a background colour scale illustrating the distribution over 10^6 randomly composed RB walks and their average (yellow line). Here gates are defined as constituent Clifford operations of length $\tau_{\pi/2}$. **c)** Flow diagram for the numerical analysis of the diamond norm estimation under correlated errors concurrent with gates G. **d, e)** Results of the analysis for the standard gate set G_I, G_x, G_y with the calculated diamond distance shown as solid lines (dashed lines) without (with) gauge optimisation on all graphs, and GST estimation depicted as symbols. Both over-rotation errors on the G_x, G_y gates (d) and concurrent detuning errors (e) are studied. **f, g)** Analysis is repeated by extending the gate set to include $-G_x, -G_y$. In panels (d) and (f) which employ only over-rotation errors, the calculated diamond distance for G_I vanishes and we do not show the noise floor for visual clarity. **h)** Experimental investigation of concurrent detuning $\hat{\sigma}_z$ errors via a deliberately engineered detuning Δ. Markers indicate GST estimates from experimental data and solid lines represent analytical calculations performed within the pyGSTi toolkit.

As a self-consistent QCVV implementation, the experimental GST estimation procedure incorporates a gauge optimisation by construction, as it makes no assumptions in regard to the qubit and its measurement basis. It performs two rounds of gauge optimisation, allowing identification of a frame in which to minimise the distance of the entire set of estimated gates in relation to the target gates. The relevance of this gauge freedom on RB-derived estimates of gate performance was highlighted recently in Ref. [**180**]. To illustrate how gauge freedom affects the results, we separately calculate the diamond distance with and without gauge optimising our analytic gate set G_{err} using routines included in the pyGSTi toolkit.

We plot the calculated and estimated diamond norms for $G_{I,x,y}$, subject to processes similar to either a constant over-rotation (i.e. proportional to $\hat{\sigma}_x$ or $\hat{\sigma}_y$ depending on the gate in question, with no error on G_I operations such that the ideal rotation angle, $\theta \to (1+\epsilon)\ \theta$), or a constant detuning error (i.e. proportional to $\hat{\sigma}_z$), as shown Fig. 5.5(d,e). Here we see that the estimated diamond distance for operators $G_{I,x,y}$ closely matches the calculated value in the presence of numerical over-rotation errors. When used with its standard gate set $\{G_x, G_y, G_I\}$, pyGSTi's estimate of G_x and G_y errors arising from constant unitary $\hat{\sigma}_z$ errors differs significantly, however, and only the diamond norm estimate for G_I appears similar to the directly calculated value. Other estimated quantities such as process infidelity and the associated Choi matrices are affected in a similar way. However, performing gauge optimisation on the analytically calculated matrices G_{err} as well (within the pyGSTi package) reduces the difference in the reported diamond distance for $\hat{\sigma}_z$ errors, and produces agreement with the much lower $G_{x,y}$ diamond distance reported by the GST estimation procedure (Fig. 5.5(e)). Among the error models we have tested for this gate set, such behaviour is only manifested in the presence of temporally correlated $\hat{\sigma}_z$ errors and does not appear using various other error processes built into the pyGSTi analysis package. We note that full gauge optimisation is a requirement for self-consistency of results within GST.

To further investigate the influence of the gauge degree of freedom, we repeat our numerical analysis under the application of identical unitary errors, but extend the gate set by adding negative rotations $-G_x$, $-G_y$ corresponding to $-\pi/2\ \hat{\sigma}_x$ and $\hat{\sigma}_y$ rotations and incorporating a number of associated compound germs (Fig. 5.5(f,g)). The resulting gauge-optimised calculated and estimated diamond-distance values now increase, moving closer to the analytic calculation obtained *without* gauge optimisation. The behaviour of estimated diamond distances for operations $-G_x$ and $-G_y$ are indistinguishable from those presented to within numerical uncertainty. This simple change in the gate set directly reveals the role of gauge optimisation in the discrepancies we noted above. The additional information now available to experimental GST via the extended gate and germ set effectively constrains the optimisation procedure, allowing it to detect errors that could previously be absorbed in a gauge transformation.

We follow up on these numerical investigations by performing experiments using experimental GST sequences subjected to engineered unitary $\hat{\sigma}_z$-errors of varying strength. As before, we generate an operation with known error magnitude and form, allowing us to directly produce a matrix representation for the gate and hence calculate the diamond distance for the (deliberately) imperfect gates we apply to our trapped-ion system. Again the experimental GST procedure produces an estimate of the diamond distance that matches the calculation for G_I, but yields estimates of the diamond distance from experimental data approximately an order of magnitude below the (un-optimised) calculated value for $G_{x,y}$ (Fig. 5.5(h)). Allowing gauge optimisation on the calculated diamond distance changes its scaling with error magnitude as in simulations above. We do not find strong agreement between data for $G_{x,y}$ and this gauge-optimised scaling, but cannot exclude the possibility that other finite sampling effects may cause saturation of small reported diamond distances.

5.5 Discussion

In our studies we have employed a simple analytic framework - a formalism mapping noise to error accumulation in sequences of Clifford operations - to explore the sensitivity of RB and GST to slowly varying noise processes. Theoretical predictions derived from this framework match RB experiments employing engineered noise with known characteristics: either slowly varying or rapidly varying on the sequence timescale. This highlights the utility of the random-walk analysis in determining sequence-dependent sensitivities of QCVV protocols in the presence of temporally correlated noise.

We have compared RB survival probabilities over sequences to a gamma distribution $\Gamma(a = 1, b)$, where b is determined by the type of error model employed in the experiment, and shown good agreement using no free parameters. In addition we have demonstrated that in the presence of slowly varying noise, the mode of the distribution of survival probabilities over sequences is shifted towards lower error rates than the mean and that a long tail of high-error outcomes appears as predicted in Ref. [**165**].

Overall, the experiments reported here give a clear experimental signature of the violation of the assumption that errors between gates are independent. While we do not claim that the features we observe are in general uniquely derived from this interpretation, we hope these results may help experimentalists seeking to interpret complex RB data sets. We believe that more detailed reporting of RB outcomes including the publication of distributions of the survival probability $\mathcal{P}$, as well as the sequences employed, will facilitate more meaningful comparisons between RB data sets derived from different physical systems, as the relevance of p_{RB} is diminished when error processes exhibit temporal correlations.

Through a combination of analytic calculations, numerics, and experiments with engineered errors we have found a similar bias towards lower estimates of diamond distance in experimental GST procedures when using the standard $G_{I,x,y}$ gate set subjected to strongly correlated, unitary $\hat{\sigma}_z$ errors. The asymmetry we observe between the manifestation of correlated $\hat{\sigma}_x/\hat{\sigma}_y$ and $\hat{\sigma}_z$ error-sensitivity has previously only been reported in the context of randomised benchmarking [**180**]. We have shown explicitly how the low diamond-distance estimates under this kind of noise are related to the gauge optimisation performed as part of the protocol; limiting the gauge freedom by extending the gate set under application of an identical error process dramatically changed the estimated diamond distance of the very same gates in numerical simulations. This highlights that estimates are always reported up to an implicit gauge degree of freedom, making absolute comparisons of diamond norms challenging.

These observations are commensurate with a simple physical interpretation of the effect of an optimised gauge transformation in the circumstances we examine. In the presence of correlated $\hat{\sigma}_z$ errors, when the gate set is limited to $G_{I,x,y}$ gates, the reconstructed operator includes an extra error component along the z-axis. The effect of gauge optimisation is to rotate the axis of rotation of the G_x and G_y operators back to the equatorial plane, effectively cancelling this error. Under this circumstance the magnitude of rotation of these gates is smaller than expected in a fixed lab frame, and the second-order nature of the residual errors result in a steeper gradient of the dotted line in Fig. 5.5(e). In contrast the G_I rotation should have no net rotation and therefore this error will not be cancelled by a simple gauge transformation.

Gauge optimisation is designed to produce the best estimate for errors over the entire gate set in relation to a given target, and in a sense acts to "distribute" nominal errors over all constituent rotations in the gate set. The validity of such a gauge transformation in the presence of independent protocols for establishing a measurement basis remains an open question and has been highlighted recently by Rudnicki et al. [**181**]. The variation of calculated and estimated diamond distances under correlated $\hat{\sigma}_z$ errors when subjected to seemingly small modifications of the default gate set has again not been reported previously in the context of GST, and indicates an important dependence of its output on the specific gate set employed, the characteristics of the underlying error source, and the gauge optimisation procedure.

Clearly the observed performance of experimental GST in the presence of correlated $\hat{\sigma}_x$ noise, such as resulting from experimental over-rotations, can make GST a valuable tool in debugging an experimental system [**182**], although precise calibrations can also be carried out efficiently using a subset of the full experimental GST protocol [**183**]. The effect of gauge optimisation in the presence of $\hat{\sigma}_z$ errors and with use of the default gate set, however, is concerning as a key implied benefit of experimental GST is its ability to provide a rigorous upper bound on gate errors using a fully self-contained analysis package. Recent experimental work [**163**] on the topic claimed such upper bounds on gate errors using experimental GST and compared these to the fault-tolerance threshold with high reported confidence and tight uncertainties. The results above and observations made [**181**] suggest that there may be residual uncertainty in interpretation of such data due to the potential unresolved conflict between full gauge freedom and the nominal existence of a measurement basis constraining that freedom. Furthermore, when acquiring and evaluating data, care has to be taken to to suppress any form of model violations reported by the GST toolkit in its likelihood analysis, as otherwise the extracted performance metrics may become unreliable. These deviations are currently not reflected in the uncertainties (i.e. error bars) calculated for those metrics by the toolkit and discussions with its authors suggest that a connection between the two is a non-trivial process.

In light of the investigations reported here, we believe that there is a need for greater awareness of the subtleties of the use of both RB and GST in the presence of temporally correlated noise environments. In order to enhance the meaning and utility of reported results we advocate that QCVV benchmarks such as p_{RB} and experimental GST diamond distances should be reported together with a quantitative measure of violation from a purely Markovian, temporally uncorrelated model. In the case of RB, this could be the difference between the extracted p_{RB} of long and short walk sequences; in experimental GST the deviation is already being reported as part of the routine, yet the question about the impact of gauge optimisation that we identified remains. Similarly, if using experimental GST as a standalone gate evaluation procedure one cannot know a priori the form of the underlying noise – and hence any associated experimental GST insensitivities. Increasing the rigour of resultant upper bounds on diamond distances could require performing experimental GST using multiple different gate sets to identify potential “blind spots”, owing to the implicitly required gauge transformations. Given the experimental overhead, however, this brute force approach is not necessarily attractive and further modifications to experimental GST could resolve the issue with greater efficiency. Overall, we hope that these observations will assist in both the interpretation of QCVV experiments when model violation may occur, and the development of new techniques with improved rigour and efficiency for larger scale systems.

CHAPTER 6

Dynamically corrected gates suppress spatio-temporal error correlations as measured by randomised benchmarking

---

"You were sick, but now you're well again, and there's work to do."

- Kurt Vonnegut, *Timequake*

*In this chapter, I present a first-principles analysis of the manifestation of error correlations in randomised benchmarking, and validate this model through experiments performed using engineered errors. Furthermore, I demonstrate that the use of dynamically corrected gates (DCGs), generally considered for the reduction of error magnitudes, can also suppress error correlations in space and time throughout quantum circuits. This work is reproduced with minimal changes from "Dynamically corrected gates suppress spatio-temporal error correlations as measured by randomised benchmarking" published in Phys. Rev. Research 2, 013156 (2020) [**4**].*

Suppressing and correcting errors in quantum circuits is a critical challenge driving a substantial fraction of research in the quantum information science community. These efforts build on quantum error correction (QEC) and the theory of fault tolerance [**18, 184–188**] as the fundamental developments that support the concept of large-scale quantum computation [**189–191**]. In combination, these theoretical constructs suggest that so long as the probability of error in each physical quantum information carrier can be reduced below a threshold value, a properly executed QEC protocol can detect and suppress logical errors to arbitrarily low levels, and hence enable arbitrarily large computations. Underlying this proposition is an assumption that errors are statistically independent, i.e., the emergence of a qubit error at a specific time is uncorrelated with errors arising in other qubits or at any other time in the computation. Error correlations that decay with distance between qubits (spatially) can induce simultaneous multi-qubit errors [**192**], and correlations that decay with circuit length (temporally) have been shown to produce more rapid accumulation of net circuit errors [**156, 180**].

The practicality of the assumption of uncorrelated errors has long been questioned, as laboratory sources of noise commonly exhibit strong temporal correlations, captured through spectral measures exhibiting high weight at low frequencies. As such, coherent errors induced by low frequency noise and miscalibrations have recently become a larger focus of research, with their detrimental effects on QEC implementations being examined [**156**, **193**–**195**] and first ideas targeting their suppression emerging [**196**, **197**]. Attempts to address these errors in the theory of quantum error correction are challenging and results to date suggest that revision of postulated fault-tolerant thresholds may be required [**198**, **199**] relative to more optimistic predictions that have recently emerged [**200**]. Indeed, when implicit assumptions that errors are both spatially and temporally uncorrelated are weakened, the value of a tolerable error threshold can change from some value ε to ε^2, easily leading to order-of-magnitude decreases in the acceptable error rates [**189**].

The adverse effect of correlated errors on error correction procedures has been observed in the context of a repetition code both experimentally [**201**] – where they were seen to effectively negate any advantage obtained from iterative error correction – and theoretically [**193**], where an increase in the logical failure rate was identified. Furthermore, while a recent full-scale numerical simulation has shown that coherent errors at the physical layer can, in fact, be overcome by topological error correcting codes [**36**], large numbers of physical qubits are required with error rates that are *uniformly* sub-threshold. The emerging message is that, while correlated errors do not invalidate the use of QEC, their presence can significantly increase the requisite overhead, and may reduce the tolerable magnitude of physical qubit errors.

In this manuscript, we demonstrate experimentally that using a low-level abstraction known as a dynamically corrected gate (DCG), we can suppress error correlations in addition to error magnitudes. Replacing “primitive” physical quantum gate operations with logically equivalent DCGs [**202**–**206**] forms a “virtual” layer wherein error characteristics can be modified (“virtualised”) before the application of QEC [**207**, **208**]. We present a novel first-principles analysis of Clifford randomised benchmarking [**166**, **209**] in order to quantitatively model the impact of error correlations on simple experimental observables, building on concepts in Ref. [**165**] and Chapter 4. Specifically, we identify that error correlations are manifested in the scaling of the distribution over sequence randomisations, at fixed sequence length, with measurement averaging. We validate this framework using randomised benchmarking experiments performed with a single trapped Ytterbium ion. We then demonstrate that the replacement of the individual Clifford operations within each sequence with logically equivalent DCGs modifies the error correlation signatures such that they are experimentally consistent with the presence of uncorrelated errors. Single-qubit experiments performed under engineered noise with tunable correlation characteristics show consistent reduction in the correlated error component when switching from primitive to DCG sequences. We explain this behaviour using a framework that describes the action of DCGs at the operator level [**206**, **210**, **211**] as whitening the effective error spectrum experienced by each gate. Finally, we demonstrate that using DCGs in sequence construction reduces spatial error correlations between qubits, through simultaneous randomised benchmarking on five trapped ion qubits. These results provide direct and strong evidence that the use of dynamically protected physical qubit operations in a layered architecture for quantum computing [**208**] can facilitate the successful application of existing QEC theory with only minimal revision on the path to fault-tolerant quantum computation.

6.1 Identifying signatures of error correlations in circuits

We begin by laying out the challenge of establishing clear quantitative metrics allowing the identification of error correlations in quantum circuits. The types of correlated errors treated here concern unitary, coherent errors that can be represented by additive environmental coupling terms (e.g., dephasing noise) or fluctuating control field terms in the system Hamiltonian. In general, such error channels exhibit strong temporal correlations when they are induced by coloured noise spectra or systematic drifts in control parameters due to insufficiently precise or too infrequent calibrations. Correlated errors between gates can also be caused by incoherent error channels when considering, for example, changes in T_1 times, which lead to slow variations of fundamental gate error rates. We do not consider the latter form of correlated errors here; however, it is worth noting that they can also lead to detrimental and non-Markovian behaviour in gate performance.

As a first step we analyse how correlations in a physical noise process translate to correlations in the resultant unitary errors within a circuit of J gates, with gates indexed by j. In our model, any noisy operation $\tilde{U}_j$ within the circuit can be decomposed into the ideal operator $\hat{U}_j$ and an error operator $\hat{\Lambda}_j$, such that $\tilde{U}_j = \hat{\Lambda}_j \hat{U}_j$. Here, $\hat{U}_j \equiv \hat{U}(\boldsymbol{n}_j, \theta_j)$ rotates the qubit state vector by angle θ_j around an arbitrary axis $\boldsymbol{n}_j$ on the Bloch sphere. Considering unitary semi-classical noise processes, the error component in each operation can be written as $\hat{\Lambda}_j = \exp\{i \sum_{\alpha=1}^{\infty} [\boldsymbol{\epsilon}_j]_\alpha \cdot \hat{\boldsymbol{\sigma}}\}$, with $\hat{\boldsymbol{\sigma}}$ the vector of Pauli matrices, α an index denoting the Magnus expansion order [**212**], and $\boldsymbol{\epsilon}_j$ the error vector characterising the strength and nature (affected quadrature) of the error [**211**–**214**]. A quantum circuit experiences temporally correlated errors if the values of $\boldsymbol{\epsilon}_j$ across the circuit (in space or time) exhibit non-zero correlations.

Our approach to measuring error correlations is built on common quantum verification protocols employed to infer the average behaviour of gate operations [**156**, **162**, **163**, **209**, **215**–**222**]. Restricting our analysis to the single-qubit case, error correlations between gates may occur in these protocols when physical noise processes exhibit strong correlations in time. We demonstrate this numerically by calculating the error vector $\boldsymbol{\epsilon}_j$ for each operation in a single-qubit randomised benchmarking sequence exposed to detuning ($\hat{\sigma}_z$) noise with a variable block-correlation length, $\mathcal{M}_{\mathrm{n}}$; this is defined to be the number of gates over which the noise strength is constant within the sequence. The sequence is assembled from the 24 Clifford operations comprising combinations of π and $\pi/2$-rotations about the x, y and z-axes of the Bloch sphere, and an identity gate $\hat{\mathbb{I}}$. Calculating the autocorrelation function of the error vector's magnitude throughout a sequence reveals strong correlations over a length of gates, $\mathcal{M}_{\varepsilon}$, which appear to scale linearly with the correlation length of the input noise process, $\mathcal{M}_{\mathrm{n}}$ (Fig. 6.1c). This behaviour suggests a linear mapping from noise correlations to error correlations in conventional settings. As a prelude to future demonstrations in this manuscript, we note that if the individual Clifford gates are replaced by DCGs, this simple linear mapping from input noise correlations to output error correlations breaks down.

In general, the primary limitation one faces in accessing information about $\mathcal{M}_{\varepsilon}$ in a physical experiment is that using standard, projective measurements at the end of a circuit will limit the ability to probe correlations that arise throughout the circuit's execution. Most experimental quantum verification routines suffer from exactly this limitation, and primarily measure the average difference between a qubit state transformed under an imperfect operation and a predetermined target state at the end of the protocol (Fig. 6.1a). However, as we will illustrate in the following, there is additional useful information present in the outcomes of randomised benchmarking measurement routines that may be employed to extract novel insights about error correlations appearing during the sequence.

The key underlying concept is that in a randomised benchmarking sequence built up from many operations, the resultant net state transformation in the presence of noise, $\tilde{U}_{\text{eff}} |\psi\rangle$ (Fig. 6.1b), is determined by an interplay of both the sensitivity of each individual operation to the noise [**212**] and the impact of the sequence structure on error accumulation [**165**, **221**, **223**]. Specifically, nominally equivalent randomised benchmarking sequences (constructed to perform the same net operation) exhibit variations in correlated-noise susceptibility that are analytically calculable and verifiable in experiments. We use this variability and the behaviour under experimental averaging to extract a signature of error correlations within quantum sequences.

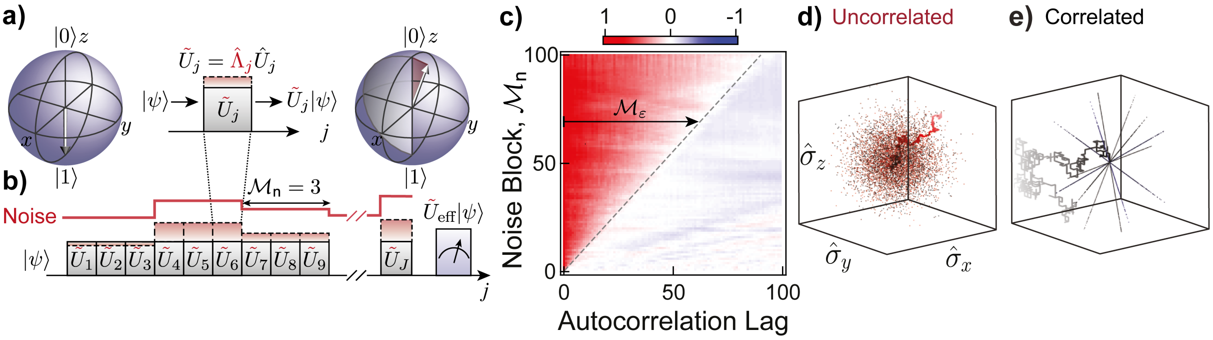

FIGURE 6.1. **Translation of noise correlations to error correlations in quantum circuits. a,** A single operation applied to a qubit in the presence of noise $\tilde{U}_j$ can be decomposed into an error operator $\hat{\Lambda}_j$ and the target operation $\hat{U}_j$. Bloch spheres schematically illustrate the effect of an imperfect π-rotation about the x-axis acting on input state $|1\rangle$, with dark shading indicating an over-rotation error. **b,** Noise (red line) exhibiting non-zero temporal correlation of length $\mathcal{M}_{\rm n} = 3$, quantised in units of gate operations, acts on a quantum circuit composed of sequentially applied unitary operations. The resultant errors accumulate and lead to a noisy effective operator $\tilde{U}_{\rm eff}$, whose effect is determined through a projective measurement at the end of the circuit. **c,** Translation of correlations in a noise process to correlations in the magnitude of the circuit error vector, $||\boldsymbol{\epsilon}_j||$. The error vector for each gate of a randomly composed sequence of 1000 primitive gates under a noise process with noise correlation length $\mathcal{M}_{\rm n}$ is calculated and the autocorrelation function of the magnitude of the error vector, $\mathbb{E}\left[||\boldsymbol{\epsilon}_{j_1}||\,||\boldsymbol{\epsilon}_{j_2}||\right]$, is shown for the first 100 gates. **d, e,** Random walks for the extreme error correlation cases, **d,** $\mathcal{M}_\varepsilon = 1$ (uncorrelated) and **e,** $\mathcal{M}_\varepsilon = J$ (fully correlated). Final walk displacements of eight sequences, each with 1000 error realisations, are shown along with the full walk for a single sequence that is common between the two cases.

6.1.1 Random walk formalism for error accumulation

We present a first-principles analysis to directly link measurement outcomes for single-qubit randomised benchmarking sequences to the nature of the underlying error correlations quantified by $\mathcal{M}_\varepsilon$, expanding the formalism introduced in Ref. [**165**]. We consider randomised benchmarking sequences composed of J single-qubit Clifford operations, $\prod_{j=1}^{J} \hat{C}_{\eta_j} = \hat{\mathbb{I}}$, with the vector $\boldsymbol{\eta}$ containing labels for the 24 Clifford operations, $\eta_j \in \{1, 2, \ldots, 24\}$. A final gate is pre-calculated to yield a net identity operation for the sequence, such that in the absence of error the final qubit state will be the same as the initial state. Due to imperfections in the operations, the physically implemented gates $\widetilde{C}_{\eta_j}$ differ from the ideal gates by an error map $\widetilde{C}_{\eta_j} = \hat{\Lambda}_{\eta_j} \hat{C}_{\eta_j}$.

The accumulation of errors throughout a sequence can be represented by a sequence-dependent "random walk" in three-dimensional Pauli-error space; the net walk length can then be related to the final sequence error [**165**]. For a particular realisation of the error i, this walk is captured by the vector

$$\boldsymbol{R}^{(i)}_{3\text{D}} = \sum_{j=1}^{J} \varepsilon^{(i)}_j \boldsymbol{r}_{3\text{D},j} \tag{6.1}$$

with gate error values $\varepsilon^{(i)}_j \sim \mathcal{N}(0, \sigma^2)$ sampled from a zero-mean Gaussian distribution with rms value σ. It will be shown in Section 6.1.3 that this leads to an average, randomised benchmarking error per gate $\propto \sigma^2$. The values of $\boldsymbol{r}_{3\text{D},j}$ define the sequence-specific random walk steps; they can be calculated deterministically for any randomised benchmarking sequence, irrespective of the strength or correlation characteristics of the gate errors. If the noise is gate independent and single axis, then the values of $\boldsymbol{r}_{3\text{D}}$ are unit-length steps. As discussed in Section 4.3.2, more complex models can be similarly modelled with step lengths that are not necessarily unit-length, i.e. $\|\boldsymbol{r}_{3\text{D}}\| \neq 1$.

In a circumstance where the normalised error takes a consistent value $\varepsilon^{(i)}_j \equiv 1$, the length of the J-step walk created by these steps $\|\boldsymbol{V}_{3\text{D}}\|$ is an intrinsic property of the sequence and will be shown to act as a proxy for its susceptibility to correlated errors. Examining individual randomised benchmarking sequences reveals the idiosyncratic nature of their walks; certain randomisations exhibit long walks, while others have walks that terminate near the origin, solely determined by the structure of the sequence and the form of the error channel. Accordingly, in the presence of correlated errors we expect a wide variance of outcomes, determined by the underlying structures of the randomly selected sequences. The general framework linking this Pauli walk to accumulated error was experimentally validated in Chapter 5, published in Ref. [**221**].

6.1.2 Signatures of error correlations

We identify that the key measurable signature of error correlations arises in the process of experimental averaging over repetitions of a sequence, and hence over different realisations of the error. In order to understand this, we begin by examining how error correlations impact the random walk introduced above, and how the behaviour of that walk changes with experimental averaging.

Gate errors induce the mapping $\boldsymbol{r}_{3\text{D},j} \rightarrow \boldsymbol{R}^{(i)}_{3\text{D}}$; the term $\varepsilon^{(i)}_j$ in Eqn. (6.1) can change the direction and scale the magnitude of each step in the random walk. Thus correlations in $\varepsilon^{(i)}_j$ are translated into correlated modifications of the steps in $\boldsymbol{R}^{(i)}_{3\text{D}}$. To see the effect of correlations in the error process, we calculate the locus of walk termination points for eight different sequences and 1000 error realisations, shown in Fig. 6.1d,e. In the presence of errors whose magnitudes are constant across all gates in a given benchmarking sequence, the error $\varepsilon_j^{(i)} \equiv \varepsilon^{(i)}$ rescales all steps in the walk uniformly, such that all termination points for a given sequence fall on a line (Fig. 6.1e). The walk terminations for the same sequence are thus dominated by the underlying sequence structure ("rays" in Fig. 6.1e). By contrast, in the presence of uncorrelated errors where $\varepsilon_j^{(i)}$ changes randomly for each step, the termination points appear randomly distributed in Pauli space for different realisations of the error (Fig. 6.1d).

These differences will manifest in an experiment that averages the experimental performance of a set of sequences over many different realisations of an error-inducing noise process. In the case of correlated errors, the preservation of sequence-structure dependence in the sequence error leads to a broad distribution of outcomes over different randomised benchmarking sequences. This breadth is maintained even when averaging experiments together over various realisations of the random but temporally correlated errors. In contrast, for uncorrelated errors, the random, formless distribution of walk termination points over the same set of sequences implies that averaging over experiments would result in a spread of outcomes that grows narrower as the experiment number increases, consistent with the central limit theorem. It is therefore in the distribution over measured results of noise-averaged, randomised benchmarking sequences that the signatures of error correlations between gates within a sequence will appear. In Sections 6.1.3 and 6.1.4 we will describe how this phenomenology can be accessed through a modified analysis of conventional randomised benchmarking experiments.

6.1.3 Mapping to measurable quantities

We now link the random-walk framework to measurements commonly performed in the laboratory – a single projective measurement in the qubit basis. Such measurements are unaffected by rotations about the z-axis, i.e., they are phase invariant. Consequently, this type of projective measurement is insensitive to the component of the random walk oriented along the $\hat{\sigma}_z$-axis, and instead probes a two-dimensional projection of the walk onto the $\hat{\sigma}_x\hat{\sigma}_y$-plane of Pauli-error space [**221**]. Considering a measurement routine involving averaging a single sequence over n realisations of the error, we may relate the two-dimensional walk length to the projective measurement results as,

$$\langle \mathcal{P} \rangle_n = 1 - \langle \| \boldsymbol{R}_{\text{2D}} \|^2 \rangle_n + \mathcal{O}\left(\sigma^4\right), \tag{6.2}$$

where $\langle \cdot \rangle_n$ is an average over n instances of the error process, $\langle \mathcal{P} \rangle_n := 1 - \langle P(|1\rangle) \rangle_n$ is the measurable, noise-averaged sequence "survival probability" when the qubit is initialised in the state $|0\rangle$, σ is the rms of the normally distributed errors, and $\boldsymbol{R}_{\text{2D}}$ denotes the random walk in the $\hat{\sigma}_x\hat{\sigma}_y$-plane of Pauli-error space. For simplicity, we will proceed by referring to $\boldsymbol{R}_{2\mathrm{D}}$, and its individual steps $\boldsymbol{r}_{2\mathrm{D},j}$, simply as $\boldsymbol{R}$ and $\boldsymbol{r}_j$ respectively.

We analyse in detail three distinct error correlation regimes for a unitary error channel with values $\varepsilon_j^{(i)} \sim \mathcal{N}(0, \sigma^2)$: (i) $\mathcal{M}_\varepsilon = J$, identically correlated errors with fixed, constant magnitude over a sequence and rms value σ_C, $\varepsilon_C \sim \mathcal{N}(0, \sigma_C^2)$; (ii) $\mathcal{M}_\varepsilon = 1$, uncorrelated, normally distributed errors that change randomly between each gate in a sequence with rms value σ_U, $\varepsilon_U \sim \mathcal{N}(0, \sigma_U^2)$; and (iii) statistically independent, contemporaneous correlated and uncorrelated error processes such that the relative strengths σ_C and σ_U determine the effective error correlation length.

The expression for survival probability in Eqn. (6.2) can be used to calculate the distribution of survival probabilities without modification for both regime (i) and (ii) simply by using the appropriately calculated random walks. In the limit of long sequences and many noise averages (large J and n), the noise-averaged survival probability is Gamma distributed over different, nominally equivalent, sequence randomisations [**221**]; the shape and scale parameters of the distribution, a and b respectively, can be calculated from first principles using the particulars of the sequence, noise averaging, and error characteristics. For these two limiting cases of identically correlated errors over a sequence and uncorrelated errors changing randomly between gates, the respective survival probabilities are sampled from Gamma distributions shaped according to

$$\langle \mathcal{P}_C \rangle_n \sim \Gamma(a = 1, b = \tfrac{2}{3} J \sigma^2), \tag{6.3a}$$

$$\langle \mathcal{P}_U \rangle_n \sim \Gamma(a = n, b = \tfrac{2}{3n} J \sigma^2). \tag{6.3b}$$

From these expressions, the variance and expectation values of the distribution over sequence randomisations can be calculated. To leading order, both distributions exhibit the same mean value $\mathbb{E} = ab$, giving a randomised benchmarking average gate error of $\frac{2}{3}\sigma^2$. However, the distributions diverge in the second moment $\mathbb{V} = ab^2$.

We may now derive the properties of the distribution associated with regime (iii) by considering two independent walks; one is induced by the correlated error component $\boldsymbol{R}_C^{(i)}$, and the other by the uncorrelated component $\boldsymbol{R}_U^{(i)}$. To begin, it is convenient to note that in the case of a correlated, fixed error process over a sequence, it is possible to factor out the constant error strength from the random walk for

Error Type	$1-\mathbb{E}\left[\langle\mathcal{P}\rangle_n\right]$	$\mathbb{V}\left[\langle\mathcal{P}\rangle_n\right]$
(i) Fully Correlated, $\mathcal{M}_\varepsilon = J$	$\frac{2}{3}J\sigma_C^2$	$\frac{2}{9}\frac{(n+2)}{n}J(2J-1)\sigma_C^4$
(ii) Uncorrelated, $\mathcal{M}_\varepsilon = 1$	$\frac{2}{3}J\sigma_U^2$	$\frac{2}{9n}J\left(4+2J+n\right)\sigma_U^4$
(iii) Correlated + Uncorrelated	$\frac{2}{3}J(\sigma_U^2+\sigma_C^2)$	$\mathbb{V}\left[\langle\mathcal{P}_U\rangle_n\right]+\mathbb{V}\left[\langle\mathcal{P}_C\rangle_n\right]+\frac{4}{9}J\sigma_C^2\sigma_U^2$

TABLE 6.1. The statistical moments for the distribution of noise-averaged sequence survival probabilities with different error correlation lengths – fully correlated across the sequence, completely uncorrelated values between gates, and a combination of two independent error processes in the same quadrature, one correlated and one uncorrelated. The variance for case (iii) incorporates contributions from each error source individually, $\mathbb{V}\left[\langle\mathcal{P}_C\rangle_n\right], \mathbb{V}\left[\langle\mathcal{P}_U\rangle_n\right]$, as well as a cross-term.

a particular realisation of the error [**165**],

$$\boldsymbol{R}_C^{(i)} = \varepsilon_C^{(i)}\sum_{j=1}^{J}\boldsymbol{r}_j = \varepsilon_C^{(i)}\boldsymbol{V}. \tag{6.4}$$

We thus introduce $\boldsymbol{V}$ to describe the two-dimensional sequence-specific walk, defined by the steps $\boldsymbol{r}_j$ that remain invariant under different realisations of the error process (Fig. 6.1e). This separability is not achievable in the presence of uncorrelated errors due to the randomisation of each step in the walk by the error process. The expression for survival probability can then be expanded in terms of these independent walks to second order in σ_C, σ_U as

$$\begin{aligned}\langle\mathcal{P}\rangle_n &= 1-\langle\|\boldsymbol{R}_U^{(i)}+\varepsilon_C^{(i)}\boldsymbol{V}\|^2\rangle_n\\ &= 1-\langle\|\boldsymbol{R}_U^{(i)}\|^2\rangle_n-\sigma_C^2\|\boldsymbol{V}\|^2,\end{aligned} \tag{6.5}$$

where the cross-term is identically zero using $\langle\varepsilon_C^{(i)}\rangle_n = 0$.

For all three correlation regimes, higher-order terms and cross-terms contribute to the second moment of the distribution and have been calculated analytically (Table 6.1). These terms reduce to those calculated using the Gamma distributions in Eqn. 6.3 in the limit of large J and n, with $J \gg n$. On inspection, we expect that in the presence of uncorrelated errors the variance will narrow with increasing n, while it will remain fixed in the presence of correlated errors. Such differences in scaling of a variance measure with averaging are reminiscent of the manifestation of noise correlations in other physical quantities, e.g., the Allan variance used in precision frequency metrology [**224, 225**]. Our analysis therefore highlights that calculating the variance of measurements of randomised benchmarking survival probabilities for different sequences, and exploring how this variance changes with experimental averaging, can give insights into the underlying error correlations. The functional dependence of the distribution variance with n will be employed throughout the remainder of this work as a key signature of error correlations in standard randomised benchmarking. In the next section we demonstrate how the model can be updated to connect to realistic laboratory noise models.

6.1.4 Modelling realistic laboratory error models

Building on the general framework introduced above, we introduce new first-principles calculations connecting the theoretical model for gate *error* with actual, error-inducing *noise* in experiments. We determine the sequence walk in the presence of arbitrary, unitary error maps, incorporating the possibility of multi-axis and gate-dependent errors. This facilitates the analysis of experimental measurements performed subject to the most common noise sources encountered in the laboratory.

We consider two physically motivated noise processes that can occur throughout a randomised benchmarking sequence. First, frequency detuning noise – either on the qubit's resonant frequency or the frequency of the control field used to drive qubit gate operations – creates an off-resonance error between the qubit and control. Second, amplitude noise, which may arise from coupling-strength variations or drifts and miscalibrations in the control, results in an over- or under-rotation error of the qubit state vector. Both of these represent "concurrent" noise sources (i.e., applied simultaneously with the execution of a gate), which ultimately produce complex gate-dependent errors.

In general, depending on their underlying cause, both frequency detuning and amplitude noise processes may possess temporally correlated and uncorrelated components. Correlated noise sources include miscalibrations, magnetic field drifts, and temperature drifts in control systems, while uncorrelated noise often stems from electrical noise or local environmental sources, e.g., anomalous heating in ion traps [**226**] or two-level system (TLS) fluctuators in superconducting qubits [**227**, **228**].

To now examine the impact of these physical noise processes on the behaviour of the sequence survival-probability distributions, we proceed by explicitly calculating the translation between the physical noise strength, $\delta_j^{(i)} \sim \mathcal{N}(0, \rho^2)$, and the effective sequence errors at the core of our model $\varepsilon = \varepsilon(\delta)$. In our notation, ρ is used to denote the rms magnitude of the noise, distinguishing it from the rms magnitude of the error operator σ. Our calculations incorporate the fact that single-axis noise (e.g., detuning) present during a non-commuting operation generally results in a multi-axis error process. Furthermore,

Error Type	$\rho \to \sigma$ **Translation for** $\mathbb{E}$	$\rho \to \sigma$ **Translation for** $\mathbb{V}$
(i) Fully Correlated, $\mathcal{M}_\mathrm{n} = J$	$\sigma_C^2 = \frac{3}{2}\mathbb{E}\left[\Vert\boldsymbol{r}_j\Vert^2\right]\rho_C^2$	$\sigma_C^4 = \frac{9}{2}\frac{\mathbb{E}\left[\Vert\boldsymbol{r}_j\Vert^4\right]+(J-2)\mathbb{E}\left[\Vert\boldsymbol{r}_j\Vert^2\right]^2}{2J-1}\rho_C^4$
(ii) Uncorrelated, $\mathcal{M}_\mathrm{n} = 1$	$\sigma_U^2 = \frac{3}{2}\mathbb{E}\left[\Vert\boldsymbol{r}_j\Vert^2\right]\rho_U^2$	$\sigma_U^4 = \frac{9}{2}\frac{(2+n)\mathbb{E}\left[\Vert\boldsymbol{r}_j\Vert^4\right]+(J-1-n)\mathbb{E}\left[\Vert\boldsymbol{r}_j\Vert^2\right]^2}{4+2J+n}\rho_U^4$
(iii) Correlated + Uncorrelated	$(\sigma_C^2 + \sigma_U^2) =$ $\frac{3}{2}\left(\mathbb{E}\left[\Vert\boldsymbol{r}_{U,j}\Vert^2\right]\rho_U^2 + \mathbb{E}\left[\Vert\boldsymbol{r}_{C,j}\Vert^2\right]\rho_C^2\right)$	$\sigma_C^2\sigma_U^2 = \frac{9}{2}\mathrm{Cov}\left(\Vert\boldsymbol{r}_{U,j}\Vert^2, \Vert\boldsymbol{r}_{C,j}\Vert^2\right)\rho_C^2\rho_U^2$

TABLE 6.2. The translation from the rms value of a physical noise process, ρ, with correlation length $\mathcal{M}_\mathrm{n}$, to the rms value of the gate error, σ, used to calculate the first and second moments of noise-averaged sequence survival probabilities. The values ρ_C, ρ_U represent the rms magnitudes of the correlated and uncorrelated noise processes respectively. Similarly, the terms $\boldsymbol{r}_{U,j}, \boldsymbol{r}_{C,j}$ represent the random walk steps for the different noise processes. Full details of the derivation of the relevant random walk step expectation values, $\mathbb{E}\left[\Vert\boldsymbol{r}_j\Vert^2\right]$, $\mathbb{E}\left[\Vert\boldsymbol{r}_j\Vert^4\right]$, and $\mathrm{Cov}\left(\Vert\boldsymbol{r}_{U,j}\Vert^2, \Vert\boldsymbol{r}_{C,j}\Vert^2\right)$ for the specific noise models employed in our verification experiments are presented in Chapter 4, Section 4.3.2.

physical implementations of Clifford operations typically employ variable gate durations, resulting in gate-dependent error operators.

In this setting, the error $\varepsilon_j^{(i)}$ employed in Eqn. (6.1) is replaced by the physical noise strength $\delta_j^{(i)}$. As a result, the previously unit-length steps $\boldsymbol{r}_{3\mathrm{D},j}$ now take more complex, but still analytically calculable, values due to the gate-dependence and multi-axis character of the errors induced by concurrent noise processes. For a particular noise process we calculate the associated random walk, which enables a mapping of the rms magnitude of the physical noise ρ to an updated rms value of the error σ. Section 4.3.2 in Chapter 4 describes the formalism to calculate the noise-to-error translation in standard Clifford gates for an arbitrary, unitary error process. Table 6.2 summarises the results which, when combined with the expressions from Table 6.1, can be used to predict both the expectation and the variance of the distribution of survival probabilities over sequence randomisation.

6.2 Experimental implementation

In this section, we proceed to validate the framework discussed above, using it to quantitatively analyse the strength of a correlated noise process affecting a quantum circuit. We perform experiments using a hyperfine $^{171}\mathrm{Yb}^+$ qubit, for which qubit rotations are driven via an I/Q-modulated 12.64 GHz microwave field generated by a Vector Signal Generator (VSG) (see Chapter 2 for full details). Rotations about the z-axis are implemented as instantaneous, pre-calculated I/Q frame shifts. The single-qubit detection data is collected and analysed in a time-resolved manner [**113**, **221**] using an avalanche photodiode (APD); multi-qubit data employs an EMCCD camera and processing through a Random Forest classifier from the scikit-learn framework [**153**].

The experiments in this manuscript are performed using k sequences each comprising J operations. The first $J-1$ gates are randomly composed Clifford operations and the final operation is selected such that the sequence implements the identity in the absence of error. The full randomised benchmarking protocol can be found in Chapter 4.1.3, with a full list of the Clifford operations and their physical implementations tabulated in Table 4.1. A single ion in the blade trap used for these experiments achieves a baseline (no engineered error) average error per gate of $p_{\mathrm{RB}} \approx 1.9 \times 10^{-5}$ and a state preparation and measurement error (SPAM) of $\kappa = (3.3 \pm 0.1) \times 10^{-3}$.

6.2.1 Verifying error correlation signatures with engineered errors

The key signature of the presence of temporally correlated errors appears in the variance of the distribution over sequence survival probabilities and its scaling with experimental averaging; averaging reduces the variance in the case of uncorrelated errors, but has limited impact when errors exhibit strong temporal correlations. We begin our experimental study by engineering experimental noise sources to test and verify the predictions of the theoretical model presented in Chapter 6.1. We perform standard randomised benchmarking, but engineer detuning and control-amplitude noise with different user-defined bandwidths. All noise values are generated numerically, and are sampled from a zero-mean Gaussian distribution $\delta \sim \mathcal{N}(0, \rho^2)$ with rms strength ρ. Off-resonance errors are induced via fractional detuning noise present during the application of the randomised benchmarking sequence, $\delta = (\Delta/\Omega)$, set by the frequency detuning Δ between the qubit transition and the microwave source in units of the Rabi frequency, Ω. Over-rotation errors are produced by amplitude noise in the microwave control field, effectively changing Ω. Two limiting noise bandwidths are treated: maximally correlated noise, $\mathcal{M}_{\mathrm{n}} = J$, with rms strength ρ_C; and uncorrelated noise, $\mathcal{M}_{\mathrm{n}} \leq 1$, with rms strength ρ_U. For the detuning (control-amplitude) noise process, the correlated noise component is engineered using a constant offset in the VSG microwave frequency (amplitude) over the entire sequence, and the uncorrelated noise is applied via an external FM (AM) modulation input, and changes value every primitive $\pi/2$-time. The relevant random walk steps calculated for these noise processes, $\mathbb{E}[\|\boldsymbol{r}_j\|^2]$ and $\mathbb{E}[\|\boldsymbol{r}_j\|^4]$, that are used to model our experimental measurements are found in Table 4.2 of Section 4.3.2, using the "1 value every primitive $\pi/2$ gate time" bandwidth.

Instead of simply calculating the randomised benchmarking decay rate, p_{RB}, derived from fitting to the mean of the distribution over different values of J, we instead focus on analysing our data to extract information that is otherwise generally discarded in averaging processes. In each individual measurement, the qubit is initialised in state $|0\rangle$ via optical pumping and one of $k = 50$ randomised benchmarking sequences with $J = 100$ gates is applied in the presence of engineered noise. A final projective measurement in each experiment yields a discretised qubit state measurement, which is used to infer the probability of finding the qubit in state $|1\rangle$ by repeating the experiment $r = 220$ times under application of the same engineered noise realisation (reducing quantum projection noise). The survival-probability measurement outcomes for each sequence are then averaged over a variable number up to $n = 200$ different realisations of noise possessing the same engineered correlations. This process is repeated for all $k = 50$ sequences, allowing us to calculate the distribution variance over noise-averaged survival probabilities.

Figs. 6.2a-c show the distributions over randomised benchmarking sequences of the measured noise-averaged survival probabilities in the presence of concurrent detuning noise. The same set of sequences is subject to correlated (grey) or uncorrelated (red) noise sampled from a common distribution. Data are represented as histograms for different fixed values of averaging number, n, for each sequence. Solid lines are theoretical predictions for the distribution of survival probabilities derived from the updated random-walk framework, as given by the Gamma distributions from Eqn. (6.3), and substituting the error rms value σ using the noise-to-error translation for the expectation value shown in Table 6.2. These theoretical predictions - which involve no free parameters - show good agreement with the data in the regimes studied.

These data clearly illustrate the differences in the distributions over the same set of randomised benchmarking sequences when subjected to noise with differing correlation properties. As shown in Ref. [**165**] and highlighted here in Table 6.1, the distributions possess approximately the same mean value, despite the differing noise-correlation properties. The skew to high fidelities in the data taken using correlated noise is a manifestation of the randomised decoupling effects known to exist within some randomised benchmarking sequences [**165**]. More importantly, the behaviour of the variance of the distributions under an increasing number of noise averages n varies substantially. For small n the distributions are

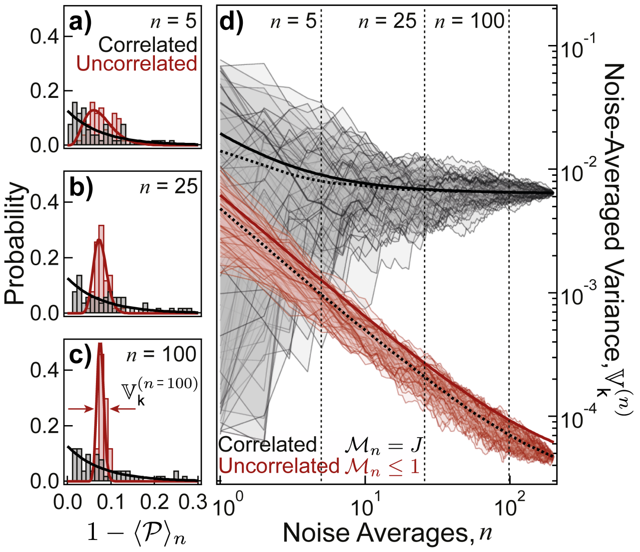

FIGURE 6.2. **Signatures of error correlations in randomised benchmarking sequences. a-c,** Distribution of measured survival probabilities for $k = 50$ randomly composed sequences averaged over $n = 5, 25$ and 100 noise realisations drawn from $\delta \sim \mathcal{N}(0, \rho^2 = 2 \times 10^{-3})$ for both maximally correlated, $\mathcal{M}_{\mathrm{n}} = J$, (grey) and uncorrelated (red) engineered noise processes. Uncorrelated noise possesses a "$\pi/2$-bandwidth", i.e., noise values change with a rate set at the inverse of the duration of a primitive $\pi/2$-rotation, and hence can take one or multiple values in a gate ($\mathcal{M}_{\mathrm{n}} \leq 1$). Solid lines are normalised Gamma distributions plotted with no free parameters. **d,** Scaling of cumulatively noise-averaged histogram variances, $\mathbb{V}_{\mathrm{k}}^{(n)} \equiv \mathbb{V}_{\mathrm{k}}\left[\langle P(|1\rangle)\rangle_n\right]$. Trajectories correspond to different orderings of noise realisations with dotted lines representing the mean of 1000 re-orderings, and solid lines are theoretical predictions with no free parameters (see main text). Vertical dashed lines indicate the values of n used in panels **a-c**.

similarly broad despite the differences in their shapes, but with further averaging the distribution measured under uncorrelated noise narrows while the variance of the distribution measured under correlated noise remains approximately constant (as discussed in Sec. 6.1.3).

To highlight the effect of noise correlations on the experimental averaging behaviour, we plot the variance of the distribution over measured sequence survival probabilities, $\mathbb{V}_{\mathrm{k}}^{(n)} \equiv \mathbb{V}_{\mathrm{k}}\left[\langle P(|1\rangle)\rangle_n\right]$, as a function of the number of noise averages n (Fig. 6.2d). Data are represented as a collection of trajectories, each constituting a randomised reshuffling of the data set (indexed by individual noise realisations). Data sets are averaged over n noise realisations sampled from the full set, and n is allowed to vary from left to right. This continues until all $n = 200$ noise realisations have been sampled. This procedure is used to mitigate potential unintended systematic bias in the scaling of the the noise-averaged variance with n. For instance, if by chance the first several noise samples over which one averages varied substantially, the variance may be artificially inflated from the ensemble average value; accordingly the resulting deviations between noise-averaging-trajectories are largest for small n and vanish at the far right of the graph where all data sets are fully averaged over all available data. For correlated noise, $\mathcal{M}_{\mathrm{n}} = J$, the resulting trajectories are initially broadly distributed and fluctuate before converging with n to a fixed, analytically calculable variance. By contrast, in the case of uncorrelated noise with $\mathcal{M}_{\mathrm{n}} \leq 1$, all trajectories show an approximate reduction in $\mathbb{V}_{\mathrm{k}}^{(n)} \propto 1/n$, commensurate with a continued narrowing of the distribution of outcomes over different sequences under averaging (Fig. 6.2a-c).

Solid lines capturing key scaling behaviours observed in both data sets of Fig. 6.2d are derived from the expression for variance in Table 6.1. We use the noise-to-error translations from Table 6.2 and the expected random walk steps for the relevant error model in Table 4.2, which are calculated for concurrent detuning noise with no free parameters. Overall, agreement with the measured experimental data are good across a wide parameter range and two orders of magnitude in $\mathbb{V}_{\mathrm{k}}^{(n)}$. For correlated noise, small deviations between the theoretical trace and measured mean scaling appear for low values of n. Numerical evidence attributes this to the limited sample size in terms of sequences, which does not always capture the rare, highly error-susceptible sequences that would lead to a larger variance. In the case of uncorrelated noise, there is an overall vertical shift between the theory and the data, which is fully compensated by adjusting the rms noise strength ρ_U by $\sim 6\%$. Numerical simulations and analytic considerations attribute the need for this adjustment to the strong noise employed in these experiments, which violates the theoretical assumption $J\rho_U^2 \ll 1$, such that higher-order terms in the theory cannot be fully ignored.

The uncorrelated noise data begin to deviate from an exact $1/n$-scaling of $\mathbb{V}_{\mathrm{k}}^{(n)}$ at large numbers of noise averages. This behaviour is captured by our theoretical model and varies in a predictable way with the applied noise bandwidth and sequence length J; we have verified it is not due to fundamental measurement limits in our system or quantum projection noise. We are able to attribute this “saturation” in variance scaling for uncorrelated noise to residual sequence dependence, even in the case of purely uncorrelated noise, and the fact that our projective measurement probes only a two-dimensional $\hat{\sigma}_x\hat{\sigma}_y$-plane in Pauli-error space. For example, one can imagine a sequence composed solely of $\hat{\mathbb{I}}$ gates, which, due to an induced off-resonance error, will experience a net phase rotation that cannot be measured by single-axis projective measurements. Hence, no amount of averaging over different noise strength realisations will produce a survival probability that converges to the distribution mean, even in the case of uncorrelated noise.

Overall we find that our theoretical models predict not only the full distribution of survival probabilities over randomised benchmarking sequences, but also the scaling of this distribution's variance with experimental averaging. The difference between the grey and red data in Fig. 6.2d, and the agreement of theory, thus constitute key experimental validations of the central theoretical contributions made in this manuscript.

6.3 Suppressing error correlations using dynamically corrected gates

In the next part of our study we explore the ability to modify error correlations within a sequence through deterministic replacement of each Clifford operation in a randomised benchmarking sequence with an error-suppressing dynamically corrected gate (DCG). Each DCG is implemented by replacing primitive physical rotations with composite pulses comprising multiple physical rotations [**210**], according to one of several prescriptions [**204**].

6.3.1 Dynamically corrected gate construction

The particular DCG constructions examined in this work are the 'Compensation for Off-Resonance with a Pulse SEquence' (CORPSE) [**229**] and 'Walsh Amplitude Modulated Filter' (WAMF) [**230**] gates, which suppress detuning errors, and the BB1 pulse family [**231**], which suppresses over-rotation errors. We also briefly discuss the use of reduced CinBB (CORPSE in BB1), which suppresses errors in both quadratures. For each of these constructions, the target angle $\theta_t = \pi$, $\pi/2$ gates are created as multi-segment pulses described by the segments' rotation angles θ_i, phase angles ϕ_i, and Rabi frequencies

Gate Construction	$(\theta_1, \Omega_1, \phi_1)$	$(\theta_2, \Omega_2, \phi_2)$	$(\theta_3, \Omega_3, \phi_3)$	$(\theta_4, \Omega_4, \phi_4)$
Primitive	$(\theta_t, \Omega, 0)$	-	-	-
CORPSE	$(2\pi + \theta_t/2 - k, \Omega, 0)$	$(2\pi - 2k, \Omega, \pi)$	$(\theta_t/2 - k, \Omega, 0)$	-
WAMF	$\left(\frac{X_0+X_3}{4}, \Omega, 0\right)$	$\left(\frac{X_0-X_3}{2}, \frac{X_0-X_3}{X_0+X_3}\Omega, 0\right)$	$\left(\frac{X_0+X_3}{4}, \Omega, 0\right)$	-
BB1	$(\theta_t, \Omega, 0)$	(π, Ω, ϕ_k)	$(2\pi, \Omega, 3\phi_k)$	(π, Ω, ϕ_k)

TABLE 6.3. Gate parameters required to construct a target rotation about the x-axis by angle θ_t using different pulse constructions. An additional $\pi/2$ shift in ϕ is required for rotations about the y-axis. Here, $k = \arcsin\left[\frac{\sin[\theta_t/2]}{2}\right]$, $\phi_k = \arccos\left[\frac{-\theta_t}{4\pi}\right]$, and for WAMF DCGs, the target rotations $\theta_t = (\frac{\pi}{4}, \frac{\pi}{2}, \pi)$ have $X_0 = (2\frac{1}{4}, 2\frac{1}{2}, 3)\pi$ and $X_3 = (0.36, 0.64, 1)\pi$ determined explicitly.

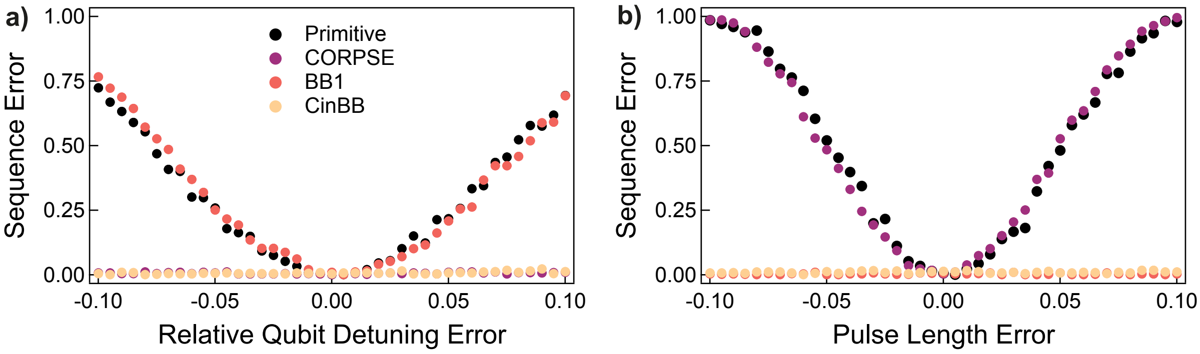

FIGURE 6.3. **Robustness of different pulse constructions to errors. a,** A sequence of 10 π-rotations is applied to a single qubit, alternating between the $+x$ and $-x$ axes to amplify detuning errors, and the final state is measured. The relative detuning error is scanned between $\pm 10\%$, which induces deviations from the ideal final state, with the resultant measured error indicated by higher points on the graph. This process is repeated using primitive (black), CORPSE (purple), BB1 (orange) and CinBB (yellow) gates. **b,** The same gate constructions are used for a sequence of 10 π-rotations all about the $+x$ axis to amplify over-rotation errors. The pulse length error is scanned between $\pm 10\%$ and the measured error in the final qubit state is again indicated by higher points on the graph.

Ω_i normalised to the maximum frequency Ω. The constructions of the different gates are shown in Table 6.3. To ensure that the error suppressing aspects of the DCGs are maintained for all Clifford gates, the identity gate is implemented as a rotary spin echo by concatenating a π rotation about the x-axis with its inverse $-\pi$ rotation. While this results in a net zero rotation, effectively identical to the simple wait time used for primitive $\hat{\mathbb{I}}$ gates, it makes the identity operation first-order insensitive to detuning errors during its implementation. The physical motivation here is that if a qubit is remaining idle at any point during a multi-qubit circuit, it may be preferable to continuously drive this type of rotary spin echo to ensure that it does not accumulate phase errors during its idle period.

Virtualising single qubit gates as DCGs introduces a robustness to a particular quadrature of error, as shown in Fig. 6.3. A single qubit is prepared in $|0\rangle$, 10 π-rotations are applied using four different pulse constructions, and the difference between the final and initial qubit states is measured, $P(|1\rangle)$, which is zero for error-free rotations. In Fig. 6.3a, an off-resonance error is added, with the relative detuning offset between the qubit frequency and the microwave drive scanned over $\pm 10\%$. The 10 π-pulses are driven around alternating axes x and $-x$ to amplify the off-resonance error. For off-resonance errors, it is observed that the CORPSE and reduced CinBB (CORPSE in BB1) pulses are more robust to the error process than the primitive gates because they minimise the difference between the final and initial qubit states over a wider range of detuning errors. For over- and under-rotations induced by a pulse length error in Fig. 6.3b, the π-pulses are all driven around a single axis x to amplify the error. Here, the BB1 and reduced CinBB pulses are found to be more robust. This demonstrates the multi-axis error suppression of reduced CinBB pulses. Primitive gates, on the other hand, are highly sensitive to errors in both quadratures.

6.3.2 Modification of variance scaling with engineered errors using DCGs

Dynamically corrected gates abstract the target state transformations away from the physical qubit manipulation in a manner that builds in error robustness via coherent averaging. In this way, these composite gates modify the error susceptibility of the target operations, and in particular change the relationship between an input correlated-noise process and output gate errors. We therefore refer to their action as "virtualising" the Clifford operations, consistent with an abstraction above the physical-layer operations presented in Ref. [**208**].

The error-virtualisation process is described quantitatively by calculating the error vector $\boldsymbol{\epsilon}_j$ at the operator level and expressing it in the Fourier domain. In the limit of classical Gaussian dephasing noise, described in the Fourier domain as the spectrum $\beta_z(\omega)$, the leading-order Magnus term ($\alpha = 1$) in the $\hat{\sigma}_z$-quadrature may be written as

$$[\epsilon_{j,z}]_1 = -i \int \frac{d\omega}{2\pi} G_z^{(1)}(\omega, T_j)\beta_z(\omega). \tag{6.6}$$

Here, $G_z^{(1)}(\omega, T_j)$ is an analytically calculable, filter-transfer function that describes the spectral characteristics of a gate active for duration T_j [**211**]. The *effective* error spectrum experienced by the gate may therefore be represented by the spectral overlap of the filter-transfer function with the noise, written as $G_z^{(1)}(\omega, T_j) \times \beta_z(\omega) \to E(\omega, T_j)$. Fig. 6.4a demonstrates the mapping between input noise and the effective error spectrum schematically for an example $1/\omega$-noise spectrum and a primitive π-rotation about the x-axis. In this example, correlations in the noise are directly transferred to the correlations in the effective error spectrum [**214**] (c.f. direct $\mathcal{M}_\mathrm{n}$ to $\mathcal{M}_\varepsilon$ translation for primitive gates in Fig. 6.1c).

Replacement of the primitive gate with a logically equivalent DCG virtualises the effective error spectrum for each operator through the process of noise filtering [**206, 210, 211, 214**]. Fig. 6.4b illustrates this effect, where the DCG's reduced susceptibility to low frequency noise (captured through its filter-transfer function) results in a "whitening" of the effective error spectrum relative to $\beta_z(\omega)$. We use the term whitening to describe the reduction of low-frequency weight, producing an error spectrum with characteristics closer to a white spectrum than the original input; we do not imply the effective error

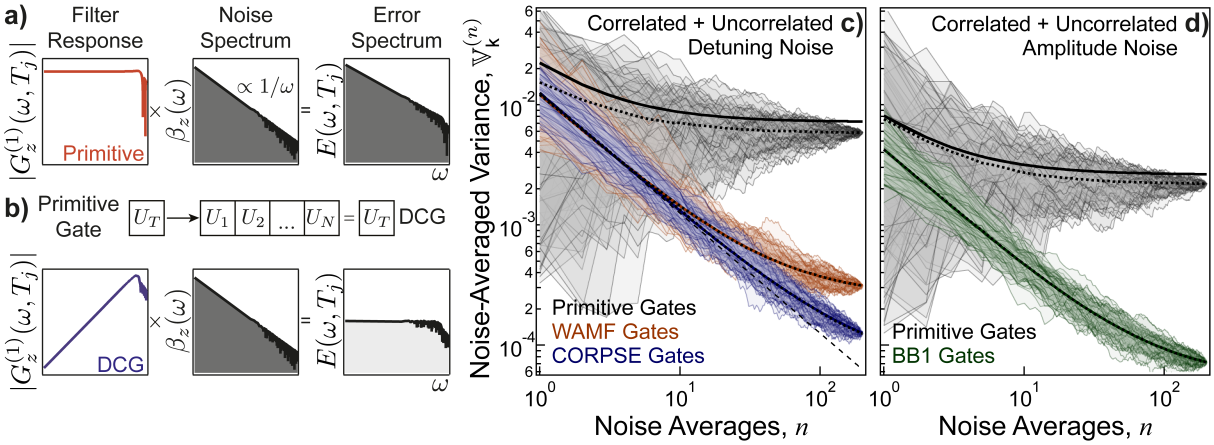

FIGURE 6.4. **Suppression of error correlations using dynamically corrected gates.** **a,** The first-order, generalised filter-transfer function for dephasing noise of a primitive operation $G_z^{(1)}(\omega, T_j)$ and the noise spectrum (here $\beta_z(\omega) \propto 1/\omega$) combine to produce an effective error spectrum $E(\omega, T_j)$ for a single gate. **b,** The modified filter functions for first-order DCGs scale as ω at low frequencies, which results in a "whitening" of $E(\omega, T_j)$ relative to the input noise spectrum. **c, d,** Variance scaling with n for primitive (grey) gates, and WAMF (orange), CORPSE (blue) and BB1 (green) DCGs all subjected to noise with both correlated and uncorrelated components. For **c**, detuning noise is engineered with strength $\delta_C \sim \mathcal{N}(0, \rho_C^2 = 2 \times 10^{-3})$, $\delta_U \sim \mathcal{N}(0, \rho_U^2 = 5 \times 10^{-4})$, and for **d**, amplitude noise is engineered with strength $\delta_C \sim \mathcal{N}(0, \rho_C^2 = 9 \times 10^{-4})$, $\delta_U \sim \mathcal{N}(0, \rho_U^2 = 2 \times 10^{-4})$. Dotted lines are means of 1000 trajectories randomised over noise realisations, and solid lines for the DCGs are theoretical fits from Table 6.1 to the mean with the values of σ_U^2 and σ_C^2 allowed to vary. Black solid lines for primitive gates are derived from the same theory with no free parameters. As with Fig. 6.2, all data is measured for $k = 50$ sequences of length $J = 100$ with $n = 200$ noise realisations and $r = 220$ repetitions.

spectrum after DCG application is formally white (frequency independent). In the current context, this whitening suggests that DCGs should not only reduce overall error magnitudes when the noise is dominated by low frequency contributions, but they should also suppress the signatures of error correlations between sequentially applied gates.

We begin by performing a detailed, quantitative study of the measured signatures of error correlations through the application of engineered noise. We experimentally implement primitive, CORPSE, WAMF and BB1 gates, where the first two DCGs are designed to suppress errors arising from frequency detuning noise and the latter is designed to suppress errors arising from amplitude noise. Using the same set of randomly generated randomised benchmarking sequences as in Fig. 6.2, we now apply a mixed noise spectrum, simultaneously containing uncorrelated, rapidly varying noise ($\mathcal{M}_{\rm n} \leq 1$), and quasi-static offsets that are constant over a full sequence giving a strongly correlated component ($\mathcal{M}_{\rm n} = J$).

In addition to performing measurements with primitive gates, we also construct DCG sequences by deterministically replacing each Clifford with its logically equivalent DCG counterpart. The relations for the mixed noise spectrum provided in Tables 6.1 and 6.2 now permit a direct study of the impact of using DCGs on error correlations appearing within the randomised benchmarking sequences via the averaging behaviour of $\mathbb{V}_{\mathrm{k}}^{(n)}$.

Beginning with frequency detuning noise, both DCG implementations shown in Fig. 6.4c exhibit an initial variance scaling with noise averaging $\mathbb{V}_{\mathrm{k}}^{(n)} \propto 1/n$, reminiscent of the application of the purely uncorrelated noise process in Fig. 6.2d. The observed saturation in $\mathbb{V}_{\mathrm{k}}^{(n)}$ at large n for the DCG data combines contributions due to both the analytically calculable component occurring in the presence of purely uncorrelated noise introduced above, and residual uncompensated error correlations. The general behaviour observed for the DCG sequences is to be contrasted with that observed for the same sequences composed of primitive gates where, as in Fig. 6.2, the strong correlated noise component causes the variance to converge to a large constant value (grey).

Similar behaviour is observed when considering the amplitude error quadrature. We demonstrate this through the application of engineered control-amplitude noise in Fig. 6.4d, where measurements on sequences composed of DCGs derived from the BB1 family exhibit a similar $\mathbb{V}_{\mathrm{k}}^{(n)} \propto 1/n$ averaging behaviour. Again, this is contrasted with the behaviour of sequences composed of primitive gates where once more the variance saturates to a high constant value, despite application of the same noise in both settings.

6.3.3 Quantitative analysis of error-correlation suppression

In order to calculate the change in error correlations realised in randomised benchmarking sequences composed of DCGs, we compare experimental measurements of $\mathbb{V}_{\mathrm{k}}^{(n)}$ with the predictions of the model summarised in Table 6.1. For the primitive gates, we explicitly translate the applied detuning noise strengths to an effective error strength using the noise-to-error relations in Table 6.2; for this, we also use the expected random walk step expressions calculated and presented in Table 4.2 of Section 4.3.2 in Chapter 4 for detuning or amplitude noise with a $\pi/2$-bandwidth in the uncorrelated component. The solid, black lines in Figs. 6.4c,d are then derived using these calculated error strengths, with no free parameters. Agreement between experimental measurements and theoretical predictions for the primitive gate sequences is good, but we observe a small ($\sim$20%) deviation that appears approximately constant over several orders of magnitude in n for both noise processes. Ongoing work is investigating the source of this discrepancy; possible sources include the unaccounted impact of higher-order terms due to the strength of the applied noise, and undersampling of the distribution over noise-averaged sequences.

To extract the relative correlated and uncorrelated error components after DCG application, we fit the data using the theoretical predictions for the scaling of $\mathbb{V}_{\mathrm{k}}^{(n)}$ shown in Table 6.1, and use the strengths of the two error components σ_U^2 and σ_C^2 as free parameters. First, for all DCGs we observe a reduction in σ_C^2 coupled with an increase in σ_U^2. Specifically, σ_C^2 is reduced by a factor of $49\times$ for CORPSE, $6\times$ for WAMF, and $10\times$ for BB1, while all experience an increase in σ_U^2 by approximately 6 - $7\times$. The relative performance of the DCGs observed in our experiments is aligned with their documented strengths, as CORPSE is known to more efficiently cancel purely static detuning errors than WAMF [**210**, **230**], although improved calibration of the pulse-amplitude values used in WAMF gates is expected to improve the efficacy of correlated-error suppression.

The increase in σ_U^2 is approximately consistent with the increase in duration of the DCGs relative to the primitive gate implementations. Considering the high-pass-filtering nature of all DCGs illustrates why uncorrelated noise processes fluctuating rapidly on the scale of the individual DCGs are transmitted by their filters and lead to residual errors that may be amplified by the DCG structure. Overall, these measurements – in particular the scaling of $\mathbb{V}_{\mathrm{k}}^{(n)}$ – are consistent with an interpretation that the action of the noise whitening in the filter-transfer-function framework transforms correlated noise into predominantly uncorrelated residual errors *at the operator level.*

6.3.4 Signatures of variable error-correlation lengths

To expand on the previous analyses, we experimentally demonstrate that the reduction in effective error correlation, indeed, resides at the virtual gate layer. Using the same sequences as before, and the same engineered ρ_U and ρ_C rms magnitudes for detuning noise, the length of the correlated noise component is now varied in terms of the number of gates at the virtual level, breaking it up into blocks of length $\mathcal{M}_{\mathrm{n}}$. The lab-frame durations of the noise blocks therefore now differ by a factor of ~ 6 between the primitive and the CORPSE gates (the average increase in the duration of the Clifford operations when using CORPSE).

In the case of sequences composed of primitive gates, the signature exhibited by the variance scaling under noise averaging in Fig. 6.5a gradually changes from indicating correlated errors (saturation at high

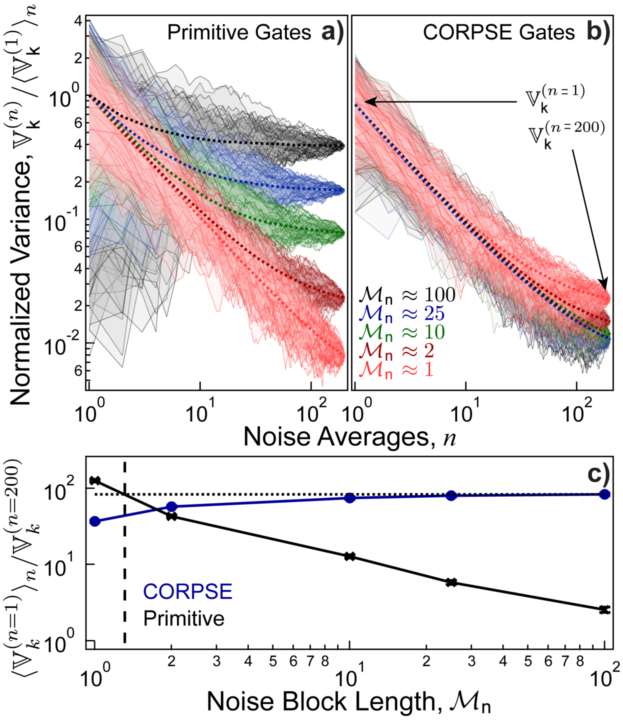

FIGURE 6.5. **Suppression of error correlations using DCGs under noise with varying $\mathcal{M}_\mathrm{n}$. a, b,** Variance scaling of $k = 20$ sequences with noise averaging for **a,** primitive and **b,** CORPSE gates. Traces are normalised to the initial mean variance for each applied noise case. Engineered noise is composed of an uncorrelated component ($\mathcal{M}_\mathrm{n} \leq 1$) and a block correlated component of length $\mathcal{M}_\mathrm{n}$ that is varied from fully correlated ($\mathcal{M}_\mathrm{n} = J$) to uncorrelated ($\mathcal{M}_\mathrm{n} = 1$) in units of virtual gates. Dotted lines are means of 1000 randomised trajectories. **c,** Ratio of initial to final variance in the upper panels as $\mathcal{M}_\mathrm{n}$ is varied for primitive (black) and CORPSE (blue) gates. Dotted line marks the ratio at which CORPSE gates saturate, and the dashed vertical line indicates the value of $\mathcal{M}_\mathrm{n}$ where this ratio crosses the scaling trend for primitive gates. Error bars calculated from the SEM of the 200 initial values of variance and normalised by the fully noise-averaged variance are smaller than point size.

variance) to purely uncorrelated errors ($1/n$-like scaling) as the block length is decreased, consistent with observations in Fig. 6.2 and Fig. 6.4. By contrast, the sequences composed of CORPSE gates in Fig. 6.5b retain their overall $1/n$-like scaling behaviour for all correlated component block lengths, demonstrating that residual uncorrelated errors remain dominant. All traces in Fig. 6.5a,b have been normalised to the initial mean variance for each engineered noise case to highlight the change in the relative correlated and uncorrelated error components, rather than the net error strength.

As a witness of the suppression of error correlations, Fig. 6.5c shows the ratio of the initial mean variance $\langle\mathbb{V}_\mathrm{k}^{(n=1)}\rangle_n$ to the final, fully noise-averaged variance $\mathbb{V}_\mathrm{k}^{(n=200)}$. This ratio scales approximately inversely with $\mathcal{M}_\mathrm{n}$ for primitive gates but remains nearly constant for CORPSE gates. Extrapolation of this ratio for CORPSE back towards small $\mathcal{M}_{\mathrm{n}}$ reveals a crossover with the primitive data that lies between $\mathcal{M}_{\mathrm{n}} \approx 1$ to 2. This suggests that CORPSE gates can reduce the noise correlation length to an error correlation length commensurate with physical noise $\mathcal{M}_{\mathrm{n}} \approx 1$ to 2. Because the noise correlation blocks were matched to the duration of the underlying Cliffords - whether through primitive or composite construction - these data highlight the efficacy of DCGs in virtualising error characteristics for the logical gates implemented.

6.4 DCG's impact on intrinsic errors

After verifying the utility of the theoretical constructs we have introduced in this work, we now turn to characterising the intrinsic errors limiting the performance of our system. In the trapped $^{171}\mathrm{Yb}^{+}$ ion experiment described in Section 2.3, we achieve a single-qubit randomised benchmarking average error per gate (EPG) of $(1.89 \pm 0.12) \times 10^{-5}$ (see App. C). Increasing the number of qubits to five and performing simultaneous randomised benchmarking using a global microwave control field reveals a monotonic increase in the EPG across the register, ranging from $(5.7{\pm}0.5){\times}10^{-5}$ to $(1.3{\pm}0.1){\times}10^{-4}$. As such, were we to run multi-ion algorithms that use global state manipulations, e.g., transversal gates in the 7-qubit Steane code [**186**], we would not see the net error rate scale linearly with respect to the initial single-qubit EPG. This non-linear scaling with increasing qubit numbers has been observed in many systems and is often due to cross-talk between qubits [**232**]. It is important to note that this experimental observation of inhomogeneous error rates also violates a common assumption on noise statistics made in studies of error correcting codes, namely that the noise is independent and *identically-distributed* (iid).

In our case, the underlying cause of the observed error inhomogeneity is a sub-percent-level gradient in the amplitude of the microwave control field across the ion chain, caused by interference from metallic surfaces in the proximity of our in-vacuum antenna. We also observe a small magnetic-field gradient across the qubit chain, such that both amplitude and detuning noise are present simultaneously. Spatially correlated errors have recently been studied in Ref. [**233**], wherein it is noted that previous studies of multi-qubit errors tend to assume either spatially independent errors or identically spatially correlated errors, facilitating the use of a decoherence free subspace. Our situation, with a gradient of spatially correlated errors, falls between these two cases, but can still induce simultaneous multi-qubit errors that lower the efficacy of QEC.

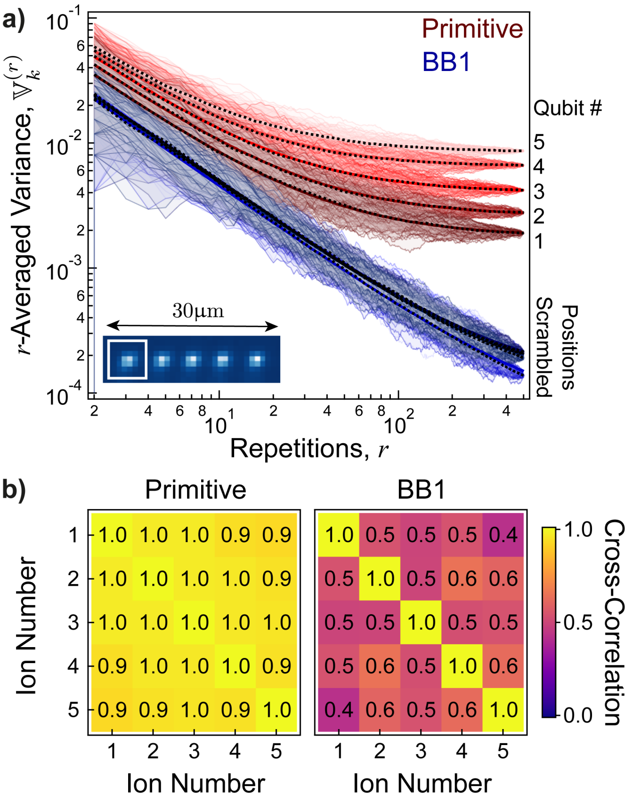

Primitive

Ion Number	1	2	3	4	5
1	1.0	1.0	1.0	0.9	0.9
2	1.0	1.0	1.0	1.0	0.9
3	1.0	1.0	1.0	1.0	1.0
4	0.9	1.0	1.0	1.0	0.9
5	0.9	0.9	1.0	0.9	1.0

BB1

Ion Number	1	2	3	4	5
1	1.0	0.5	0.5	0.5	0.4
2	0.5	1.0	0.5	0.6	0.6
3	0.5	0.5	1.0	0.5	0.5
4	0.5	0.6	0.5	1.0	0.6
5	0.4	0.6	0.5	0.6	1.0

FIGURE 6.6. **Intrinsic errors in a five-qubit chain.** **a,** Variance over noise-averaged sequence survival probabilities for five qubits using $k = 60$ sequences of length $J = 500$, averaged over up to $r = 500$ repetitions. Each trajectory is produced by shuffling the order of repetitions used in the graph to avoid bias, dotted lines indicate the means of 1000 trajectory randomisations, and solid lines are fits where the correlated and uncorrelated error strengths were free to vary. The correlated error strengths, σ_C^2, are $\{1.2, 1.5, 1.9, 2.4, 2.7\} \times 10^{-4}$ from qubit 1 to 5 for the primitive gates, and $\{2.3, 2.5, 1.1, 2.2, 2.3\} \times 10^{-5}$ for the BB1 gates. The uncorrelated error strengths, σ_U^2, are $\{7.5, 8.1, 8.5, 8.6, 8.7\} \times 10^{-4}$ from qubit 1 to 5 for the primitive gates, and $\{6.5, 6.5, 6.3, 6.6, 6.5\} \times 10^{-4}$ for the BB1 gates. (Inset) EMCCD image of a five-ion chain. The control field amplitude and frequency is calibrated with respect to the highlighted, leftmost ion. **b,** Pairwise, cross-correlation coefficients between the five-qubit survival probabilities for primitive (left) and BB1 (right) gates, revealing a $\sim 50\%$ reduction in the correlations between qubit errors when using BB1.

To characterise the impact of DCGs on spatially correlated errors, we utilise simultaneous randomised benchmarking sequences of length $J = 500$ applied to all five qubits in the register, and again explore variance scaling with experimental averaging (Fig. 6.6). We construct DCG sequences using BB1 gates to combat the dominant microwave-control-amplitude errors. Data collection proceeds by interleaving a single sequence implemented using either primitive or BB1 gates to ensure a fair comparison between the sequences in time, in the event that any systematic drifts occur.

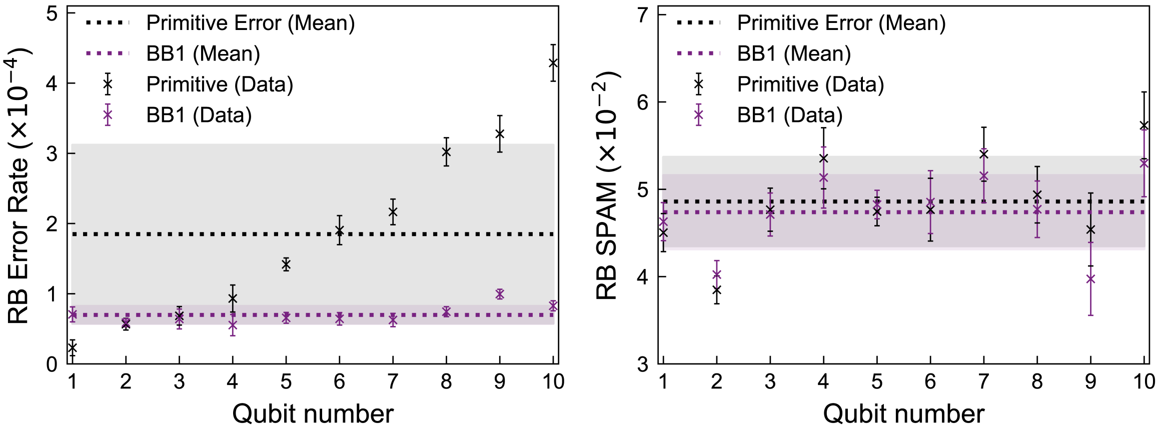

FIGURE 6.7. **Randomised benchmarking with ten qubits.** Average gate errors (left) and SPAM errors (right) extracted from global randomised benchmarking for 10 trapped ion qubits using primitive gates (black crosses), and BB1 gates (purple crosses). The mean error across the string is shown as a dotted line, and ±1 standard deviation is denoted by the shaded area. We observe a $10.2\times$ reduction in the spread of errors and a $2.6\times$ reduction in the mean error when using BB1 gates rather than primitive gates. There is no significant change in the SPAM error. Error bars are calculated from the fitting uncertainties returned by the RB exponential decay fit.

We examine the scaling of $\mathbb{V}_{\mathrm{k}}^{(r)}$ with averaging over repetitions r, up to $r = 500$; because noise is native to the system, we make the substitution $n \equiv r$. The signature of the temporally correlated intrinsic errors is observed for all ions when using sequences of primitive gates in Fig. 6.6a (red). We observe a staggered, increasing saturation value for $\mathbb{V}_{\mathrm{k}}^{(r)}$ at $r = 500$, increasing with the spatial distance from qubit 1 (leftmost qubit in Fig. 6.6a inset), which is used to calibrate the gate operations. As expected, the qubit that is furthest from the calibration qubit suffers both the worst randomised benchmarking performance and shows the highest saturation value in variance scaling. By contrast, the over-rotation error suppressing BB1 gates (blue) saturate at a value of variance over an order of magnitude lower than achieved by the primitive gates, and recover a $1/r$-like scaling for all qubits. We further find the relationship between the physical positions of the qubits and the ordering of saturation variances has become scrambled. Using the analysis introduced above, we fit the mean variance trends with the expression in Table 6.1, allowing the strengths of the error σ_C^2, σ_U^2 to vary. We extract a reduction in the correlated error strength when using BB1 gates ranging from ~ 5 to $16\times$ for the five qubits.

To directly probe the action of DCGs in virtualising the spatially correlated errors, we calculate the pairwise cross-correlation coefficient between the survival probabilities in each experimental realisation

(Fig. 6.6b). For primitive gates, all errors are highly correlated between qubits (cross-correlation coefficient ≥ 0.9 for all qubit pairs), whereas for the BB1 gates, a reduction of approximately 50% can be seen between all qubit pairs, further supporting the evidence that DCGs provide a suppression of error correlations in both time and space.

Separate investigations not presented here using the multi-axis error suppressing DCG CinBB, which combines the detuning-error robustness of CORPSE with the amplitude-error robustness of BB1 [**234**], showed no additional benefit. This observation suggests that the off-resonance error created by the magnetic-field gradient was sufficiently small that it was dominated by other larger, but rapidly fluctuating, intrinsic error sources

In addition to reducing the correlated error component, we can see that DCGs can be used to homogenise error rates across a string of qubits, an important requirement for quantum processors. Average error rates can vary between qubits for many reasons, in particular systematic field gradients or miscalibrations. Due to the magnetic and microwave field gradients in our experiment, our average error rates across a 10 ion string vary by over an order of magnitude. Replacing primitive gates with amplitude-error-suppressing BB1 gates reduces the mean error across the string by a factor of 2.6, and the spread of errors by a factor of 10.2 (Fig. 6.7). The extracted SPAM errors appear unaffected by the choice of gate, as expected. These results have been published by Ball et al. [**5**].

6.5 Outlook

The results we have presented suggest that the path to the practical implementation of QEC may be facilitated by transforming miscalibrations and common laboratory noise sources exhibiting slow drifts and low-weight noise spectra, into effective error processes with dramatically reduced correlations at the virtual layer using DCGs. We believe this is important as the pursuit of functional quantum computers – even at the mesoscale – will clearly require major advances in the control and suppression of errors, as gate counts quickly exceed 10^{10} for even moderate problems requiring only ~ 200 qubits [**235**]. Combined with the observation that certain DCGs can mitigate spatial cross-talk in multi-qubit systems [**236**], we believe that our demonstration of the suppression of temporal and spatial error correlations within quantum circuits solidifies the central importance of dynamic error suppression techniques at the virtual level for practical quantum computing.

CHAPTER 7

Theoretical background about the Mølmer-Sørensen gate

> *"Around and around and around we spin,*
> *With feet of lead and wings of tin."*
>
> - Kurt Vonnegut, *Cat's Cradle*

*The following material introduces the theory behind the Mølmer-Sørensen entangling gate, in particular, considering the bosonic motional modes used to facilitate entanglement. Parts of this chapter are partially reproduced from the Supplementary Material of "Phase-modulated entangling gates robust to static and time-varying errors" [**6**], while others constitute new material. See the Statement of Contribution for full details.*

The Mølmer-Sørensen (MS) gate is the most widely used entangling gate in trapped ion systems [**237**–**240**]. As with the earlier proposed Cirac-Zoller gate [**241**, **242**], the MS gate is able to entangle qubit states by exploiting their coupling to the collective, bosonic modes of ion motion. Unlike the Cirac-Zoller gate, which requires ground-state cooling for the initial state, the MS gate can be implemented with initial thermal states of motion, making it more easily realisable and more robust to common laboratory noise.

The focus of this chapter is to introduce the theory behind the MS gate and derive a formalism to predict the evolution of observable quantities under its application. In addition, I derive a "Filter Function" formalism to describe the performance of the MS gate in the presence of time-varying noise. I begin this chapter with a derivation of the trapped ion motional mode frequencies and eigenvectors for a system of N trapped ions.

7.1 Trapped ion motional spectra in three dimensions

The Mølmer-Sørensen gate utilises the harmonic motional modes of the trapped ions to facilitate entanglement between qubits. As such, it is important for us to be able to calculate the expected eigenvectors and frequencies characterising the modes' oscillations. In this section, I derive the full eigenspectra describing motion along all three trapping directions. This calculation is based off the work in "Quantum dynamics of cold trapped ions with application to quantum computation," D. F. V. James [**7**], which derives the expected ion positions and motion along the weakest trapping axis. To do so, it assumes that the radial confinement is significantly stronger than the axial and that the ion motion transverse to the axis is negligible. Consequently, the original formalism did not extend to calculating the transverse motion eigenspectra, nor could it predict structural phase transitions in the ion crystal configuration that extend beyond one dimension, e.g. "zig-zag" configurations.

7.1.1 Equilibrium positions of an ion string in three dimensions

The trapped ion system can be modelled as a set of harmonically oscillating particles with an additional ion-ion repulsive Coulomb interaction. The total potential energy then has contributions from both the individual harmonic oscillators and the pairwise electric potential energy between similarly charged ions. In one-dimension, the potential energy is given by

$$V^{(1\mathrm{D})} = \frac{1}{2} M \sum_{m=1}^{N} \nu_z^2 z_m(t)^2 + \frac{Z^2 e^2}{8\pi\epsilon_0} \sum_{\substack{n,m=1 \\ m\neq n}}^{N} \frac{1}{|z_n(t) - z_m(t)|} \tag{7.1}$$

where ν_z is the angular frequency of the centre-of-mass mode along the axial z direction, $z_m(t)$ is the position of the m^{th} ion at time t, M is the ion mass in kilograms, Z is the degree of ionisation (here for $^{171}\mathrm{Yb}^+$, $Z = 1$), e is the charge of an electron, and ϵ_0 is the vacuum permittivity. The potential energy can be extended to three dimensions as

$$V^{(3\mathrm{D})} = \frac{1}{2} M \sum_{m=1}^{N} \sum_{i=1}^{3} \nu_i^2 r_{mi}(t)^2 + \frac{Z^2 e^2}{8\pi\epsilon_0} \sum_{\substack{n,m=1 \\ m\neq n}}^{N} \frac{1}{\|\boldsymbol{r}_n(t) - \boldsymbol{r}_m(t)\|_2} \tag{7.2}$$

where ν_i is the i^{th} component of the vector containing the three angular centre-of-mass mode frequencies, $\boldsymbol{\nu} = [\nu_x, \nu_y, \nu_z]$, and $r_{mi}(t)$ is the i^{th} component of the position vector for the m^{th} ion at time t in three dimensions, $\boldsymbol{r}_m(t) = [x_m(t), y_m(t), z_m(t)]$. The symbol $\|\cdot\|_2$ represents the L^2 Euclidean norm, which calculates the length of a vector in Euclidean space, e.g. $\|\boldsymbol{a}\|_2 = \sqrt{\boldsymbol{a} \cdot \boldsymbol{a}}$. In all of the following, the z-axis will correspond to the "axial direction" or the weak trapping axis, and is indexed by $i = 3$.

The position of the ion can be expanded about some static equilibrium position, $\boldsymbol{r}_m^{(0)} = [x_m^{(0)}, y_m^{(0)}, z_m^{(0)}]$, with a small time-dependent displacement, $\boldsymbol{q}_m(t) = [q_{m_x}(t), q_{m_y}(t), q_{m_z}(t)]$, allowing us to rewrite $\boldsymbol{r}_m(t) = \boldsymbol{r}_m^{(0)} + \boldsymbol{q}_m(t)$. The equilibrium position of the j^{th} ion is found by calculating the stationary points of the potential energy, i.e., the value $\boldsymbol{r}_j^{(0)}$ that minimises the first partial derivative of $V^{(3\text{D})}$ with respect to $\boldsymbol{r}_j(t)$. This can be calculated as

$$\left.\frac{\partial V^{(3\text{D})}}{\partial r_{j_i}}\right|_{r_{j_i}(t) = r_{j_i}^{(0)}} = 0, \qquad \text{for all } j \in \{1, \ldots, N\},\ i \in \{1, 2, 3\} \tag{7.3}$$

where the notation $\big|_{r_{j_i}(t) = r_{j_i}^{(0)}}$ refers to taking the partial derivative at the equilibrium position where $r_{j_i}(t) = r_{j_i}^{(0)}$ and $q_{j_i}(t) = 0$.

To find the equilibrium positions of the ion string in three dimensions, one must solve the $3N$ simultaneous equations from Eqn. (7.3) for $j \in \{1, \ldots, N\}$ ions and the three dimensions $i \in \{1, 2, 3\}$. Using the expression in Eqn. (7.2) for $V^{(3\text{D})}$, the first derivative with respect to the j^{th} ion's position along the i^{th} (i.e. $r_{j_i}(t)$) can be expanded and simplified.

$$M\nu_i^2 r_{j_i}^{(0)} - \frac{Z^2 e^2}{8\pi\epsilon_0} \sum_{\substack{m=1 \\ m\neq j}}^{N} \sum_{\substack{n=1 \\ n\neq m}}^{N} \delta_{n,j} \frac{\left(r_{n_i}^{(0)} - r_{m_i}^{(0)}\right)}{\|\boldsymbol{r}_n^{(0)} - \boldsymbol{r}_m^{(0)}\|_2^3} - \frac{Z^2 e^2}{8\pi\epsilon_0} \sum_{m=1}^{N} \delta_{m,j} \sum_{\substack{n=1 \\ n\neq m}}^{N} \frac{-\left(r_{n_i}^{(0)} - r_{m_i}^{(0)}\right)}{\|\boldsymbol{r}_n^{(0)} - \boldsymbol{r}_m^{(0)}\|_2^3} = 0$$

$$M\nu_i^2 r_{j_i}^{(0)} - \frac{Z^2 e^2}{4\pi\epsilon_0} \sum_{\substack{m=1 \\ m\neq j}}^{N} \frac{\left(r_{j_i}^{(0)} - r_{m_i}^{(0)}\right)}{\|\boldsymbol{r}_j^{(0)} - \boldsymbol{r}_m^{(0)}\|_2^3} = 0 \tag{7.4}$$

I proceed analogously to James by defining a natural length scale, l_z, corresponding the weak trapping axis to simplify the expressions, where

$$l_z^3 = \frac{Z^2 e^2}{4\pi\epsilon_0 M \nu_z^2}. \tag{7.5}$$

The normalised equilibrium positions are then defined as $\boldsymbol{u}_j = \boldsymbol{r}_j^{(0)}/l_z = \left[\frac{x_j^{(0)}}{l_z}, \frac{y_j^{(0)}}{l_z}, \frac{z_j^{(0)}}{l_z}\right]$, allowing us to rewrite Eqn. (7.4) in terms of the normalised coordinates. After dividing through by $M\nu_i^2$, we find

$$r_{j_i}^{(0)} - \frac{l_z^3 \nu_z^2}{\nu_i^2} \sum_{\substack{m=1 \\ m\neq j}}^{N} \frac{\left(r_{j_i}^{(0)} - r_{m_i}^{(0)}\right)}{\|\boldsymbol{r}_j^{(0)} - \boldsymbol{r}_m^{(0)}\|_2^3} = 0 \tag{7.6}$$

$$r_{j_i}^{(0)} - \frac{\nu_z^2}{\nu_i^2} \sum_{\substack{m=1 \\ m \neq j}}^{N} \frac{\left(r_{j_i}^{(0)} - r_{m_i}^{(0)}\right)}{\|\boldsymbol{u}_j - \boldsymbol{u}_m\|_2^3} = 0 \tag{7.7}$$

The fraction ν_z^2/ν_i^2 will rescale the normalisation for the stronger trapping radial axes, $i \neq 3$. Dividing this expression through by l_z then produces an equation wholly in terms of the normalised coordinates,

$$u_{j_i} - \frac{\nu_z^2}{\nu_i^2} \sum_{\substack{m=1 \\ m \neq j}}^{N} \frac{\left(u_{j_i} - u_{mi}\right)}{\|\boldsymbol{u}_j - \boldsymbol{u}_m\|_2^3} = 0. \tag{7.8}$$

From Eqn. (7.8), one can numerically solve the $3N$ simultaneously equations for $j \in \{1, \ldots, N\}$ and the three axes $i \in \{1, 2, 3\}$ to calculate the values of $\boldsymbol{u}_j$. Unlike James, we cannot further simplify this expression. In the one-dimensional form this expression can be rewritten as

$$u_{j3} - \sum_{\substack{m=1 \\ m \neq j}}^{N} \frac{\left(u_{j3} - u_{m3}\right)}{|u_{j3} - u_{m3}|^3} = u_{j3} - \sum_{m=1}^{j-1} \frac{1}{\left(u_{j3} - u_{m3}\right)^2} - \sum_{m=j+1}^{N} \frac{1}{\left(u_{j3} - u_{m3}\right)^2} \tag{7.9}$$

by assuming that the ion axial positions are ordered with their index, i.e., $z_i^{(0)} > z_j^{(0)}$ for all $i > j$ with $i, j \in \{1, \ldots, N\}$. This simplification *cannot* be extended to three dimensions as the transverse equilibrium positions do not necessarily increase monotonically with index, e.g. zigzag configurations.

As an example, consider a string of $N = 5$ ions. The centre-of-mass mode (COM) frequencies are an indication of the trapping potential strength in each direction; the frequencies scale as the square root of the axial potential/radial pseudo-potential. The axial potential scales linearly with the endcap DC voltages, U_0, and the radial pseudo-potential scales quadratically with the electrode RF voltages, V_0, such that, $[\nu_x, \nu_y, \nu_z] \propto \left[V_0, V_0, \sqrt{U_0}\right]$.

In Fig. 7.1(a)-(c), the normalised equilibrium positions $\boldsymbol{u}_m$ are illustrated for three COM frequencies $\boldsymbol{\nu}/2\pi = [1.6, 1.5, 0.5]$ MHz. The positions are tabulated in Fig. 7.1(a), and the axial cross-sections are plotted showing the z-axis positions vs. the x-axis positions (Fig. 7.1(b)), and the z-axis vs. y-axis positions (Fig. 7.1(c)). For this trapping potential, the ions are spaced along the z-axis with increasing separation as they move away from the ion centre, and are centred along the x- and y-axes. If the axial potential is increased, the ions move closer together along the weak trapping z-axis, and eventually show a "zigzag" configuration in the transverse directions. This is illustrated in Fig. 7.1(d)-(f) where the axial COM frequency has been increased from $2\pi \times 0.5$ MHz to $2\pi \times 0.9$ MHz.

(a)

Ion i	u_{1i}	u_{2i}	u_{3i}	u_{4i}	u_{5i}
1	0	0	0	0	0
2	0	0	0	0	0
3	-1.74	-0.82	0	0.82	1.74

(d)

Ion i	u_{1i}	u_{2i}	u_{3i}	u_{4i}	u_{5i}
x	0	0	0	0	0
y	-0.35	0.56	0	-0.56	0.35
z	-1.32	-0.82	0	0.82	1.32

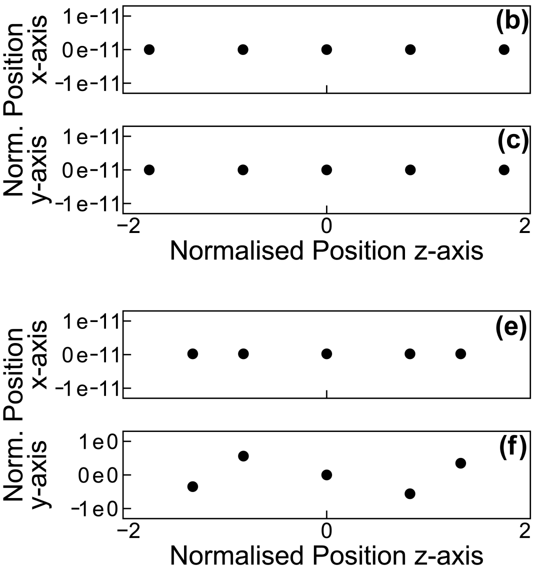

FIGURE 7.1. Normalised positions $\boldsymbol{u}_m = \boldsymbol{r}_m^{(0)}/l_z$ for $N = 5$ ions along the $i = 1, 2, 3$ directions corresponding to the x-, y-, z-axes respectively. (a)-(c) COM frequencies $\boldsymbol{\nu}/2\pi = [1.6, 1.5, 0.5]$ MHz, and (d)-(f) $\boldsymbol{\nu}/2\pi = [1.6, 1.5, 0.9]$ MHz. (a),(d) The normalised positions are tabulated for each axis. As the axial confinement is increased, the ions become more closely spaced along the z-axis. (b),(e) The cross-section positions are shown for z-axis vs. x-axis positions, with the ions approximately centred at $u_{m1} = 0$ for all ions. (c),(f) The cross-section positions are shown for z-axis vs. y-axis. Here, a "zig-zag" equilibrium position has been found along the y-axis due to the tighter axial potential.

7.1.2 Motional mode eigenvectors of an ion string in three dimensions

Having now calculated the equilibrium positions, we return to the term $\boldsymbol{q}_m(t)$ describing a time-dependent displacement from the equilibrium. I proceed by deriving the three-dimensional motional eigenspectra that will be crucial to implementing the MS gate. The N ion string will have N secular modes of oscillation along each of the three trap axes. The motion is *collective* for the entire ion string because the positively charged ions are coupled by the repulsive Coulomb interaction. The centre-of-mass (COM) mode is defined to be the mode in which all ions oscillate with equal eigenvectors and eigenvalues, as if the ions were rigidly held together. The COM mode is the lowest frequency "axial" mode, along the direction of the weak trap axis z, and the highest frequency "transverse/radial" mode, perpendicular to the trap axis x, y. The amplitude of the COM oscillation decreases with the number of ions as $1/\sqrt{N}$.

For clarity, I begin by introducing and restating several important vector quantities for the m^{th} ion.

- $\boldsymbol{r}_m(t) = [x_m(t), y_m(t), z_m(t)]$ – the position at time t
- $\boldsymbol{r}_m^{(0)} = [x_m^{(0)}, y_m^{(0)}, z_m^{(0)}]$ – the equilibrium position
- $\boldsymbol{u}_m = \boldsymbol{r}_m^{(0)}/l_z = [u_{mx}, u_{my}, u_{mz}]$ – the dimensionless equilibrium position, normalised by the natural length scale along the weak trapping axis l_z
- $\boldsymbol{q}_m(t) = [q_{mx}(t), q_{my}(t), q_{mz}(t)]$ – the displacement from equilibrium at time t, such that the position can be written as $\boldsymbol{r}_m(t) = \boldsymbol{r}_m^{(0)} + \boldsymbol{q}_m(t)$
- $\dot{\boldsymbol{q}}_m(t) = [\dot{q}_{mx}(t), \dot{q}_{my}(t), \dot{q}_{mz}(t)]$ – the first time derivative of the displacement at time t

In the following calculations, all of these vectors will be indexed by $i = 1, 2, 3$ corresponding to axis x, y, z respectively. For example, $q_{m1}(t)$ is the displacement of the m^{th} ion at time t along the x-axis.

To calculate the eigenvectors and eigenvalues for each of the motional modes, I examine the Lagrangian function describing the motion. The Lagrangian in three dimensions is

$$\mathcal{L}^{(3\text{D})} = \frac{M}{2}\sum_{m=1}^{N}\sum_{i=1}^{3}\dot{q}_{mi}(t)^2 - \frac{1}{2}\sum_{n,m=1}^{N}\sum_{i=1}^{3} q_{ni}(t) q_{mi}(t) \left.\frac{\partial^2 V^{(3\text{D})}}{\partial r_{ni}\partial r_{mi}}\right|_{r_{m_i}^{(0)}, r_{n_i}^{(0)}} + \mathcal{O}(q_{n_i}^3) \tag{7.10}$$

where the second-order partial derivative is evaluated at the equilibrium position, i.e., $r_{mi}(t) = r_{m_i}^{(0)}$ and $r_{ni}(t) = r_{n_i}^{(0)}$, or equivalently $q_{mi}(t) = q_{ni}(t) = 0$. Using the expression for the first-order derivative of $V^{(3\text{D})}$ with respect to $r_{j_i}(t)$ in Eqn. (7.4), the second-order partial derivative can be expanded.

$$\begin{aligned}
\left.\frac{\partial^2 V^{(3\text{D})}}{\partial r_{ni}\partial r_{mi}}\right|_{r_{m_i}^{(0)}, r_{n_i}^{(0)}} &= \frac{\partial}{\partial r_{ni}}\left.\left(M\nu_i^2 r_{mi}(t) - \frac{Z^2 e^2}{4\pi\epsilon_0}\sum_{\substack{p=1\\ p\neq m}}^{N} \frac{(r_{mi}(t) - r_{p_i}(t))}{\|\boldsymbol{r}_m(t) - \boldsymbol{r}_p(t)\|_2^3}\right)\right|_{r_{m_i}^{(0)}, r_{n_i}^{(0)}} \\
&= \begin{cases} M\nu_i^2\left(1 + \dfrac{\nu_z^2}{\nu_i^2}\displaystyle\sum_{\substack{p=1\\ p\neq m}}^{N}\frac{1}{\|\boldsymbol{u}_m - \boldsymbol{u}_p\|_2^3}\left(-1 + 3\frac{(u_{mi} - u_{p_i})^2}{\|\boldsymbol{u}_m - \boldsymbol{u}_p\|_2^2}\right)\right) & \text{if } n = m \\ \dfrac{M\nu_z^2}{\|\boldsymbol{u}_m - \boldsymbol{u}_n\|_2^3}\left(1 - 3\dfrac{(u_{mi} - u_{ni})^2}{\|\boldsymbol{u}_m - \boldsymbol{u}_n\|_2^2}\right) & \text{if } n \neq m \end{cases}
\end{aligned} \tag{7.11}$$

Then, the Lagrangian can be rewritten to second order in $\boldsymbol{q}_n(t)$ as

$$\mathcal{L}^{(3\text{D})} = \frac{M}{2}\sum_{i=1}^{3}\left(\sum_{m=1}^{N}\dot{q}_{mi}(t)^2 - \nu_i^2\sum_{n,m=1}^{N} A_{inm} q_{ni}(t) q_{mi}(t)\right) \tag{7.12}$$

where

$$A_{inm} = \begin{cases} 1 + \dfrac{\nu_z^2}{\nu_i^2} \displaystyle\sum_{\substack{p=1 \\ p\neq m}}^{N} \dfrac{1}{\|\boldsymbol{u}_m - \boldsymbol{u}_p\|_2^3} \left(-1 + 3\dfrac{(u_{mi} - u_{p_i})^2}{\|\boldsymbol{u}_m - \boldsymbol{u}_p\|_2^2} \right) & \text{if } n = m \\ \dfrac{\nu_z^2}{\nu_i^2} \dfrac{1}{\|\boldsymbol{u}_m - \boldsymbol{u}_n\|_2^3} \left(1 - 3\dfrac{(u_{mi} - u_{ni})^2}{\|\boldsymbol{u}_m - \boldsymbol{u}_n\|_2^2} \right) & \text{if } n \neq m \end{cases} \tag{7.13}$$

are the components of the matrices $\overset{\leftrightarrow}{\boldsymbol{A}}_i$ for the x-, y- and z-axes indexed by $i = 1, 2, 3$ respectively. The eigenspectra of the three matrices $\overset{\leftrightarrow}{\boldsymbol{A}}_i$ will determine the behaviour of the trapped ions. The N eigenvectors and eigenvalues along the i^{th} direction are defined as $\boldsymbol{b}_p^{(i)}$ and $\mu_p^{(i)}$ respectively, such that

$$\overset{\leftrightarrow}{\boldsymbol{A}}_i \boldsymbol{b}_p^{(i)} = \mu_p^{(i)} \boldsymbol{b}_p^{(i)} \quad p \in \{1, \ldots, N\},\, i \in \{1, 2, 3\}. \tag{7.14}$$

For each direction, the eigenvectors and eigenvalues of $\overset{\leftrightarrow}{\boldsymbol{A}}_i$ can be determined numerically. The matrix $\overset{\leftrightarrow}{\boldsymbol{A}}_i$ is real, symmetric and semi-positive definite, and must hence have non-negative eigenvalues and orthonormal eigenvectors. Orthonormality implies that the modal matrix $\overset{\leftrightarrow}{\boldsymbol{V}}_i$ created with the eigenvectors of $\overset{\leftrightarrow}{\boldsymbol{A}}_i$ as its columns, $\overset{\leftrightarrow}{\boldsymbol{V}}_i = [\boldsymbol{b}_1^{(i)} \ldots \boldsymbol{b}_N^{(i)}]$, is orthogonal, such that $\overset{\leftrightarrow}{\boldsymbol{V}}_i^{\dagger} \overset{\leftrightarrow}{\boldsymbol{V}}_i = \overset{\leftrightarrow}{\boldsymbol{V}}_i \overset{\leftrightarrow}{\boldsymbol{V}}_i^{\dagger} = \hat{\mathbb{I}}$. The orthonormality condition can be re-expressed in terms of a sum over eigenvector components as

$$\sum_{m=1}^{N} b_{p_m}^{(i)} b_{q_m}^{(i)} = \delta_{p,q} \tag{7.15}$$

$$\sum_{p=1}^{N} b_{p_m}^{(i)} b_{p_n}^{(i)} = \delta_{m,n} \tag{7.16}$$

where $b_{p_m}^{(i)}$ is the m^{th} element of the p^{th} eigenvector along the i^{th} axis, $\boldsymbol{b}_p^{(i)}$.

The eigenvectors describe the motion of each ion m for each motional mode p. The collective modes can be expressed in terms of individual local ion coordinates $q_{mi}(t)$ as

$$Q_p^{(i)}(t) = \sum_{m=1}^{N} b_{p_m}^{(i)} q_{mi}(t), \tag{7.17}$$

or equivalently, the local ion coordinates can be expressed in terms of the collective motion,

$$q_{mi}(t) = \sum_{p=1}^{N} b_{p_m}^{(i)} Q_p^{(i)}(t). \tag{7.18}$$

To transform between these two expressions, the orthonormality rules in Eqns. (7.15), (7.16) can be straightforwardly applied.

Using the expression for the local ion coordinates (Eqn. 7.18), the Lagrangian can be rewritten in terms of the collective motional modes. For the kinetic energy term,

$$\begin{aligned}\frac{M}{2}\sum_{i=1}^{3}\sum_{m=1}^{N}\dot{q}_{m_i}(t)^2 &= \frac{M}{2}\sum_{i=1}^{3}\sum_{m=1}^{N}\sum_{p,q=1}^{N} b_{p_m}^{(i)} b_{q_m}^{(i)} \dot{Q}_p^{(i)}(t)\dot{Q}_q^{(i)}(t)\\ &= \frac{M}{2}\sum_{i=1}^{3}\sum_{p,q=1}^{N}\dot{Q}_p^{(i)}(t)\dot{Q}_q^{(i)}(t)\sum_{m=1}^{N} b_{p_m}^{(i)} b_{q_m}^{(i)}\\ &= \frac{M}{2}\sum_{i=1}^{3}\sum_{p=1}^{N}\dot{Q}_p^{(i)}(t)^2, \end{aligned} \tag{7.19}$$

where I have used the eigenvector orthonormality (Eqn. (7.15)) in the last line. For the potential energy term, the matrix $\overset{\leftrightarrow}{\boldsymbol{A}}_i$ is rewritten in terms of its modal matrix $\overset{\leftrightarrow}{\boldsymbol{V}}_i$, formed using the eigenvectors of $\overset{\leftrightarrow}{\boldsymbol{A}}_i$ as its columns, and special diagonal matrix $\overset{\leftrightarrow}{\boldsymbol{D}}_i$, which consists of the eigenvalues of $\overset{\leftrightarrow}{\boldsymbol{A}}_i$ along its diagonal.

$$\overset{\leftrightarrow}{\boldsymbol{A}}_i = \overset{\leftrightarrow}{\boldsymbol{V}}_i \overset{\leftrightarrow}{\boldsymbol{D}}_i \overset{\leftrightarrow}{\boldsymbol{V}}_i^{\dagger} \tag{7.20}$$

$$\begin{aligned} A_{inm} &= \sum_{p=1}^{N} V_{inp} D_{ipp} V_{imp}\\ &= \sum_{p=1}^{N} \mu_p^{(i)} b_{p_n}^{(i)} b_{p_m}^{(i)} \end{aligned} \tag{7.21}$$

Then the potential energy term can be rewritten as

$$\begin{aligned}\frac{M}{2}\sum_{i=1}^{3}\nu_i^2\sum_{n,m=1}^{N} A_{inm} q_{n_i}(t) q_{m_i}(t) &= \frac{M}{2}\sum_{i=1}^{3}\nu_i^2\sum_{n,m=1}^{N}\sum_{p=1}^{N}\mu_p^{(i)} b_{p_n}^{(i)} b_{p_m}^{(i)} q_{n_i}(t) q_{m_i}(t)\\ &= \frac{M}{2}\sum_{i=1}^{3}\nu_i^2\sum_{p=1}^{N}\mu_p^{(i)}\left(\sum_{m=1}^{N} b_{p_m}^{(i)} q_{m_i}(t)\right)^2\\ &= \frac{M}{2}\sum_{i=1}^{3}\sum_{p=1}^{N}{\nu_i^{(p)}}^2 {Q_p^{(i)}(t)}^2. \end{aligned} \tag{7.22}$$

Here, I have introduced a new term for the frequency of the p^{th} motional mode along the i^{th} axis, $\nu_i^{(p)}$. This term is calculated from the centre-of-mass mode frequency along the i^{th} axis ν_i as

$$\nu_i^{(p)} = \sqrt{\mu_p^{(i)}}\,\nu_i. \tag{7.23}$$

In particular, the centre-of-mass mode corresponds to an eigenvalue of $\mu_p^{(i)} = 1$.

	Eigenvectors b_{p_m}			Eigenvalues			Mode frequency (MHz)		
Mode p	Ion 1	Ion 2	Ion 3	x	y	z	x	y	z
1	0.577	0.577	0.577	1.0	1.0	1.0	1.6	1.5	0.5
2	-0.707	0	0.707	0.902	0.889	3.0	1.520	1.414	0.866
3	0.408	-0.817	0.408	0.766	0.733	5.8	1.400	1.285	1.204

TABLE 7.1. Eigenvectors, eigenvalues and mode frequencies for an $N = 3$ ion string with $3N = 9$ modes, with centre-of-mass frequencies $\boldsymbol{\nu}/2\pi = [1.6, 1.5, 0.5]$ MHz. Each axis has three collective motional modes; these modes have common eigenvectors across the three axes but differing eigenvalues. The first mode ($p = 1$) is the COM mode, where all ions have equal eigenvectors. This is the lowest frequency mode in the axial (z) direction, and the highest frequency mode along the transverse (x, y) directions. Equation (7.23) is used to convert between the mode eigenvalues and frequencies.

When the axial potential is sufficiently relaxed for the ions to be centred along the transverse axes, with normalised equilibrium positions $u_{xm} = u_{y_m} = 0$ for all ions, the matrix $\overleftrightarrow{\boldsymbol{A}}$ simplifies to

$$A_{inm} = \begin{cases} 1 + \dfrac{\nu_z^2}{\nu_i^2} \displaystyle\sum_{\substack{p=1 \\ p \neq m}}^{N} \dfrac{1}{|u_{m3} - u_{p3}|^3} (-1 + 3\delta_{i,3}) & \text{if } n = m \\ \dfrac{\nu_z^2}{\nu_i^2} \dfrac{1}{|u_{m3} - u_{n3}|^3} (1 - 3\delta_{i,3}) & \text{if } n \neq m \end{cases} \tag{7.24}$$

where $\delta_{i,3}$ is the Kronecker delta. In this case, because the matrices for each axis commute, then if the matrices are diagonalisable it implies that they must be *simultaneously* diagonalisable. Consequently, all three axes have equal eigenvectors describing the motional modes, although they will have differing eigenvalues.

As an example, we consider $N = 3$ ions with COM frequencies $\boldsymbol{\nu}/2\pi = [1.6, 1.5, 0.5]$ MHz. The eigenvectors, eigenvalues and mode frequencies are shown in Tab. 7.1. As the ions are centred along the transverse axes for this potential, the eigenvectors are common for the three axes and are only written explicitly once. Figure 7.2 shows an example of the oscillatory movement when an axial motional mode is excited for three trapped $^{171}\text{Yb}^+$ ions. Voltages were applied to the ion trap endcaps to excite the axial COM (left) and "breathing" (right) modes, corresponding to modes $p = 1$ and $p = 2$ in Tab. 7.1 respectively.

The expressions derived in this first section can be used to calculate the equilibrium positions, motional mode directions/eigenvectors, and motional mode frequencies for any number of trapped ions along

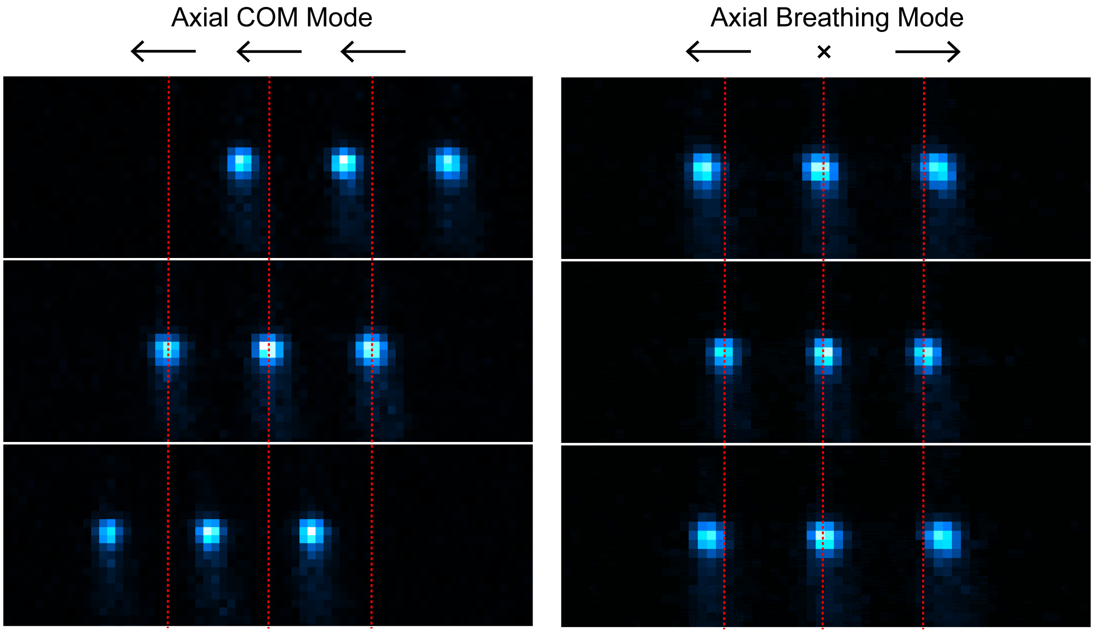

FIGURE 7.2. Images of a three-ion ^{171}Yb^{+} chain when the axial centre-of-mass mode (left), and the breathing mode (right) are excited. The eigenvector directions for each ion are shown at the top of each column. Red dashed lines provide guides to the eye to indicate the ions' displacements. Image credit to C. Hempel, Quantum Control Laboratory, University of Sydney.

each of the three trapping directions. This work has been a critical element for predicting Mølmer-Sørensen gate fidelity and optimising gate parameters, as well as designing experiments such as chemical simulations in trapped ion systems [**243**].

7.2 Description of the Mølmer-Sørensen evolution

Now that we have arrived at a formalism to calculate the behaviour of the collective modes of oscillation for an ion string, we can move onto describing the Mølmer-Sørensen gate, which couples the motional degrees of freedom with the ions' electronic degrees of freedom to achieve qubit-qubit entanglement. In this section, I will simplify the notation from the previous section for motional mode frequencies and eigenvectors. Rather than explicitly separating the $3N$ modes into the three axis components and then labelling them from $p = 1, \dots N$, e.g. $\nu_p^{(x)}$, I instead combine all modes into one set and index them from $k = 1, \dots, 3N$, e.g. ν_k.

In the following sections, I will discuss large Hilbert spaces describing multiple qubits and oscillator modes. To describe coupling between operators acting on different subspaces I use the symbol $\otimes$, which represents a tensor product. The relevant operators for the qubit and oscillator modes are defined in the following manner. The Pauli operator in a two-dimensional Hilbert space for basis $j \in \{x, y, z\}$ is represented as $\hat{\sigma}_j$: this is the operator that acts on a *single* qubit. By contrast, the operator denoted $\hat{\sigma}_j^{(\mu)}$ is the Pauli operator in basis j acting on the μ^{th} qubit *embedded* in the entire relevant qubit subspace, i.e. $\hat{\sigma}_j^{(\mu)} = \hat{\mathbb{I}} \otimes \cdots \otimes \hat{\mathbb{I}} \otimes \hat{\sigma}_j \otimes \hat{\mathbb{I}} \otimes \cdots \hat{\mathbb{I}}$, such that all qubits other than the μ^{th} are acted upon by the two-dimensional identity operator, $\hat{\mathbb{I}}$. Similarly, $\hat{a}^\dagger, \hat{a}$ are the creation and annihilation operators for a single mode, and $\hat{a}_k^\dagger, \hat{a}_k$ are the operators for the k^{th} mode embedded in the full motional subspace, $\hat{a}_k^\dagger = \hat{\mathbb{I}} \otimes \cdots \otimes \hat{\mathbb{I}} \otimes \hat{a}^\dagger \otimes \hat{\mathbb{I}} \otimes \cdots \hat{\mathbb{I}}$. To couple the qubit and motional subspaces, I will use an explicit tensor product, e.g. $\hat{\sigma}_x^{(\mu)} \otimes \hat{a}_k^\dagger$. Finally, the collective Pauli-x operator acting on the two qubits μ and ν is defined as,

$$\hat{S}_x^{(\mu\nu)} = \hat{\sigma}_x^{(\mu)} + \hat{\sigma}_x^{(\nu)} \tag{7.25}$$

$$\hat{S}_x^{(\mu\nu)^2} = 2\hat{\mathbb{I}} \otimes \hat{\mathbb{I}} + 2\hat{\sigma}_x^{(\mu)}\hat{\sigma}_x^{(\nu)} \tag{7.26}$$

using a basic property of Pauli matrices, $\hat{\sigma}_x^{(\mu)^2} = \hat{\mathbb{I}} \otimes \hat{\mathbb{I}}$, and the commutation of matrices acting on different subspaces, $\hat{\sigma}_x^{(\mu)}\hat{\sigma}_x^{(\nu)} = \hat{\sigma}_x^{(\nu)}\hat{\sigma}_x^{(\mu)}$.

The qubit-motion interaction can be mediated by a bichromatic laser pulse, with components tuned below (red) and above (blue) the bare qubit transition. The components are detuned by an amount equivalent to one motional mode quanta for the k^{th} mode, ν_k, with an additional detuning δ_k. The detuning is defined as $\delta_k = \omega_b - \omega_0 - \nu_k = \omega_0 - \nu_k - \omega_r$, where ω_b (ω_r) is the frequency of the blue (red) component of the bichromat, ω_0 is the qubit frequency, and ν_k is the frequency of the k^{th} motional mode. All of these frequencies are angular. The qubit-qubit interaction basis $\hat{\sigma}_{\phi_s} \otimes \hat{\sigma}_{\phi_s}$ is determined by the optical phases ϕ_r and ϕ_b of the red and blue components respectively, such that

$$\phi_s = \frac{\phi_b + \phi_r}{2} \tag{7.27}$$

$$\hat{\sigma}_{\phi_s} = \cos{(\phi_s)}\hat{\sigma}_x + \sin{(\phi_s)}\hat{\sigma}_y. \tag{7.28}$$

By setting $\phi_r = -\phi_b$, the interaction basis is fixed as $\hat{\sigma}_{\phi_s} \otimes \hat{\sigma}_{\phi_s} = \hat{\sigma}_x \otimes \hat{\sigma}_x$.

We consider a system of N qubits coupled to M bosonic oscillator modes described by the Hamiltonian

$$\hat{H}_{\text{MS}}(t) = i\hbar \sum_{\mu=1}^{N} \hat{\sigma}_{\phi_s}^{(\mu)} \otimes \sum_{k=1}^{M} \left(\gamma_k^{(\mu)}(t)\hat{a}_k^\dagger - \gamma_k^{(\mu)^*}(t)\hat{a}_k \right) \tag{7.29}$$

$$\gamma_k^{(\mu)}(t) = \Omega f_k^{(\mu)} e^{-i\delta_k t} \tag{7.30}$$

where the creation and annihilation operators $\hat{a}_k^\dagger$, $\hat{a}_k$ act on the k^{th} oscillator mode. The term $\gamma_k^{(\mu)}(t)$ describes the coupling between the μ^{th} qubit and k^{th} mode; it can be represented as a trajectory in phase space. The coupling strength is determined by the overall coupling strength between the qubits and the driving field Ω (Rabi frequency), and a hardware-specific coupling parameter $f_k^{(\mu)}$.

In a system of trapped ions, the oscillator modes correspond to collective motional modes of the ions in the trapping potential. The interaction strength between the μ^{th} ion and the k^{th} motional mode with the driving field is captured by the Lamb-Dicke parameter $\eta_k^{(\mu)}$,

$$f_k^{(\mu)} = \frac{-i\eta_k^{(\mu)}}{2} = \frac{-i}{2} b_{k\mu} \tilde{k} \cos(\theta) \sqrt{\frac{\hbar}{2M\nu_k}}, \tag{7.31}$$

which incorporates the motional mode eigenvector for mode k and ion μ, $b_{k\mu}$, and the overlap of the spatial structure of the motional mode with the effective wavevector of the driving field [**7**]. This uses the following parameters: the mediating laser wavevector, $\tilde{k}$; the angle between the wavevector and the mode orientation, θ; the angular frequency of the mode, ν_k; the mass of a single $^{171}\text{Yb}^+$ ion, M; and Planck's constant, $\hbar$.

The Hamiltonian (7.29) produces a state-dependent force in the $[\hat{\sigma}_x]^{\otimes N}$-eigenbasis, as described by the unitary evolution

$$\begin{aligned} \hat{U}_{\text{MS}}(t) &= \exp\left\{-i\int_0^t \hat{H}_{\text{MS}}(t_1)dt_1 + \frac{(-i)^2}{2}\int_0^t dt_1 \int_0^{t_1} dt_2 [\hat{H}_{\text{MS}}(t_1), \hat{H}_{\text{MS}}(t_2)] + \ldots\right\} \\ &= \exp\left\{\sum_{\mu=1}^{N} \hat{\sigma}_x^{(\mu)} \otimes \hat{B}_\mu(t)\right\} \exp\left\{i \sum_{\mu,\nu=1}^{N} \varphi_{\mu\nu}(t) \hat{\sigma}_x^{(\mu)} \hat{\sigma}_x^{(\nu)}\right\}, \end{aligned} \tag{7.32}$$

which is obtained from the Magnus expansion, where all higher order terms after the first two are identically zero. These first two terms commute and can hence be separated into individual exponentials describing two key components of the evolution.

For $N > 1$ qubits, the second component produces pairwise entanglement between qubits μ and ν, captured by the phase

$$\varphi_{\mu\nu}(t) = \text{Im}\left[\sum_{k=1}^{M} \int_0^t dt_1 \int_0^{t_1} dt_2 \gamma_k^{(\mu)}(t_1) \gamma_k^{(\nu)*}(t_2)\right], \tag{7.33}$$

which will achieve maximum qubit-qubit entanglement when $\varphi_{\mu\nu}(t) = \pi/8$.

The first component in Eqn. (7.32) describes a qubit-state-dependent displacement of the oscillator modes,

$$\exp\left\{\sum_{\mu=1}^{N}\hat{\sigma}_x^{(\mu)}\otimes\hat{B}_\mu(t)\right\}=\exp\left\{\sum_{\mu=1}^{N}\hat{\sigma}_x^{(\mu)}\otimes\sum_{k=1}^{M}\left(f_k^{(\mu)}\alpha_k(t)\hat{a}_k^\dagger-f_k^{(\mu)*}\alpha_k(t)^*\hat{a}_k\right)\right\} \tag{7.34}$$

$$\alpha_k(t)=\Omega\int_0^t dt'e^{-i\delta_k t'} \tag{7.35}$$

where the term $\alpha_k(t)$ represents the circular displacement trajectory in the phase space corresponding to the k^{th} oscillator.

The action of Eqn. (7.34) on the qubit-oscillator system can be expressed in terms of the "displacement operators", $\hat{D}(\alpha)=\exp\{\alpha\hat{a}^\dagger-\alpha^*\hat{a}\}$, which use the creation and annihilation operators to displace a state in phase space along a trajectory described by the argument α. One can consider the different phase space trajectories corresponding to each individual oscillator mode using $\hat{D}_k(\alpha_k)=\exp\{\alpha_k\hat{a}_k^\dagger-\alpha_k^*\hat{a}_k\}$. To incorporate the qubit-state dependence into the displacement, the qubit and motional operators are coupled via a tensor product within the displacement operator,

$$\hat{D}_k(\hat{\sigma}_x^{(\mu)}\alpha_k)=\exp\{\hat{\sigma}_x^{(\mu)}\otimes(\alpha_k\hat{a}_k^\dagger-\alpha_k^*\hat{a}_k)\}. \tag{7.36}$$

For more details on the properties of the displacement operator, see App. A.

I rewrite the first term of the unitary as a product of displacement operators,

$$\exp\left\{\sum_{\mu=1}^{N}\hat{\sigma}_x^{(\mu)}\otimes\hat{B}_\mu(t)\right\}=\prod_{k=1}^{M}\hat{D}_k\left(\sum_{\mu=1}^{N}\hat{\sigma}_x^{(\mu)}f_k^{(\mu)}\alpha_k(t)\right), \tag{7.37}$$

to show that the operator creates a qubit-state-dependent displacement for each qubit-oscillator wave-packet. More explicitly, the N-qubit system can be described by 2^N eigenstates in the $[\hat{\sigma}_x]^{\otimes N}$-basis. Under the action of the displacement operator, the wave packet associated with the k^{th} oscillator splits as each component becomes entangled with one of the qubit eigenstates and is coherently displaced along a circular trajectory in phase space proportional to $\alpha_k(t)$. Any residual oscillator excitation, captured by non-zero $\alpha_k(\tau_g)$ at the conclusion of the gate time τ_g, results in a loss of qubit-qubit entanglement fidelity because the motional and qubit state spaces are still coupled.

The magnitude and orientation of the phase-space displacement are determined by an interplay between the wave packet's $\hat{\sigma}_x^{(\mu)}$ eigenvalues and the mode's Lamb-Dicke parameters. More precisely, each eigenstate in the $[\hat{\sigma}_x]^{\otimes N}$-basis written as $|E_l\rangle$ has an associated eigenvalue $E_l^{(\mu)}=\pm1$ for the $\hat{\sigma}_x^{(\mu)}$ operator, which acts on the μ^{th} qubit. For a particular mode k, acting the state-dependent displacement operator (Eqn. (7.37)) on the separable qubit-oscillator state $|E_l\rangle \otimes \rho_k$, with the oscillator ρ_k in a thermal state, displaces the wave packet in phase space along the trajectory

$$\alpha_{k,l}(t) = \sum_{\mu=1}^{N} E_l^{(\mu)} f_k^{(\mu)} \alpha_k(t). \tag{7.38}$$

Here, both $E_l^{(\mu)}$ and $f_k^{(\mu)}$ can be positive or negative, giving interference between different terms in the sum, and hence their combination over the sum of ions will set the net orientation and magnitude of the wave packet displacement.

For example, consider the motion of two ions along a particular axis, with a COM mode (equal eigenvectors for both ions, such that $f_k^{(1)} = f_k^{(2)}$) and a "tilt" mode (equal magnitude and opposite sign Lamb-Dicke parameters for both ions, $f_k^{(1)} = -f_k^{(2)}$). Here, the even eigenstates $|{+}{+}\rangle, |{-}{-}\rangle$ will be displaced when the COM mode is excited because the terms $E_l^{(\mu)}$ and $f_k^{(\mu)}$ add constructively, whereas the odd eigenstates $|{+}{-}\rangle, |{-}{+}\rangle$ will remain at the origin in phase space. The opposite will be true of the tilt mode.

Despite the unique interference patterns, all of the displaced wave packet trajectories remain proportional to the base trajectory $\alpha_k(t)$, and hence are forced to return periodically to the origin with a period of $2\pi/|\delta_k|$. Consequently, the motional decoupling condition can be expressed as

$$\alpha_k(\tau_g) = \Omega \int_0^{\tau_g} dt e^{-i\delta_k t} = 0 \qquad \text{for all } k \in \{1, \ldots, M\}. \tag{7.39}$$

For an individual mode this condition can be satisfied by setting $\delta_k \tau_g = 2\pi n$, $n \in \mathbb{Z}$, which will conclude the gate at the natural trajectory period. However, as the number of oscillator modes is increased, this condition becomes intractably difficult to solve for all values of δ_k simultaneously, and necessitates prohibitively long gate times. To address this, we introduce a time-dependent modulation of the motional phase of the driving force, $\phi(t) = (\phi_b(t) - \phi_r(t))/2$, allowing us to rewrite the decoupling condition as

$$\alpha_k(\tau_g) = \Omega \int_0^{\tau_g} dt e^{-i[\delta_k t + \phi(t)]} = 0 \qquad \text{for all } k \in \{1, \ldots, M\}, \tag{7.40}$$

which can be solved for piece-wise constant values of $\phi(t)$ either analytically [**9**] or using a multi-objective numerical optimisation. Both solutions are experimentally validated in the work in Chapter 8.

7.3 Measurement of observables after Mølmer-Sørensen evolution

In this section, I calculate analytic expressions for an observable after the application of the Mølmer-Sørensen (MS) time evolution operator. This work facilitates the use of arbitrary phase shifts, as required for the experimental work in Chapter 8, and calculates a generalised expression describing any two addressed ions embedded within an N-ion register and coupled to any number of modes. The derivation presented here follows and extends the original approach presented by Roos et al. [**10**] and Kirchmair et al. [**8**], which was restricted to considering two ions from a two-ion register coupled to one motional mode. Examples of observables that can be calculated include the state populations, used to validate experimental measurements in Figs. 8.4 and 8.6 of Chapter 8, and the experimentally measurable Bell state fidelity, used in Fig. 8.5 of Chapter 8.

7.3.1 General observable calculation for two qubits

I begin the derivation by considering two specific qubits, indexed by μ and ν, embedded within an N-ion register, that are coupled to M motional modes and addressed by the MS interaction. The MS unitary operator can be separated into its two commuting components, $\hat{U}_{\text{MS}}(t) = \hat{U}_1(t)\hat{U}_2(t)$, with $\hat{U}_1(t)$ describing the qubit-qubit entanglement and $\hat{U}_2(t)$ describing qubit-oscillator coupling.

$$\begin{aligned}\hat{U}_1(t) &= \exp\left\{ i \sum_{\mu',\nu'=\mu,\nu} \varphi_{\mu'\nu'}(t)\hat{\sigma}_x^{(\mu')}\hat{\sigma}_x^{(\nu')} \right\} \\ &\equiv \exp\left\{ i\varphi(t)\hat{S}_x^{(\mu\nu)^2} \right\}, \end{aligned} \tag{7.41}$$

$$\hat{U}_2(t) = \prod_{k=1}^{M} \hat{D}_k \left(\sum_{\mu'=\mu,\nu} \hat{\sigma}_x^{(\mu')} \alpha_k^{(\mu')}(t) \right) \tag{7.42}$$

Here, the summations have changed from being over all N qubits, as in Eqn. (7.32), to selectively choosing the two addressed qubits μ and ν. The entangling phase accumulated between the two qubits, $\varphi(t) \equiv \varphi_{\mu\nu}(t) = \varphi_{\nu\mu}(t)$, can be calculated using Eqn. (7.33) and the final equivalence for $\hat{U}_1(t)$ holds up to a global phase. I introduce the term

$$\alpha_k^{(\mu)}(t) = f_k^{(\mu)}\alpha_k(t) = f_k^{(\mu)}\Omega \int_0^t dt' e^{-i(\delta_k t' + \phi(t'))} \tag{7.43}$$

to describe the motional coupling between the k^{th} mode and μ^{th} qubit with scaling factors added to characterise the coupling strength.

To measure a qubit observable given by the operator $\hat{\mathcal{O}}$, one can take the trace after multiplying $\hat{\mathcal{O}}$ with the final density matrix, ρ_f: $O(t) = \mathrm{Tr}\left[\hat{\mathcal{O}}\rho_f\right]$. To represent the qubit-oscillator state, I introduce the notation $\bigotimes_{k=1}^{M}$ to represent a tensor product between many terms, in analogy to the big Sigma and big Pi notation for summation and multiplication. An initially separable qubit-oscillator state of two targeted qubits and M oscillators is prepared in,

$$\begin{aligned} \rho_Q \bigotimes_{k=1}^{M} \rho_k &= |00\rangle\langle 00| \bigotimes_{k=1}^{M} \sum_{n_k=0}^{\infty} p_{n_k} |n_k\rangle\langle n_k| \qquad (7.44) \\ &= |00\rangle\langle 00| \otimes \sum_{n_1,\ldots,n_k,\ldots,n_M=0}^{\infty} p_{n_1}\cdots p_{n_k}\cdots p_{n_M} |n_1\ldots n_k\ldots n_M\rangle\langle n_1\ldots n_k\ldots n_M| \end{aligned}$$

where each oscillator is in a thermal state with mean phonon number $\bar{n}_k$ such that the coefficient is given by $p_{n_k} = [1/(\bar{n}_k+1)][\bar{n}_k/(\bar{n}_k+1)]^{n_k}$. The initial density matrices ρ_Q and ρ_k correspond to the two-qubit subspace and the oscillator subspace for mode k respectively, with both qubits prepared in $|0\rangle$. In the final line, I remove the explicit tensor notation to rewrite the motional states as $|n_1\ldots n_k\ldots n_M\rangle := |n_1\rangle\otimes\cdots\otimes|n_k\rangle\otimes\cdots\otimes|n_M\rangle$, with M sums over all possible phonon occupancy values (zero to infinity) for each mode $k\in\{1,\ldots,M\}$.

For this initial state, the evolution of an observable quantity after applying the MS operator is given by

$$\begin{aligned} O(t) &= \mathrm{Tr}\left[\hat{\mathcal{O}}\hat{U}_1\hat{U}_2\left(\rho_Q \bigotimes_{k=1}^{M}\rho_k\right)\hat{U}_2^\dagger\hat{U}_1^\dagger\right] \\ &= \sum_{n_1,\ldots,n_M=0}^{\infty} p_{n_1}\cdots p_{n_M}\mathrm{Tr}_Q\left[\rho_Q\langle n_1\cdots n_M|\,\hat{U}_2^\dagger\hat{U}_1^\dagger\hat{\mathcal{O}}\hat{U}_1\hat{U}_2\,|n_1\cdots n_M\rangle\right] \qquad (7.45) \end{aligned}$$

where $\mathrm{Tr}_Q\left[.\right]$ is the trace over the qubit subspace. Note that neither operator $\hat{U}_1(t)$ or $\hat{\mathcal{O}}$ act on the oscillator states and will hence commute with any purely motional subspace operators.

To calculate the outcome of Eqn. (7.45), we first rewrite $\hat{U}_2(t)$ in terms of the projection operators onto the four eigenstates of $\hat{S}_x^{(\mu\nu)}$: $\hat{P}_{++}, \hat{P}_{+-}, \hat{P}_{-+}, \hat{P}_{--}$, corresponding to the eigenstates $|{++}\rangle_x, |{+-}\rangle_x$, $|{-+}\rangle_x, |{--}\rangle_x$ respectively. Note, μ is referenced as the first qubit for each state and ν is the second.

$$\begin{aligned} \hat{U}_2(t) &= \prod_{k=1}^{M}\hat{D}_k\left(\sum_{\mu'=\mu,\nu}\hat{\sigma}_x^{(\mu')}\alpha_k^{(\mu')}(t)\right) \\ &= \prod_{k=1}^{M}\exp\left\{\sum_{\mu'=\mu,\nu}\hat{\sigma}_x^{(\mu')}\otimes\left(\alpha_k^{(\mu')}(t)\hat{a}_k^\dagger - \alpha_k^{(\mu')}(t)^*\hat{a}_k\right)\right\} \end{aligned}$$

$$= \prod_{k=1}^{M} \Big[\hat{P}_{++} \otimes \hat{D}_k \left(+\alpha_k^{(\mu)}(t) + \alpha_k^{(\nu)}(t) \right) + \hat{P}_{+-} \otimes \hat{D}_k \left(+\alpha_k^{(\mu)}(t) - \alpha_k^{(\nu)}(t) \right)$$

$$+ \hat{P}_{-+} \otimes \hat{D}_k \left(-\alpha_k^{(\mu)}(t) + \alpha_k^{(\nu)}(t) \right) + \hat{P}_{--} \otimes \hat{D}_k \left(-\alpha_k^{(\mu)}(t) - \alpha_k^{(\nu)}(t) \right) \Big]$$

$$=: \left[\hat{P}_{++} \otimes \prod_{k=1}^{M} \hat{D}_k(\alpha_{k++}) + \hat{P}_{+-} \otimes \prod_{k=1}^{M} \hat{D}_k(\alpha_{k+-}) \right.$$

$$\left. + \hat{P}_{-+} \otimes \prod_{k=1}^{M} \hat{D}_k(\alpha_{k-+}) + \hat{P}_{--} \otimes \prod_{k=1}^{M} \hat{D}_k(\alpha_{k--}) \right] \tag{7.46}$$

The term $\alpha_{kXY} := X\alpha_k^{(\mu)} + Y\alpha_k^{(\nu)}$ for $X, Y \in \{+, -\}$ has been introduced for simplicity. In the final line, the product over M modes has been moved to the individual displacement operator terms; this is possible using the identities of the projection operators, $\hat{P}_{ij}\hat{P}_{kl} = \hat{P}_{ij}\delta_{ik}\delta_{jl}$.

When the four terms in Eqn. (7.46) are substituted for $\hat{U}_2$ and $\hat{U}_2^\dagger$ in the observable evolution given by Eqn. (7.45), 16 cross-terms are produced. The terms can be separated using trace linearity. We consider the form of one such term created from $\hat{P}_{X_1Y_1} \otimes \hat{D}_k(\alpha_{kX_1Y_1})$ in $\hat{U}_2^\dagger$ and $\hat{P}_{X_2Y_2} \otimes \hat{D}_k(\alpha_{kX_2Y_2})$ in $\hat{U}_2$.

$$O_{X_1Y_1X_2Y_2} = \sum_{n_1,\ldots,n_M=0}^{\infty} p_{n_1} \cdots p_{n_M} \mathrm{Tr}_Q \left[\rho_Q \langle n_1 \ldots n_M | \left(\hat{P}^\dagger_{X_1Y_1} \otimes \prod_{k=1}^{M} \hat{D}_k^\dagger(\alpha_{kX_1Y_1}) \right) \hat{U}_1^\dagger \hat{O} \hat{U}_1 \right.$$

$$\left. \times \left(\hat{P}_{X_2Y_2} \otimes \prod_{k'=1}^{M} \hat{D}_{k'}(\alpha_{k'X_2Y_2}) \right) | n_1 \ldots n_M \rangle \right]$$

$$= \mathrm{Tr}_Q \left[\hat{U}_1^\dagger \hat{O} \hat{U}_1 \hat{P}_{X_2Y_2} \rho_Q \hat{P}_{X_1Y_1} \right.$$

$$\left. \otimes \sum_{n_1,\ldots,n_M=0}^{\infty} p_{n_1} \cdots p_{n_M} \langle n_1 \ldots n_M | \prod_{k=1}^{M} \hat{D}_k(-\alpha_{kX_1Y_1}) \hat{D}_k(\alpha_{kX_2Y_2}) | n_1 \ldots n_M \rangle \right] \tag{7.47}$$

Here, I have utilised the relations $\hat{D}_k(\alpha)^\dagger = \hat{D}_k(-\alpha)$ and $\hat{P}^\dagger_{XY} = \hat{P}_{XY}$. To separate the qubit and motional components, the phonon sums and coefficients have been brought into the trace using the linearity of the trace. The two products over the M modes indexed by k, k' have been combined by gathering the displacement operators for the same mode using the relation $[\hat{D}_k(\alpha), \hat{D}_j(\beta)] = 0$ if $j \neq k$.

This expression can be simplified using properties of the displacement operator. Namely,

$$\hat{D}_k(\alpha)\hat{D}_k(\beta) = \hat{D}_k(\alpha + \beta) e^{(\alpha\beta^* - \alpha^*\beta)/2}, \tag{7.48}$$

$$\sum_{n_k=0}^{\infty} p_{n_k} \langle n_k | \hat{D}_k(\alpha_k) | n_k \rangle = e^{-|\alpha_k|^2 \left(\bar{n}_k + \frac{1}{2}\right)} \tag{7.49}$$

when the coefficients p_{n_k} describe a thermal state [**10**]. Using these relations, the cross-term becomes

$$\begin{aligned} O_{X_1Y_1X_2Y_2} &= \mathrm{Tr}_Q \Big[\hat{U}_1^\dagger \hat{O} \hat{U}_1 \hat{P}_{X_2Y_2} \rho_Q \hat{P}_{X_1Y_1} e^{(-\alpha_{kX_1Y_1}\alpha^*_{kX_2Y_2} + \alpha^*_{kX_1Y_1}\alpha_{kX_2Y_2})/2} \\ &\qquad \times \sum_{n_1,\ldots,n_M=0}^{\infty} p_{n_1}\cdots p_{n_M} \langle n_1 \ldots n_M | \prod_{k=1}^{M} \hat{D}_k(-\alpha_{kX_1Y_1} + \alpha_{kX_2Y_2}) | n_1 \ldots n_M \rangle \Big] \\ &= \mathrm{Tr}_Q \Big[\hat{U}_1^\dagger \hat{O} \hat{U}_1 \hat{P}_{X_2Y_2} \rho_Q \hat{P}_{X_1Y_1} e^{-\sum_{k=1}^{M} |\alpha_{kX_2Y_2} - \alpha_{kX_1Y_1}|^2 \left(\bar{n}_k + \frac{1}{2}\right)}\Big]. \end{aligned} \tag{7.50}$$

In the final line, we are able to eliminate the term

$$e^{(-\alpha_{kX_1Y_1}\alpha^*_{kX_2Y_2} + \alpha^*_{kX_1Y_1}\alpha_{kX_2Y_2})/2} = e^{-\mathcal{I}m\left[\alpha_{kX_1Y_1}\alpha^*_{kX_2Y_2}\right]} = 1 \tag{7.51}$$

because the exponent simplifies to zero. This can be seen by noting that $\alpha_{kX_1Y_1}\alpha^*_{kX_2Y_2}$ is real,

$$\begin{aligned} \alpha_{kX_1Y_1}\alpha^*_{kX_2Y_2} &= \left(X_1\alpha_k^{(\mu)} + Y_1\alpha_k^{(\nu)}\right)\left(X_2\alpha_k^{(\mu)*} + Y_2\alpha_k^{(\nu)*}\right) \\ &= \left(X_1\frac{-i\eta_k^{(\mu)}}{2}\alpha_k + Y_1\frac{-i\eta_k^{(\nu)}}{2}\alpha_k\right)\left(X_2\frac{i\eta_k^{(\mu)}}{2}\alpha_k^* + Y_2\frac{i\eta_k^{(\nu)}}{2}\alpha_k^*\right) \\ &= \frac{|\alpha_k|^2}{4}\left(X_1\eta_k^{(\mu)} + Y_1\eta_k^{(\nu)}\right)\left(X_2\eta_k^{(\mu)} + Y_2\eta_k^{(\nu)}\right) \in \mathbb{R}. \end{aligned} \tag{7.52}$$

The 16 cross-terms of the form $O_{X_1Y_1X_2Y_2}(t)$ that make up the observable evolution can be grouped into four groups of four terms for different combinations of $X_1, Y_1, X_2, Y_2 \in \{+,-\}$. To simplify notation, I introduce a symbol to negate X and Y: $\tilde{X} = -X, \tilde{Y} = -Y$. Furthermore, I note that $\alpha_{kXX} = -\alpha_{k\tilde{X}\tilde{X}}$. The four groups of motional terms are as follows.

1. Four terms when $X_2 = X_1$ and $Y_2 = Y_1$:

$$e^{-\sum_{k=1}^{M} |\alpha_{kX_1Y_1} - \alpha_{kX_1Y_1}|^2 \left(\bar{n}_k + \frac{1}{2}\right)} = 1 \tag{7.53}$$

2. Four terms when $X_2 = -X_1 =: \tilde{X}_1$ and $Y_2 = -Y_1 =: \tilde{Y}_1$:

$$\begin{aligned} e^{-\sum_{k=1}^{M} |\alpha_{k\tilde{X}_1\tilde{Y}_1} - \alpha_{kX_1Y_1}|^2 \left(\bar{n}_k + \frac{1}{2}\right)} &= e^{-\sum_{k=1}^{M} |-\alpha_{kX_1Y_1} - \alpha_{kX_1Y_1}|^2 \left(\bar{n}_k + \frac{1}{2}\right)} \\ &= e^{-4\sum_{k=1}^{M} |\alpha_{kX_1Y_1}|^2 \left(\bar{n}_k + \frac{1}{2}\right)} \end{aligned} \tag{7.54}$$

3. Four terms when $X_2 = -X_1 =: \tilde{X}_1$ and $Y_2 = Y_1$:

$$\begin{aligned} e^{-\sum_{k=1}^{M} |\alpha_{k\tilde{X}_1Y_1} - \alpha_{kX_1Y_1}|^2 \left(\bar{n}_k + \frac{1}{2}\right)} &= e^{-\sum_{k=1}^{M} |-X_1\alpha_k^{(\mu)} + Y_1\alpha_k^{(\nu)} - X_1\alpha_k^{(\mu)} - Y_1\alpha_k^{(\nu)}|^2 \left(\bar{n}_k + \frac{1}{2}\right)} \\ &= e^{-4\sum_{k=1}^{M} |\alpha_k^{(\mu)}(t)|^2 \left(\bar{n}_k + \frac{1}{2}\right)} \end{aligned} \tag{7.55}$$

4. Four terms when $X_2 = X_1$ and $Y_2 = -Y_1 =: \tilde{Y}_1$, which follow similarly:

$$e^{-\sum_{k=1}^{M}|\alpha_{kX_1\tilde{Y}_1}-\alpha_{kX_1Y_1}|^2\left(\bar{n}_k+\frac{1}{2}\right)} = e^{-4\sum_{k=1}^{M}|\alpha_k^{(\nu)}(t)|^2\left(\bar{n}_k+\frac{1}{2}\right)} \tag{7.56}$$

Now the sum of the 16 cross-terms that appear in the expansion of the observable evolution can be written out using Eqn. (7.50), where each term can be expressed using Eqns. (7.53)-(7.56).

$$\begin{aligned} O(t) = \mathrm{Tr}_Q \Big[& \hat{U}_1^{\dagger}\hat{\mathcal{O}}\hat{U}_1 \\ & \times \Big\{ \left(\hat{P}_{++}\rho_Q\hat{P}_{++} + \hat{P}_{+-}\rho_Q\hat{P}_{+-} + \hat{P}_{+-}\rho_Q\hat{P}_{+-} + \hat{P}_{--}\rho_Q\hat{P}_{--}\right) \\ & + \left(\hat{P}_{--}\rho_Q\hat{P}_{++} + \hat{P}_{++}\rho_Q\hat{P}_{--}\right) e^{-4\sum_{k=1}^{M}|\alpha_{k++}|^2\left(\bar{n}_k+\frac{1}{2}\right)} \\ & + \left(\hat{P}_{-+}\rho_Q\hat{P}_{+-} + \hat{P}_{+-}\rho_Q\hat{P}_{-+}\right) e^{-4\sum_{k=1}^{M}|\alpha_{k+-}|^2\left(\bar{n}_k+\frac{1}{2}\right)} \\ & + \left(\hat{P}_{-+}\rho_Q\hat{P}_{++} + \hat{P}_{--}\rho_Q\hat{P}_{+-} + \hat{P}_{++}\rho_Q\hat{P}_{-+} + \hat{P}_{+-}\rho_Q\hat{P}_{--}\right) e^{-4\sum_{k=1}^{M}|\alpha_k^{(\mu)}(t)|^2\left(\bar{n}_k+\frac{1}{2}\right)} \\ & + \left(\hat{P}_{+-}\rho_Q\hat{P}_{++} + \hat{P}_{++}\rho_Q\hat{P}_{+-} + \hat{P}_{--}\rho_Q\hat{P}_{-+} + \hat{P}_{-+}\rho_Q\hat{P}_{--}\right) e^{-4\sum_{k=1}^{M}|\alpha_k^{(\nu)}(t)|^2\left(\bar{n}_k+\frac{1}{2}\right)} \Big\} \Big] \end{aligned} \tag{7.57}$$

Several of the terms with the form $O_{X_1Y_1\tilde{X}_1\tilde{Y}_1}(t)$ (from Eqn. (7.54)) have been combined and simplified by noting that $|\alpha_{k++}| = |\alpha_{k--}|$ and $|\alpha_{k+-}| = |\alpha_{k-+}|$. Substituting in the initial qubit condition, $\rho_Q = |00\rangle\langle 00|$, and using the projection matrices defined in App. A gives,

$$\begin{aligned} O(t) = \frac{1}{16}\mathrm{Tr}_Q \Big[\hat{\mathcal{O}}\hat{U}_1 \Big\{ & 4\hat{\mathbb{1}} + \left(\hat{S}_z^{(\mu\nu)2} - \hat{S}_y^{(\mu\nu)2}\right) e^{-4\sum_{k=1}^{M}|\alpha_{k++}|^2\left(\bar{n}_k+\frac{1}{2}\right)} \\ & + \left(\hat{S}_z^{(\mu\nu)2} + \hat{S}_y^{(\mu\nu)2} - 4\hat{\mathbb{1}}\right) e^{-4\sum_{k=1}^{M}|\alpha_{k+-}|^2\left(\bar{n}_k+\frac{1}{2}\right)} \\ & + 4\hat{\sigma}_z^{(\mu)} e^{-4\sum_{k=1}^{M}|\alpha_k^{(\mu)}(t)|^2\left(\bar{n}_k+\frac{1}{2}\right)} + 4\hat{\sigma}_z^{(\nu)} e^{-4\sum_{k=1}^{M}|\alpha_k^{(\nu)}(t)|^2\left(\bar{n}_k+\frac{1}{2}\right)} \Big\} \hat{U}_1^{\dagger} \Big]. \end{aligned} \tag{7.58}$$

Finally, I conjugate the Pauli operators by $\hat{U}_1(t) = e^{i\varphi(t)\hat{S}_x^{(\mu\nu)2}}$ using the matrix relations in App.A. This produces the final expression describing the evolution of the expectation value of an observable for two qubits embedded within an N-ion register that are excited by the MS interaction.

$$\boxed{\begin{aligned} O(t) = \frac{1}{16}\mathrm{Tr}_Q \Big[\hat{\mathcal{O}} \Big\{ & 4\hat{\mathbb{1}} + \left(\hat{S}_z^{(\mu\nu)2} - \hat{S}_y^{(\mu\nu)2}\right) e^{-\sum_{k=1}^{M}|(\eta_k^{(\mu)}+\eta_k^{(\nu)})\alpha_k(t)|^2\left(\bar{n}_k+\frac{1}{2}\right)} \\ & + \left(\hat{S}_z^{(\mu\nu)2} + \hat{S}_y^{(\mu\nu)2} - 4\hat{\mathbb{1}}\right) e^{-\sum_{k=1}^{M}|(\eta_k^{(\mu)}-\eta_k^{(\nu)})\alpha_k(t)|^2\left(\bar{n}_k+\frac{1}{2}\right)} \\ & + 4\left(\sin\left[4\varphi(t)\right]\hat{\sigma}_y^{(\mu)}\hat{\sigma}_x^{(\nu)} + \cos\left[4\varphi(t)\right]\hat{\sigma}_z^{(\mu)}\right) e^{-\sum_{k=1}^{M}|\eta_k^{(\mu)}\alpha_k(t)|^2\left(\bar{n}_k+\frac{1}{2}\right)} \\ & + 4\left(\sin\left[4\varphi(t)\right]\hat{\sigma}_x^{(\mu)}\hat{\sigma}_y^{(\nu)} + \cos\left[4\varphi(t)\right]\hat{\sigma}_z^{(\nu)}\right) e^{-\sum_{k=1}^{M}|\eta_k^{(\nu)}\alpha_k(t)|^2\left(\bar{n}_k+\frac{1}{2}\right)} \Big\} \Big] \end{aligned}} \tag{7.59}$$

where I have expanded the short-hand terms $\alpha_{kXY} = X\alpha_k^{(\mu)} + Y\alpha_k^{(\nu)}$ and $\alpha_k^{\mu} = f_k^{\mu}\alpha_k = -i\eta_k^{\mu}\alpha_k/2$.

7.3.2 Examples of observables evolving under the MS interaction

From Eqn. (7.59), one can calculate the expectation value of a qubit observable $\hat{\mathcal{O}}$ after the MS evolution. I begin with the two-qubit populations, P_n, defined to be the likelihood of measuring n qubits in $|1\rangle$. For this, I use the projection operators $\hat{\mathcal{O}} = \hat{P}_{ij} = |ij\rangle\,\langle ij|,\;\; i,j \in \{0,1\}$.

$$\begin{aligned} P_0(t) &= \langle \hat{P}_{00}(t)\rangle \\ &= \frac{1}{8}\Big\{2 + e^{-\sum_{k=1}^{M}|(\eta_k^{(\mu)}+\eta_k^{(\nu)})\alpha_k(t)|^2\left(\bar{n}_k+\frac{1}{2}\right)} + e^{-\sum_{k=1}^{M}|(\eta_k^{(\mu)}-\eta_k^{(\nu)})\alpha_k(t)|^2\left(\bar{n}_k+\frac{1}{2}\right)} \\ &\qquad +2\cos\left[4\varphi(t)\right]\Big(e^{-\sum_{k=1}^{M}|\eta_k^{(\mu)}\alpha_k(t)|^2\left(\bar{n}_k+\frac{1}{2}\right)} + e^{-\sum_{k=1}^{M}|\eta_k^{(\nu)}\alpha_k(t)|^2\left(\bar{n}_k+\frac{1}{2}\right)}\Big)\Big\} \qquad (7.60a) \\ P_1(t) &= \langle \hat{P}_{01}(t)\rangle + \langle \hat{P}_{10}(t)\rangle \\ &= \frac{1}{4}\Big\{2 - e^{-\sum_{k=1}^{M}|(\eta_k^{(\mu)}+\eta_k^{(\nu)})\alpha_k(t)|^2\left(\bar{n}_k+\frac{1}{2}\right)} - e^{-\sum_{k=1}^{M}|(\eta_k^{(\mu)}-\eta_k^{(\nu)})\alpha_k(t)|^2\left(\bar{n}_k+\frac{1}{2}\right)}\Big\} \qquad (7.60b) \\ P_2(t) &= \langle \hat{P}_{11}(t)\rangle \\ &= \frac{1}{8}\Big\{2 + e^{-\sum_{k=1}^{M}|(\eta_k^{(\mu)}+\eta_k^{(\nu)})\alpha_k(t)|^2\left(\bar{n}_k+\frac{1}{2}\right)} + e^{-\sum_{k=1}^{M}|(\eta_k^{(\mu)}-\eta_k^{(\nu)})\alpha_k(t)|^2\left(\bar{n}_k+\frac{1}{2}\right)} \\ &\qquad -2\cos\left[4\varphi(t)\right]\Big(e^{-\sum_{k=1}^{M}|\eta_k^{(\mu)}\alpha_k(t)|^2\left(\bar{n}_k+\frac{1}{2}\right)} + e^{-\sum_{k=1}^{M}|\eta_k^{(\nu)}\alpha_k(t)|^2\left(\bar{n}_k+\frac{1}{2}\right)}\Big)\Big\} \qquad (7.60c) \end{aligned}$$

If the two addressed qubits are embedded within a two-qubit register ($N = 2$), then there are only six motional modes and they all have symmetric or anti-symmetric Lamb-Dicke parameters between the ions, i.e., $\eta_k^{(1)} = \pm\eta_k^{(2)}$ for all $k \in \{1,\ldots,6\}$. Hence, the populations for two qubits addressed in a two-qubit register simplify to

$$\begin{aligned} P_0(t) &= \frac{1}{8}\Big\{2 + e^{-\sum_{k=1}^{M}|(\eta_k^{(1)}+\eta_k^{(2)})\alpha_k(t)|^2\left(\bar{n}_k+\frac{1}{2}\right)} + e^{-\sum_{k=1}^{M}|(\eta_k^{(1)}-\eta_k^{(2)})\alpha_k(t)|^2\left(\bar{n}_k+\frac{1}{2}\right)} \\ &\qquad +4\cos\left[4\varphi(t)\right]e^{-\sum_{k=1}^{M}|\eta_k^{(1)}\alpha_k(t)|^2\left(\bar{n}_k+\frac{1}{2}\right)}\Big\} \qquad (7.61a) \\ P_1(t) &= \frac{1}{4}\Big\{2 - e^{-\sum_{k=1}^{M}|(\eta_k^{(1)}+\eta_k^{(2)})\alpha_k(t)|^2\left(\bar{n}_k+\frac{1}{2}\right)} - e^{-\sum_{k=1}^{M}|(\eta_k^{(1)}-\eta_k^{(2)})\alpha_k(t)|^2\left(\bar{n}_k+\frac{1}{2}\right)}\Big\} \qquad (7.61b) \\ P_2(t) &= \frac{1}{8}\Big\{2 + e^{-\sum_{k=1}^{M}|(\eta_k^{(1)}+\eta_k^{(2)})\alpha_k(t)|^2\left(\bar{n}_k+\frac{1}{2}\right)} + e^{-\sum_{k=1}^{M}|(\eta_k^{(1)}-\eta_k^{(2)})\alpha_k(t)|^2\left(\bar{n}_k+\frac{1}{2}\right)} \\ &\qquad -4\cos\left[4\varphi(t)\right]e^{-\sum_{k=1}^{M}|\eta_k^{(1)}\alpha_k(t)|^2\left(\bar{n}_k+\frac{1}{2}\right)}\Big\} \qquad (7.61c) \end{aligned}$$

To calculate the expected ion population for a *single* ion being excited by the MS interaction, one must redo the observable calculation for the case of a single qubit. In this case, $\hat{U}_1(t)$ is a global phase term proportional to the identity. When prepared in the initially separable qubit-oscillator state

$|0\rangle\langle 0| \bigotimes_{k=1}^{M} \sum_n p_{n_k} |n_k\rangle\langle n_k|$, the final expression for the evolution of the expectation value of an observable becomes

$$O(t) = \frac{1}{2}\mathrm{Tr}_Q\left[\hat{\mathcal{O}}\left(\hat{\mathbb{I}} + \hat{\sigma}_z e^{-\sum_{k=1}^{M}|\eta_k^{(1)}\alpha_k(t)|^2\left(\bar{n}_k+\frac{1}{2}\right)}\right)\right]. \tag{7.62}$$

The single ion populations are then

$$P_0(t) = \frac{1}{2}\left(1 + e^{-\sum_{k=1}^{M}|\eta_k^{(1)}\alpha_k(t)|^2\left(\bar{n}_k+\frac{1}{2}\right)}\right) \tag{7.63a}$$

$$P_1(t) = \frac{1}{2}\left(1 - e^{-\sum_{k=1}^{M}|\eta_k^{(1)}\alpha_k(t)|^2\left(\bar{n}_k+\frac{1}{2}\right)}\right). \tag{7.63b}$$

The expressions in Eqns. (7.61) and (7.63) were utilised in Figs. 8.4 and 8.6 of Chapter 8 for the theoretical ion populations after an MS interaction, both with and without phase modulation.

Additionally, we can use the calculations here to predict the Bell state fidelity of the qubit states after the MS interaction. The fidelity is given by the overlap between the final qubit state ρ_f, and the ideal Bell state, $|\Phi_B\rangle = \frac{1}{\sqrt{2}}(|00\rangle - i|11\rangle)$ created when $\varphi(t) = -\frac{\pi}{8}$,

$$\begin{aligned} F_B &= \langle\Phi_B|\rho_f|\Phi_B\rangle \\ &= \frac{1}{2}\big(\langle 00|\rho_f|00\rangle + \langle 11|\rho_f|11\rangle - i\langle 00|\rho_f|11\rangle + i\langle 11|\rho_f|00\rangle\big) \\ &= \frac{1}{2}\left(P_0 + P_2 - 2\,\mathrm{Im}[\rho_{f,30}]\right). \end{aligned} \tag{7.64}$$

This can be calculated using the even population expressions P_0 and P_2 and the off-diagonal element of the qubit density matrix $\rho_{f,30}$. For the latter, one can calculate ρ_f from the expression inside the trace of Eqn. (7.59) when $\mathcal{O} = \hat{\mathbb{I}}$. Then, taking the imaginary component of the off-diagonal element gives

$$\begin{aligned} F_B = \frac{1}{8}\Big\{&2 + e^{-\sum_{k=1}^{M}|(\eta_k^{(\mu)}+\eta_k^{(\nu)})\alpha_k(t)|^2\left(\bar{n}_k+\frac{1}{2}\right)} + e^{-\sum_{k=1}^{M}|(\eta_k^{(\mu)}-\eta_k^{(\nu)})\alpha_k(t)|^2\left(\bar{n}_k+\frac{1}{2}\right)} \\ &-2\sin\left[4\varphi(t)\right]\left(e^{-\sum_{k=1}^{M}|\eta_k^{(\mu)}\alpha_k(t)|^2\left(\bar{n}_k+\frac{1}{2}\right)} + e^{-\sum_{k=1}^{M}|\eta_k^{(\nu)}\alpha_k(t)|^2\left(\bar{n}_k+\frac{1}{2}\right)}\right)\Big\}. \end{aligned} \tag{7.65}$$

To experimentally measure the value of the off-diagonal coherence, $\rho_{f,30}$, we apply a global $\pi/2$-pulse after the MS operation. Scanning the phase of the pulse and measuring the parity $(P_{\text{even}} - P_{\text{odd}})$ reveals sinusoidal oscillations; the contrast Π_c is equal to twice the *magnitude* of $\rho_{f,30}$. This procedure physically extracts the value $2|\rho_{f,30}|$, rather than $2\,\mathrm{Im}[\rho_{f,30}]$, which modifies the experimentally measured value of fidelity as follows.

$$
\begin{aligned}
F_{\text{exp}} &= \frac{1}{2}(P_0 + P_2 + \Pi_C) \\
&= \frac{1}{8}\Big\{2 + e^{-\sum_{k=1}^{M}|(\eta_k^{(\mu)}+\eta_k^{(\nu)})\alpha_k(t)|^2\left(\bar{n}_k+\frac{1}{2}\right)} + e^{-\sum_{k=1}^{M}|(\eta_k^{(\mu)}-\eta_k^{(\nu)})\alpha_k(t)|^2\left(\bar{n}_k+\frac{1}{2}\right)} \\
&\qquad + \text{Abs}\Big[e^{-\sum_{k=1}^{M}|(\eta_k^{(\mu)}+\eta_k^{(\nu)})\alpha_k(t)|^2\left(\bar{n}_k+\frac{1}{2}\right)} - e^{-\sum_{k=1}^{M}|(\eta_k^{(\mu)}-\eta_k^{(\nu)})\alpha_k(t)|^2\left(\bar{n}_k+\frac{1}{2}\right)} \\
&\qquad\qquad + 2i\sin\left[4\varphi(t)\right]\left(e^{-\sum_{k=1}^{M}|\eta_k^{(\mu)}\alpha_k(t)|^2\left(\bar{n}_k+\frac{1}{2}\right)} + e^{-\sum_{k=1}^{M}|\eta_k^{(\nu)}\alpha_k(t)|^2\left(\bar{n}_k+\frac{1}{2}\right)}\right)\Big]\Big\} \qquad (7.66)
\end{aligned}
$$

When the residual motional entanglement is negligible, these two expressions for fidelity are equivalent (recalling that we calculate the Bell state fidelity for $\varphi(t) = -\frac{\pi}{8}$). The expression for F_{exp} was used in Fig. 8.5 of Chapter 8 showing the parameter regime flexibility of phase-modulated MS gates.

7.4 Prediction of the effect of time-varying noise on the Mølmer-Sørensen gate

Until now, the only "error" we have considered to affect the MS gate implementation is that of a poor gate construction. That is, due to the qubits coupling to many modes, it is difficult to facilitate disentanglement from all the motional subspaces simultaneously. In the next chapter, we will go into further detail about how to construct a gate that can simultaneously decouple from all modes using analytically or numerically calculated phase shifts in the interaction laser. In this section, I discuss a second source of error that can affect the gate performance – noise. Noise in the interaction laser amplitude or frequency, or in the frequencies of the motional modes themselves, will alter the gate performance, modifying it from the ideal evolution. Predicting the effect of systematic static errors is straightforward – one can use the observable calculations from the previous section and alter the values of Rabi rate, Ω, and detuning, δ, from the ideal to the error-shifted values. However, understanding the effect of *time-varying* noise is more complicated. To enable a calculation of the gate performance under noise, we introduce the concept of the "filter function".

The filter function framework presented by Green et al. [**244**] and experimentally validated by Soare et al. [**147**] captures the sensitivity of an operator to time-varying noise processes. If an error channel transforms the control operation $\hat{U}_C$ into the noisy operator $\tilde{U}$, then the infidelity of the operator can be quantified using the Hilbert-Schmidt inner product,

$$\mathcal{I} = 1 - \frac{1}{d^2}\left|\text{Tr}\left(\hat{U}_C^{\dagger}\tilde{U}\right)\right|^2, \qquad (7.67)$$

where d is the dimension of the operator. In physical experiments the infidelity can only be measured over an ensemble average of noise samples, yielding the noise-averaged infidelity,

$$\mathcal{I}_{\text{av}} = 1 - \mathbb{E}\left[\frac{1}{d^2}\left|\text{Tr}\left(\hat{U}_C^\dagger \tilde{U}\right)\right|^2\right]. \tag{7.68}$$

The expected infidelity of an operation due to a noise process ϵ can be calculated from the overlap of the noise spectrum, $S_\epsilon(\omega)$, and the operation's filter function, $F_\epsilon(\omega)$,

$$\mathcal{I}_{\text{av}} = \frac{1}{2\pi}\int_{-\infty}^{\infty} d\omega S_\epsilon(\omega) F_\epsilon(\omega). \tag{7.69}$$

The performance of the MS gate is captured by two quantities: (1) the residual qubit-oscillator coupling and (2) the qubit-qubit entangling phase, $\varphi(\tau_g)$. The former should ideally be zero at the gate's conclusion, whilst maximal qubit-qubit entanglement necessitates that the latter be $\varphi(\tau_g) = \pi/8$. Here, we modify the filter function framework to derive a filter function $F_\delta(\omega)$ that predicts infidelity solely due to residual qubit-oscillator coupling caused by noise on the mode frequencies (a time-dependent detuning error). As the residual qubit-oscillator coupling will be independent of any entangling phase acquired with two or more ions, we proceed by considering a gate-equivalent operation performed on a single ion.

We alter our metric from the total gate infidelity in Eqn. (7.68) to the residual qubit-oscillator coupling, $\frac{1}{4}\sum_{k=1}^{M}\left|\eta_k^{(1)}\alpha_k(\tau_g)\right|^2$. If the residual motional displacement is small, that is $\frac{1}{4}\sum_{k=1}^{M}\left|\eta_k^{(1)}\alpha_k(\tau_g)\right|^2 \ll 1$, then from Eqn. (7.63) we see that it can be directly inferred from a measurement of P_1,

$$\begin{aligned} P_1 &= \frac{1}{2}\left(1 - e^{-\sum_{k=1}^{M}|\eta_k^{(1)}\alpha_k(\tau_g)|^2\left(\bar{n}_k+\frac{1}{2}\right)}\right) \\ &\approx \frac{1}{2}\sum_{k=1}^{M}\left|\eta_k^{(1)}\alpha_k(\tau_g)\right|^2\left(\bar{n}_k + \frac{1}{2}\right) \\ &=: \frac{1}{4}\sum_{k=1}^{M}\left|\eta_k^{(1)}\alpha_k(\tau_g)\right|^2 T_k \end{aligned} \tag{7.70}$$

with $T_k := 2\left(\bar{n}_k + \frac{1}{2}\right)$, where $\bar{n}_k$ is the mean phonon number of mode k.

We consider time-varying noise on the laser detuning, δ_k, or equivalently fluctuations of the motional frequencies, which could be induced by variations in the electric trapping potential. Figure 8.6 of Chapter 8 demonstrates the improved robustness to quasi-static detuning noise for ΦM gates with increasing orders of noise suppression. We now explore their enhanced robustness for time-varying noise.

The detuning is modified as $\delta_k \to \delta_k + \epsilon(t)$, where $\epsilon(t)$ is a zero-mean noise process, altering the phase space mode trajectories in Eqn. (7.40) to

$$\alpha_k(\tau_g) = \Omega \int_0^{\tau_g} dt e^{-i[(\delta_k+\epsilon(t))t+\phi(t)]}. \tag{7.71}$$

The assumption that the residual motional displacement remains small requires "weak" noise, that is $\mathbb{E}\left[\epsilon(t)^2\right] {\tau_g}^2 \ll 1$. As with the infidelity in the traditional filter function formalism, we can only experimentally consider noise-averaged measurements. Taking the ensemble average over the noise process yields

$$\begin{aligned}
\mathbb{E}[P_1] &\approx \mathbb{E}\left[\frac{1}{4}\sum_{k=1}^{M}\left|\eta_k^{(1)}\alpha_k(\tau_g)\right|^2 T_k\right] \\
&\approx \frac{1}{4}\sum_k T_k \left|\Omega\eta_k^{(1)}\right|^2 \int_0^{\tau_g} dt_1 \int_0^{\tau_g} dt_2 e^{-i[\delta_k(t_1-t_2)+\phi(t_1)-\phi(t_2)]} \\
&\quad \times \mathbb{E}\left[\left(1 - i\epsilon(t_1)t_1 - \frac{\epsilon(t_1)^2 t_1^2}{2}\right)\left(1 + i\epsilon(t_2)t_2 - \frac{\epsilon(t_2)^2 t_2^2}{2}\right)\right] \\
&= \sum_k T_k \left|\Omega\frac{\eta_k^{(1)}}{2}\right|^2 \int_0^{\tau_g} dt_1 \int_0^{\tau_g} dt_2 e^{-i[\delta_k(t_1-t_2)+\phi(t_1)-\phi(t_2)]}\mathbb{E}\left[\epsilon(t_1)\epsilon(t_2)\right] t_1 t_2
\end{aligned} \tag{7.72}$$

considering terms up to $\mathbb{E}\left[\epsilon(t)^2\right] t^2 \le \mathbb{E}\left[\epsilon(t)^2\right] \tau_g^2$. Assuming that the gate has been constructed to decouple from all modes in the absence of noise, we can ignore all terms dependent on only one integral variable, as they will be multiplied by exactly zero due to the complete mode decoupling condition in the other integral. The Wiener–Khinchin Theorem then relates the autocorrelation function in the noise ensemble expectation to the noise spectrum in the frequency domain,

$$\mathbb{E}\left[\epsilon(t_1)\epsilon(t_2)\right] = \frac{1}{2\pi}\int_{-\infty}^{\infty} d\omega S_\delta(\omega) e^{i\omega(t_1-t_2)}. \tag{7.73}$$

Applying this, we can rewrite the expectation of P_1 in terms of the noise spectrum, $S_\delta(\omega)$, and the "modal filter functions", $F_{\delta,k}(\omega)$:

$$\begin{aligned}
\mathbb{E}[P_1] &\approx \frac{1}{2\pi}\int_{-\infty}^{\infty} d\omega S_\delta(\omega) \sum_{k=1}^{M} T_k \left|\Omega\frac{\eta_k^{(1)}}{2}\right|^2 \int_0^{\tau_g} dt_1 \int_0^{\tau_g} dt_2 e^{-i[(\delta_k-\omega)(t_1-t_2)+\phi(t_1)-\phi(t_2)]} t_1 t_2 \\
&= \frac{1}{2\pi}\int_{-\infty}^{\infty} d\omega S_\delta(\omega) \frac{1}{4}\sum_{k=1}^{M} T_k \left|\Omega\frac{\eta_k^{(1)}}{2}\int_0^{\tau_g} dt e^{-i[(\delta_k-\omega)t+\phi(t)]} t\right|^2 \\
&=: \frac{1}{2\pi}\int_{-\infty}^{\infty} d\omega S_\delta(\omega) \sum_{k=1}^{M} F_{\delta,k}(\omega).
\end{aligned} \tag{7.74}$$

The total filter function $F_\delta(\omega)$ is defined as a summation of the individual modal filter functions, $F_{\delta,k}(\omega)$,

$$\begin{aligned} F_\delta(\omega) &= \sum_{k=1}^{M} F_{\delta,k}(\omega) \\ &= \sum_{k=1}^{M} T_k \left| \Omega \frac{\eta_k^{(1)}}{2} \int_0^{\tau_g} dte^{-i[(\delta_k-\omega)t+\phi(t)]}t \right|^2 . \end{aligned} \tag{7.75}$$

The spectral overlap in Eqn. (7.74) predicts the expected value of P_1 (and thus the residual motional displacement) in the presence of a given noise spectrum $S_\delta(\omega)$, allowing us to compare the performance of ΦM gates with different levels of noise suppression for each motional mode.

In Fig. 8.7 of Chapter 8, we experimentally validate the analytic filter function theory. A sinusoidal modulation at frequency ω_{mod} is added to the detuning of the interaction laser and, to obtain an ensemble average of the engineered noise process, the measurement is averaged over the starting phase of the modulation. This produces the noise spectrum $S_\delta(\omega) = \pi(\delta(\omega - \omega_{\text{mod}}) + \delta(\omega + \omega_{\text{mod}}))$, consisting of two delta functions. The gate is calibrated to decouple from the motional mode in the absence of noise, so any residual coupling is solely due to the engineered noise process and will result in $P_1 > 0$. The frequency of the detuning modulation is scanned and from the phase-averaged $\mathbb{E}[P_1]$, we directly infer $(F(\omega) + F(-\omega))$.

Following a similar procedure, we can also derive $F_\delta(\omega)$ for a targeted entangling operation between a pair of ions μ, ν in an N ion chain. In this case, the residual motional coupling is given by

$$\frac{1}{4}\sum_{k=1}^{M} \left|(\eta_k^{(\mu)} + \eta_k^{(\nu)})\alpha_k(\tau_g)\right|^2 + \frac{1}{4}\sum_{k=1}^{M} \left|(\eta_k^{(\mu)} - \eta_k^{(\nu)})\alpha_k(\tau_g)\right|^2 , \tag{7.76}$$

which can be approximated by the expression for P_1 from Eqn. (7.60),

$$\begin{aligned} P_1(t) &= \frac{1}{4}\left\{2 - e^{-\sum_{k=1}^{M} |(\eta_k^{(\mu)}+\eta_k^{(\nu)})\alpha_k(\tau_g)|^2\left(\bar{n}_k+\frac{1}{2}\right)} - e^{-\sum_{k=1}^{M} |(\eta_k^{(\mu)}-\eta_k^{(\nu)})\alpha_k(\tau_g)|^2\left(\bar{n}_k+\frac{1}{2}\right)}\right\} \\ &\approx \frac{1}{4}\sum_{k=1}^{M} \left|(\eta_k^{(\mu)} + \eta_k^{(\nu)})\alpha_k(\tau_g)\right|^2 \left(\bar{n}_k + \frac{1}{2}\right) + \frac{1}{4}\sum_{k=1}^{M} \left|(\eta_k^{(\mu)} - \eta_k^{(\nu)})\alpha_k(\tau_g)\right|^2 \left(\bar{n}_k + \frac{1}{2}\right) \\ &= \frac{1}{4}\sum_{k=1}^{M} \left(|\eta_k^{(\mu)}|^2 + |\eta_k^{(\nu)}|^2\right) |\alpha_k(\tau_g)|^2 T_k \end{aligned} \tag{7.77}$$

with $T_k = 2\left(\bar{n}_k + \frac{1}{2}\right)$. The filter function becomes

$$F_\delta(\omega) = \sum_{k=1}^{M} T_k \left(\left|\frac{\eta_k^{(\mu)}}{2}\right|^2 + \left|\frac{\eta_k^{(\nu)}}{2}\right|^2 \right) \left| \Omega \int_0^{\tau_g} dte^{-i[(\delta_k-\omega)t+\phi(t)]}t \right|^2 . \tag{7.78}$$

CHAPTER 8

Phase-modulated entangling gates robust to static and time-varying errors

---

> *"And a step backward, after making a wrong turn, is a step in the right direction."*
>
> - Kurt Vonnegut, *Player Piano*

The work in this chapter aimed to create highly flexible, robust two-qubit entangling gates in trapped ions. High-fidelity two-qubit gates are a critical element of the quantum computing architecture, complementing the work of previous chapters (Chapter 6) to engineer high-fidelity, robust single-qubit gates using microwaves. This chapter is reproduced with minor changes from "Phase-modulated entangling gates robust to static and time-varying errors" published in Physical Review Applied ***13****, 024022 [**6**].*

The ability to perform robust, high fidelity entangling gates in multi-qubit systems is a key requirement for realising scalable quantum information processing [**245**]. In several hardware architectures, qubits are entangled through shared bosonic oscillator modes via an interaction that is moderated by an external driving field. The Mølmer-Sørensen (MS) gate [**238**, **239**, **246**] and the σ_z-gate [**29**] in trapped ions as well as the resonator-induced phase gate in superconducting circuits [**247**–**249**] are of this type. In addition, interactions simultaneously employing multiple bosonic modes have been explored to improve gate fidelities [**250**] and probe novel types of interactions [**251**] in superconducting circuits.

A major source of error for oscillator-mediated gates is residual qubit-oscillator entanglement at the end of the operation [**252**]. This detrimental effect can arise due to the presence of quasi-static or time-varying noise on the driving field, slow drifts in experimental parameters such as the qubit and oscillator frequencies, or the presence of spectator modes that are not properly accounted for in the gate construction. In trapped ion systems, various schemes have been demonstrated that minimise this residual coupling [**253**–**258**], with some also incorporating the ability to simultaneously decouple from multiple modes [**9**,**88**,**90**,**259–264**]. Their common feature is a temporal modulation of the driving field, modifying the trajectories of the joint qubit-oscillator states in each oscillator's phase space.

In this work, we experimentally demonstrate a class of phase-modulated (ΦM) entangling gates using trapped ions in the presence of multi-mode motional spectra. Specifically, we implement an MS-type interaction and employ discrete phase shifts of the driving field to suppress dominant gate errors. Using both an analytic scheme [**9**] and numerical optimisation to calculate the required phase shifts, we experimentally validate that phase modulation permits motional mode decoupling for arbitrary laser frequencies in a way not otherwise achievable through the conventional gate construction [**265**]. We achieve an average two-qubit gate fidelity of 99.4(2)% (including SPAM errors) across a range of laser detunings near a pair of motional modes, reducing errors by up to two orders of magnitude relative to the best unmodulated alternative. We also demonstrate that proper construction of the ΦM sequence provides the ability to systematically increase gate-robustness to static offsets in the laser detuning, as well as time-varying laser detuning and amplitude noise. Experimental measurements are in agreement with a theoretical model developed in the filter function framework [**244**] to capture the influence of time-dependent noise. Finally, we study the scaling behaviour of both the analytic and numerically derived phase-modulated gate constructions with system size, and demonstrate that the use of numerical optimisation reduces scaling behaviour from exponential to linear with mode number, providing a means to accommodate high-fidelity, time-optimised ΦM gate construction in large multi-ion registers.

8.1 Oscillator-mediated entangling gates

In oscillator-mediated entangling gates, the application of an external driving field, typically a microwave or laser, produces a qubit-state-dependent displacement of the oscillator wave packet in phase space. As presented in Section 7.2, the MS coupling between a system of N qubits and M bosonic oscillator modes can be described by the following time-dependent Hamiltonian

$$\hat{H}(t) = i\hbar \sum_{\mu=1}^{N} \hat{\sigma}_s^{(\mu)} \otimes \sum_{k=1}^{M} \left(\gamma_k^{(\mu)}(t) \hat{a}_k^\dagger - \gamma_k^{(\mu)*}(t) \hat{a}_k \right), \tag{8.1}$$

where $\hat{\sigma}_s^{(\mu)}$ is the Pauli spin operator in the basis $s \in \{x, y, z\}$ acting on the μ^{th} qubit, which is tensored with $\hat{a}_k^\dagger$, $\hat{a}_k$ the creation and annihilation operators acting on the k^{th} oscillator mode. The complex-valued function $\gamma_k^{(\mu)}(t) = \Omega f_k^{(\mu)} e^{-i\delta_k t}$ describes the coupling of the μ^{th} qubit and k^{th} oscillator mode, where the effective coupling strength is given by the product between the strength of the driving field

Ω and a hardware-specific factor, $f_k^{(\mu)}$. Here, δ_k is the angular frequency difference (detuning) of the driving field from the k^{th} oscillator mode. Under the application of the driving field, the coupled system undergoes a unitary evolution [**8, 10**] including both a qubit-qubit entangling term and a qubit-state-dependent displacement $\hat{D}$ of the oscillator modes in phase space. The latter is central to our discussion and is described by

$$\hat{D} = \exp\left\{\sum_{\mu=1}^{N} \hat{\sigma}_s^{(\mu)} \otimes \sum_{k=1}^{M} \left[f_k^{(\mu)}\alpha_k(t)\hat{a}_k^\dagger - f_k^{(\mu)*}\alpha_k^*(t)\hat{a}_k\right]\right\}. \tag{8.2}$$

Due to the detuning δ_k, the wave packets associated with joint qubit-oscillator states undergo circular phase space trajectories proportional to the coherent displacement $\alpha_k(t) = \Omega\int_0^t dt' e^{-i[\delta_k t' + \phi(t')]}$. The k^{th} mode trajectory returns to its starting point with a period of $2\pi/|\delta_k|$ and the enclosed area of all wave packet trajectories is commensurate with the accumulated qubit-qubit entangling phase. Here, $\phi(t)$ is the phase difference between the oscillator and the driving field, which we refer to as the coupling phase and modulate in our approach.

Successful completion of a qubit-qubit entangling operation requires the elimination of qubit-oscillator entanglement; for a gate of length $t = \tau_g$, this is achieved by satisfying the condition $\alpha_k(\tau_g) = 0$, for each mode k. For example, Fig. 8.1 shows two modes being displaced along phase space trajectories described by $\alpha_k(t)$ with frequencies $\delta_2 = 2\delta_1$, such that mode 2 rotates twice as fast as mode 1, and $\phi(t) = 0$. The gate time must be chosen to allow both phase space loops to return to the origin simultaneously. Here, this is straightforward as the two frequencies are commensurate. Choosing $\tau_g = \frac{2\pi}{\delta_1} = \frac{4\pi}{\delta_2}$, as in Fig. 8.1(c), causes mode 1 to complete a full phase space loop returning to the origin, and mode 2 to complete two loops. However, if the frequencies are not commensurate, particularly as more motional modes are considered, this becomes increasingly difficult to achieve. Modulation of the coupling phase $\phi(t)$ may be used to direct the phase space trajectories, returning each trajectory to the origin in a shorter time than the typical approach of ensuring that the gate time and drive detuning are related by an integer multiple for all modes, $\delta_k\tau_g = 2\pi j$, for $j \in \pm\{1, 2, ...\}$. The ability to actively steer these trajectories is particularly important with large mode numbers where the gate time would otherwise grow prohibitively long, and even allows us to ensure effective mode decoupling in the presence of time-dependent parameter fluctuations. The required phase modulations may be determined through analytic calculation [**9**] or numerical optimisation, and we now outline the details of these two approaches.

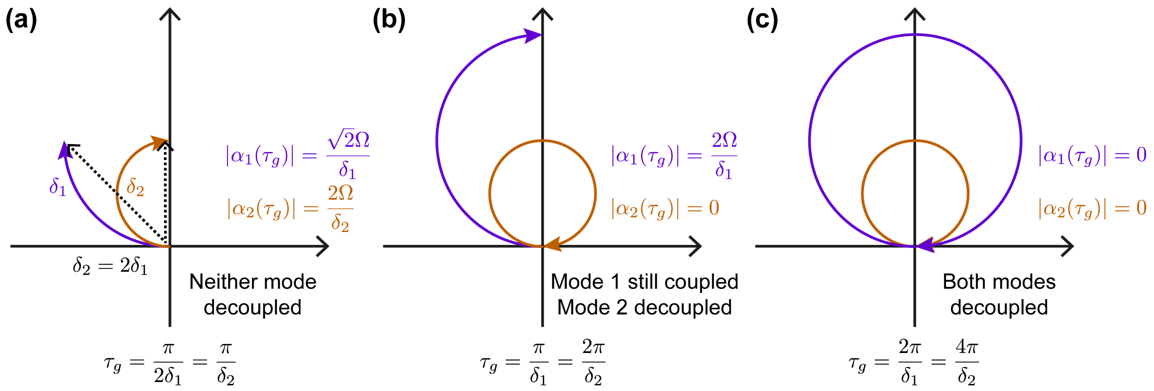

FIGURE 8.1. Schematic of two oscillator modes being displaced in phase space at different frequencies, δ_1 (purple) and $\delta_2 = 2\delta_1$ (orange). The modes are displaced along circular trajectories at frequency δ_k with a radius inversely proportional to the frequency, described by $\alpha_k(\tau_g) = \Omega \int_0^{\tau_g} dt e^{-i\delta_k t}$. The trajectories are shown for three gates times: (a) $\tau_g = \frac{\pi}{2\delta_1} = \frac{\pi}{\delta_2}$ when neither mode is decoupled, (b) $\tau_g = \frac{\pi}{\delta_1} = \frac{2\pi}{\delta_2}$ when mode 2 is decoupled (returns to the origin) but mode 1 is maximally displaced, and (c) $\tau_g = \frac{2\pi}{\delta_1} = \frac{4\pi}{\delta_2}$ when both modes have returned to the origin and are decoupled. At the final time in panel (c), mode 2 has actually completed two full circles in phase space, returning it to the origin for a second time. The net displacement is described by the absolute value $|\alpha_k(t)| = \frac{\sqrt{2}\Omega}{\delta_k}\sqrt{1 - \cos\left[\delta_k t\right]}$. The net displacements are indicated by dashed black arrows in panel (a).

8.1.1 Calculation of phase modulation sequences

The key to the analytic ΦM scheme is that for any time evolution of the k^{th} oscillator state over the interval $t \in [0, \tau]$, its phase space trajectory can be returned to the origin by repeating the same evolution over the interval $t \in [\tau, 2\tau]$ with an overall shift of the coupling phase, $\phi(t)$, equal to $-(\pi + \delta_k\tau)$ (Fig. 8.2(a)). Using the Heaviside function $\Theta(x)$, a segment τ of this evolution may be represented by $r(x = t; \tau) = \Theta(t)\,\Theta(\tau - t)\,e^{-i\phi(t)}$, modifying the qubit-oscillator coupling $\gamma_k^{(\mu)}(t) \to \gamma_k^{(\mu)}(t) r(t; \tau)$. We define a family of operators R_{δ_k}, that are parameterised by δ_k and act on the function $r(x; \tau)$ as $R_{\delta_k} r(x = t; \tau) = r(t; \tau) + e^{i(\delta_k\tau + \pi)} r(t - \tau; \tau)$. This captures a two-segment, piecewise-constant modulation sequence over the interval $t \in [0, 2\tau]$, which returns the trajectory of mode k to its initial state, $\alpha_k(2\tau) = 0$. As illustrated in Fig. 8.2(b, c), this process of phase-shifted concatenation may be repeated to construct sequences that close any number of oscillator trajectories in a desired gate time τ_g. In order to decouple M oscillators, the gate is divided into 2^M time segments of length $\tau_s = \tau_g/2^M$ and the phase modulation sequence is constructed as $R_{\delta_M} ... R_{\delta_1} r_0(t; \tau_s)$, where $r_0(t; \tau_s) = \Theta(t)\Theta(\tau_s - t)$ is the “base” sequence for which we take $\phi(t) \equiv 0$. The reduced notation $r_{\delta_M ... \delta_1}(t; \tau_g) \equiv R_{\delta_M} \cdots R_{\delta_1} r_0(t; \tau_s)$ is used to refer to the full sequence of 2^M phase segments, where the phase in each segment may be calculated exactly using a closed-form expression [**9**].

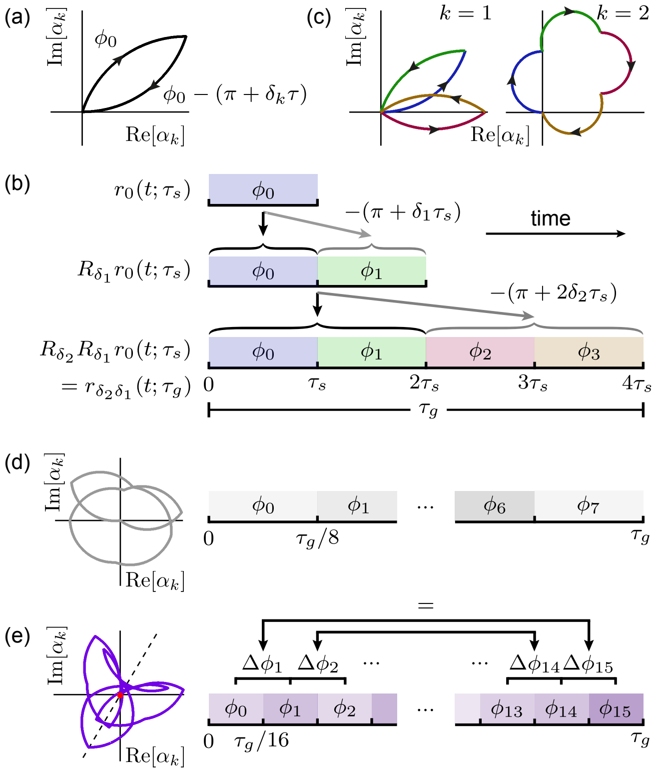

FIGURE 8.2. Construction of phase modulation sequences. (a) Schematic plot of $\alpha_k(t)$ for $0 \leq t \leq 2\tau$. Shifting the coupling phase, initially ϕ_0, by an amount $-(\pi + \delta_k \tau)$ at $t = \tau$ returns the oscillator trajectory to the origin at $t = 2\tau$. (b) Construction of the ΦM sequence $R_{\delta_2} R_{\delta_1} r_0(t; \tau_s)$ from the base sequence $r_0(t; \tau_s)$. Each application of R_{δ_k} produces a new sequence consisting of the original sequence (black arrow) followed by the entire original sequence phase-shifted by $-(\pi + \delta_k \tau)$ (grey arrow), where τ is the duration of the original sequence. The example sequence closes the trajectories of two modes $k = 1, 2$, shown in (c), with detunings δ_1, δ_2 in four time segments of length $\tau_s = \tau_g/4$. Colours indicate the varying coupling phase ϕ_n in each time segment $t \in [n\tau_s, (n+1)\tau_s]$. (d) Example phase space trajectory (left) and schematic showing the construction (right) of a standard numerically optimised phase modulation sequence targeting two modes with $S = 8$ phase segments of $\tau_g/8$ duration each. (e) For the robust numerical sequence, the number of phase segments is doubled to $S = 16$, with each $\tau_g/16$ in length. The time-averaged position of the phase space trajectory (red dot) lies at the origin. This condition, combined with the constraint that $\Delta\phi_{n+1} = \Delta\phi_{S-(n+1)}$ results in a trajectory symmetric about a line through the origin (dashed line).

ΦM sequences that provide increased robustness to parameter fluctuations during the gate operation can be constructed by repeated application of the operator R_{δ_k} on the base sequence $r_0(t; \tau_s)$. The number of times the operator is applied determines the "order" of noise suppression associated with decoupling from mode k. A sequence that suppresses noise to order $(p + 1)$ will achieve decoupling in the presence of noise that modifies the qubit-oscillator coupling via $\gamma_k^{(\mu)}(t) \rightarrow \gamma_k^{(\mu)}(t)\beta_k^{(p)}(t)$, where $\beta_k^{(p)}(t) = \sum_{j=0}^{p} \beta_{k,j} t^j$ is a p^{th}-order polynomial in terms of the noise strength. For example, the sequence described by $R_{\delta_2} R_{\delta_2} R_{\delta_1} r_0(t;\tau_s) = r_{\delta_2\delta_2\delta_1}(t;\tau_g)$ will decouple modes $k = 1$ and $k = 2$, providing additional noise suppression to second order for mode $k = 2$. These robust sequences result in mode trajectories that return to the origin repeatedly throughout the operation and, in the presence of noise, coherently average away deviations from the ideal oscillator trajectories.

Numerical optimisation can also be used to produce ΦM sequences that enable multi-mode decoupling. This approach is designed to mitigate the unfavourable exponential scaling of the number of phase shifts with mode-number M encountered in our analytic approach, trading closed-form solutions for the need to rely on numeric techniques (rather than a transparent physical argument) in finding them. For a specified gate time τ_g, set of drive-field detunings $\{\delta_k\}$, and number of phase segments S, the optimisation procedure finds ΦM sequences that ensure all M modes exhibit residual motional displacement below an arbitrarily defined threshold $\sum_\mu \sum_k \left| f_k^{(\mu)} \alpha_k(\tau_g) \right|^2 \leq \epsilon$. We find empirically that good solutions yielding $\epsilon \lesssim 10^{-4}$ are achievable using only a linear scaling in segment number M with a small prefactor, $S = 4M$ (see Fig. 8.2(d)).

The numerical optimisation is performed utilising MATLAB's inbuilt constrained optimisation routine *fmincon*. For the optimisation, we consider a targeted entangling operation between two ions μ, ν in an N ion chain with $2N$ radial motional modes. The motional frequency spectrum is either numerically calculated using the COM frequencies and the eigenspectra calculation in Section 7.1 from the previous chapter, or manually input from experimental measurements. We specify the number of phase segments S, drive field detunings $\{\delta_k\}$, gate time τ_g and maximum Rabi frequency Ω_{max}. For these parameters, the optimisation procedure finds ΦM sequences that maximise the acquired entangling phase between the two target ions $\varphi_{\mu\nu}(\tau_g)$. This optimisation occurs subject to the constraint that the residual motional displacement remain below a threshold of 10^{-4}, that is

$$\sum_{i=\mu,\nu} \sum_{k=1}^{M} \left| \frac{1}{2} \eta_k^{(i)} \alpha_k(\tau_g) \right|^2 \leq 10^{-4}. \tag{8.3}$$

The optimisation procedure will converge once the constraint (Eqn. (8.3)) has been satisfied and the improvement in $\varphi_{\mu\nu}(\tau_g)$ between successive iterations drops below a set threshold, chosen to be 10^{-4}. A maximally entangling gate may be successfully achieved if $\varphi_{\mu\nu}(\tau_g) \geq \pi/8$. For ΦM sequences that exceed this value, the Rabi frequency may be scaled down to exactly achieve the target phase $\varphi_{\mu\nu}(\tau_g) = \pi/8$.

Robustness to fluctuations in experimental parameters may be realised in numerically optimised ΦM sequences by imposing the additional constraint that the time-averaged positions of the phase space trajectories for all modes lie at the origin, that is $\alpha_{k,\text{avg}}(\tau_g) = \frac{1}{\tau_g}\int_0^{\tau_g}\alpha_k(t)dt = 0$. By further requiring that the trajectories be symmetric about half the gate time [**253**, **260**], minimising $\alpha_{k,\text{avg}}(\tau_g)$ is equivalent to minimising $\alpha_k(\tau_g)$ and the optimisation constraint becomes $\sum_\mu \sum_k \left| f_k^{(\mu)} \alpha_{k,\text{avg}}(\tau_g)\right|^2 \leq \epsilon$. The realisation of symmetric phase space trajectories may be expressed as a condition on phase *differences* between time segments in the two halves of the sequence, such that $\Delta\phi_{n+1} = \Delta\phi_{S-(n+1)}$. Here, $\Delta\phi_n = (\phi_n - \phi_{n-1})$ and ϕ_n is the coupling phase in the time segment $t \in [n\tau_g/S, (n+1)\tau_g/S]$. In order to account for the additional symmetry constraint, the number of phase segments employed in the optimisation is increased to $S = 8M$, which ensures the optimiser routinely finds gate constructions satisfying the constraints. The difference in construction between the standard and robust numerically optimised ΦM sequences is illustrated in Fig. 8.2(d,e).

8.1.2 Experimental implementation of the Mølmer-Sørensen interaction in ^{171}Yb$^+$

In ^{171}Yb$^+$ the qubit-oscillator laser interaction is commonly implemented via a two-photon Raman transition using a high power, pulsed laser at 355 nm. The interaction uses two phase-coherent laser beams, usually from the same initial laser, to inelastically excite the ion by changing its internal state. The net transition frequency is equivalent to the frequency *difference* between the two Raman components, $\Delta\omega = \omega_1 - \omega_2$.

We show three example Raman transitions that can be driven in Fig. 8.3 by changing the Raman frequency difference. The "carrier" transition is defined to be the excitation between the two qubit states, $|0\rangle \leftrightarrow |1\rangle$. This is illustrated in Fig. 8.3(a) by tuning the beat frequency to be equal to the qubit transition, $\Delta\omega = \omega_0$. By changing the beat frequency to be offset from the qubit transition by a motional quanta, we can not just drive electronic transitions, but also *motional* changes. In Fig. 8.3(b) we tune the beat frequency above the qubit transition by the frequency of the k^{th} mode, $\Delta\omega = \omega_0 + \nu_k$. Consequently, when the ion is driven from $|0\rangle$ to $|1\rangle$, it adds one motional quanta to the mode, transitioning from $n_k \rightarrow n_k + 1$ phonons. This transition is called a "Blue Sideband" transition (BSB), as we drive the motional sideband on the blue side of the qubit transition. A similar "Red Sideband" transition (RSB) can be driven by tuning the beat frequency below the qubit frequency, $\Delta\omega = \omega_0 - \nu_k$, as shown in Fig. 8.3(c).

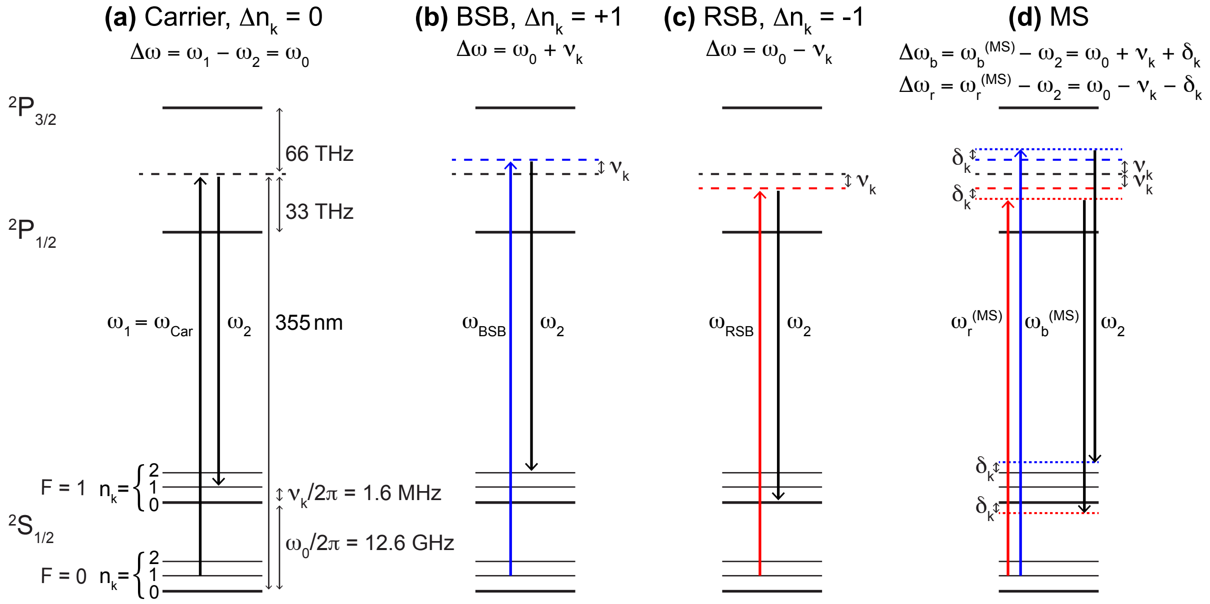

FIGURE 8.3. Energy levels showing two-photon Raman interactions performed using a 355 nm laser. The difference between the two frequency components of the Raman interaction, $\Delta\omega = \omega_1 - \omega_2$, determines which transition is driven. (a)-(c) Three different frequency differences are shown: (a) $\Delta\omega = \omega_0$, equal to the qubit frequency to drive the "carrier" transition; (b) $\Delta\omega = \omega_0 + \nu_k$, equal to the carrier frequency with one quanta of energy added for the k^{th} motional mode to drive a blue sideband (BSB) transition; and (c) $\Delta\omega = \omega_0 - \nu_k$, equal to the carrier frequency with one quanta of energy for mode k subtracted to drive a red sideband (RSB) transition. (d) A bichromat replaces the single frequency ω_1 to drive the MS interaction. The two bichromat frequencies are set symmetrically around the qubit frequency with $\Delta\omega_b = \omega_b^{(MS)} - \omega_2 = \omega_0 + \nu_k + \delta_k$, and $\Delta\omega_r = \omega_r^{(MS)} - \omega_2 = \omega_0 - \nu_k - \delta_k$. They are detuned from the carrier transition by one motional mode quanta in addition to a detuning, δ_k. For all four panels, the Raman beat frequency is shown above the energy levels, as is the change in phonon occupancy n_k for panels (a)-(c).

In panel (d), we illustrate the implementation of the MS interaction using a Raman transition. Here, the detuning is defined as $\delta_k = \Delta\omega_b - \omega_0 - \nu_k = \omega_0 - \nu_k - \Delta\omega_r$, where $\Delta\omega_b$ ($\Delta\omega_r$) is the frequency difference between the two Raman beams for the blue (red) component of the bichromat. To change the phase of the red or blue component to tune either the "spin phase" ($\phi_s = (\phi_b + \phi_r)/2$) or the "motional phase" ($\phi = (\phi_b - \phi_r)/2$), it is sufficient to modulate the phase of one of two Raman beams used for that component.

The hardware-specific coupling parameter in Eqn. (7.31) is altered to be

$$f_k^{(\mu)} = \frac{-i\eta_k^{(\mu)}}{2} = \frac{-i}{2} b_{k\mu} \Delta\tilde{k} \cos\theta \sqrt{\frac{\hbar}{2M\nu_k}}, \tag{8.4}$$

where we use the *net* wavevector between the two Raman beams to calculate the Lamb-Dicke parameter $\Delta\tilde{k}$, and the angle θ is similarly defined to be between the mode orientation and the net Raman wavevector.

8.2 Experimental Setup

We experimentally implement the schemes outlined above using a system of $^{171}\mathrm{Yb}^{+}$ ions confined in a linear Paul trap (similar to [**266**]) with centre-of-mass (COM) trap frequencies along the three trap axes, $\nu_{x,y,z}/2\pi \approx [1.6, 1.5, 0.5]$ MHz. Qubits are encoded in the $^2\mathrm{S}_{1/2}$ ground-state manifold where we associate the hyperfine states $|F = 0, m_F = 0\rangle \equiv |0\rangle$ and $|F = 1, m_F = 0\rangle \equiv |1\rangle$, split by 12.6 GHz, with qubit states $|0\rangle$ and $|1\rangle$ respectively. State initialisation to $|0\rangle$ via optical pumping and state detection are performed using a laser resonant with the $^2\mathrm{S}_{1/2} - {}^2\mathrm{P}_{1/2}$ transition near 369.5 nm.

A pulsed laser near 355 nm is used to drive stimulated Raman transitions between the qubit states [**70**] via two orthogonal laser beams in a geometry where they only couple to the x, y radial motional modes of the trapped ions. To implement entangling gates, a two-tone radio-frequency signal produced by an arbitrary waveform generator is applied to an acousto-optic modulator controlling one of these beams. This produces a bichromatic light field that off-resonantly drives the red and blue sideband transitions, creating the state-dependent force used in the gate. Modulation of the coupling phase $\phi(t)$ is achieved by adjusting the phase difference between the red and blue frequency components, $\phi(t) = \left[\phi_b(t) - \phi_r(t)\right]/2$. The maximum achievable gate Rabi frequency is $\Omega = 2\pi \times 40$ kHz, limited by the available optical power.

8.3 Results and Discussion

8.3.1 Motional mode decoupling

We begin by demonstrating the ability to arbitrarily decouple multiple motional modes using the analytic ΦM scheme. A single qubit is prepared in state $|0\rangle$ and the bichromatic Raman fields are applied for $\tau_g = 80$ µs. The Raman beams' frequency difference is scanned over a range including two radial modes. Here, the application of the state-dependent force produces a purely qubit-oscillator interaction and any residual mutual coupling at the conclusion of the operation will result in $P_1 > 0$, where population P_i is the probability of i ions being projected into state $|1\rangle$.

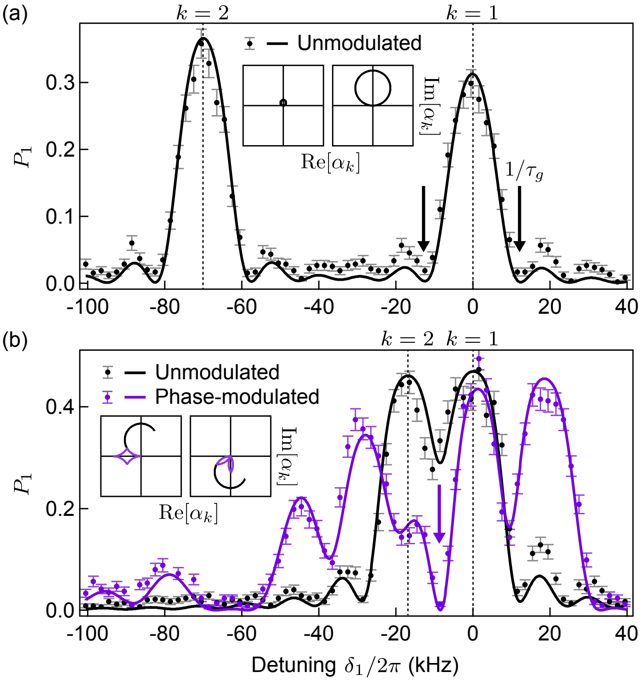

Figure 8.4. Motional mode decoupling in the single ion case. Population P_1 as a function of laser detuning scanned about two radial modes, $k = 1$ and $k = 2$ (dashed vertical lines). Solid lines are fits to the data, with each mode's initial average phonon number after sideband cooling ($\bar{n}_k$) a free parameter. (a) Mode frequencies split far apart. Arrows indicate detunings at which $\delta_1 = \pm 2\pi/\tau_g$ and the inset shows corresponding phase space trajectories for each mode, with $\bar{n}_{1,2} = (0.2, 0.4)$. (b) Mode frequencies closely spaced. The phase modulation sequence $r_{\delta_2\delta_1}(t; \tau_g)$ (purple) achieves decoupling at an arbitrary detuning $\delta_1/2\pi = -8.5$ kHz (arrow), with phase segments $\phi_{0,1,2,3} \approx (0, 1.34, 0.343, 1.68)\,\pi$. The inset compares unmodulated and ΦM trajectories. Fits give $\bar{n}_{1,2} = (1.2, 1.2)$ for the unmodulated and $\bar{n}_{1,2} = (2.5, 1)$ for the ΦM data.

In Fig. 8.4(a), we tune the modes to have a frequency splitting sufficiently large that the predominant interaction is with only a single mode. In this configuration, complete decoupling is achieved for the detunings $\delta_1 = \pm 2\pi/\tau_g$, indicated by P_1 dropping to zero symmetrically about $\delta_1 = 0$ (similarly about $\delta_1 = -70$ kHz, corresponding to $\delta_2 = 0$). In Fig. 8.4(b), the mode splitting has been decreased via electrostatic tuning of the trap potential such that both modes will become excited when the laser is detuned close to either, illustrating the problem of mode crowding typically experienced in larger systems. For an unmodulated Raman drive, the black data in Fig. 8.4(b) show a large value of P_1 at intermediate detunings (-17 to 0 kHz), where decoupling was previously achievable for mode $k = 1$. By contrast, we may drive P_1 to zero at an arbitrarily chosen detuning (arrow) using a four-segment ΦM sequence to decouple both modes (purple data). The resulting phase space trajectories at this detuning are illustrated in the insets to Fig. 8.4(b), showing how the modulation protocol steers both trajectories back towards the origin at the conclusion of the gate. We have achieved similar decoupling at a range of arbitrary detunings via appropriate construction of the ΦM sequence.

8.3.2 Flexibility in gate operation

We now validate the impact of phase modulation in two-qubit MS entangling gates and demonstrate the flexibility it affords in choice of experimental parameters. For two qubits, there are four radial motional modes that may be excited by the Raman laser; we denote them from highest to lowest frequency as $k = 1$ to $k = 4$. Starting in state $|00\rangle$, we produce the entangled Bell-state $(|00\rangle - i\,|11\rangle)/\sqrt{2}$ by tuning the Raman laser fields to excite both the x-tilt ($k = 2$) and y-COM ($k = 3$) modes in our trap, separated by $\Delta/2\pi \approx 10$ kHz (Fig. 8.5). The remaining two modes are detuned by ~ 80 kHz, far enough to not be significantly excited. The gate time is chosen such that when the detuning from either mode is an integer multiple of $\Delta/3$, the spin and motion fully decouple, giving $\tau_g = 2\pi \times 3/\Delta$ (~ 310 μs). Based on populations P_0, P_1 and P_2, the gate fidelity is estimated as $\mathcal{F} = (P_0 + P_2)/2 + \pi_c/2$. Here,

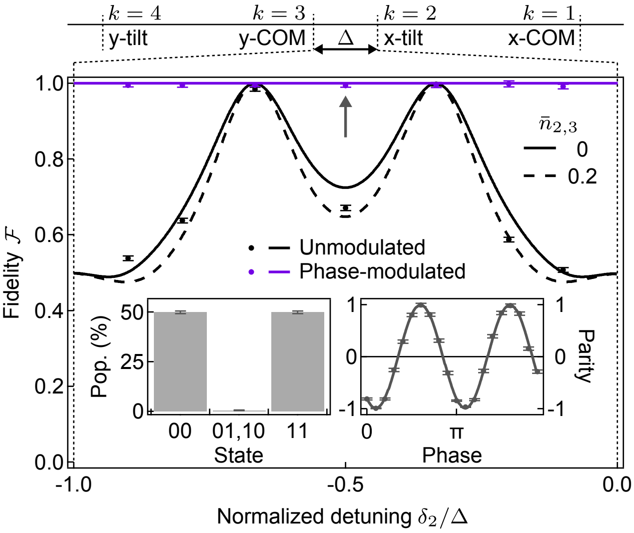

FIGURE 8.5. Maximum achievable gate fidelity as a function of detuning. Solid lines show theoretical predictions for initial phonon-numbers of $\bar{n}_{2,3} = 0$ and the dashed line show predictions for $\bar{n}_{2,3} = 0.2$. Different ΦM sequences are implemented over the detuning range, with $r_{\delta_2\delta_3}(t;\tau_g)$ used for $\delta_2/\Delta \geq -0.5$ and $r_{\delta_3\delta_2}(t;\tau_g)$ for $\delta_2/\Delta < -0.5$. The required Rabi frequency Ω ranges from $2\pi \times (24 - 26)$ kHz for the ΦM gates and $2\pi \times (19 - 26)$ kHz for the unmodulated gates. Error bars are derived from quantum projection noise on the state population estimates and a fit of the parity contrast. The inset shows the underlying data for the ΦM gate at $\delta_2/\Delta = -0.5$ (arrow), for which $\mathcal{F} = 99.4(5)\%$.

π_c is the parity contrast of the created Bell-state observed upon scanning the phase of an additional $\pi/2$-pulse after the gate.

To demonstrate the flexibility of the analytic ΦM scheme, we vary the laser detuning over a range between the y-COM and x-tilt modes, optimising the Rabi frequency Ω at each detuning to achieve a maximally entangling gate. Fig. 8.5 compares the highest theoretically achievable fidelity (lines) for unmodulated and ΦM-MS gates, along with experimental measurements (markers). For the unmodulated gate (black), maximum fidelity can only be achieved at two particular detunings where both mode trajectories naturally close. Elsewhere, the measured two-qubit gate fidelity drops to as low as 50% due to strong residual mode excitation at the conclusion of the gate. In contrast, by implementing an appropriate ΦM gate, maximum fidelity can be ideally achieved for any detuning (purple line). For the ΦM data, we obtain an average experimental Bell-state fidelity of 99.4(2)% across the range of detunings shown, without any form of SPAM subtraction. We estimate the contribution to the Bell state infidelity from imperfect state estimation to be 0.4(4)%.

8.3.3 Suppressing static gate errors

An additional benefit of ΦM gates is the ability to incorporate robustness to imperfections in gate implementation. We explore this phenomenology by engineering static detuning offset errors during application of an entangling gate, and measuring P_1 as a proxy for gate infidelity associated with residual qubit-oscillator coupling. Such offsets are a common error and may arise due to slow drifts or incorrect calibration of the oscillator mode frequencies.

In Fig. 8.6(a) we illustrate this feature by performing two-ion ΦM-MS gates constructed analytically with different orders of noise suppression for the target mode ($k = 4$). As the suppression order in the gate construction is increased, the range of detunings around zero for which $P_1 \approx 0$ broadens, demonstrating robustness for deviations up to ± 1 kHz from the target detuning value with third-order suppression. Data agree well with analytic theory calculated using Eqn. (7.61) from Section 7.3 predicting the functional dependence of the measured P_1 on detuning. Fig. 8.6(b) demonstrates in the phase space picture how the process of phase-shifted sequence concatenation results in repeated decoupling of the mode throughout the gate, reducing residual excitation even for large detuning errors.

Similar benefits are also observed using robust numerically optimised ΦM sequences in Fig. 8.6(c), where we compare the standard and robust numerical gate constructions, again in the presence of static

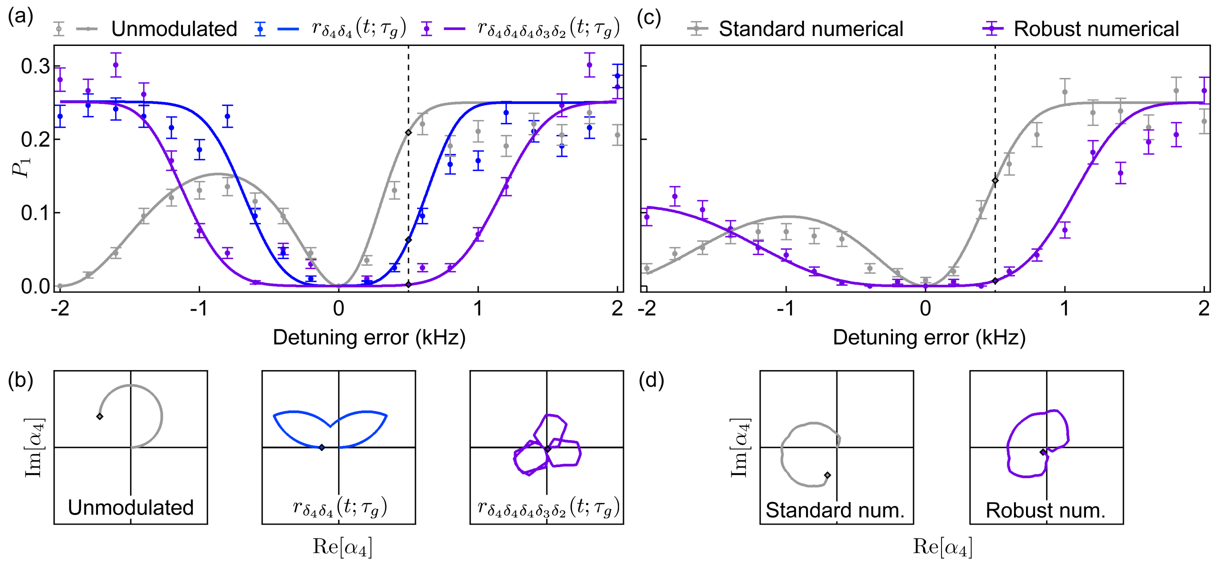

FIGURE 8.6. Robustness of ΦM gates to detuning offsets. (a) Motional excitation quantified by P_1 at the conclusion of a two-qubit entangling gate as a function of detuning offset magnitude. Solid lines are theory with $\bar{n}_4 = 0.1$. The gate time is fixed at $\tau_g = 500$ µs, with a target detuning of -2 kHz from mode 4. The unmodulated gate (grey) is compared to the ΦM sequences $r_{\delta_4\delta_4}(t;\tau_g)$ (blue) and $r_{\delta_4\delta_4\delta_4\delta_3\delta_2}(t;\tau_g)$ (purple), which provide second and third order noise suppression for mode 4, respectively. Rabi frequency Ω is scaled to enact a maximally entangling gate at zero detuning error and ranges from $2\pi \times (18-39)$ kHz. The scaling required for the third-order sequence also necessitates the decoupling of modes 2 and 3. (b) Phase space trajectories for mode 4 with a detuning error of +500 Hz, marked via the dashed line in (a). All plots are of equal scale. (c) P_1 at the conclusion of a two-qubit entangling gate for numerically optimised phase modulation sequences, constructed to sufficiently decouple from all four modes. Solid lines are theory with $\bar{n}_4 = 0.05$. The gate time is fixed at $\tau_g = 400$ µs with a target detuning of -4 kHz from mode 4. The standard numerically optimised gate (grey) with 16 phase segments is compared to a robust solution (purple) with 32 phase segments. Rabi frequencies are $2\pi \times 23$ kHz and $2\pi \times 28$ kHz for the standard and robust gates, respectively. (d) Corresponding phase space trajectories for mode 4 with a detuning error of +500 Hz, marked via the dashed line in (c).

detuning offset errors. In our experiments, the standard sequence does not provide robustness to such offsets, and we observe that P_1 as a function of the applied detuning error behaves similarly to the unmodulated gate in Fig. 8.6(a). The symmetrisation procedure and requirement that the time-averaged positions of the phase space trajectories are approximately zero for the robust gate solution reduces sensitivity to detuning errors, again indicated by the broadening of the dip in P_1.

8.3.4 Reducing sensitivity to time-dependent noise

Phase-modulated gates provide a third advantage in that they can provide robustness to time-varying experimental parameters in addition to static systematic offsets. This is useful in circumstances where parameters can drift or suffer from fluctuations due to, for example, electrical interference. In the following, we experimentally validate that ΦM gates may be used to provide robustness against errors induced by fluctuations in the motional mode frequencies and laser amplitude, which result in a time-dependent detuning offset and coupling-strength error, respectively.

Gate effectiveness in suppressing time-dependent noise is conveniently captured using a filter function formalism [**9**,**147**,**244**,**267**], which describes the noise-susceptibility of an arbitrary control operation as a function of noise frequency. Modifications to the framework allow us to predict infidelity solely due to residual qubit-oscillator coupling in two-qubit entangling gates. For a given noise spectrum, $S_\epsilon(\omega)$, the decoupling error is inferred from the noise-averaged P_1 population,

$$\mathbb{E}\left[P_1\right] \approx \frac{1}{2\pi}\int_{-\infty}^{\infty} d\omega S_\epsilon\left(\omega\right) F_\epsilon\left(\omega\right). \tag{8.5}$$

Here, the filter function $F_\epsilon(\omega)$ expresses the susceptibility or "admittance" of the gate operation to a given noise source, with $\epsilon \in \{\Omega, \delta\}$ denoting laser amplitude or detuning noise, respectively. For laser amplitude noise, the analytic form of the filter function has been previously described [**9**]. The filter function for detuning noise represents an original contribution of this work and, and for the case of an operation performed on a single qubit, is given by

$$F_\delta(\omega) = \sum_k T_k \left|\Omega f_k^{(1)} \int_0^{\tau_g} dt e^{-i[(\delta_k-\omega)t+\phi(t)]} t\right|^2. \tag{8.6}$$

Here we have defined $T_k = 2\left(\bar{n}_k + 1/2\right)$, which incorporates the average phonon occupancy for each mode, $\bar{n}_k$. The derivation of this filter function, as well as that for a targeted entangling operation between a pair of qubits *embedded* in an N-qubit system, is described in Section 7.4 in the previous chapter.

To probe gate sensitivity under application of the two noise types described above with the highest possible measurement fidelity, we perform a gate-equivalent operation on a single ion in the presence of engineered noise in the respective quadrature. The gate detuning is set such that the motional interaction

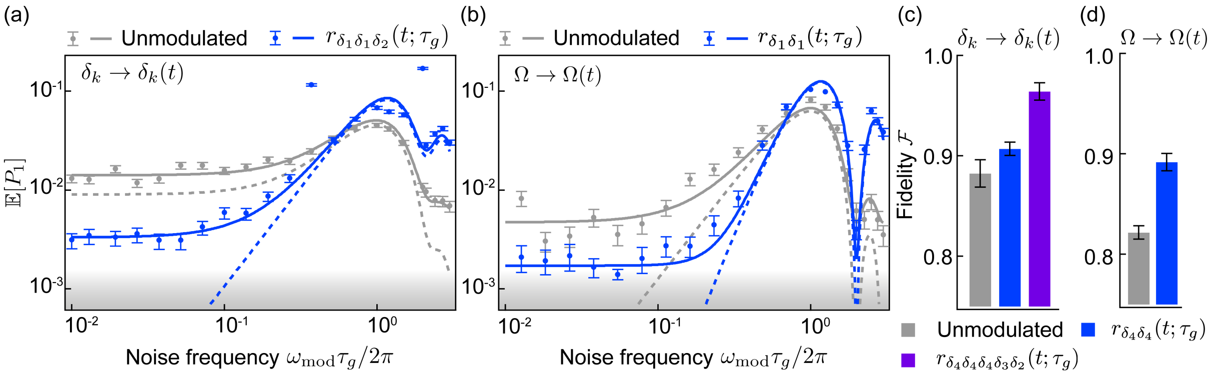

FIGURE 8.7. Suppression of time-dependent noise. (a,b) Noise-averaged measurements of P_1 for a single ion plotted against applied (a) detuning and (b) amplitude noise frequency. Overlaid are the analytic filter function predictions with $\bar{n}_{1,2} = 0.9$ (dashed lines) and the predictions with an added frequency-independent offset (solid lines), determined by the average of the six lowest-frequency data points. For (a), the added offsets are 5.1×10^{-3} (unmodulated) and 3.3×10^{-3} (ΦM). For (b), the added offsets are 4.7×10^{-3} (unmodulated) and 1.7×10^{-3} (ΦM). For (a) the modulation depth is $\beta = 0.1$ with $\tau_g = 300$ µs and for (b) $\beta = 0.29$ with $\tau_g = 250$ µs. The Rabi frequencies range from $2\pi \times (14 - 34)$ kHz and Ω is scaled in the ΦM operations to enclose the same phase space area as the equivalent unmodulated operation. Shading indicates the measurement floor. (c, d) Two-qubit gate fidelities with engineered (c) detuning and (d) amplitude noise. For both noise types, $\tau_g = 500$ µs and Ω ranges from $2\pi \times (18 - 36)$ kHz. Here, the detuning noise is engineered by directly modulating the frequency of the motional modes via the application of a sinusoidally oscillating voltage to the DC trap electrodes. Measured gate fidelities for (c) are 86%, 91% and 96%, respectively, under $\beta = 0.25$. For (d), the measured gate fidelities are 82% and 87%, under $\beta = 0.2$. Due to limitations on the experimentally achievable Rabi frequency in our setup ($\Omega = 2\pi \times 40$ kHz), only a second-order ΦM sequence is performed for the amplitude noise case shown in (d).

predominantly occurs with a single mode, and the decoupling condition is met ($\delta_1 = 2\pi/\tau_g$). We experimentally implement a system-identification procedure [**147**] in which a single-frequency "noise" modulation is applied and produces an effective spectrum $S(\omega_{\rm mod}) = \beta^2(\delta(\omega - \omega_{\rm mod}) + \delta(\omega + \omega_{\rm mod}))/4$, where β quantifies the strength of the modulation. A measurement of $\mathbb{E}\,[P_1]$ under this phase-averaged noise spectrum then gives a direct probe of the filter function at a single frequency, $\omega_{\rm mod}$. We then vary $\omega_{\rm mod}$ and measure $\mathbb{E}\,[P_1]$ at each value, effectively reconstructing the frequency-dependent filter function of the underlying gate operation. This approach is possible as the filter function Eqn. (8.6) is only dependent on the residual qubit-oscillator coupling and independent of any entangling phase that would be acquired with two or more ions.

We engineer detuning noise via frequency-modulation of the two-tone RF signal producing the bichromatic gate beam; this has an effect on the gate interaction equivalent to fluctuating motional mode frequencies and modifies the laser detuning as $\delta_k \rightarrow \delta_k(1+\beta \sin(\omega_{\text{mod}} t + \phi_{\text{mod}}))$, where ω_{mod} quantifies the frequency of the modulation and ϕ_{mod} its phase. In a similar manner, laser amplitude noise is engineered by a direct modulation of the overall laser intensity via an acousto-optic modulator, yielding $\Omega \rightarrow \Omega(1+\beta \sin(\omega_{\text{mod}} t + \phi_{\text{mod}}))$.

The noise-suppressing properties of ΦM gates are experimentally validated in Fig. 8.7(a,b). In these experiments, we perform frequency-dependent system identification on an unmodulated and an analytic ΦM sequence constructed to exhibit second-order suppression of both detuning and laser-amplitude noise. Experimentally, we observe that the ΦM gate (blue) exhibits lower measured error across the range of applied noise frequencies until a crossover is reached near the inverse gate time $\omega_{\text{mod}}\tau_g/2\pi \approx 1$. This behaviour indicates a trade-off between low frequency error suppression and sensitivity to noise near the inverse gate time, consistent with observations for single-qubit operations [**147**].

We find good agreement between experimental measurements and an empirical model combining the prediction for gate error from the filter function with a frequency-independent error offset extracted from measurement (solid lines). For both noise types, the filter function predictions for ΦM gates (dashed lines) show decreased noise sensitivity in the regime $\omega_{\text{mod}}\tau_g/2\pi < 1$, captured by an enhanced slope on a log-log plot. In the case of detuning noise shown in (a), the base filter function prediction for the unmodulated gate exhibits broadband sensitivity to noise, manifested in the saturation of $\mathbb{E}\left[P_1\right]$ towards lower noise frequencies. For the unmodulated gate exposed to amplitude noise as shown in (b), the filter function prediction drops towards zero in the low frequency regime, as a quasi-static error will simply result in a scaling of the Rabi frequency and will not affect the closure of the phase space trajectories.

The error offset employed in our empirical model may arise in the experiment due to uncompensated noise from some uncontrolled source, or potentially from higher-order modulation-frequency-dependent terms in the filter function [**267**, **268**] (i.e. higher-order sensitivity to the applied single-frequency noise source). In error-suppressing gates we have previously observed that when studying agreement between measurements and filter function predictions, higher-order filter function contributions grow in importance when leading-order error terms are cancelled by a compensating pulse [**147**]. However, in these measurements we find larger error offsets associated with unmodulated gates, consistent with the presence of an intrinsic noise process to which the unmodulated gate is more susceptible.

We next demonstrate that ΦM gates provide error-suppression in two-qubit entangling operations subjected to time-dependent noise, measuring the full gate fidelity. As in the system-identification routine above, we apply a single-frequency noise modulation, with a normalised frequency $\omega_{\text{mod}}\tau_g/2\pi = 0.1$. Here, the noise modulation is sufficiently strong to reduce the unmodulated (no ΦM) gate fidelity below 90%. This fidelity-loss can be substantially recovered though use of ΦM; replacing an unmodulated gate with a ΦM construction (Fig. 8.7(c,d)), we observe an increase in gate fidelity as the order of error suppression is increased for both noise types.

8.3.5 Scaling to larger systems

When performing ΦM gates in systems with a large number of oscillator modes, one needs to consider the associated growth in the number of phase segments required to achieve mode decoupling. In ion trap systems, every additional ion contributes one axial and two radial modes to the spectrum. Increasing the number of phase segments typically results in trajectories that enclose a smaller phase space area, necessitating either an increase in the Rabi frequency or gate time in order to accumulate the desired entangling phase. Ideally, both of these quantities should be minimised, reducing sensitivity to error sources such as photon scattering [**269**] or, in the case of increased gate time, motional heating and motional dephasing. To explore the relevant scaling behaviour for both analytic and numerically optimised constructions, we consider the case of a fixed maximum Rabi frequency and calculate the shortest achievable gate time realised in the two approaches, as a function of ion number in a linear chain.

As a concrete example, we consider an entangling operation between the two outermost adjacent ions in an N-ion chain of $^{171}\text{Yb}^+$ ions. For each N, we fix $\Omega = 2\pi \times 100$ kHz and perform a discretised search over detuning and gate time, choosing the ΦM sequence that results in a maximally entangled pair in the shortest time τ_B. The ΦM sequences are constructed to decouple from all $M = 2N$ radial motional modes such that $\epsilon \lesssim 10^{-4}$. As shown in Fig. 8.8(a), with increasing N, the numerically optimised sequences scale more favourably than those calculated analytically. For the standard numerically optimised sequences, we find the shortest gate time is constant (140 µs) for up to $N = 10$ ions. In the robust case, τ_B is slower than the standard sequences by a small offset and grows gradually with ion number from 170 µs ($N = 2$) to 210 µs ($N = 10$). The rapid increase in τ_B for the analytic gate construction, combined with the simultaneous exponential growth in the required number of phase segments (2^M), ultimately render it less suitable for larger systems than the numerically derived alternative. Also, despite the fact that a specific analytic ΦM sequence may be calculated in closed form, the process of choosing the best analytic construction from all possible permutations of $r_{\delta_M \ldots \delta_1}(t;\tau_g)$ sequences can add computational complexity, as the ordering of mode closure represents an additional degree of

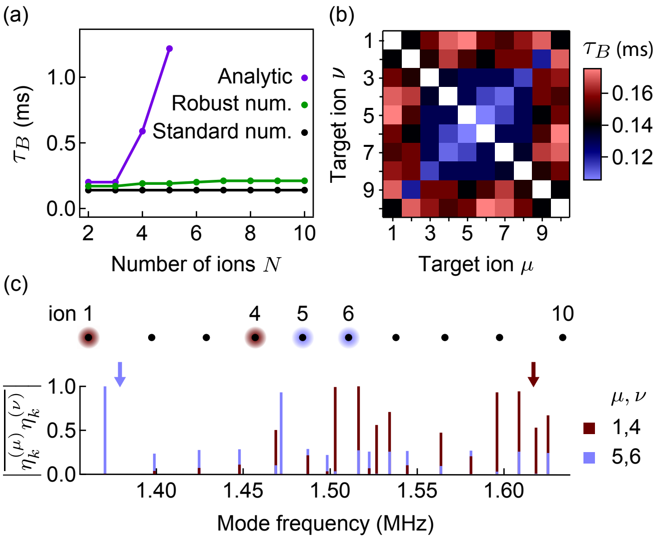

FIGURE 8.8. Scaling to larger qubit systems. (a) Shortest achievable gate time (τ_B) as a function of the number of qubits, decoupling from all $M = 2N$ radial modes. The number of phase shifts for each ΦM approach is fixed at: $S = 2^M$ (analytic), $S = 4M$ (standard numerical) and $S = 8M$ (robust numerical). The mode spectrum is calculated using COM trapping frequencies of $\nu_{x,y,z}/2\pi = [1.62, 1.54, 0.15]$ MHz with the maximum Rabi frequency limited to $\Omega = 2\pi \times 100$ kHz. (b) Shortest achievable gate time (τ_B) represented as a colour-scale for standard numerically optimised entangling gates between different target pairs in an $N = 10$ ion chain, decoupling from the radial modes. Black represents the median gate time, red indicates slower gates and blue indicates faster. (c) Schematic depiction of the equilibrium positions for a $N = 10$ ion chain and corresponding radial mode spectrum. Vertical bars positioned at the frequency of each mode k indicate the value of $\overline{|\eta_k^{(\mu)}\eta_k^{(\nu)}|}$, which is $|\eta_k^{(\mu)}\eta_k^{(\nu)}|$ normalised to the maximum value of $|\eta_k^{(\mu)}\eta_k^{(\nu)}|$ for all k. Arrows indicate the detunings corresponding to τ_B for two target pairs: 1,4 (red) and 5,6 (blue).

freedom that impacts gate time. To avoid this computational overhead, for the analytic data shown in Fig. 8.8(a), we consider only a single permutation corresponding to mode closure in order from largest to smallest detuning. This ordering tends to minimise the error-contribution from far-detuned modes by keeping their trajectories close to the origin, while also producing trajectories for the strongly excited modes that result in a larger accumulated entangling phase.

These observations also hold for entangling operations performed on arbitrary ion pairs within a larger chain, where spatial variation in ion-motion coupling across the chain provides an additional consideration in gate construction. In Fig. 8.8(b), we investigate the dependence of τ_B on the choice of target ion pair within an $N = 10$ ion crystal for standard numerically optimised gates, again requiring decoupling from just the radial motional modes. Assuming a $2\pi \times 100$ kHz maximum Rabi frequency, τ_B ranges from 120 μs to 175 μs. This variation highlights the fact that the rate at which entanglement is accumulated between ions μ, ν will depend on how strongly the ions are coupled to the dominant excited modes, as quantified by the Lamb-Dicke parameters $\eta_k^{(\mu)}, \eta_k^{(\nu)}$. For example, a particular mode may involve a large displacement of the outer ions, while the central ions remain almost stationary. This mode would therefore be unsuitable for use in entangling gates attempting to induce coupling between central and outer ions. Such variability in the coupling strength across a chain is shown for two different ion pairs in Fig. 8.8(c), where we plot the magnitude of the Lamb-Dicke parameters across a complex multi-mode spectrum.

Considering this additional complexity, the flexibility provided by ΦM sequences to set the detuning arbitrarily within the mode spectrum enables the leveraging of entangling-phase contributions from multiple modes where $\left|\eta_k^{(\mu)}\eta_k^{(\nu)}\right|$ is greatest for the given ion pair. As such, the use of ΦM gates also offers speed advantages relative to conventional techniques where the detuning would simply be fixed close to a COM mode and the gate speed limited by the requirement that the other modes are not significantly excited. Using phase modulation, we are free to set the detuning arbitrarily for gates implemented between different target ion pairs; the arrows in Fig. 8.8(c) show the detuning values corresponding to τ_B for gates between two different ion pairs. Without phase modulation, the detuning could not be set arbitrarily while still achieving a high-fidelity gate (see Fig. 8.5).

8.4 Conclusion

We have demonstrated that phase modulation provides a robust and flexible framework for performing high-fidelity entangling gates in qubit-oscillator systems, validated using trapped ions. We have implemented two-qubit entangling gates with an average fidelity of $99.4(2)\%$, achieving maximum fidelity for arbitrary laser detunings, including settings where unmodulated gates cannot be achieved with high fidelity. In addition, we have shown that the ΦM framework provides robustness to static and time-dependent errors in the laser amplitude and gate detuning, captured through a new theoretical model in the filter function framework.

The ΦM approach to constructing oscillator-mediated entangling gates gates holds several practical advantages relative to alternative modulation approaches [**88**,**257**]. First, the amplitude and frequency of the driving field remain fixed throughout the gate operation, meaning experimental -– often duty-cycle-dependent — nonlinearities and the effect of time-dependent AC Stark shifts need not be considered.

Next, the ΦM technique is also readily extensible to multi-qubit entangling gates in larger systems, where we have shown that numerical optimisation may be utilised to exponentially reduce the number of phase shifts required to decouple from an increasing number of modes, and flexibility in gate detuning can be used to extract speedups in gate implementation. We hope that the ΦM techniques demonstrated here may be employed beyond ion trap systems to improve gate fidelity in other architectures that utilise oscillator-mediated operations.

CHAPTER 9

Conclusion

---

*“**Computers Aren’t So Smart, After All**: During the "computer craze" of the 1950s and 1960s some people envisioned the machine replacing the human brain. It hasn’t happened and, says the author, it probably never will. So we must still think for ourselves.”* [**270**]

*****

An article from 1974 in The Atlantic proudly foreshadowed the dimming of the era of electrical computation, claiming that the previous decades of hype and growth had reached a natural conclusion and could provide no further innovation [**270**]. With little assumption, I presume that the subsequent events of the following 47 years are well-enough known to the reader to conclude that this scepticism was misplaced. However, it was not unfounded.

The development of the computer was an extraordinarily challenging task riddled with missteps and failures, that are only evident as such with the perspective of history. It was a pathway filled with broken vacuum tubes, hardware “bugs” created by their literal namesake, thousands of hours of woman and man-power, and hundreds of unfulfilled promises. It would be simple in hindsight to dismiss early critics as modern Luddites but the reality is considerably more complex. In many ways, critics were able to penetrate the obscuring veil of hype with a clearer-eyed view to illuminate the underlying faults hindering progress. The difficultly of managing hardware errors and creating robust programs threatened the scalability and reliability of programmable computers, and led to the need to revise expectations and early promises. While computers eventually became a revolutionary and powerful technology, their development was not without its struggles, and the problem of how to reduce and manage errors was a foremost consideration.

With every new generation of the computer, we expand our capability to innovate and explore interesting, nuanced questions but we also introduce a greater number of ways in which subtle errors can affect the final output. Early iterations of programmable computing devices were often single purpose but also more robust to errors. If a Jacquard loom dropped a stitch, the textile would still have integrity, whereas the fidelity of our gates is affected by the magnetic field distortions of the local train timetable. Similarly, early classical digital computers may have required air conditioning to prevent overheating, but never needed liquid helium. Whilst we may not wake up to discover a moth inside our vacuum chamber,[1] trapped alongside our ions, we are still susceptible to hundreds of sources of error, many not even considered for classical computers. Growth in our technological capabilities enables growth in both the potential of the devices we can create and the sources of error that can render them useless.

In the last two decades, the field of quantum computing has seen growth unlike anything it has encountered before. Innovations and investment are being contributed from a diverse range of sources – academia, government, private industries, and startups. Some fear that the field has reached its "peak of inflated expectations" in the "hype cycle", and is ready to crash. Many others, myself included, believe modern quantum technology stands on the threshold of creating a truly effectual device for the purpose of solving computationally complex – and even intractable – problems. However, efforts are encountering resistance in both reliability and scalability.

Just as with classical computers, the development of a practical large-scale quantum processor requires collaboration from contributors across the entire quantum computing architecture – software, hardware, firmware, error correction – in parallel. Groups can no longer operate independently, refining hardware or developing software algorithms without communication and integration. A critical component of this integration will be dynamic quantum control to reduce errors at a logical level in order to precondition a system for quantum error correction, or possibly, in some circumstances, obviate the need for it entirely.

Summary and Outlook

The demonstrations I have presented in this thesis are a collection of tools from the "quantum control toolkit" that can be used for two broad purposes.

Firstly, noise characterisation allows us to understand the *nature* of underlying errors affecting the quantum processor. This knowledge can then be used as a probe to sense where errors are occurring, allowing us to make informed improvements to the physical hardware. The theoretical work in Chapter 4 forms the basis of a characterisation protocol experimentally verified in Chapters 5 and 6. By modifying the analysis of the results measured during common QCVV protocols with minimal to no alterations

---

[1] or certainly hope not!

to the protocols themselves, we are able to reveal more subtle information about not just the *average* errors, but also underlying temporal correlations in the error process. Identifying the correlation characteristics of the dominant error process can be used to eliminate many possible sources of error. For example, in a trapped-ion system, detecting primarily uncorrelated errors removes the need to probe for slow drifts or poor calibrations in the control field, but does not preclude the possibility of laser light leakage scrambling the information through a depolarising process.

Secondly, once all reasonable improvements to the physical hardware have been made – limited possibly by physical constraints, ability or finances – the tools presented here can be used to tailor dynamic control solutions to improve the system reliability and scalability beyond that achieved with primitive gates. Chapters 3, 6 and 8 all demonstrate the use of quantum control to push experimental fidelities past their physical limits.

In Chapter 3, I demonstrate a specific application for trapped ion systems, using electron shelving to improve the measurement fidelity achieved in a hyperfine ion qubit, which is typically limited by off-resonant scattering during the detection period. Chapter 6 demonstrates the use of dynamically corrected gates for single qubits to both improve net error rates and reduce temporal and spatial error correlations between gates and qubits. Moving from single-qubit rotations to two-qubit entangling gates, Chapter 8 is the first example of using phase-modulated Mølmer-Sørensen gates to improve entangling gate fidelities by reducing residual qubit-motional coupling at the gate's conclusion. The theoretical work in Chapter 7 explores the physics behind the Mølmer-Sørensen gate, calculating the eigenspectra of the motional modes required for its operation and predicting the gate output in both the ideal operation and in the presence of time-varying noise. This work was fundamental in predicting the output of different MS gate constructions, and was necessary to build numerically optimised phase modulation sequences.

Chapters 6 and 8 are examples of more general quantum control techniques that can be extended to other platforms beyond trapped ions. Indeed, initial work implementing dynamically corrected gates on superconducting qubits shows promising advancements, demonstrating the first model-based robust control [**271**]. Likewise, two-qubit entangling gates in superconducting circuits could utilise phase modulation to reduce residual coupling errors, just as we have demonstrated with the Mølmer-Sørensen gate. These tools also extend beyond quantum computing, being equally pertinent to applications in trapped-ion metrology or sensing.

Already in our setup, we see several practical examples of using quantum control to improve our performance. For instance, scaling to larger numbers of qubits and using global simultaneous microwave rotations necessitates the use of BB1 dynamically corrected gates to account for the microwave field intensity gradient. Furthermore, the electron-shelving based detection in Chapter 3 will almost certainly require dynamically corrected gates to correct for frequency and amplitude errors, eliminating the need for frequent recalibrations in the shelving parameters.

Moving forwards, one of the most critical next steps is integration. We must work with groups to improve the performance of their algorithms by introducing these tools into existing setups. Already, there are opportunities proposed to improve the reliability of variational quantum eigensolvers (VQE) and digital quantum simulators by incorporating quantum control techniques. With the integration of quantum control into noisy intermediate-scale quantum systems, I believe we will begin to achieve truly advantageous results. I hope that the work in this thesis has contributed to the rich and developing field of quantum control.

“All this happened, more or less.”

- Kurt Vonnegut, *Slaughterhouse-Five*

References

[1] C. L. Edmunds, T. R. Tan, A. R. Milne, A. Singh, M. J. Biercuk, and C. Hempel, "Scalable hyperfine qubit state detection via electron shelving in the $^2\mathrm{D}_{5/2}$ and $^2\mathrm{F}_{7/2}$ manifolds in $^{171}\mathrm{Yb}^+$." arXiv:quant-ph/2012.14606, 2020.

[2] T. R. Tan, C. L. Edmunds, A. R. Milne, M. J. Biercuk, and C. Hempel, "Precision characterization of the $^2\mathrm{D}_{5/2}$ state and quadratic zeeman coefficient in $^{171}\mathrm{Yb}^+$." arXiv:physics.atom-ph/2012.14187, 2021.

[3] S. Mavadia, C. L. Edmunds, C. Hempel, H. Ball, F. Roy, T. M. Stace, and M. J. Biercuk, "Experimental quantum verification in the presence of temporally correlated noise," *npj Quantum Information*, vol. 4, no. 7, 2018.

[4] C. L. Edmunds, C. Hempel, R. J. Harris, V. Frey, T. M. Stace, and M. J. Biercuk, "Dynamically corrected gates suppressing spatiotemporal error correlations as measured by randomized benchmarking," *Phys. Rev. Research*, vol. 2, p. 013156, Feb 2020.

[5] H. Ball, M. J. Biercuk, A. Carvalho, J. Chen, M. Hush, L. A. D. Castro, L. Li, P. J. Liebermann, H. J. Slatyer, C. Edmunds, V. Frey, C. Hempel, and A. Milne, "Software tools for quantum control: Improving quantum computer performance through noise and error suppression." arXiv:quant-ph/2001.04060, 2020.

[6] A. R. Milne, C. L. Edmunds, C. Hempel, F. Roy, S. Mavadia, and M. J. Biercuk, "Phase-Modulated Entangling Gates Robust to Static and Time-Varying Errors," *Phys. Rev. Applied*, vol. 13, p. 024022, Feb 2020.

[7] D. F. V. James, "Quantum dynamics of cold trapped ions with application to quantum computation," *Applied Physics B-Lasers And Optics*, vol. 66, no. 2, pp. 181–190, 1998.

[8] G. Kirchmair, J. Benhelm, F. Zähringer, R. Gerritsma, C. F. Roos, and R. Blatt, "Deterministic entanglement of ions in thermal states of motion," *New Journal of Physics*, vol. 11, no. 2, p. 023002, 2009.

[9] T. J. Green and M. J. Biercuk, "Phase-Modulated Decoupling and Error Suppression in Qubit-Oscillator Systems," *Physical Review Letters*, vol. 114, no. 12, p. 120502, 2015.

[10] C. F. Roos, "Ion trap quantum gates with amplitude-modulated laser beams," *New Journal of Physics*, vol. 10, no. 1, p. 013002, 2008.

[11] P. Benioff, "The computer as a physical system: A microscopic quantum mechanical Hamiltonian model of computers as represented by Turing machines," *Journal of Statistical Physics*, vol. 22,

pp. 563–591, May 1980.

[12] D. Deutsch, “Quantum theory, the Church-Turing principle and the universal quantum computer,” *Proceedings of the Royal Society of London. A. Mathematical and Physical Sciences*, vol. 400, pp. 97–117, July 1985.

[13] R. P. Feynman, “Simulating physics with computers,” *International Journal of Theoretical Physics*, vol. 21, pp. 467–488, June 1982.

[14] P. Shor, “Algorithms for quantum computation: discrete logarithms and factoring,” in *Proceedings 35th Annual Symposium on Foundations of Computer Science*, IEEE Comput. Soc. Press, 2004.

[15] P. W. Shor, “Polynomial-Time Algorithms for Prime Factorization and Discrete Logarithms on a Quantum Computer,” *SIAM Journal on Computing*, vol. 26, pp. 1484–1509, Oct. 1997.

[16] C. Monroe, D. M. Meekhof, B. E. King, W. M. Itano, and D. J. Wineland, “Demonstration of a Fundamental Quantum Logic Gate,” *Phys. Rev. Lett.*, vol. 75, pp. 4714–4717, Dec 1995.

[17] A. Peres, “Reversible logic and quantum computers,” *Phys. Rev. A*, vol. 32, pp. 3266–3276, Dec 1985.

[18] P. W. Shor, “Scheme for reducing decoherence in quantum computer memory,” *Phys. Rev. A*, vol. 52, pp. R2493–R2496, Oct 1995.

[19] J. Zhang, G. Pagano, P. W. Hess, A. Kyprianidis, P. Becker, H. Kaplan, A. V. Gorshkov, Z.-X. Gong, and C. Monroe, “Observation of a many-body dynamical phase transition with a 53-qubit quantum simulator,” *Nature*, vol. 551, pp. 601–604, Nov. 2017.

[20] F. Arute *et al.*, “Quantum supremacy using a programmable superconducting processor,” *Nature*, vol. 574, pp. 505–510, Oct. 2019.

[21] H.-S. Zhong *et al.*, “Quantum computational advantage using photons,” *Science*, vol. 370, no. 6523, pp. 1460–1463, 2020.

[22] J. Preskill, “Quantum computing and the entanglement frontier.” arXiv:quant-ph/1203.5813, 2012.

[23] C. Song *et al.*, “10-Qubit Entanglement and Parallel Logic Operations with a Superconducting Circuit,” *Phys. Rev. Lett.*, vol. 119, p. 180511, Nov 2017.

[24] Y. Wang, Y. Li, Z. qi Yin, and B. Zeng, “16-qubit IBM universal quantum computer can be fully entangled,” *npj Quantum Information*, vol. 4, Sept. 2018.

[25] X.-L. Wang *et al.*, “18-Qubit Entanglement with Six Photons’ Three Degrees of Freedom,” *Phys. Rev. Lett.*, vol. 120, p. 260502, Jun 2018.

[26] T. Monz, P. Schindler, J. T. Barreiro, M. Chwalla, D. Nigg, W. A. Coish, M. Harlander, W. Hänsel, M. Hennrich, and R. Blatt, “14-Qubit Entanglement: Creation and Coherence,” *Phys. Rev. Lett.*, vol. 106, p. 130506, Mar 2011.

[27] N. Friis *et al.*, “Observation of Entangled States of a Fully Controlled 20-Qubit System,” *Phys. Rev. X*, vol. 8, p. 021012, Apr 2018.

[28] I. Pogorelov *et al.*, “A compact ion-trap quantum computing demonstrator.” arXiv:quant-ph/2101.11390, 2021.

[29] D. Leibfried *et al.*, “Experimental demonstration of a robust, high-fidelity geometric two ion-qubit phase gate,” *Nature*, vol. 422, pp. 412–415, 2003.

[30] A. Wallraff, D. I. Schuster, A. Blais, L. Frunzio, R.-S. Huang, J. Majer, S. Kumar, S. M. Girvin, and R. J. Schoelkopf, “Strong coupling of a single photon to a superconducting qubit using circuit quantum electrodynamics,” *Nature*, vol. 431, pp. 162–167, Sept. 2004.

[31] J. R. Petta, “Coherent Manipulation of Coupled Electron Spins in Semiconductor Quantum Dots,” *Science*, vol. 309, pp. 2180–2184, Sept. 2005.

[32] E. Knill, R. Laflamme, and G. J. Milburn, “A scheme for efficient quantum computation with linear optics,” *Nature*, vol. 409, pp. 46–52, Jan. 2001.

[33] A. Gruber, “Scanning Confocal Optical Microscopy and Magnetic Resonance on Single Defect Centers,” *Science*, vol. 276, pp. 2012–2014, June 1997.

[34] V. Mourik, K. Zuo, S. M. Frolov, S. R. Plissard, E. P. A. M. Bakkers, and L. P. Kouwenhoven, “Signatures of Majorana Fermions in Hybrid Superconductor-Semiconductor Nanowire Devices,” *Science*, vol. 336, pp. 1003–1007, Apr. 2012.

[35] A. G. Fowler, M. Mariantoni, J. M. Martinis, and A. N. Cleland, “Surface codes: Towards practical large-scale quantum computation,” *Phys. Rev. A*, vol. 86, p. 032324, Sep 2012.

[36] S. Bravyi, M. Englbrecht, R. König, and N. Peard, “Correcting coherent errors with surface codes,” *npj Quantum Information*, vol. 4, Oct. 2018.

[37] D. Wineland, C. Monroe, W. Itano, D. Leibfried, B. King, and D. Meekhof, “Experimental issues in coherent quantum-state manipulation of trapped atomic ions,” *Journal of Research of the National Institute of Standards and Technology*, vol. 103, p. 259, May 1998.

[38] S. Olmschenk, K. C. Younge, D. L. Moehring, D. N. Matsukevich, P. Maunz, and C. Monroe, “Manipulation and detection of a trapped Yb^+ hyperfine qubit,” *Phys. Rev. A*, vol. 76, p. 052314, Nov 2007.

[39] S. M. Olmschenk, *Quantum Teleportation Between Distant Matter Qubits*. PhD thesis, The University of Michigan, 2009.

[40] J. Preskill, “Introduction to quantum information.” `https://quantumfrontiers.com/2012/12/17/introduction-to-quantum-information/`.

[41] J. Preskill, “John Preskill - Introduction to quantum information (part 1) - CSSQI 2012.” `https://www.youtube.com/watch?v=Q4xBlSi_fOs`.

[42] J. Preskill, “John Preskill - Introduction to quantum information (part 2) - CSSQI 2012.” `https://www.youtube.com/watch?v=PJ6HbxBKZ68`.

[43] J. Preskill, "Lecture notes for Physics 229: Quantum information and computation." `http://theory.caltech.edu/~preskill/ph219/index.html`.

[44] T. D. Ladd, F. Jelezko, R. Laflamme, Y. Nakamura, C. Monroe, and J. L. O'Brien, "Quantum computers," *Nature*, vol. 464, pp. 45–53, Mar. 2010.

[45] S. J. Devitt, W. J. Munro, and K. Nemoto, "Quantum error correction for beginners," *Reports on Progress in Physics*, vol. 76, p. 076001, jun 2013.

[46] J. Preskill, "Quantum Computing in the NISQ era and beyond," *Quantum*, vol. 2, p. 79, Aug. 2018.

[47] Q-CTRL Pty Ltd, "An introduction to quantum computing (ep1)." `https://www.youtube.com/watch?v=0XnnTlCc-vg`.

[48] Q-CTRL Pty Ltd, "Quantum fundamentals (ep2)." `https://www.youtube.com/watch?v=LqDf_4GeogA`.

[49] Q-CTRL Pty Ltd, "Quantum circuits and algorithms (ep3)." `https://www.youtube.com/watch?v=dXvmCSfCPms`.

[50] Q-CTRL Pty Ltd, "Noise in quantum computing (ep4)." `https://www.youtube.com/watch?v=AUAkoEiutOE`.

[51] "Q-CTRL Pty Ltd", "The NISQ era and beyond (ep5)." `https://www.youtube.com/watch?v=LILcw1irAmA`.

[52] J. T. Merrill and K. R. Brown, "Progress in Compensating Pulse Sequences for Quantum Computation," in *Advances in Chemical Physics*, pp. 241–294, John Wiley & Sons, Inc., Mar. 2014.

[53] W. Paul and H. Steinwedel, "Notizen: Ein neues Massenspektrometer ohne Magnetfeld," *Zeitschrift für Naturforschung A*, vol. 8, pp. 448–450, July 1953.

[54] P. Wolfgang and S. Helmut, "Apparatus for separating charged particles of different specific charges," June 7 1960. US 2939952A.

[55] W. Paul, "Electromagnetic traps for charged and neutral particles," *Rev. Mod. Phys.*, vol. 62, pp. 531–540, Jul 1990.

[56] F. Penning, "Die glimmentladung bei niedrigem druck zwischen koaxialen zylindern in einem axialen magnetfeld," *Physica*, vol. 3, pp. 873–894, Nov. 1936.

[57] F. Penning, "Ein neues manometer für niedrige gasdrucke, insbesondere zwischen l0-3 und 10-5 mm," *Physica*, vol. 4, pp. 71–75, Feb. 1937.

[58] H. G. Dehmelt and F. L. Walls, ""Bolometric" Technique for the rf Spectroscopy of Stored Ions," *Phys. Rev. Lett.*, vol. 21, pp. 127–131, Jul 1968.

[59] L. S. Brown and G. Gabrielse, "Geonium theory: Physics of a single electron or ion in a Penning trap," *Rev. Mod. Phys.*, vol. 58, pp. 233–311, Jan 1986.

[60] H. B. Ball, *Robust Quantum Control & Verification & Quantum Simulation with Trapped Ions*. PhD thesis, School of Physics, The University of Sydney, 2018.

[61] M. G. Raizen, J. M. Gilligan, J. C. Bergquist, W. M. Itano, and D. J. Wineland, "Ionic crystals in a linear Paul trap," *Phys. Rev. A*, vol. 45, pp. 6493–6501, May 1992.

[62] F. Major, V. Gheorghe, and G. Werth, *Charged Particle Traps, Physics and Techniques of Charged Particle Field Confinement*. Heidelberg, Germany: Springer, 2005.

[63] R. Blatt, H. Schnatz, and G. Werth, "Ultrahigh-resolution microwave spectroscopy on trapped $^{171}\mathrm{Yb}^{+}$ ions," *Phys. Rev. Lett.*, vol. 48, pp. 1601–1603, Jun 1982.

[64] S. Ejtemaee, R. Thomas, and P. C. Haljan, "Optimization of Yb^{+} fluorescence and hyperfine-qubit detection," *Phys. Rev. A*, vol. 82, no. 6, p. 063419, 2010.

[65] Y. Wang, M. Um, J. Zhang, S. An, M. Lyu, J.-N. Zhang, L.-M. Duan, D. Yum, and K. Kim, "Single-qubit quantum memory exceeding ten-minute coherence time," *Nature Photonics*, vol. 11, pp. 646–650, Sept. 2017.

[66] J. G. Hartnett, N. R. Nand, and C. Lu, "Ultra-low-phase-noise cryocooled microwave dielectric-sapphire-resonator oscillators," *Applied Physics Letters*, vol. 100, no. 18, p. 183501, 2012.

[67] H. Ball, W. D. Oliver, and M. J. Biercuk, "The role of master clock stability in quantum information processing," *npj Quantum Inf.*, vol. 2, p. 16033, Nov. 2016.

[68] M. Roberts, P. Taylor, G. P. Barwood, W. R. C. Rowley, and P. Gill, "Observation of the $^{2}\mathrm{S}_{1/2}$-$^{2}\mathrm{F}_{7/2}$ electric octupole transition in a single $^{171}\mathrm{Yb}^{+}$ ion," *Phys. Rev. A*, vol. 62, p. 020501(R), Jul 2000.

[69] W. C. Campbell, J. Mizrahi, Q. Quraishi, C. Senko, D. Hayes, D. Hucul, D. N. Matsukevich, P. Maunz, and C. Monroe, "Ultrafast Gates for Single Atomic Qubits," *Phys. Rev. Lett.*, vol. 105, p. 090502, Aug 2010.

[70] D. Hayes, D. N. Matsukevich, P. Maunz, D. Hucul, Q. Quraishi, S. Olmschenk, W. Campbell, J. Mizrahi, C. Senko, and C. Monroe, "Entanglement of Atomic Qubits Using an Optical Frequency Comb," *Phys. Rev. Lett.*, vol. 104, p. 140501, Apr 2010.

[71] F. Schmidt-Kaler, H. Häffner, S. Gulde, M. Riebe, G. P. T. Lancaster, T. Deuschle, C. Becher, W. Hänsel, J. Eschner, C. F. Roos, and R. Blatt, "How to realize a universal quantum gate with trapped ions," *Appl. Phys. B*, vol. 77, pp. 789–796, December 2003.

[72] A. R. Milne, *Forthcoming*. PhD thesis, School of Physics, The University of Sydney, 2021.

[73] W. F. Meggers, "The Second Spectrum of Ytterbium (Yb II).," *Journal of research of the National Bureau of Standards. Section A, Physics and chemistry*, vol. 71A, no. 6, pp. 396–546, 1967.

[74] C. D. Marciniak, H. B. Ball, A. T.-H. Hung, and M. J. Biercuk, "Towards fully commercial, UV-compatible fiber patch cords," *Optics Express*, vol. 25, p. 15643, June 2017.

[75] E. A. Donley, T. P. Heavner, F. Levi, M. O. Tataw, and S. R. Jefferts, "Double-pass acousto-optic modulator system," *Review of Scientific Instruments*, vol. 76, p. 063112, June 2005.

[76] C. Wunderlich, C. Balzer, T. Hannemann, F. Mintert, W. Neuhauser, D. Rei, and P. E. Toschek, “Spin resonance with trapped ions,” *Journal of Physics B: Atomic, Molecular and Optical Physics*, vol. 36, pp. 1063–1072, Feb. 2003.

[77] I. I. Rabi, “Space quantization in a gyrating magnetic field,” *Phys. Rev.*, vol. 51, pp. 652–654, Apr 1937.

[78] J. Vanier and C. Audoin, *The Quantum Physics of Atomic Frequency Standards*. IOP Publishing Ltd, 1989.

[79] N. F. Ramsey, “A Molecular Beam Resonance Method with Separated Oscillating Fields,” *Phys. Rev.*, vol. 78, pp. 695–699, Jun 1950.

[80] N. F. Ramsey, “Experiments with Separated Oscillatory Fields and Hydrogen Masers (Nobel Lecture),” *Angewandte Chemie International Edition in English*, vol. 29, pp. 725–733, July 1990.

[81] M. Chwalla *et al.*, “Absolute Frequency Measurement of the $^{40}\mathrm{Ca}^{+}$ $4s\,^{2}S_{1/2} - 3d\,^{2}D_{5/2}$ Clock Transition,” *Phys. Rev. Lett.*, vol. 102, p. 023002, Jan 2009.

[82] C. Hempel, *Digital quantum simulation, Schrödinger cat state spectroscopy and setting up a linear ion trap*. PhD thesis, Leopold-Franzens University of Innsbruck, 2014.

[83] J. Benhelm, *Precision Spectroscopy and Quantum Information Processing with Trapped Calcium Ions*. PhD thesis, Leopold-Franzens University of Innsbruck, 2008.

[84] T. P. Harty, D. T. C. Allcock, C. J. Ballance, L. Guidoni, H. A. Janacek, N. M. Linke, D. N. Stacey, and D. M. Lucas, “High-Fidelity Preparation, Gates, Memory, and Readout of a Trapped-Ion Quantum Bit,” *Phys. Rev. Lett.*, vol. 113, p. 220501, Nov 2014.

[85] J. P. Gaebler, T. R. Tan, Y. Lin, Y. Wan, R. Bowler, A. C. Keith, S. Glancy, K. Coakley, E. Knill, D. Leibfried, and D. J. Wineland, “High-Fidelity Universal Gate Set for $^{9}\mathrm{Be}^{+}$Ion Qubits,” *Physical Review Letters*, vol. 117, no. 6, p. 060505, 2016.

[86] M. A. Sepiol, A. C. Hughes, J. E. Tarlton, D. P. Nadlinger, T. G. Ballance, C. J. Ballance, T. P. Harty, A. M. Steane, J. F. Goodwin, and D. M. Lucas, “Probing Qubit Memory Errors at the Part-per-Million Level,” *Phys. Rev. Lett.*, vol. 123, no. 11, p. 110503, 2019.

[87] C. J. Ballance, T. P. Harty, N. M. Linke, M. A. Sepiol, and D. M. Lucas, “High-Fidelity Quantum Logic Gates Using Trapped-Ion Hyperfine Qubits,” *Physical Review Letters*, vol. 117, no. 6, p. 060504, 2016.

[88] T. Choi, S. Debnath, T. A. Manning, C. Figgatt, Z. X. Gong, L. M. Duan, and C. R. Monroe, “Optimal Quantum Control of Multimode Couplings between Trapped Ion Qubits for Scalable Entanglement,” *Physical Review Letters*, vol. 112, no. 19, p. 190502, 2014.

[89] P. H. Leung, K. A. Landsman, C. Figgatt, N. M. Linke, C. Monroe, and K. R. Brown, “Robust 2-Qubit Gates in a Linear Ion Crystal Using a Frequency-Modulated Driving Force,” *Phys. Rev. Lett.*, vol. 120, p. 020501, Jan 2018.

[90] V. M. Schäfer, C. J. Ballance, K. Thirumalai, L. J. Stephenson, T. G. Ballance, A. M. Steane, and D. M. Lucas, “Fast quantum logic gates with trapped-ion qubits,” *Nature*, vol. 555, pp. 75–78,

2018.

[91] C. Zhang, F. Pokorny, W. Li, G. Higgins, A. Pöschl, I. Lesanovsky, and M. Hennrich, “Submicrosecond entangling gate between trapped ions via Rydberg interaction,” *Nature*, vol. 580, no. 7803, pp. 345–349, 2020.

[92] K. Wright *et al.*, “Benchmarking an 11-qubit quantum computer,” *Nat. Commun*, vol. 10, no. 1, p. 5464, 2019.

[93] C. D. B. Bentley, H. Ball, M. J. Biercuk, A. R. R. Carvalho, M. R. Hush, and H. J. Slatyer, “Numeric Optimization for Configurable, Parallel, Error-Robust Entangling Gates in Large Ion Registers,” *Adv. Quantum Technol.*, vol. 3, no. 11, p. 2000044, 2020.

[94] Y. Nam *et al.*, “Ground-state energy estimation of the water molecule on a trapped-ion quantum computer,” *npj Quantum Inf.*, vol. 6, no. 1, p. 33, 2020.

[95] A. Erhard *et al.*, “Entangling logical qubits with lattice surgery,” *Nature*, vol. 589, pp. 220–224, Jan. 2021.

[96] L. Egan, D. M. Debroy, C. Noel, A. Risinger, D. Zhu, D. Biswas, M. Newman, M. Li, K. R. Brown, M. Cetina, and C. Monroe, “Fault-Tolerant Operation of a Quantum Error-Correction Code.” arXiv:quant-ph/2009.11482, 2020.

[97] P. Schindler, J. T. Barreiro, T. Monz, V. Nebendahl, D. Nigg, M. Chwalla, M. Hennrich, and R. Blatt, “Experimental Repetitive Quantum Error Correction,” *Science*, vol. 332, no. 6033, pp. 1059–1061, 2011.

[98] D. Nigg, M. Müller, E. A. Martinez, P. Schindler, M. Hennrich, T. Monz, M. A. Martin-Delgado, and R. Blatt, “Quantum computations on a topologically encoded qubit,” *Science*, vol. 345, no. 6194, pp. 302–305, 2014.

[99] A. Bermudez *et al.*, “Assessing the Progress of Trapped-Ion Processors Towards Fault-Tolerant Quantum Computation,” *Phys. Rev. X*, vol. 7, no. 4, p. 041061, 2017.

[100] C. D. Bruzewicz, J. Chiaverini, R. McConnell, and J. M. Sage, “Trapped-ion quantum computing: Progress and challenges,” *Appl. Phys. Rev.*, vol. 6, no. 2, p. 021314, 2019.

[101] J. Benhelm, G. Kirchmair, C. F. Roos, and R. Blatt, “Experimental quantum-information processing with $^{43}\mathrm{Ca}^{+}$ ions,” *Phys. Rev. A*, vol. 77, no. 6, p. 062306, 2008.

[102] G. Kirchmair, J. Benhelm, F. Zähringer, R. Gerritsma, C. F. Roos, and R. Blatt, “High-fidelity entanglement of $^{43}\mathrm{Ca}^{+}$ hyperfine clock states,” *Phys. Rev. A*, vol. 79, p. 020304(R), Feb 2009.

[103] D. J. Wineland, J. C. Bergquist, J. J. Bollinger, and W. M. Itano, “Quantum effects in measurements on trapped ions,” *Phys. Scripta*, vol. T59, pp. 286–293, 1995.

[104] A. H. Myerson, D. J. Szwer, S. C. Webster, D. T. C. Allcock, M. J. Curtis, G. Imreh, J. A. Sherman, D. N. Stacey, A. M. Steane, and D. M. Lucas, “High-Fidelity Readout of Trapped-Ion Qubits,” *Phys. Rev. Lett.*, vol. 100, no. 20, p. 200502, 2008.

[105] A. H. Burrell, D. J. Szwer, S. C. Webster, and D. M. Lucas, “Scalable simultaneous multiqubit readout with 99.99% single-shot fidelity,” *Phys. Rev. A*, vol. 81, no. 4, p. 040302(R), 2010.

[106] S. Debnath, N. M. Linke, C. Figgatt, K. A. Landsman, K. Wright, and C. Monroe, “Demonstration of a small programmable quantum computer with atomic qubits,” *Nature*, vol. 536, pp. 63–66, Aug. 2016.

[107] A. Seif, K. A. Landsman, N. M. Linke, C. Figgatt, C. Monroe, and M. Hafezi, “Machine learning assisted readout of trapped-ion qubits,” *J. Phys. B: At. Mol. Opt. Phys.*, vol. 51, no. 17, p. 174006, 2018.

[108] S. Crain, C. Cahall, G. Vrijsen, E. E. Wollman, M. D. Shaw, V. B. Verma, S. W. Nam, and J. Kim, “High-speed low-crosstalk detection of a 171Yb^+ qubit using superconducting nanowire single photon detectors,” *Communications Physics*, vol. 2, p. 97, Aug. 2019.

[109] S. L. Todaro, V. B. Verma, K. C. McCormick, D. T. C. Allcock, R. P. Mirin, D. J. Wineland, S. W. Nam, A. C. Wilson, D. Leibfried, and D. H. Slichter, “State Readout of a Trapped Ion Qubit Using a Trap-Integrated Superconducting Photon Detector,” *Phys. Rev. Lett.*, vol. 126, p. 010501, Jan 2021.

[110] L. A. Zhukas, P. Svihra, A. Nomerotski, and B. B. Blinov, “High-Fidelity Simultaneous Detection of Trapped Ion Qubit Register.” arXiv:quant-ph/2006.12801, 2020.

[111] D. B. Hume, T. Rosenband, and D. J. Wineland, “High-Fidelity Adaptive Qubit Detection through Repetitive Quantum Nondemolition Measurements,” *Phys. Rev. Lett.*, vol. 99, p. 120502, Sep 2007.

[112] B. Hemmerling, F. Gebert, Y. Wan, and P. O. Schmidt, “A novel, robust quantum detection scheme,” *New J. Phys.*, vol. 14, no. 2, p. 023043, 2012.

[113] S. Wölk, C. Piltz, T. Sriarunothai, and C. Wunderlich, “State selective detection of hyperfine qubits,” *Journal of Physics B: Atomic, Molecular and Optical Physics*, vol. 48, p. 075101, March 2015.

[114] Z.-H. Ding, J.-M. Cui, Y.-F. Huang, C.-F. Li, T. Tu, and G.-C. Guo, “Fast High-Fidelity Readout of a Single Trapped-Ion Qubit via Machine-Learning Methods,” *Phys. Rev. Applied*, vol. 12, no. 1, p. 014038, 2019.

[115] H. Dehmelt, “Proposed 10^{14} $\delta\nu/\nu$ laser fluorescence spectroscopy on Tl^+ mono–ion oscillator II (spontaneous quantum jumps),” *Bull. Am. Phys. Soc.*, vol. 20, p. 60, 1975.

[116] W. Nagourney, J. Sandberg, and H. Dehmelt, “Shelved optical electron amplifier: Observation of quantum jumps,” *Phys. Rev. Lett.*, vol. 56, no. 26, pp. 2797–2799, 1986.

[117] J. E. Christensen, D. Hucul, W. C. Campbell, and E. R. Hudson, “High-fidelity manipulation of a qubit enabled by a manufactured nucleus,” *npj Quantum Inf.*, vol. 6, p. 35, Apr. 2020.

[118] A. Keselman, Y. Glickman, N. Akerman, S. Kotler, and R. Ozeri, “High-fidelity state detection and tomography of a single-ion Zeeman qubit,” *New Journal of Physics*, 2011.

[119] C. Roman, A. Ransford, M. Ip, and W. C. Campbell, "Coherent control for qubit state readout," *New J. Phys.*, vol. 22, p. 073038, jul 2020.

[120] R. Noek, G. Vrijsen, D. Gaultney, E. Mount, T. Kim, P. Maunz, and J. Kim, "High speed, high fidelity detection of an atomic hyperfine qubit," *Opt. Lett.*, vol. 38, no. 22, p. 4735, 2013.

[121] M. Acton, K. A. Brickman, P. C. Haljan, P. J. Lee, L. Deslauriers, and C. Monroe, "Near-Perfect Simultaneous Measurement of a Qubit Register," *Quantum Inf. Comput*, vol. 6, no. 6, pp. 465–482, 2005.

[122] P. Gill, H. A. Klein, A. P. Levick, M. Roberts, W. R. C. Rowley, and P. Taylor, "Measurement of the $^2\mathrm{S}_{1/2}$-$^2\mathrm{D}_{5/2}$ 411-nm interval in laser-cooled trapped $^{171}\mathrm{Yb}^+$ ions," *Phys. Rev. A*, vol. 52, no. 2, pp. R909–R912, 1995.

[123] M. Roberts, P. Taylor, S. V. Gateva-Kostova, R. B. M. Clarke, W. R. C. Rowley, and P. Gill, "Measurement of the $^2\mathrm{S}_{1/2}$-$^2\mathrm{D}_{5/2}$ clock transition in a single $^{171}\mathrm{Yb}^+$ ion," *Phys. Rev. A*, vol. 60, no. 4, pp. 2867 – 2872, 1999.

[124] J. Keller, *Spectroscopic characterization of ion motion for an optical clock based on Coulomb crystals*. PhD thesis, University of Hannover, 2015.

[125] T. Feldker, H. Fürst, H. Hirzler, N. V. Ewald, M. Mazzanti, D. Wiater, M. Tomza, and R. Gerritsma, "Buffer gas cooling of a trapped ion to the quantum regime," *Nat. Phys.*, vol. 16, no. 4, pp. 413–416, 2020.

[126] N. Huntemann, M. Okhapkin, B. Lipphardt, S. Weyers, C. Tamm, and E. Peik, "High-Accuracy Optical Clock Based on the Octupole Transition in $^{171}\mathrm{Yb}^+$," *Phys. Rev. Lett.*, vol. 108, no. 9, p. 090801, 2012.

[127] Y.-Y. Jau, J. D. Hunker, and P. D. D. Schwindt, "F-state quenching with CH_4 for buffer-gas cooled $^{171}\mathrm{Yb}^+$ frequency standard," *AIP Adv.*, vol. 5, no. 11, p. 117209, 2015.

[128] S. Mulholland, H. A. Klein, G. P. Barwood, S. Donnellan, P. B. R. Nisbet-Jones, G. Huang, G. Walsh, P. E. G. Baird, and P. Gill, "Compact laser system for a laser-cooled ytterbium ion microwave frequency standard," *Rev. Sci. Instrum.*, vol. 90, no. 3, p. 033105, 2019.

[129] K. Sugiyama, "Laser Cooling of Single $^{174}\mathrm{Yb}^+$ Ions Stored in a RF Trap," *Jpn. J. Appl. Phys.*, vol. 38, pp. 2141–2147, apr 1999.

[130] H. A. Fürst, C.-H. Yeh, D. Kalincev, A. P. Kulosa, L. S. Dreissen, R. Lange, E. Benkler, N. Huntemann, E. Peik, and T. E. Mehlstäubler, "Coherent Excitation of the Highly Forbidden Electric Octupole Transition in $^{172}\mathrm{Yb}^+$," *Phys. Rev. Lett.*, vol. 125, p. 163001, Oct 2020.

[131] P. Taylor, M. Roberts, S. V. Gateva-Kostova, R. B. M. Clarke, G. P. Barwood, W. R. C. Rowley, and P. Gill, "Investigation of the $^2S_{1/2}{-}^2D_{5/2}$ clock transition in a single ytterbium ion," *Phys. Rev. A*, vol. 56, pp. 2699–2704, Oct 1997.

[132] N. Yu and L. Maleki, "Lifetime measurements of the $4f^{14}5d$ metastable states in single ytterbium ions," *Phys. Rev. A*, vol. 61, p. 022507, Jan 2000.

[133] B. Fawcett and M. Wilson, “Computed oscillator strengths, Landé g values, and lifetimes in Yb ii,” *At. Data. Nucl. Data Tables*, vol. 47, no. 2, pp. 241 – 317, 1991.

[134] W. M. Itano, “External-field shifts of the $^{199}\mathrm{Hg}^{+}$ optical frequency standard,” *J Res Natl Inst Stand Technol*, vol. 105, p. 829–837, Dec 2000.

[135] W. M. Itano, “Quadrupole moments and hyperfine constants of metastable states of Ca^{+}, Sr^{+}, Ba^{+}, Yb^{+}, Hg^{+}, and Au,” *Phys. Rev. A*, vol. 73, p. 022510, Feb 2006.

[136] B. K. Sahoo and B. P. Das, “Parity nonconservation in ytterbium ion,” *Phys. Rev. A*, vol. 84, p. 010502, Jul 2011.

[137] S. G. Porsev, M. S. Safronova, and M. G. Kozlov, “Correlation effects in Yb^{+} and implications for parity violation,” *Phys. Rev. A*, vol. 86, p. 022504, Aug 2012.

[138] D. K. Nandy and B. K. Sahoo, “Quadrupole shifts for the $^{171}\mathrm{Yb}^{+}$ ion clocks: Experiments versus theories,” *Phys. Rev. A*, vol. 90, p. 050503, Nov 2014.

[139] R. W. Berends, E. H. Pinnington, B. Guo, and Q. Ji, “Beam-laser lifetime measurements for four resonance levels of Yb II,” *J. Phys. B: At. Mol. Opt. Phys.*, vol. 26, pp. L701–L704, oct 1993.

[140] R. Tycko, “Broadband Population Inversion,” *Phys. Rev. Lett.*, vol. 51, no. 9, pp. 775 – 777, 1983.

[141] M. H. Levitt, “Composite pulses,” *Prog Nucl Mag Res Sp*, vol. 18, no. 2, pp. 61–122, 1986.

[142] C. Kabytayev, T. J. Green, K. Khodjasteh, M. J. Biercuk, L. Viola, and K. R. Brown, “Robustness of composite pulses to time-dependent control noise,” *Phys. Rev. A*, vol. 90, no. 1, p. 012316, 2014.

[143] N. V. Vitanov, T. Halfmann, B. W. Shore, and K. Bergmann, “Laser-induced population transfer by adiabatic passage techniques,” *Annu. Rev. Phys. Chem.*, vol. 52, no. 1, pp. 763–809, 2001.

[144] C. Wunderlich, T. Hannemann, T. Körber, H. Häffner, C. Roos, W. Hänsel, R. Blatt, and F. Schmidt-Kaler, “Robust state preparation of a single trapped ion by adiabatic passage,” *J. Modern Opt.*, vol. 54, no. 11, pp. 1541–1549, 2007.

[145] T. Noel, M. R. Dietrich, N. Kurz, G. Shu, J. Wright, and B. B. Blinov, “Adiabatic passage in the presence of noise,” *Phys. Rev. A*, vol. 85, p. 023401, Feb 2012.

[146] X.-J. Lu, X. Chen, A. Ruschhaupt, D. Alonso, S. Guérin, and J. G. Muga, “Fast and robust population transfer in two-level quantum systems with dephasing noise and/or systematic frequency errors,” *Phys. Rev. A*, vol. 88, p. 033406, Sep 2013.

[147] A. Soare, H. Ball, D. Hayes, J. Sastrawan, J. M. C., J. J. McLoughlin, X. Zhen, T. J. Green, and M. J. Biercuk, “Experimental noise filtering by quantum control,” *Nature Physics*, vol. 10, no. 19, pp. 825–829, 2014.

[148] C. Zener, “Non-adiabatic crossing of energy levels,” *Proc. R. Soc. London A.*, vol. 137, pp. 696–702, Sept. 1932.

[149] X. Lacour, S. Guérin, L. P. Yatsenko, N. V. Vitanov, and H. R. Jauslin, "Uniform analytic description of dephasing effects in two-state transitions," *Phys. Rev. A*, vol. 75, p. 033417, Mar 2007.

[150] N. Huntemann, B. Lipphardt, M. Okhapkin, C. Tamm, E. Peik, A. V. Taichenachev, and V. I. Yudin, "Generalized Ramsey Excitation Scheme with Suppressed Light Shift," *Phys. Rev. Lett.*, vol. 109, no. 21, p. 213002, 2012.

[151] N. V. Vitanov, A. A. Rangelov, B. W. Shore, and K. Bergmann, "Stimulated Raman adiabatic passage in physics, chemistry, and beyond," *Rev. Modern Phys.*, vol. 89, no. 1, p. 015006, 2017.

[152] M. Schacht, J. R. Danielson, S. Rahaman, J. R. Torgerson, J. Zhang, and M. M. Schauer, "^{171}Yb^{+} 5D$_{3/2}$ hyperfine state detection and F = 2 lifetime," *J. Phys. B: At. Mol. Opt. Phys.*, vol. 48, no. 6, p. 065003, 2015.

[153] F. Pedregosa *et al.*, "Scikit-learn: Machine Learning in Python," *Journal of Machine Learning Research*, vol. 12, pp. 2825–2830, 2011.

[154] J. Emerson, R. Alicki, and K. Życzkowski, "Scalable noise estimation with random unitary operators," *Journal of Optics B: Quantum and Semiclassical Optics*, vol. 7, pp. S347–S352, Oct. 2005.

[155] E. Knill, D. Leibfried, R. Reichle, J. Britton, R. B. Blakestad, J. D. Jost, C. Langer, R. Ozeri, S. Seidelin, and D. J. Wineland, "Randomized benchmarking of quantum gates," *Physical Review A*, vol. 77, p. 012307, Jan. 2008.

[156] J. Wallman, C. Granade, R. Harper, and S. T. Flammia, "Estimating the coherence of noise," *New Journal of Physics*, vol. 17, p. 113020, Nov. 2015.

[157] J. Poyatos, J. Cirac, and P. Zoller, "Complete Characterization of a Quantum Process: The Two-Bit Quantum Gate," *Physical Review Letters*, vol. 78, pp. 390–393, Jan. 1997.

[158] I. L. Chuang and M. A. Nielsen, "Prescription for experimental determination of the dynamics of a quantum black box," *Journal Of Modern Optics*, vol. 44, pp. 2455–2467, Nov. 1997.

[159] M. Holzäpfel, T. Baumgratz, M. Cramer, and M. B. Plenio, "Scalable reconstruction of unitary processes and Hamiltonians," *Phys. Rev. A*, vol. 91, p. 042129, Apr 2015.

[160] S. Flammia, D. Gross, Y.-K. Liu, and J. Eisert, "Quantum tomography via compressed sensing: error bounds, sample complexity and efficient estimators," *New Journal of Physics*, vol. 14, p. 095022, September 2012.

[161] C. Granade, C. Ferrie, and S. T. Flammia, "Practical adaptive quantum tomography," *New J. Phys. in press*, p. 1605.05039, 2017.

[162] S. T. Merkel, J. M. Gambetta, J. A. Smolin, S. Poletto, A. D. Córcoles, B. R. Johnson, C. A. Ryan, and M. Steffen, "Self-consistent quantum process tomography," *Physical Review A*, vol. 87, p. 062119, June 2013.

[163] R. Blume-Kohout, J. K. Gamble, E. Nielsen, K. Rudinger, J. Mizrahi, K. Fortier, and P. Maunz, "Demonstration of qubit operations below a rigorous fault tolerance threshold with gate set tomography," *Nature Communications*, vol. 8, p. 14485, Feb. 2017.

[164] M. Riebe, K. Kim, P. Schindler, T. Monz, P. O. Schmidt, T. K. Körber, W. Hänsel, H. Häffner, C. F. Roos, and R. Blatt, "Process Tomography of Ion Trap Quantum Gates," *Phys. Rev. Lett.*, vol. 97, p. 220407, Dec 2006.

[165] H. Ball, T. M. Stace, S. T. Flammia, and M. J. Biercuk, "Effect of noise correlations on randomized benchmarking," *Physical Review A*, vol. 93, p. 022303, Feb. 2016.

[166] C. Dankert, R. Cleve, J. Emerson, and E. Livine, "Exact and approximate unitary 2-designs and their application to fidelity estimation," *Phys. Rev. A*, vol. 80, p. 012304, Jul 2009.

[167] D. Gottesman, "Stabilizer Codes and Quantum Error Correction." arXiv:quant-ph/9705052, 1997.

[168] S. Aaronson and D. Gottesman, "Improved simulation of stabilizer circuits," *Phys. Rev. A*, vol. 70, p. 052328, Nov 2004.

[169] E. Nielsen, K. Rudinger, J. K. Gamble, and R. Blume-Kohout, "pyGSTi: A python implementation of gate set tomography. Available at http://github.com/pyGSTio," 2016.

[170] J. Rutman, "Characterization of Phase and Frequency Instabilities in Precision Frequency Sources: Fifteen Years of Progress," *Proc. IEEE*, vol. 66, pp. 1048–1075, 1978.

[171] F. N. Hooge, T. G. M. Kleinpenning, and L. K. J. Vandamme, "Experimental studies on 1/f noise," *Reports on Progress in Physics*, vol. 44, no. 5, p. 479, 1981.

[172] D. J. V. Harlingen, B. L. T. Plourde, T. L. Robertson, P. A. Reichardt, and J. Clarke, "Decoherence in Flux Qubits due to $1/f$ noise in Josephson Junctions," in *Quantum Computing and Quantum Bits in Mesoscopic Systems* (A. Leggett, B. Ruggiero, and P. Silvestini, eds.), pp. 171–184, New York: Kluwer Academic Press, 2004.

[173] M. A. Fogarty, M. Veldhorst, R. Harper, C. H. Yang, S. D. Bartlett, S. T. Flammia, and A. S. Dzurak, "Nonexponential fidelity decay in randomized benchmarking with low-frequency noise," *Phys. Rev. A*, vol. 92, p. 022326, Aug 2015.

[174] J. J. Wallman and S. T. Flammia, "Randomized benchmarking with confidence," *New Journal of Physics*, vol. 16, no. 10, p. 103032, 2014.

[175] R. Kueng, D. M. Long, A. C. Doherty, and S. T. Flammia, "Comparing Experiments to the Fault-Tolerance Threshold," *Physical Review Letters*, vol. 117, no. 17, p. 170502, 2016.

[176] B. H. Fong and S. T. Merkel, "Randomized Benchmarking, Correlated Noise, and Ising Models." arXiv:quant-ph/1703.09747, 2017.

[177] J. J. Wallman, "Randomized benchmarking with gate-dependent noise," *Quantum*, vol. 2, p. 47, Jan. 2018.

[178] E. Nielsen, "Private communications: Erik Nielsen." Interleaving different sequences with single shot measurements could reduce model violations in GST.

[179] N. F. Ramsey, "A Molecular Beam Resonance Method with Separated Oscillating Fields," *Phys. Rev.*, vol. 78, pp. 695–699, Jun 1950.

[180] T. Proctor, K. Rudinger, K. Young, M. Sarovar, and R. Blume-Kohout, "What Randomized Benchmarking Actually Measures," *Physical Review Letters*, vol. 119, p. 58, Sept. 2017.

[181] Ł. Rudnicki, Z. Puchała, and K. Zyczkowski, "Gauge invariant information concerning quantum channels," *Quantum*, vol. 2, p. 60, Apr. 2018.

[182] J. P. Dehollain, J. T. Muhonen, R. Blume-Kohout, K. M. Rudinger, J. K. Gamble, E. Nielsen, A. Laucht, S. Simmons, R. Kalra, A. S. Dzurak, and A. Morello, "Optimization of a solid-state electron spin qubit using gate set tomography," *New Journal of Physics*, vol. 18, pp. 1–9, Oct. 2016.

[183] K. Rudinger, S. Kimmel, D. Lobser, and P. Maunz, "Experimental Demonstration of a Cheap and Accurate Phase Estimation," *Phys. Rev. Lett.*, vol. 118, p. 190502, May 2017.

[184] P. W. Shor, "Fault-tolerant quantum computation," in *Proceedings of 37th Conference on Foundations of Computer Science*, pp. 56–65, Oct 1996.

[185] A. M. Steane, "Error Correcting Codes in Quantum Theory," *Phys. Rev. Lett.*, vol. 77, pp. 793–797, Jul 1996.

[186] A. Steane, "Multiple-particle interference and quantum error correction," *Proceedings of the Royal Society of London. Series A: Mathematical, Physical and Engineering Sciences*, vol. 452, no. 1954, pp. 2551–2577, 1996.

[187] D. Aharonov and M. Ben-Or, "Fault-tolerant Quantum Computation with Constant Error," in *Proceedings of the 29th Annual ACM Symposium on Theory of Computing*, STOC '97, (New York, NY, USA), pp. 176–188, ACM, 1997.

[188] D. Gottesman, "Theory of fault-tolerant quantum computation," *Physical Review A*, vol. 57, pp. 127–137, Jan. 1998.

[189] J. Preskill, "Reliable quantum computers," *Proceedings of the Royal Society of London. A. Mathematical and Physical Sciences*, vol. 454, pp. 385–410, Jan. 1998.

[190] D. A. Lidar and T. A. Brun, *Quantum Error Correction.* New York: Cambridge University Press, 2013.

[191] E. T. Campbell, B. M. Terhal, and C. Vuillot, "Roads towards fault-tolerant universal quantum computation," *Nature*, vol. 549, pp. 172–179, Sept. 2017.

[192] J. Preskill, "Sufficient condition on noise correlations for scalable quantum computing," *Quantum Info. & Comp.*, vol. 13, pp. 0181–0194, 2013.

[193] D. Greenbaum and Z. Dutton, "Modeling coherent errors in quantum error correction," *Quantum Science and Technology*, vol. 3, p. 015007, Jan. 2018.

[194] E. Huang, A. C. Doherty, and S. T. Flammia, "Performance of quantum error correction with coherent errors," *Phys. Rev. A*, vol. 99, p. 022313, Feb 2019.

[195] C. T. Chubb and S. T. Flammia, "Statistical mechanical models for quantum codes with correlated noise." arXiv:quant-ph/1809.10704v2, 2018.

[196] D. M. Debroy, M. Li, M. Newman, and K. R. Brown, "Stabilizer Slicing: Coherent Error Cancellations in Low-Density Parity-Check Stabilizer Codes," *Physical Review Letters*, vol. 121, p. 250502, Dec. 2018.

[197] S. Majumder, L. A. de Castro, and K. R. Brown, "Real-time calibration with spectator qubits," *npj Quantum Information*, vol. 6, Feb. 2020.

[198] H. K. Ng and J. Preskill, "Fault-tolerant quantum computation versus Gaussian noise," *Phys. Rev. A*, vol. 79, p. 032318, Mar 2009.

[199] D. Aharonov, A. Kitaev, and J. Preskill, "Fault-Tolerant Quantum Computation with Long-Range Correlated Noise," *Phys. Rev. Lett.*, vol. 96, p. 050504, Feb 2006.

[200] A. G. Fowler, M. Mariantoni, J. M. Martinis, and A. N. Cleland, "Surface codes: Towards practical large-scale quantum computation," *Phys. Rev. A*, vol. 86, p. 032324, 2012.

[201] P. Schindler, J. T. Barreiro, T. Monz, V. Nebendahl, D. Nigg, M. Chwalla, M. Hennrich, and R. Blatt, "Experimental Repetitive Quantum Error Correction," *Science*, vol. 332, pp. 1059–1061, May 2011.

[202] K. R. Brown, A. W. Harrow, and I. L. Chuang, "Arbitrarily accurate composite pulse sequences," *Phys. Rev. A*, vol. 70, p. 052318, 2004.

[203] K. Khodjasteh and L. Viola, "Dynamically error-corrected gates for universal quantum computation," *Phys. Rev. Lett.*, vol. 102, p. 080501, 2009.

[204] J. T. Merrill and K. R. Brown, *Progress in Compensating Pulse Sequences for Quantum Computation*, pp. 241–294. John Wiley & Sons, Inc., 2014.

[205] X. Wang, L. S. Bishop, J. P. Kestner, E. Barnes, K. Sun, and S. Das Sarma, "Composite Pulses for Robust Universal Control of Singlet-Triplet Qubits," *Nat. Commun.*, vol. 3, p. 997, 2012.

[206] A. Soare, H. Ball, D. Hayes, J. Sastrawan, M. C. Jarratt, J. J. McLoughlin, X. Zhen, T. J. Green, and M. J. Biercuk, "Experimental noise filtering by quantum control," *Nat. Phys.*, vol. 10, 2014.

[207] H. K. Ng, D. A. Lidar, and J. Preskill, "Combining dynamical decoupling with fault-tolerant quantum computation," *Phys. Rev. A*, vol. 84, p. 012305, 2011.

[208] N. C. Jones, R. Van Meter, A. G. Fowler, P. L. McMahon, J. Kim, T. D. Ladd, and Y. Yamamoto, "Layered Architecture for Quantum Computing," *Phys. Rev. X*, vol. 2, p. 031007, 2012.

[209] J. Emerson, R. Alicki, and K. Życzkowski, "Scalable noise estimation with random unitary operators," *Journal of Optics B: Quantum and Semiclassical Optics*, vol. 7, no. 10, p. S347, 2005.

[210] C. Kabytayev, T. J. Green, K. Khodjasteh, M. J. Biercuk, L. Viola, and K. R. Brown, "Robustness of composite pulses to time-dependent control noise," *Phys. Rev. A*, vol. 90, p. 012316, 2014.

[211] G. A. Paz-Silva and L. Viola, "General Transfer-Function Approach to Noise Filtering in Open-Loop Quantum Control," *Phys. Rev. Lett.*, vol. 113, p. 250501, Dec 2014.

[212] T. J. Green, J. Sastrawan, H. Uys, and M. J. Biercuk, “Arbitrary quantum control of qubits in the presence of universal noise,” *New J. Phys.*, vol. 15, p. 095004, 2013.

[213] A. G. Kofman and G. Kurizki, “Unified Theory of Dynamically Suppressed Qubit Decoherence in Thermal Baths,” *Phys. Rev. Lett.*, vol. 93, p. 130406, 2004.

[214] T. Green, H. Uys, and M. J. Biercuk, “High-Order Noise Filtering in Nontrivial Quantum Logic Gates,” *Phys. Rev. Lett.*, vol. 109, p. 020501, Jul 2012.

[215] E. Knill, D. Leibfried, R. Reichle, J. Britton, R. B. Blakestad, J. D. Jost, C. Langer, R. Ozeri, S. Seidelin, and D. J. Wineland, “Randomized benchmarking of quantum gates,” *Phys. Rev. A*, vol. 77, p. 012307, Jan 2008.

[216] E. Magesan *et al.*, “Efficient Measurement of Quantum Gate Error by Interleaved Randomized Benchmarking,” *Phys. Rev. Lett.*, vol. 109, p. 080505, Aug 2012.

[217] E. Magesan, J. M. Gambetta, and J. Emerson, “Scalable and Robust Randomized Benchmarking of Quantum Processes,” *Phys. Rev. Lett.*, vol. 106, p. 180504, May 2011.

[218] E. Magesan, J. M. Gambetta, and J. Emerson, “Characterizing quantum gates via randomized benchmarking,” *Physical Review A*, vol. 85, p. 042311, Apr. 2012.

[219] S. Kimmel, M. P. da Silva, C. A. Ryan, B. R. Johnson, and T. Ohki, “Robust Extraction of Tomographic Information via Randomized Benchmarking,” *Physical Review X*, vol. 4, p. 011050, Mar. 2014.

[220] S. Sheldon, L. S. Bishop, E. Magesan, S. Filipp, J. M. Chow, and J. M. Gambetta, “Characterizing errors on qubit operations via iterative randomized benchmarking,” *Physical Review A*, vol. 93, p. 012301, Jan. 2016.

[221] S. Mavadia, C. L. Edmunds, C. Hempel, H. Ball, F. Roy, T. M. Stace, and M. J. Biercuk, “Experimental quantum verification in the presence of temporally correlated noise,” *Nature Quantum Information*, vol. 4, p. 7, Feb. 2018.

[222] E. Onorati, A. H. Werner, and J. Eisert, “Randomized Benchmarking for Individual Quantum Gates,” *Physical Review Letters*, vol. 123, no. 6, p. 060501, 2019.

[223] J. J. Wallman and J. Emerson, “Noise tailoring for scalable quantum computation via randomized compiling,” *Physical Review A*, vol. 94, p. 052325, Nov. 2016.

[224] D. W. Allan, “Statistics of Atomic Frequency Standards,” *Proceedings of the Institute of Electrical and Electronics Engineers*, vol. 54, no. 2, pp. 221–230, 1966.

[225] J. Rutman, “Characterization of phase and frequency instabilities in precision frequency sources: Fifteen years of progress,” *Proceedings of the IEEE*, vol. 66, no. 9, pp. 1048–1075, 1978.

[226] J. A. Sedlacek, J. Stuart, D. H. Slichter, C. D. Bruzewicz, R. McConnell, J. M. Sage, and J. Chiaverini, “Evidence for multiple mechanisms underlying surface electric-field noise in ion traps,” *Phys. Rev. A*, vol. 98, p. 063430, Dec 2018.

[227] S. Schlör, J. Lisenfeld, C. Müller, A. Bilmes, A. Schneider, D. P. Pappas, A. V. Ustinov, and M. Weides, "Correlating Decoherence in Transmon Qubits: Low Frequency Noise by Single Fluctuators," *Phys. Rev. Lett.*, vol. 123, p. 190502, Nov 2019.

[228] J. J. Burnett, A. Bengtsson, M. Scigliuzzo, D. Niepce, M. Kudra, P. Delsing, and J. Bylander, "Decoherence benchmarking of superconducting qubits," *npj Quantum Information*, vol. 5, no. 1, p. 54, 2019.

[229] H. K. Cummins and J. A. Jones, "Use of composite rotations to correct systematic errors in NMR quantum computation," *New Journal of Physics*, vol. 2, pp. 6–6, Mar. 2000.

[230] H. Ball and M. J. Biercuk, "Walsh-synthesized noise filters for quantum logic," *EPJ Quantum Technology*, vol. 2, no. 1, 2015.

[231] S. Wimperis, "Broadband, Narrowband, and Passband Composite Pulses for Use in Advanced NMR Experiments," *Journal of Magnetic Resonance, Series A*, vol. 109, no. 2, pp. 221 – 231, 1994.

[232] T. J. Proctor, A. Carignan-Dugas, K. Rudinger, E. Nielsen, R. Blume-Kohout, and K. Young, "Direct Randomized Benchmarking for Multiqubit Devices," *Phys. Rev. Lett.*, vol. 123, p. 030503, Jul 2019.

[233] L. Postler, Á. Rivas, P. Schindler, A. Erhard, R. Stricker, D. Nigg, T. Monz, R. Blatt, and M. Müller, "Experimental quantification of spatial correlations in quantum dynamics," *Quantum*, vol. 2, p. 90, Sept. 2018.

[234] M. Bando, T. Ichikawa, Y. Kondo, and M. Nakahara, "Concatenated Composite Pulses Compensating Simultaneous Systematic Errors," *Journal of the Physical Society of Japan*, vol. 82, no. 1, p. 014004, 2013.

[235] M. Reiher, N. Wiebe, K. M. Svore, D. Wecker, and M. Troyer, "Elucidating reaction mechanisms on quantum computers.," *Proceedings of the National Academy of Sciences of the United States of America*, vol. 114, pp. 7555–7560, July 2017.

[236] J. T. Merrill, S. C. Doret, G. Vittorini, J. P. Addison, and K. R. Brown, "Transformed composite sequences for improved qubit addressing," *Phys. Rev. A*, vol. 90, p. 040301(R), Oct 2014.

[237] K. Mølmer and A. Sørensen, "Multiparticle Entanglement of Hot Trapped Ions," *Phys. Rev. Lett.*, vol. 82, pp. 1835–1838, Mar 1999.

[238] A. Sørensen and K. Mølmer, "Quantum Computation with Ions in Thermal Motion," *Physical Review Letters*, vol. 82, no. 9, pp. 1971–1974, 1999.

[239] A. Sørensen and K. Mølmer, "Entanglement and quantum computation with ions in thermal motion," *Physical Review A*, vol. 62, no. 2, p. 22311, 2000.

[240] P. C. Haljan, K.-A. Brickman, L. Deslauriers, P. J. Lee, and C. Monroe, "Spin-Dependent Forces on Trapped Ions for Phase-Stable Quantum Gates and Entangled States of Spin and Motion," *Phys. Rev. Lett.*, vol. 94, p. 153602, Apr 2005.

[241] J. I. Cirac and P. Zoller, “Quantum Computations with Cold Trapped Ions,” *Phys. Rev. Lett.*, vol. 74, pp. 4091–4094, May 1995.

[242] F. Schmidt-Kaler, H. Häffner, M. Riebe, S. Gulde, G. P. T. Lancaster, T. Deuschle, C. Becher, C. F. Roos, J. Eschner, and R. Blatt, “Realization of the Cirac–Zoller controlled-NOT quantum gate,” *Nature*, vol. 422, pp. 408–411, Mar. 2003.

[243] R. J. MacDonell, C. E. Dickerson, C. J. T. Birch, A. Kumar, C. L. Edmunds, M. J. Biercuk, C. Hempel, and I. Kassal, “Analog quantum simulation of chemical dynamics.” arXiv:quant-ph/2012.01852, 2020.

[244] T. J. Green, J. Sastrawan, H. Uys, and M. J. Biercuk, “Arbitrary quantum control of qubits in the presence of universal noise,” *New Journal of Physics*, vol. 15, no. 9, p. 095004, 2013.

[245] M. A. Nielsen and I. L. Chuang, *Quantum Computation and Quantum Information*. Cambridge University Press, 2010.

[246] E. Solano, R. de Matos Filho, and N. Zagury, “Deterministic Bell states and measurement of the motional state of two trapped ions,” *Physical Review A*, vol. 59, no. 4, pp. R2539–R2543, 1999.

[247] A. W. Cross and J. M. Gambetta, “Optimized pulse shapes for a resonator-induced phase gate,” *Phys. Rev. A*, vol. 91, p. 032325, Mar 2015.

[248] H. Paik *et al.*, “Experimental Demonstration of a Resonator-Induced Phase Gate in a Multiqubit Circuit-QED System,” *Physical Review Letters*, vol. 117, p. 250502, Dec. 2016.

[249] C. Song *et al.*, “Continuous-variable geometric phase and its manipulation for quantum computation in a superconducting circuit,” *Nature Communications*, vol. 8, no. 1, p. 1061, 2017.

[250] D. C. McKay, R. Naik, P. Reinhold, L. S. Bishop, and D. I. Schuster, “High-Contrast Qubit Interactions Using Multimode Cavity QED,” *Physical Review Letters*, vol. 114, no. 8, p. 080501, 2015.

[251] N. M. Sundaresan, Y. Liu, D. Sadri, L. J. Szőcs, D. L. Underwood, M. Malekakhlagh, H. E. Türeci, and A. A. Houck, “Beyond Strong Coupling in a Multimode Cavity,” *Physical Review X*, vol. 5, no. 2, p. 021035, 2015.

[252] A. Bermudez *et al.*, “Assessing the Progress of Trapped-Ion Processors Towards Fault-Tolerant Quantum Computation,” *Phys. Rev. X*, vol. 7, p. 041061, Dec 2017.

[253] D. Hayes, S. M. Clark, S. Debnath, D. Hucul, I. V. Inlek, K. W. Lee, Q. Quraishi, and C. Monroe, “Coherent Error Suppression in Multiqubit Entangling Gates,” *Phys. Rev. Lett.*, vol. 109, p. 020503, Jul 2012.

[254] F. Haddadfarshi and F. Mintert, “High fidelity quantum gates of trapped ions in the presence of motional heating,” *New Journal of Physics*, vol. 18, no. 12, p. 123007, 2016.

[255] T. Manovitz, A. Rotem, R. Shaniv, I. Cohen, Y. Shapira, N. Akerman, A. Retzker, and R. Ozeri, “Fast Dynamical Decoupling of the Mølmer-Sørensen Entangling Gate,” *Physical Review Letters*, vol. 119, no. 22, p. 220505, 2017.

[256] Y. Shapira, R. Shaniv, T. Manovitz, N. Akerman, and R. Ozeri, "Robust Entanglement Gates for Trapped-Ion Qubits," *Physical Review Letters*, vol. 121, p. 180502, Nov. 2018.

[257] A. E. Webb, S. C. Webster, S. Collingbourne, D. Bretaud, A. M. Lawrence, S. Weidt, F. Mintert, and W. K. Hensinger, "Resilient Entangling Gates for Trapped Ions," *Phys. Rev. Lett.*, vol. 121, p. 180501, Nov 2018.

[258] G. Zarantonello, H. Hahn, J. Morgner, M. Schulte, A. Bautista-Salvador, R. F. Werner, K. Hammerer, and C. Ospelkaus, "Robust and Resource-Efficient Microwave Near-Field Entangling $^{9}\mathrm{Be}^{+}$ Gate," *Phys. Rev. Lett.*, vol. 123, p. 260503, Dec 2019.

[259] A. M. Steane, G. Imreh, J. P. Home, and D. Leibfried, "Pulsed force sequences for fast phase-insensitive quantum gates in trapped ions," *New Journal of Physics*, vol. 16, p. 053049, 2014.

[260] P. H. Leung, K. A. Landsman, C. Figgatt, N. M. Linke, C. R. Monroe, and K. R. Brown, "Robust 2-Qubit Gates in a Linear Ion Crystal Using a Frequency-Modulated Driving Force," *Physical Review Letters*, vol. 120, no. 2, p. 020501, 2018.

[261] P. H. Leung and K. R. Brown, "Entangling an arbitrary pair of qubits in a long ion crystal," *Physical Review A*, vol. 98, p. 032318, Sept. 2018.

[262] L. Yao, S. Zhang, K. Zhang, W. Chen, Y. Shen, J. Zhang, J. Zhang, and K. Kim, "Global entangling gates on arbitrary ion qubits," *Nature*, 2019.

[263] N. Grzesiak, R. Blümel, K. Wright, K. M. Beck, N. C. Pisenti, M. Li, V. Chaplin, J. M. Amini, S. Debnath, J.-S. Chen, and Y. Nam, "Efficient arbitrary simultaneously entangling gates on a trapped-ion quantum computer," *Nature Communications*, vol. 11, June 2020.

[264] K. A. Landsman, Y. Wu, P. H. Leung, D. Zhu, N. M. Linke, K. R. Brown, L. Duan, and C. Monroe, "Two-qubit entangling gates within arbitrarily long chains of trapped ions," *Phys. Rev. A*, vol. 100, p. 022332, Aug 2019.

[265] C. Sackett, D. Kielpinski, B. King, C. Langer, V. Meyer, C. Myatt, M. Rowe, Q. Turchette, W. M. Itano, D. J. Wineland, and C. R. Monroe, "Experimental entanglement of four particles," *Nature*, vol. 404, no. 6775, pp. 256–259, 2000.

[266] M. Guggemos, *Precision spectroscopy with trapped $^{40}Ca^{+}$ and $^{27}Al^{+}$ ions*. PhD thesis, University of Innsbruck, 2017.

[267] T. Green, H. Uys, and M. J. Biercuk, "High-Order Noise Filtering in Nontrivial Quantum Logic Gates," *Phys. Rev. Lett.*, vol. 109, p. 020501, Jul 2012.

[268] G. A. Paz-Silva and L. Viola, "General Transfer-Function Approach to Noise Filtering in Open-Loop Quantum Control," *Phys. Rev. Lett.*, vol. 113, p. 250501, Dec 2014.

[269] R. Ozeri *et al.*, "Errors in trapped-ion quantum gates due to spontaneous photon scattering," *Phys. Rev. A*, vol. 75, p. 042329, Apr 2007.

[270] F. Hapgood, "Computers Aren't So Smart, After All," *The Atlantic*, Aug. 1974.

[271] A. R. R. Carvalho, H. Ball, M. J. Biercuk, M. R. Hush, and F. Thomsen, “Error-robust quantum logic optimization using a cloud quantum computer interface.” arXiv:quant-ph/2010.08057, 2020.

[272] C. J. Ballance, *High-Fidelity Quantum Logic in Ca*$^+$. PhD thesis, University of Oxford, 2014.

“So it goes.”

- Kurt Vonnegut, *Slaughterhouse-Five*

APPENDIX A

Useful mathematical relations and definitions

A1 Basic operations

1. The Pauli group:

$$\hat{\mathbb{I}} = \begin{pmatrix} 1 & 0 \\ 0 & 1 \end{pmatrix} \hat{\sigma}_x = \begin{pmatrix} 0 & 1 \\ 1 & 0 \end{pmatrix} \hat{\sigma}_y = \begin{pmatrix} 0 & -i \\ i & 0 \end{pmatrix} \hat{\sigma}_z = \begin{pmatrix} 1 & 0 \\ 0 & -1 \end{pmatrix} \tag{A.1}$$

2. The Hadamard operator rotates by $\theta = \pi/2$ about the axis 45° between the x and z-axes, expressed as $\mathbf{n} = [\frac{1}{\sqrt{2}}, 0, \frac{1}{\sqrt{2}}]$.

$$\hat{H} = \frac{1}{\sqrt{2}} \begin{pmatrix} 1 & 1 \\ 1 & -1 \end{pmatrix}. \tag{A.2}$$

3. The phase gate:

$$\hat{P} = \begin{pmatrix} 1 & 0 \\ 0 & i \end{pmatrix} \tag{A.3}$$

A2 Useful mathematical relations

A2.1 General identities

1. Baker–Campbell–Hausdorff formula simplification : if the commutator of two operators is a complex-valued scalar, $[\hat{X}, \hat{Y}] = c \in \mathbb{C}$, then

$$\begin{aligned} e^{a\hat{X}} e^{b\hat{Y}} &= e^{a\hat{X} + b\hat{Y} + \frac{ab}{2}[\hat{X},\hat{Y}]} \\ &= e^{a\hat{X} + b\hat{Y}} e^{abc/2}. \end{aligned} \tag{A.4}$$

2. The displacement operator for oscillator mode k with creation and annihilation operators $\hat{a}_k^\dagger, \hat{a}_k$ and the (potentially complex valued) displacement α is defined to be

$$\hat{D}_k(\alpha) = e^{\alpha \hat{a}_k^\dagger - \alpha^* \hat{a}_k}. \tag{A.5}$$

The operator $\hat{D}_k$ obeys the following rules.

$$\begin{aligned}(i) \quad \hat{D}_k(\alpha)\hat{D}_k(\beta) &= \hat{D}_k(\alpha+\beta)e^{(\alpha\beta^* - \alpha^*\beta)/2} \\ &= e^{\alpha\beta^* - \alpha^*\beta}\hat{D}_k(\beta)\hat{D}_k(\alpha)\end{aligned} \tag{A.6}$$

$$(ii) \quad [\hat{D}_j(\alpha), \hat{D}_k(\beta)] = 0 \qquad \text{if } j \neq k \tag{A.7}$$

$$(iii) \quad \hat{D}_k(\alpha)^\dagger = e^{\alpha^* \hat{a}_k - \alpha \hat{a}_k^\dagger} = \hat{D}_k(-\alpha) \tag{A.8}$$

$$(iv) \quad \hat{D}_k(\alpha)^\dagger \hat{D}_k(\alpha) = \hat{\mathbb{I}} \tag{A.9}$$

$$(v) \quad \sum_{n_k=0}^{\infty} p_{n_k} \langle n_k | \hat{D}_k(\alpha) | n_k \rangle = e^{-|\alpha|^2(\bar{n}_k + \frac{1}{2})} \tag{A.10}$$

$$\begin{aligned}(vi) \quad \hat{D}_k(\alpha \hat{S}_x) &= e^{(\hat{\sigma}_x^{(\mu)} + \hat{\sigma}_x^{(\nu)}) \otimes (\alpha \hat{a}_k^\dagger - \alpha^* \hat{a}_k)} \\ &= \hat{P}_0 \otimes e^0 + \hat{P}_{+2} \otimes e^{2(\alpha \hat{a}_k^\dagger - \alpha^* \hat{a}_k)} + \hat{P}_{-2} \otimes e^{-2(\alpha \hat{a}_k^\dagger - \alpha^* \hat{a}_k)} \\ &= \hat{P}_0 \otimes \hat{\mathbb{I}} + \hat{P}_{+2} \otimes \hat{D}_k(2\alpha) + \hat{P}_{-2} \otimes \hat{D}_k(-2\alpha)\end{aligned}$$

Here, the total Pauli-x spin operator is defined as $\hat{S}_x = \hat{\sigma}_x^{(\mu)} + \hat{\sigma}_x^{(\nu)}$, the mean phonon number of mode k is given $\bar{n}_k$, and the operators $\hat{P}_{+2} = \hat{P}_{++} = |{+}{+}\rangle \langle{+}{+}|, \hat{P}_{-2} = \hat{P}_{--} = |{-}{-}\rangle \langle{-}{-}|, \hat{P}_0 = \hat{P}_{+-} + \hat{P}_{-+} = (|{+}{-}\rangle \langle{+}{-}|) + (|{-}{+}\rangle \langle{-}{+}|)$ are the projection operators onto to eigenvalues +2, -2 and 0 respectively.

3. The following conjugation relations as used in the Mølmer-Sørensen observable evolution derivations.

$$[\hat{S}_j^2, \hat{S}_k^2] = 0 \tag{A.11}$$

$$e^{i\gamma \hat{S}_x^2} \hat{S}_j^2 e^{-i\gamma \hat{S}_x^2} = \hat{S}_j^2 \tag{A.12}$$

$$e^{i\gamma \hat{S}_x^2} \hat{\sigma}_z^{(\mu)} e^{-i\gamma \hat{S}_x^2} = \sin(4\gamma) \hat{\sigma}_y^{(\mu)} \hat{\sigma}_x^{(\nu)} + \cos(4\gamma) \hat{\sigma}_z^{(\mu)} \tag{A.13}$$

$$e^{i\gamma \hat{S}_x^2} \hat{\sigma}_z^{(\nu)} e^{-i\gamma \hat{S}_x^2} = \sin(4\gamma) \hat{\sigma}_x^{(\mu)} \hat{\sigma}_y^{(\nu)} + \cos(4\gamma) \hat{\sigma}_z^{(\nu)} \tag{A.14}$$

A3 Matrices for calculating observables under evolution of the Mølmer-Sørensen gate

In the $\hat{\sigma}_z \otimes \hat{\sigma}_z$-basis (the computational basis), the total Pauli spin matrices are given by the following.

$$\hat{S}_x = \begin{pmatrix} 0 & 1 & 1 & 0 \\ 1 & 0 & 0 & 1 \\ 1 & 0 & 0 & 1 \\ 0 & 1 & 1 & 0 \end{pmatrix} \hat{S}_y = \begin{pmatrix} 0 & -i & -i & 0 \\ i & 0 & 0 & -i \\ i & 0 & 0 & -i \\ 0 & i & i & 0 \end{pmatrix} \hat{S}_z = 2 \begin{pmatrix} 1 & 0 & 0 & 0 \\ 0 & 0 & 0 & 0 \\ 0 & 0 & 0 & 0 \\ 0 & 0 & 0 & -1 \end{pmatrix} \tag{A.15}$$

$$\hat{S}_x^2 = 2 \begin{pmatrix} 1 & 0 & 0 & 1 \\ 0 & 1 & 1 & 0 \\ 0 & 1 & 1 & 0 \\ 1 & 0 & 0 & 1 \end{pmatrix} \hat{S}_y^2 = 2 \begin{pmatrix} 1 & 0 & 0 & -1 \\ 0 & 1 & 1 & 0 \\ 0 & 1 & 1 & 0 \\ -1 & 0 & 0 & 1 \end{pmatrix} \hat{S}_z^2 = 4 \begin{pmatrix} 1 & 0 & 0 & 0 \\ 0 & 0 & 0 & 0 \\ 0 & 0 & 0 & 0 \\ 0 & 0 & 0 & 1 \end{pmatrix} \tag{A.16}$$

In the $\hat{\sigma}_x \otimes \hat{\sigma}_x$-basis, the projection matrices for the four eigenstates $|{+}{+}\rangle, |{+}{-}\rangle, |{-}{+}\rangle, |{-}{-}\rangle$ are as follows.

$$\hat{P}_{++} = \begin{pmatrix} 1 & 0 & 0 & 0 \\ 0 & 0 & 0 & 0 \\ 0 & 0 & 0 & 0 \\ 0 & 0 & 0 & 0 \end{pmatrix}, \hat{P}_{+-} = \begin{pmatrix} 0 & 0 & 0 & 0 \\ 0 & 1 & 0 & 0 \\ 0 & 0 & 0 & 0 \\ 0 & 0 & 0 & 0 \end{pmatrix},$$

$$\hat{P}_{-+} = \begin{pmatrix} 0 & 0 & 0 & 0 \\ 0 & 0 & 0 & 0 \\ 0 & 0 & 1 & 0 \\ 0 & 0 & 0 & 0 \end{pmatrix}, \hat{P}_{--} = \begin{pmatrix} 0 & 0 & 0 & 0 \\ 0 & 0 & 0 & 0 \\ 0 & 0 & 0 & 0 \\ 0 & 0 & 0 & 1 \end{pmatrix}. \tag{A.17}$$

Ideally, we would like to express these matrices in terms of the computational basis, $\hat{\sigma}_z \otimes \hat{\sigma}_z$. To perform a basis transformation for the matrix $\hat{A}$ from the basis states $\{|e_i\rangle\}$ to the new states $\{|f_i\rangle\}$, use the following expressions.

$$\hat{A}_{\{|f_i\rangle\}} = \hat{E}^{\dagger}_{e\to f} \hat{A}_{\{|e_i\rangle\}} \hat{E}_{e\to f} \tag{A.18}$$

$$\hat{E}_{e\to f} = \{\langle e_i|\}\{|f_i\rangle\} = \begin{pmatrix} \langle e_1|f_1\rangle & \langle e_1|f_2\rangle & \langle e_1|f_3\rangle & \langle e_1|f_4\rangle \\ \langle e_2|f_1\rangle & \langle e_2|f_2\rangle & \langle e_2|f_3\rangle & \langle e_2|f_4\rangle \\ \langle e_3|f_1\rangle & \langle e_3|f_2\rangle & \langle e_3|f_3\rangle & \langle e_3|f_4\rangle \\ \langle e_4|f_1\rangle & \langle e_4|f_2\rangle & \langle e_4|f_3\rangle & \langle e_4|f_4\rangle \end{pmatrix} \tag{A.19}$$

We consider the basis states $\hat{\sigma}_z \otimes \hat{\sigma}_z$ and $\hat{\sigma}_x \otimes \hat{\sigma}_x$. The basis states for $\hat{\sigma}_x \otimes \hat{\sigma}_x$ can be written in the computational basis as,

$$|{+}{+}\rangle = \frac{1}{\sqrt{2}}\begin{pmatrix}1\\1\end{pmatrix} \otimes \frac{1}{\sqrt{2}}\begin{pmatrix}1\\1\end{pmatrix} = \frac{1}{2}\begin{pmatrix}1\\1\\1\\1\end{pmatrix},$$

$$|{+}{-}\rangle = \frac{1}{2}\begin{pmatrix}1\\-1\\1\\-1\end{pmatrix}, |{-}{+}\rangle = \frac{1}{2}\begin{pmatrix}1\\1\\-1\\-1\end{pmatrix}, |{-}{-}\rangle = \frac{1}{2}\begin{pmatrix}1\\-1\\-1\\1\end{pmatrix}. \tag{A.20}$$

Then, the transformation matrix is given by

$$\hat{E}_{xx\to zz} = \begin{pmatrix}\langle + + |00\rangle & \langle + + |01\rangle & \langle + + |10\rangle & \langle + + |11\rangle \\ \langle + - |00\rangle & \langle + - |01\rangle & \langle + - |10\rangle & \langle + - |11\rangle \\ \langle - + |00\rangle & \langle - + |01\rangle & \langle - + |10\rangle & \langle - + |11\rangle \\ \langle - - |00\rangle & \langle - - |01\rangle & \langle - - |10\rangle & \langle - - |11\rangle\end{pmatrix} = \frac{1}{2}\begin{pmatrix}1 & 1 & 1 & 1\\ 1 & -1 & 1 & -1\\ 1 & 1 & -1 & -1\\ 1 & -1 & -1 & 1\end{pmatrix}. \tag{A.21}$$

Finally, we can re-express the projection matrices from Eqn. (A.17) in the $\hat{\sigma}_z \otimes \hat{\sigma}_z$-basis.

$$\hat{P}_{++} \doteq \frac{1}{4}\begin{pmatrix}1 & 1 & 1 & 1\\ 1 & 1 & 1 & 1\\ 1 & 1 & 1 & 1\\ 1 & 1 & 1 & 1\end{pmatrix} = \frac{1}{8}(\hat{S}_x^2 + 2\hat{S}_x),$$

$$\hat{P}_{+-} \doteq \frac{1}{4}\begin{pmatrix}1 & -1 & 1 & -1\\ -1 & 1 & -1 & 1\\ 1 & -1 & 1 & -1\\ -1 & 1 & -1 & 1\end{pmatrix} = \frac{1}{4}(2\hat{\mathbb{1}} - \frac{1}{2}\hat{S}_x^2 + \hat{\sigma}_x^{(\mu)} - \hat{\sigma}_x^{(\nu)}),$$

$$\hat{P}_{-+} \doteq \frac{1}{4}\begin{pmatrix}1 & 1 & -1 & -1\\ 1 & 1 & -1 & -1\\ -1 & -1 & 1 & 1\\ -1 & -1 & 1 & 1\end{pmatrix} = \frac{1}{4}(2\hat{\mathbb{1}} - \frac{1}{2}\hat{S}_x^2 - \hat{\sigma}_x^{(\mu)} + \hat{\sigma}_x^{(\nu)}),$$

$$\hat{P}_{--} \doteq \frac{1}{4}\begin{pmatrix}1 & -1 & -1 & 1\\ -1 & 1 & 1 & -1\\ -1 & 1 & 1 & -1\\ 1 & -1 & -1 & 1\end{pmatrix} = \frac{1}{8}(\hat{S}_x^2 - 2\hat{S}_x) \tag{A.22}$$

APPENDIX B

Bayesian measurement analysis protocols for one and two-qubits on the APD

The fluorescence detected during single-qubit experiments is measured using an avalanche photodiode (APD). The data is analysed with a either standard thresholding protocol or a time-resolved maximum likelihood analysis. We explain the time-resolved maximum likelihood analysis protocol in detail here, used for time-resolved photon data collected on the APD. The description here is taken from the Supplementary Materials of S. Mavadia, C. L. Edmunds, et al. [**221**], presented in Chapters 4 and 5.

Two-qubit experiments are often recorded on the EMCCD to obtain spacial resolution, however, the results in Chapter 8 use the APD to reduce electrical noise and improve detection fidelity. To analyse the two-qubit results, two separate maximum likelihoods are used, one returning the state probabilities and the other estimating the Bell state fidelity error. The descriptions for two-qubit measurement analysis on the APD are taken from the Methods section of A. R. Milne, C. L. Edmunds, et al. [**6**] which is presented in Chapters 8.

B1 "Subbinning" protocol for temporally resolved qubit state detection

We use the photon information we collect from the ion to determine the projected state of the qubit after each repetition of an experiment. This is done via a Markov model initially published for $^{171}\text{Yb}^{+}$ by Wolk et al. [**113**]. For the RB experiments described in the main text we combine this information over r repetitions to calculate the most likely projection of the Bloch vector on the z-axis. This methodology has a reduced measurement error compared to a simple threshold detection technique that assigns a state based on whether the total number of detected photon counts is above or below a certain level.

To detect the state of the ion at the end of a sequence of microwave-driven rotations, we apply light at 369.4 nm resonant with the optical dipole transition between the $\text{S}_{1/2}$, $F = 1$ and $\text{P}_{1/2}$, $F = 0$ states

(Figure B.1). During this detection period, an avalanche photodiode registers photons that are scattered if the qubit was projected into the $|F=1, m_F=0\rangle$ state, hence denoted 'bright state', and no photons if the qubit was projected into the $|F=0, m_F=0\rangle$ 'dark' state.

Due to the proximity of the other electronic levels in the S and P manifolds, off-resonant excitations (proportional to the applied laser power) can occur and change the state of the qubit during the detection period, adversely affecting the detection fidelity. The rate at which these changes occur can be expressed in terms of a bright (dark) state lifetime τ_{B} (τ_{D}).

Rather than simply considering a single transition between the bright and dark states (or vice versa) we can generalise this to multiple transitions within a single measurement detection period [**113**]. To identify these individual transitions we split the photon detection time into equal length sub-bins and make the assumption that there is at most one transition between bright and dark state per sub-bin. We then use the number of photons within each sub-bin and the distribution of photons across sub-bins within a single detection period to determine the likelihood of the ion initially having been projected into the bright or the dark state. For full details of this procedure and a mathematical derivation, see [**113**].

In this work we divided the total detection time into 5 sub-bins. In each experimental repetition we calculate the mean detected photon rate in the bright state, R_B, and the dark state, R_D, by fitting a double Poisson function to a histogram of the entire data set. For a given detection laser power, the decay rates $\tau_{B,D}^{-1}$ are obtained from a separately performed calibration where we initialise the ion in either the bright or dark state and then observe the average photon count rate over many repetitions as a function of detection time.

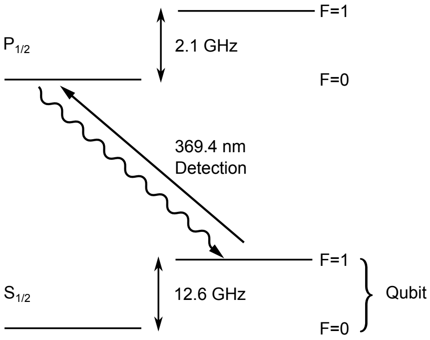

FIGURE B.1. Relevant energy levels for $^{171}\mathrm{Yb}^+$ and their energy splittings, with the Zeeman structure omitted. The qubit is encoded in the $\mathrm{S}_{1/2}$, $|F=0, m_F=0\rangle$ and $\mathrm{S}_{1/2}$, $|F=1, m_F=0\rangle$ states and controlled via microwave radiation resonant with a magnetic dipole transition at 12.64 GHz.

In addition to analysing photons in the detection period using sub-bins, we also remove experimental repetitions which do not emit a certain number of photons during the laser cooling period prior to the microwave rotations. This accounts for the rare occurrences when the ion is subject to a collision or other heating effect that may impact the efficacy of the experiment.

The above protocol returns the most likely outcome for each single repetition. To improve the accuracy of state-estimation, we calculate the most likely projection ϕ along the z-axis. To do this we implement a Bayesian approach to find the probability distribution over all possible projections. The distribution is discretised in steps of 10^{-3} and initialised such that the likelihood of measuring any projection along the z-axis is equal,

$$\text{Pr}(\phi) = 1/K, \tag{B.1}$$

where K is a normalisation term. We then condition this probability on the observed photon distribution, p_φ, such that

$$\text{Pr}(\phi|p_\varphi) = K^{-1} \prod \text{Pr}(p_\varphi|\phi) \tag{B.2}$$

where $\text{Pr}(p_\varphi|\phi)$ is calculated from the likelihood of finding the qubit in either the $|1\rangle$ or $|0\rangle$ state,

$$\text{Pr}(p_\varphi|\phi) = \text{Pr}(p_\varphi||1\rangle)\text{Pr}(|1\rangle|\phi) + \text{Pr}(p_\varphi||0\rangle)\text{Pr}(|0\rangle|\phi). \tag{B.3}$$

The terms $\text{Pr}(p_\varphi||1\rangle)$ and $\text{Pr}(p_\varphi||0\rangle)$ are the likelihoods of measuring the photon distribution p_φ given that we start in the bright or dark state respectively and are calculated via the Markov model described above. The values $\text{Pr}(|1\rangle|\phi)$ and $\text{Pr}(|0\rangle|\phi)$ are the probabilities of projecting the qubit into either the $|1\rangle$ or $|0\rangle$ state during detection given a particular ϕ. We incrementally update $\text{Pr}(\phi|p_\varphi)$ by adding information for each repetition across all of the noise realisations. To find the most likely outcome for a particular sequence we then calculate the mean of this distribution.

B2 Maximum-likelihood procedure for two-qubit state estimation

Hyperfine qubits such as $^{171}\text{Yb}^+$ are susceptible to leakage between the qubit states from off-resonant excitations during the laser-induced fluorescence measurement. We employ a maximum-likelihood state estimation procedure [**257**], which reduces measurement error by accounting for the effect of state decay based on independent calibrations. In a given two-qubit experiment, we would like to determine the resultant state populations P_i, which are the probabilities for measuring i ions in the $|1\rangle$ state. To do this, the ions are illuminated with a 369 nm laser, projecting each qubit into either the $|1\rangle$ (bright) or

$|0\rangle$ (dark) state. The experiment is repeated n times and the number of photon counts measured on an avalanche photodiode (APD) for each repetition is recorded. The resultant count rates are plotted in a histogram and by setting two count rate thresholds c_1 and c_2 between the resulting distributions, each repetition is assigned a outcome of 'i ions bright', where $i \in \{0, 1, 2\}$. We denote the number of repetitions assigned to each outcome as x_i, with $x_0 + x_1 + x_2 = n$. Due to state decays, there will be an overlap in the count rate distributions, meaning the true probabilities P_i are not simply the proportion of repetitions assigned to outcome i. Instead, we define a linear map relating the measured probabilities $P_i' = x_i/n$ to the true probabilities P_i, which takes the form $P_i' = \sum_j P(i|j)P_j$. Here, $P(i|j)$ is the probability of classifying a repetition as 'i ions bright' given the ions were prepared in the state 'j ions bright'. The probabilities $P(i|0)$ and $P(i|2)$ are obtained by preparing and measuring the states $|00\rangle$ and $|11\rangle$, respectively, in calibration experiments. Without the ability to individually address ions, it is not possible to prepare the state $|01\rangle$ or $|10\rangle$, hence to determine the probabilities $P(i|1)$, we assume $P(2|1) = 0$ (which is a fair assumption given our detection duration and laser powers) and utilise a single ion to obtain $P(0|1)$ and $P(1|1)$. For a given set of repetitions, we compute the log-likelihood function $f(P_1, P_2)$ for discretised values of P_1, P_2 between 0 and 1. The values of P_1, P_2 that maximise $f(P_1, P_2)$ are the most probable given the data [**257**].

$$f(P_1, P_2) = \log\left(\frac{(n+1)(n+2)n!P_1'(P_1, P_2)^{x_1}P_2'(P_1, P_2)^{x_2}(1 - P_1'(P_1, P_2) - P_2'(P_1, P_2))^{n-x_1-x_2}}{x_1!x_2!(n - x_1 - x_2)!}\right) \tag{B.4}$$

Note that Eqn. (B.4) only depends on populations P_1 and P_2 as normalisation always enables P_0 to be expressed as $1 - P_1 - P_2$. In order to make $f(P_1, P_2)$ computable, Stirling's approximation ($\log(n!) \approx n\log(n) - n$) must be used as terms such as $n!$ diverge too rapidly to be calculated for large n.

B3 Two-qubit Bell state measurement fidelity

To calculate how the measured Bell state fidelity is affected by imperfect state estimation via the maximum likelihood (ML) scheme, we follow an approach similar to the one outlined in [**272**]. By preparing and measuring known input states, we again construct a linear map relating the true populations P_i to the population outcomes determined by the ML procedure P_i''. In this case, the values $P(i|j)$ represent the probability that the ML procedure assigns some population 'i ions bright' to the measurement outcome, given that a state with population 'j ions bright' is prepared.

As described in the main text, the application of the MS gate results in the Bell state $(|00\rangle + i\,|11\rangle)/\sqrt{2}$, the fidelity of which may be expressed as

$$\mathcal{F} = \frac{P_0 + P_2}{2} + \frac{\pi_c}{2}. \tag{B.5}$$

Here, π_c is parity contrast of the resultant state, measured by varying the phase of an additional $\pi/2$ analysis pulse at the conclusion of the gate. Assuming a Bell state with perfect fidelity, π_c may be expressed as half the difference in parity between two states $|E\rangle = (|00\rangle - i\,|11\rangle)/\sqrt{2}$ and $|O\rangle = (|01\rangle + i\,|10\rangle)/\sqrt{2}$ with parities $\mathcal{P} = 1$ and $\mathcal{P} = -1$, respectively. Hence the expression for the fidelity (Eqn. B.5) becomes

$$\begin{aligned}\mathcal{F} &= \frac{P_{0,E} + P_{2,E}}{2} \\ &+ \frac{(P_{0,E} + P_{2,E} - P_{1,E}) - (P_{0,O} + P_{2,O} - P_{1,O})}{4},\end{aligned} \tag{B.6}$$

where $P_{i,k}$ indicate the populations for the ideal Bell states $|k\rangle$, with $k \in \{E, O\}$.

We model the effect of imperfect state estimation by substituting the true populations $P_{i,k}$ in Eqn. B.6 with the measured populations $P''_{i,k}$, which are related to the true populations by the linear map. As an example, we may calculate the measured populations $P''_{i,E}$ as

$$\begin{pmatrix} P''_{0,E} \\ P''_{1,E} \\ P''_{2,E} \end{pmatrix} = \begin{pmatrix} P(0|0) & P(0|1) & P(0|2) \\ P(1|0) & P(1|1) & P(1|2) \\ P(2|0) & P(2|1) & P(2|2) \end{pmatrix} \begin{pmatrix} 1/2 \\ 0 \\ 1/2 \end{pmatrix} \tag{B.7}$$

$$= \begin{pmatrix} P(0|0) + P(0|2) \\ P(1|0) + P(1|2) \\ P(2|0) + P(2|2) \end{pmatrix}. \tag{B.8}$$

Re-expressing Eqn. B.6 in terms of the probabilities $P(i|j)$, we arrive at an expression for the Bell state fidelity incorporating imperfect state estimation.

$$\begin{aligned}\mathcal{F} &= 1 - \frac{1}{2}\left[P(0|1) + P(1|2) + P(1|0) + P(2|1)\right] \\ &= 1 - \epsilon\end{aligned} \tag{B.9}$$

Hence the contribution to the measured infidelity due to state estimation is given by

$$1-\mathcal{F}=\epsilon=\frac{1}{2}\left[P(0|1)+P(1|2)+P(1|0)+P(2|1)\right]. \tag{B.10}$$

The matrix below shows typical values of $P(i|j)$, which inserted into Eqn. B.10 give an error contribution of $\epsilon\approx$ 0.4(4)%. The quoted uncertainties are the standard deviation over multiple calibration measurements.

$$P(i|j)=\begin{pmatrix} 0.997(4) & 0.001(3) & 0.0002(6) \\ 0.002(4) & 0.997(3) & 0.003(6) \\ 0.0002(4) & 0.001(1) & 0.996(6) \end{pmatrix} \tag{B.11}$$

APPENDIX C

Randomised benchmarking on $^{171}\mathrm{Yb}^{+}$ qubits

We characterise the trap's baseline performance (with no engineered noise) using single-qubit RB with microwave primitive gates produced by the I/Q-modulated VSG. The RB sequence survival probabilities are plotted in Fig. C.1 for sequence lengths from $J = 2$ to $J = 500$. The mean survival probability for each sequence length is fitted to an exponential decay,

$$\mathcal{P} = 0.5 + (0.5 - \kappa)\mathrm{e}^{-p_{\mathrm{RB}} J}, \tag{C.1}$$

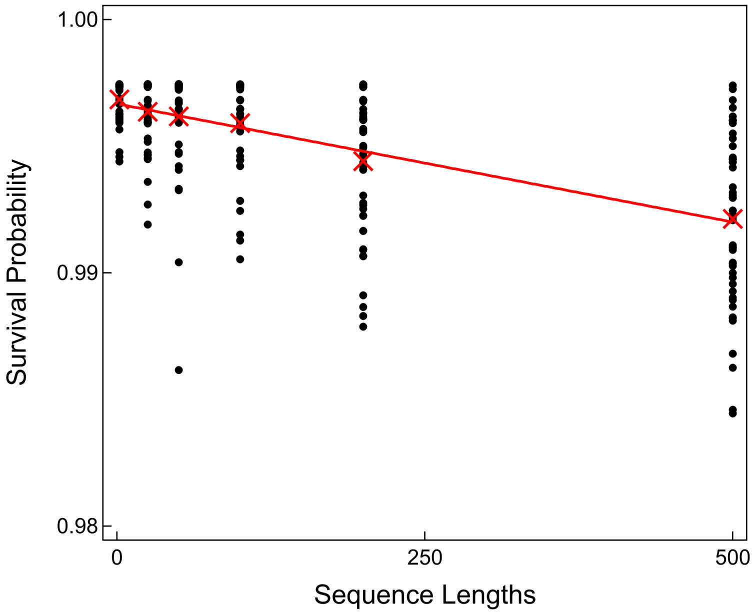

FIGURE C.1. **Single-qubit randomised benchmarking.** Randomised benchmarking is performed on a single qubit using a total of 300 sequences composed of primitive gates, with 50 sequences each of length $J = 2,\ 25,\ 50,\ 100,\ 200,$ and 500. Each sequence was repeated $r = 500$ times to reduce quantum projection noise. Black markers represent individual sequence survival probabilities, red crosses indicate the mean survival probabilities for each sequence length, and the solid red line in a fit to the means to extract the average error per gate.

to extract the average error per gate (EPG). A single ion in the blade trap achieves a baseline average EPG of $p_{\mathrm{RB}} \approx 1.9 \times 10^{-5}$ and a state preparation and measurement error (SPAM) of $\kappa = (3.3 \pm 0.1) \times 10^{-3}$.

APPENDIX D

Supplementary Material about the results of noise engineering in GST experiments

---

D1 Limitations of random walk model

In the main text we suggest that the magnitude of the noise and sequence averaged error in some cases exceeds the validity bounds for the first-order approximations employed in the random walk framework for RB. While the formal bound in [**165**] requires $J\rho^2 \ll 1$, the data presented in Figs. 5.3 in the main text ranges from $J\rho^2 = 0.05$ to $J\rho^2 = 0.40$ for 25 gate and 200 gate sequences respectively. Figure D.1 shows several simulated survival probability distributions as a function of expectation value $J\rho^2$. As the value of $J\rho^2$ increases the shape of the distribution diverges from a gamma distribution with shape parameter $\alpha = 1$ (which is mathematically equivalent to an exponential PDF).

To a first-order approximation we can also incorporate the effects of measurement error (SPAM) by introducing an offset into the gamma distribution describing measured survival probabilities over sequences. We can see this effect using data sets similar to those shown in Fig. 5.3 of the main text, but measured using a detector with higher background counts and analysed with a lower-fidelity detection protocol called “threshold detection".

Threshold detection determines whether each single repetition was in the $|0\rangle$ or $|1\rangle$ state by checking if the detected number of photons is above a certain fixed threshold. To find the noise-averaged survival probability we find the mean of all repetitions over noise realisations associated with each sequence. This ultimately leads to a larger measurement error than the method employed in the main text, permitting quantitative comparisons of the effects. As shown in Fig. D.1, the shape parameter diverges from the model if the expectation of the distribution is large, and accordingly we restrict our analysis to data using $J = 10$ to numerically fit an offset for all data sets.

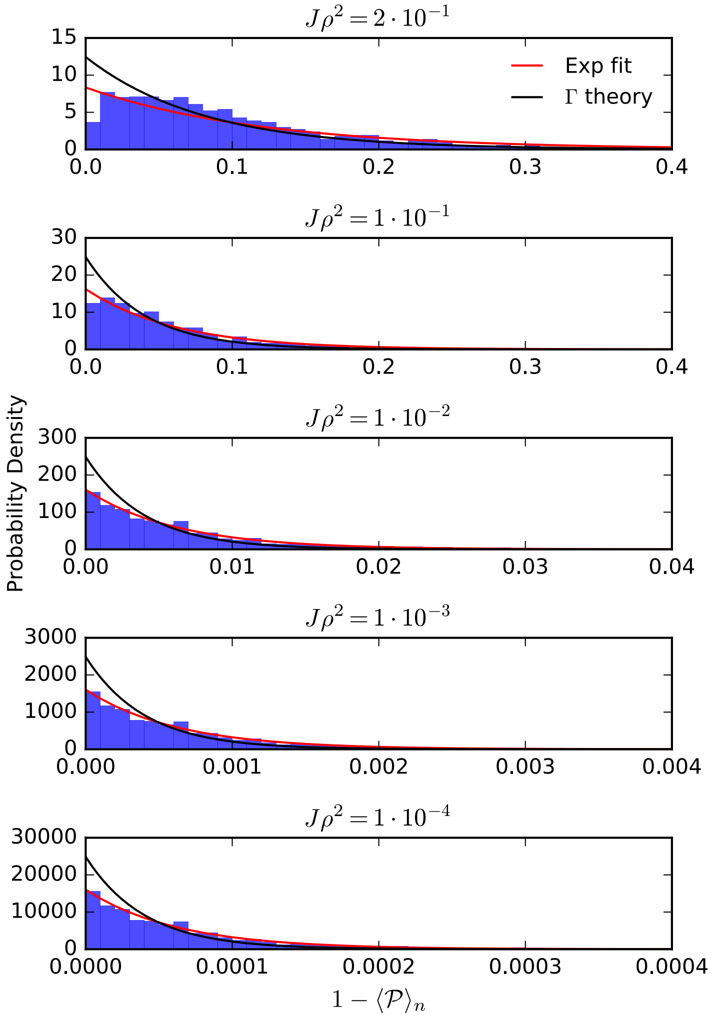

FIGURE D.1. Survival probability distributions as a function of expectation value $J\rho^2$. The integral of the simulated histogram values and PDFs are equal to unity. In each case the sequences and noise realisations were kept constant and the magnitude of errors is multiplied by a scalar to produce the correct displayed value of $J\rho^2$ and the number of gates in a sequence is held constant at $J = 100$. Fits are constrained to maintain shape parameter, $\alpha = 1$, in the gamma distributions.

We show such data in Fig. D.2 and overlay the distribution from Eqn. (4.87) with the extracted offset. For comparison we show the same data which is subject to the Bayesian estimation technique described in Sec. B1, which is more effective in reducing measurement error. Data remain well described by the gamma distribution with $\alpha = 1$ after incorporation of a fixed offset from unit survival probability.

Finally, we suggest that the scatter of the points in Fig. 5.4 of the main text partially arises because $\|\boldsymbol{V}\|^2$ is calculated using only the simplified error model that was originally studied in reference [**165**], where

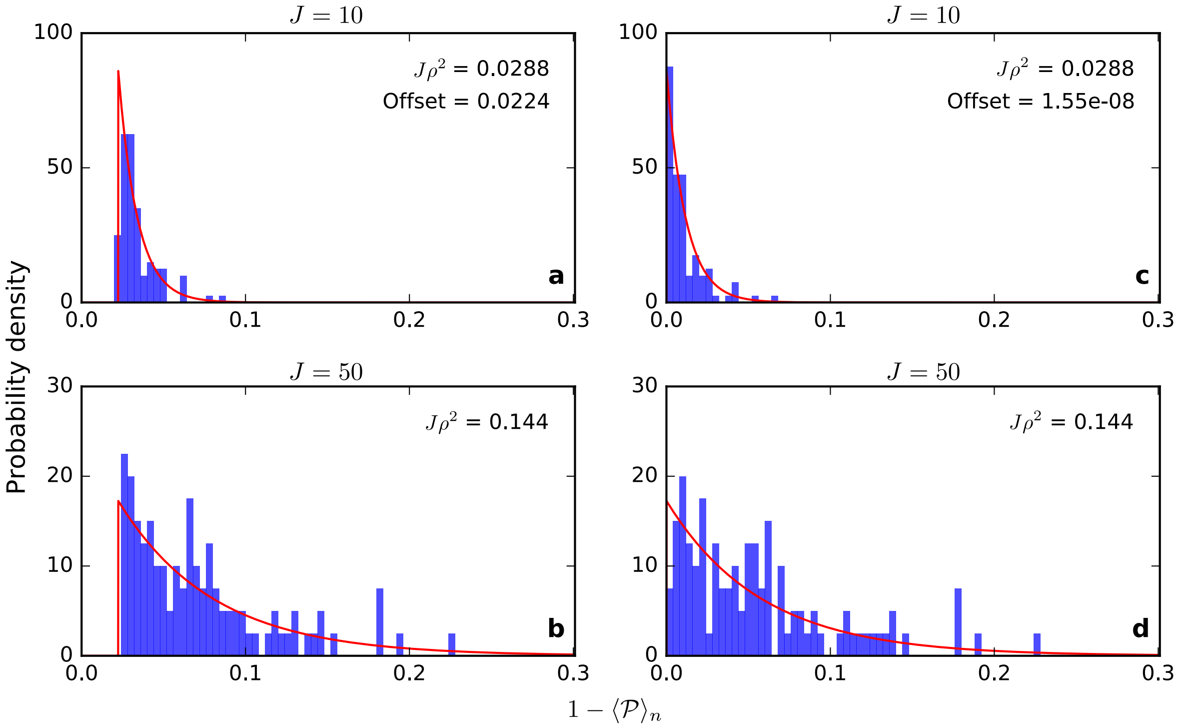

FIGURE D.2. Survival probabilities distributions of sequences with different numbers of gates with $\rho^2 = 2.9 \times 10^{-3}$. Panels **a,b** use a simplified analysis technique called “threshold detection" (see text) and panels **c,d** use the Bayesian estimation technique outlined in section B1. These are overlaid with gamma distributions derived from Eqn. (4.87) with an additional offset to take into account the level of measurement error in the system calculated from the $J = 10$ data independently for the two sets of panels.

the errors are interleaved throughout the sequence and between gates. To verify this we have performed numerical simulations of sequence survival probabilities under application of the original error model and compare against measured data for the same sequences, but the experimentally relevant concurrent mode (Fig. D.3). We observe that the root-mean-square error between the data points and the best linear fit for the interleaved error case is approximately half that for the concurrently applied error case. However, in both cases we still observe a clear linear relationship between walk length and survival probability under the influence of slowly varying noise.

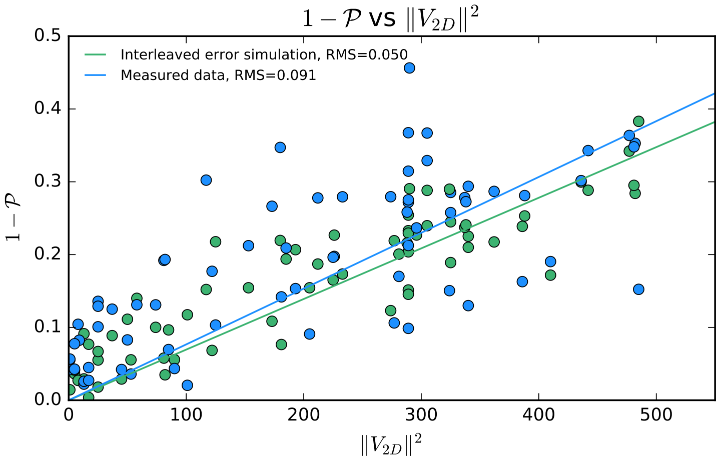

FIGURE D.3. Noise averaged survival probabilities for measured data subject to concurrently applied noise (blue circles) and simulated outcomes where the interleaved error model matches ref [**165**] (green circles) as a function of calculated $\|\boldsymbol{V}_{2D}\|^2$. The solid lines represent linear fits to their associated data sets. The root-mean-square error between the data and linear fit is halved for the interleaved error model (green), which more closely matches how the random walk was calculated.

D2 GST error simulations

All numerical simulations conducted here have been implemented within the pyGSTi toolkit. We have also independently verified that error models developed in Matlab perform similarly. In addition to the analytic concurrent error models described in the main text we have also compared our findings to a variety of other error models found as inbuilt options within pyGSTi. The toolkit includes the .rotate() function, corresponding to a post-multiplied error of an amount θ around the x, y or z-axis of the Bloch sphere. It is also possible to simulate the effect of depolarising noise using pyGSTi built-in functionality. In Fig. D.4 below we are using both to investigate the effect of gauge freedom under a variety of error models and using both gate sets.

The extended gate set associated with integration of negative rotations about x and y, $\{G_x, G_y, G_i\} \rightarrow \{G_x, G_y, G_i, -G_x, -G_y\}$, also involves extending the set of germs from the original 11 listed in the methods section to the following enlarged list of 39 entries, where Gxm and Gym stand for the negative rotations:

('Gx'), ('Gy'), ('Gi'), ('Gxm'), ('Gym'),
('Gx', 'Gy'), ('Gxm', 'Gym'), ('Gxm', 'Gy'), ('Gx', 'Gym'),
('Gx', 'Gy', 'Gi'), ('Gx', 'Gi', 'Gy'), ('Gx', 'Gi', 'Gi'), ('Gy', 'Gi', 'Gi'),

('Gxm', 'Gy', 'Gi'), ('Gx', 'Gym', 'Gi'), ('Gxm', 'Gi', 'Gy'), ('Gx', 'Gi', 'Gym'),
('Gxm', 'Gym', 'Gi'), ('Gxm', 'Gi', 'Gym'), ('Gxm', 'Gi', 'Gi'), ('Gym', 'Gi', 'Gi'),
('Gx', 'Gx', 'Gi', 'Gy'), ('Gx', 'Gy', 'Gy', 'Gi'), ('Gxm', 'Gxm', 'Gi', 'Gy'), ('Gxm', 'Gx', 'Gi', 'Gym'),
('Gx', 'Gxm', 'Gi', 'Gym'),('Gx', 'Gx', 'Gi', 'Gym'),('Gx', 'Gxm', 'Gi', 'Gy'),('Gxm', 'Gx', 'Gi', 'Gy'),
('Gxm', 'Gym', 'Gy', 'Gi'), ('Gxm', 'Gy', 'Gym', 'Gi'), ('Gx', 'Gym', 'Gym', 'Gi'),
('Gxm', 'Gy', 'Gy', 'Gi'), ('Gx', 'Gy', 'Gym', 'Gi'), ('Gx', 'Gym', 'Gy', 'Gi'),
('Gxm', 'Gxm', 'Gi', 'Gym'), ('Gxm', 'Gym', 'Gym', 'Gi'),
('Gx', 'Gx', 'Gy', 'Gx', 'Gy', 'Gy'), ('Gxm', 'Gxm', 'Gym', 'Gxm', 'Gym', 'Gym')

Following the example outlined in pyGSTi's tutorial '12 Germ selection', we have confirmed that this set of germs remains amplificationally complete under our new extended gate set.

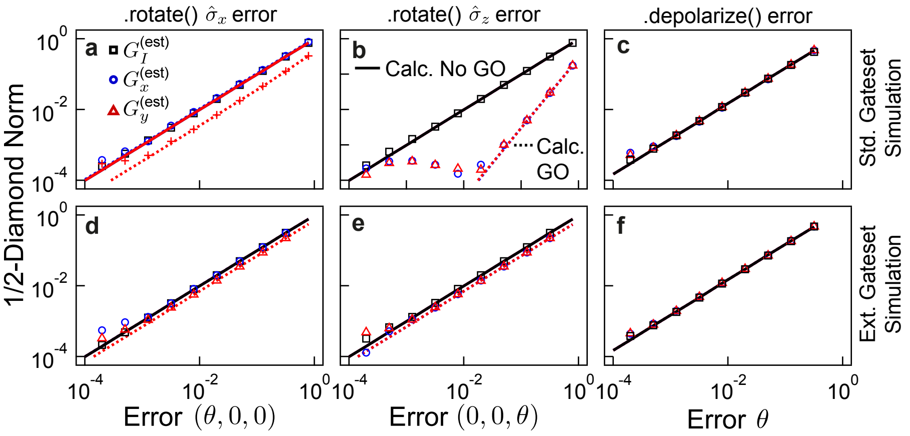

FIGURE D.4. Comparison of the sensitivity of the standard $\{G_x, G_y, G_i\}$ gate set and an extended version$\{G_x, G_y, G_i, -G_x, -G_y\}$ using the built-in .rotate() and .depolarize function.

D3 GST experiments and results

In this section we provide a summary of the key results reported by the pyGSTi analysis toolkit [**169**], version 0.9.2. We show the raw estimates and selected derived quantities from the reports generated by the toolkit and refer to its included tutorials for further descriptions and explanations of the reported quantities. We also provide the datasets, python analysis notebooks and generated reports as separate supplementary files. In these other quantities such as process matrices and the visualised likelihood analyses linked to model violations can be found.

All error cases were measured in direct succession, i.e. for every prescribed GST sequence, $r = 220$ repetitions were recorded for each detuning before proceeding to the next GST sequence. In this way, long term drifts are common mode to all of the separate datasets. The Rabi frequency during all experiments was $\Omega = 22.5$ kHz.

Additional engineered noise cases not considered in detail in the main text are also presented following these tables in a final section.

TABLE D.1. GST estimate of SPAM probabilities

	$\Delta = 0$	$\Delta = 75$ Hz	$\Delta = 500$ Hz	$\Delta = 1$ kHz	$\Delta = 1.4$ kHz
E	0.0044 ± 0.0007	0.0043 ± 0.0007	0.0061 ± 0.0008	0.0064 ± 0.0008	0.0069 ± 0.0009
E_c	0.9956 ± 0.0033	0.9967 ± 0.001	0.995 ± 0.0008	0.9943 ± 0.0007	0.992 ± 0.0008

Target rotation angles are $\{G_i, G_x, G_y\} = \{0, 0.5, 0.5\}$. Process infidelity, trace distance and diamond norm are ideally 0.

TABLE D.2. Estimated performance in the absence of any additive detuning error (Δ =0 Hz).

Gate	Rotation Angle	Process Infidelity	1/2 Trace Distance	1/2 ◇-Norm
Gi	$(0.0022$ $\pm 0.0001)\pi$	0.0012 ± 0.0001	0.0048 ± 0.0002	0.0048 ± 0.0002
Gx	$(0.4995$ $\pm 0.0001)\pi$	0.0001 ± 0.0001	0.0011 ± 0.0001	0.0011 ± 0.0001
Gy	$(0.4998$ $\pm 0.0001)\pi$	0.0004 ± 0.0001	0.0009 ± 0.0001	0.0009 ± 0.0002

TABLE D.3. Estimated performance under $\Delta = 75$ Hz detuning error

Gate	Rotation Angle	Process Infidelity	$^1/_2$ Trace Distance	$^1/_2$ $\diamond$-Norm
Gi	$(0.0032 \pm 0.0001)\pi$	0.0012 ± 0.0001	0.0059 ± 0.0002	0.006 ± 0.0002
Gx	$(0.4996 \pm 0.0001)\pi$	0.0001 ± 0.0001	0.0011 ± 0.0001	0.0011 ± 0.0001
Gy	$(0.5001 \pm 0.0001)\pi$	0.0004 ± 0.0001	0.0009 ± 0.0002	0.0011 ± 0.0002

TABLE D.4. Estimated performance under $\Delta = 500$ Hz detuning error

Gate	Rotation Angle	Process Infidelity	$^1/_2$ Trace Distance	$^1/_2$ $\diamond$-Norm
Gi	$(0.0119 \pm 4 \times 10^{-5})\pi$	0.0002 ± 0.0001	0.019 ± 0.0002	0.0191 ± 0.0002
Gx	$(0.4999 \pm 0.0001)\pi$	0.0003 ± 0.0001	0.0011 ± 0.0001	0.0012 ± 0.0001
Gy	$(0.5007 \pm 0.0001)\pi$	0.0003 ± 0.0001	0.0016 ± 0.0001	0.0018 ± 0.0002

TABLE D.5. Estimated performance under $\Delta = 1000$ Hz detuning error

Gate	Rotation Angle	Process Infidelity	$^1/_2$ Trace Distance	$^1/_2$ $\diamond$-Norm
Gi	$(0.0236 \pm 5 \times 10^{-5})\pi$	0.0014 ± 0.0001	0.0371 ± 0.0001	0.0372 ± 0.0001
Gx	$(0.5009 \pm 0.0001)\pi$	0.0002 ± 0.0001	0.0022 ± 0.0001	0.0022 ± 0.0002
Gy	$(0.5013 \pm 5 \times 10^{-5})\pi$	0.0001 ± 0.0001	0.0027 ± 0.0001	0.0028 ± 0.0002

TABLE D.6. Estimated performance under $\Delta = 1400$ Hz detuning error

Gate	Rotation Angle	Process Infidelity	$1/2$ Trace Distance	$1/2$ $\diamond$-Norm
Gi	$(0.033$ $\pm 4 \times 10^{-5})\pi$	0.0027 ± 0.0001	0.052 ± 0.0003	0.052 ± 0.0003
Gx	$(0.5016$ $\pm 0.0001)\pi$	-5×10^{-6} ± 0.0001	0.0035 ± 0.0001	0.0035 ± 0.0002
Gy	$(0.5016$ $\pm 5 \times 10^{-5})\pi$	0.0002 ± 0.0001	0.0036 ± 0.0001	0.0036 ± 0.0001

TABLE D.7. GST estimate of the logic gate operations in the absence of any additive detuning error ($\Delta = 0$ Hz).

Gate	Superoperator (Pauli basis)	95% C.I. $1/2$-width
Gi	$\begin{pmatrix} 1 & 0.0001 & -0.0001 & 1 \times 10^{-5} \\ 0.0002 & 1 & 0.0005 & -0.0055 \\ -0.0001 & 0.0009 & 1 & 0.0052 \\ -0.0001 & 0.0047 & -0.0046 & 0.9954 \end{pmatrix}$	$\begin{pmatrix} 0.0001 & 0.0001 & 0.0001 & 0.0001 \\ 0.0001 & 0.0001 & 0.0002 & 0.0003 \\ 0.0002 & 0.0002 & 0.0001 & 0.0003 \\ 0.0003 & 0.0003 & 0.0003 & 0.0003 \end{pmatrix}$
Gx	$\begin{pmatrix} 1 & 1 \times 10^{-5} & -0.0002 & 0.0002 \\ 0.0001 & 1 & 0.0007 & 0.001 \\ 4 \times 10^{-5} & 0.0004 & 0.0018 & -0.9998 \\ 0.0001 & -0.0007 & 0.9998 & 0.0011 \end{pmatrix}$	$\begin{pmatrix} 0.0001 & 0.0001 & 0.0001 & 0.0001 \\ 0.0002 & 0.0001 & 0.0003 & 0.0003 \\ 0.0002 & 0.0003 & 0.0003 & 0.0001 \\ 0.0001 & 0.0003 & 0.0001 & 0.0003 \end{pmatrix}$
Gy	$\begin{pmatrix} 1 & 0.0002 & -0.0001 & 0.0002 \\ 0.0002 & 0.0004 & 0.0012 & 0.9991 \\ -0.0002 & 0.0009 & 1 & -0.0002 \\ -0.0002 & -0.9991 & 0.0005 & 0.0007 \end{pmatrix}$	$\begin{pmatrix} 0.0001 & 0.0001 & 0.0001 & 0.0001 \\ 0.0002 & 0.0004 & 0.0003 & 0.0001 \\ 0.0002 & 0.0003 & 0.0001 & 0.0003 \\ 0.0002 & 0.0001 & 0.0003 & 0.0004 \end{pmatrix}$

TABLE D.8. GST estimate of the logic gate operations under $\Delta = 75$ Hz detuning error.

Gate	Superoperator (Pauli basis)	95% C.I. ½-width
Gi	$\begin{pmatrix} 1 & -2\times10^{-5} & -3\times10^{-5} & 2\times10^{-5} \\ -1\times10^{-5} & 0.9999 & 0.0055 & -0.0067 \\ -0.0001 & -0.0041 & 0.9998 & 0.0058 \\ 0.0001 & 0.0065 & -0.0068 & 0.9956 \end{pmatrix}$	$\begin{pmatrix} 0.0001 & 0.0001 & 0.0001 & 0.0001 \\ 0.0002 & 0.0001 & 0.0003 & 0.0005 \\ 0.0002 & 0.0002 & 0.0001 & 0.0003 \\ 0.0003 & 0.0004 & 0.0004 & 0.0003 \end{pmatrix}$
Gx	$\begin{pmatrix} 1 & 5\times10^{-5} & -0.0002 & 0.0002 \\ 0.0002 & 1 & 0.0007 & 0.0012 \\ 0.0001 & 0.0001 & 0.0018 & -0.9998 \\ 0.0001 & -0.0007 & 0.9998 & 0.0007 \end{pmatrix}$	$\begin{pmatrix} 0.0001 & 0.0001 & 0.0001 & 0.0001 \\ 0.0002 & 0.0001 & 0.0003 & 0.0003 \\ 0.0001 & 0.0003 & 0.0003 & 0.0001 \\ 0.0001 & 0.0003 & 0.0001 & 0.0003 \end{pmatrix}$
Gy	$\begin{pmatrix} 1 & 0.0002 & -0.0001 & 0.0002 \\ 0.0003 & -0.0006 & 0.0015 & 0.9993 \\ -0.0001 & 0.0009 & 1 & 0.0002 \\ -0.0003 & -0.9993 & 0.0004 & -2\times10^{-6} \end{pmatrix}$	$\begin{pmatrix} 0.0001 & 0.0001 & 0.0001 & 0.0001 \\ 0.0001 & 0.0004 & 0.0003 & 0.0001 \\ 0.0002 & 0.0003 & 0.0001 & 0.0003 \\ 0.0001 & 0.0001 & 0.0003 & 0.0004 \end{pmatrix}$

TABLE D.9. GST estimate of the logic gate operations under $\Delta = 500$ Hz detuning error.

Gate	Superoperator (Pauli basis)	95% C.I. ½-width
Gi	$\begin{pmatrix} 1 & -5\times10^{-5} & -0.0001 & 0.0001 \\ -0.0001 & 0.9993 & 0.0357 & -0.0097 \\ -0.0001 & -0.0347 & 0.9994 & 0.0083 \\ 0.0001 & 0.0092 & -0.0088 & 1.0004 \end{pmatrix}$	$\begin{pmatrix} 0.0001 & 0.0001 & 0.0001 & 0.0001 \\ 0.0002 & 0.0001 & 0.0003 & 0.0004 \\ 0.0002 & 0.0003 & 0.0001 & 0.0004 \\ 0.0002 & 0.0004 & 0.0004 & 0.0001 \end{pmatrix}$
Gx	$\begin{pmatrix} 1 & 0.0001 & -0.0002 & 0.0002 \\ 0.0002 & 1 & 0.0011 & 0.0018 \\ 3\times10^{-5} & 0.0005 & 0.0003 & -0.9995 \\ 0.0001 & -0.0012 & 0.9994 & 3\times10^{-5} \end{pmatrix}$	$\begin{pmatrix} 0.0001 & 0.0001 & 0.0001 & 0.0001 \\ 0.0002 & 0.0001 & 0.0003 & 0.0003 \\ 0.0001 & 0.0003 & 0.0003 & 0.0001 \\ 0.0001 & 0.0003 & 0.0001 & 0.0003 \end{pmatrix}$
Gy	$\begin{pmatrix} 1 & 0.0002 & -0.0001 & 0.0002 \\ 0.0002 & -0.0026 & 0.0016 & 0.9994 \\ -0.0002 & 0.0011 & 1 & -0.0007 \\ -0.0002 & -0.9995 & 0.0012 & -0.0018 \end{pmatrix}$	$\begin{pmatrix} 0.0001 & 0.0001 & 0.0001 & 0.0001 \\ 0.0001 & 0.0003 & 0.0003 & 0.0001 \\ 0.0002 & 0.0003 & 0.0001 & 0.0003 \\ 0.0001 & 0.0001 & 0.0003 & 0.0003 \end{pmatrix}$

TABLE D.10. GST estimate of the logic gate operations under $\Delta = 1$ kHz detuning error.

Gate	Superoperator (Pauli basis)	95% C.I. ½-width
Gi	$\begin{pmatrix} 1 & 4\times10^{-5} & -0.0001 & 3\times10^{-6} \\ -1\times10^{-5} & 0.9973 & 0.0732 & -0.0073 \\ -0.0002 & -0.0731 & 0.9972 & 0.0078 \\ 0.0001 & 0.0093 & -0.009 & 1 \end{pmatrix}$	$\begin{pmatrix} 0.0001 & 0.0001 & 0.0001 & 0.0001 \\ 0.0003 & 0.0001 & 0.0005 & 0.0005 \\ 0.0002 & 0.0005 & 0.0001 & 0.0005 \\ 0.0002 & 0.0005 & 0.0005 & 0.0001 \end{pmatrix}$
Gx	$\begin{pmatrix} 1 & 4\times10^{-5} & -0.0002 & 0.0002 \\ 0.0001 & 0.9999 & 0.0017 & 0.0023 \\ -2\times10^{-5} & 0.0014 & -0.0026 & -0.9997 \\ -1\times10^{-5} & -0.0021 & 0.9997 & -0.003 \end{pmatrix}$	$\begin{pmatrix} 0.0001 & 0.0001 & 0.0001 & 0.0001 \\ 0.0002 & 0.0001 & 0.0003 & 0.0003 \\ 0.0001 & 0.0003 & 0.0003 & 0.0001 \\ 0.0001 & 0.0003 & 0.0001 & 0.0003 \end{pmatrix}$
Gy	$\begin{pmatrix} 1 & 0.0002 & -0.0001 & 0.0002 \\ 0.0002 & -0.0045 & 0.0022 & 0.9998 \\ -0.0002 & 0.0019 & 1 & -0.0015 \\ -0.0001 & -0.9998 & 0.0018 & -0.0037 \end{pmatrix}$	$\begin{pmatrix} 0.0001 & 0.0001 & 0.0001 & 0.0001 \\ 0.0001 & 0.0002 & 0.0003 & 0.0001 \\ 0.0002 & 0.0003 & 0.0001 & 0.0003 \\ 0.0001 & 0.0001 & 0.0003 & 0.0002 \end{pmatrix}$

TABLE D.11. GST estimate of the logic gate operations under $\Delta = 1.4$ kHz detuning error.

Gate	Superoperator (Pauli basis)	95% C.I. ½-width
Gi	$\begin{pmatrix} 1 & 0.0001 & -4\times10^{-5} & -4\times10^{-5} \\ 0.0001 & 0.9947 & 0.1035 & -0.0045 \\ -0.0001 & -0.1032 & 0.9946 & 0.005 \\ 0.0001 & 0.0053 & -0.0054 & 1 \end{pmatrix}$	$\begin{pmatrix} 0.0001 & 0.0001 & 0.0001 & 0.0001 \\ 0.0003 & 0.0001 & 0.0006 & 0.0005 \\ 0.0003 & 0.0006 & 0.0001 & 0.0005 \\ 0.0002 & 0.0006 & 0.0005 & 0.0001 \end{pmatrix}$
Gx	$\begin{pmatrix} 1 & 0.0001 & -0.0002 & 0.0002 \\ 0.0002 & 1 & 0.0035 & 0.0031 \\ 0.0001 & 0.0031 & -0.0051 & -1.0001 \\ 3\times10^{-5} & -0.0027 & 1 & -0.0047 \end{pmatrix}$	$\begin{pmatrix} 0.0001 & 0.0001 & 5\times10^{-5} & 0.0001 \\ 0.0002 & 0.0001 & 0.0003 & 0.0002 \\ 0.0001 & 0.0002 & 0.0003 & 0.0001 \\ 0.0001 & 0.0003 & 0.0001 & 0.0003 \end{pmatrix}$
Gy	$\begin{pmatrix} 1 & 0.0002 & -0.0001 & 0.0002 \\ 0.0002 & -0.005 & 0.0031 & 0.9995 \\ -0.0003 & 0.0027 & 0.9999 & -0.0031 \\ -0.0002 & -0.9996 & 0.0035 & -0.0052 \end{pmatrix}$	$\begin{pmatrix} 0.0001 & 0.0001 & 0.0001 & 5\times10^{-5} \\ 0.0001 & 0.0002 & 0.0003 & 0.0001 \\ 0.0002 & 0.0003 & 0.0001 & 0.0003 \\ 0.0001 & 0.0001 & 0.0003 & 0.0002 \end{pmatrix}$

The tables below report the comparison between the computed estimate based on GST's completely positive trace preserving (CPTP) model and the experimental data given to the analysis routine. Here, N_S and N_p are the number of gate strings and fit parameters, respectively. The quantity $2\Delta\log(\mathcal{L})$ measures the goodness of fit of the GST model (small is better) and is expected to lie within $[k - \sqrt{2k}, k + \sqrt{2k}]$ where $k = N_s - N_p$. $N_\sigma = (2\Delta\log(\mathcal{L}) - k)/\sqrt{2k}$ is the number of standard deviations from the mean and provides an indication of the agreement with the model underlying the GST analysis. The star rating is a crude indication of the strength of model violation seen. Detailed reports and data are available on request. More detailed explanations can be found in the tutorials and generated reports of the pyGSTi toolkit [**169**].

TABLE D.12. GST goodness of fit in the absence of any additive detining error ($\Delta = 0$ Hz)

L	$2\Delta\log(\mathcal{L})$	k	$2\Delta\log(\mathcal{L}) - k$	$\sqrt{2k}$	N_σ	N_s	N_p	Rating
1	49.457	52	-2.5432	10.198	-0.25	92	40	★★★★★
2	119.78	128	-8.2157	16	-0.51	168	40	★★★★★
4	456.12	401	55.122	28.32	1.95	441	40	★★★★
8	860.83	777	83.827	39.421	2.13	817	40	★★★★
16	1368.5	1161	207.46	48.187	4.31	1201	40	★★★★
32	1922.7	1545	377.69	55.588	6.79	1585	40	★★★★
64	3082.7	1929	1153.7	62.113	18.6	1969	40	★★★★
128	7860	2313	5547	68.015	81.6	2353	40	★★★
256	2×10^4	2697	2×10^4	73.444	2×10^2	2737	40	★★

TABLE D.13. GST goodness of fit under Δ =75 Hz detuning error

L	$2\Delta\log(\mathcal{L})$	k	$2\Delta\log(\mathcal{L}) - k$	$\sqrt{2k}$	N_σ	N_s	N_p	Rating
1	59.185	52	7.1851	10.198	0.7	92	40	★★★★★
2	145.12	128	17.117	16	1.07	168	40	★★★★
4	448.75	401	47.751	28.32	1.69	441	40	★★★★
8	889.84	777	112.84	39.421	2.86	817	40	★★★★
16	1358	1161	197.02	48.187	4.09	1201	40	★★★★
32	1882.3	1545	337.29	55.588	6.07	1585	40	★★★★
64	2903.9	1929	974.94	62.113	15.7	1969	40	★★★★
128	7715.9	2313	5402.9	68.015	79.4	2353	40	★★★
256	2×10^4	2697	2×10^4	73.444	2×10^2	2737	40	★★

Table D.14. GST goodness of fit under Δ =500 Hz detuning error

L	$2\Delta\log(\mathcal{L})$	k	$2\Delta\log(\mathcal{L})-k$	$\sqrt{2k}$	N_σ	N_s	N_p	Rating
1	67.508	52	15.508	10.198	1.52	92	40	★★★★
2	138.08	128	10.082	16	0.63	168	40	★★★★★
4	424.26	401	23.261	28.32	0.82	441	40	★★★★★
8	882.46	777	105.46	39.421	2.68	817	40	★★★★
16	1329.8	1161	168.78	48.187	3.5	1201	40	★★★★
32	1857.7	1545	312.67	55.588	5.62	1585	40	★★★★
64	2861.8	1929	932.76	62.113	15	1969	40	★★★★
128	5637	2313	3324	68.015	48.9	2353	40	★★★★
256	1×10^4	2697	7957.3	73.444	1×10^2	2737	40	★★★

Table D.15. GST goodness of fit under Δ =1 kHz detuning error

L	$2\Delta\log(\mathcal{L})$	k	$2\Delta\log(\mathcal{L})-k$	$\sqrt{2k}$	N_σ	N_s	N_p	Rating
1	55.22	52	3.2203	10.198	0.32	92	40	★★★★★
2	129.21	128	1.2101	16	0.08	168	40	★★★★★
4	426.82	401	25.821	28.32	0.91	441	40	★★★★★
8	774.03	777	-2.9656	39.421	-0.08	817	40	★★★★★
16	1308.9	1161	147.9	48.187	3.07	1201	40	★★★★
32	1862.4	1545	317.37	55.588	5.71	1585	40	★★★★
64	2565.1	1929	636.14	62.113	10.2	1969	40	★★★★
128	4743.6	2313	2430.6	68.015	35.7	2353	40	★★★★
256	7622.6	2697	4925.6	73.444	67.1	2737	40	★★★★

Table D.16. GST goodness of fit under Δ =1.4 Hz detuning error

L	$2\Delta\log(\mathcal{L})$	k	$2\Delta\log(\mathcal{L})-k$	$\sqrt{2k}$	N_σ	N_s	N_p	Rating
1	80.609	52	28.609	10.198	2.81	92	40	★★★★
2	149.36	128	21.356	16	1.33	168	40	★★★★
4	447.87	401	46.871	28.32	1.66	441	40	★★★★
8	897.86	777	120.86	39.421	3.07	817	40	★★★★
16	1427.1	1161	266.15	48.187	5.52	1201	40	★★★★
32	1970	1545	425.04	55.588	7.65	1585	40	★★★★
64	2585.6	1929	656.62	62.113	10.6	1969	40	★★★★
128	4421.8	2313	2108.8	68.015	31	2353	40	★★★★
256	7240.9	2697	4543.9	73.444	61.9	2737	40	★★★★